

¹ **Searches for Supersymmetric signatures in
2 all hadronic final states with the α_T
3 variable.**

⁴ Darren Burton

⁵ Imperial College London
⁶ Department of Physics

⁷ A thesis submitted to Imperial College London
⁸ for the degree of Doctor of Philosophy

Abstract

A search for supersymmetric particles with in events with a missing energy signature and high p_T jets, is conducted using data recorded by the Compact Muon Solenoid detector based at the Large Hadron Collider. The analysis is performed with 11.7 fb^{-1} of data, collected with a center-of-mass collision energy of 8 TeV during the 2012 run period. The dimensionless kinematic variable α_T is used as a tool to select events with genuine missing energy signatures, whilst Standard Model backgrounds in the signal region are estimated using data driven control samples, which have similar kinematic to the signal region. No excess of over Standard Model expectations is found. Exclusion limits are set at the 95% confidence level in the parameter space of a range of supersymmetric simplified model topologies, with special emphasis on those with compressed spectra (small mass splittings) and natural SUSY scenarios (large number of b flavoured quarks). A complementary method to search for natural SUSY signatures with a high number of b-flavoured jets, through the use of a simple template fit is also presented. The event selections of the α_T search are used as a vehicle to demonstrate proof of principle of the technique in both data and simulation. Estimated Standard Model backgrounds from the template fits are compared with those determined from the data driven background estimation method of the α_T search within the signal search region, where good agreement between the individual predictions and that of data are observed. Additionally the efficiency of the hadronic Level-1 single jet triggers are measured throughout the 2012 run period, where a change to the jet seed algorithm was implemented during the data taking period. This change was introduced to negate an increase in rate which can be attributed to pileup jets, whilst maintaining similar performance in the triggering of physics events.

39

Declaration

40 I, the author of this thesis, declare that the work presented within this
41 document to be my own. The work presented in Chapters 4, 5, 6 and Section
42 3.4, is a result of the author's own work or that of which I have been a major
43 contributor unless explicitly stated otherwise, and is carried out within the
44 context of the Imperial College London and CERN SUSY groups, itself a
45 subsection of the greater CMS collaboration. All figures and studies taken
46 from external sources are referenced appropriately throughout this document.

47

Darren Burton

48

Acknowledgements

49 I would like to thank the many people whom I have had the pleasure of working with
50 during the course of the last three and a half years. The opportunity to work as part one
51 of the largest scientific collaborations during one of the most exciting times in particle
52 physics for decades, has been a real privilege to be a part of. I could not have achieved
53 the results presented in this thesis without the help of my colleagues who were part of the
54 RA1 team, Edward Laird, Chris Lucas, Henning Flaecher, Yossof Eshaq, Bryn Mathais,
55 Sam Rogerson, Zhaoxia Meng and Georgia Karapostoli whom I worked with on L1 jets. I
56 also thank my supervisor Oliver Buchmuller for his guidance in getting me to this point.

57 I also feel it important to single out thanks to the postdocs that I have worked with during
58 my PhD. Jad Marrouche from whom I have learnt a great deal and Robert Bainbridge
59 who has been like a second supervisor to me, helping me during my time at Imperial and
60 CERN, especially during those most stressful of times approaching conference deadlines!

61 My fellow PhD students who I live with and have seen on an almost daily basis for the
62 last few years, Andrew Gilbert, Patrick Owen, Indrek Sepp, Matthew Kenzie and my
63 girlfriend Hannah. Thanks for putting up with the whinging, complaining and clopping.

64 Finally my largest thanks go to my Mum and Dad whose patience, encouragement and
65 considerable financial support have allowed me to take the many steps that lead me here
66 today.

67 **Contents**

68	List of Figures	viii
69	List of Tables	xiv
70	1. Introduction	2
71	2. A Theoretical Overview	5
72	2.1. The Standard Model	5
73	2.1.1. Gauge Symmetries of the SM	7
74	2.1.2. The Electroweak Sector and Electroweak Symmetry Breaking	9
75	2.2. Motivation for Physics Beyond the Standard Model	13
76	2.3. Supersymmetry Overview	14
77	2.3.1. R-Parity	16
78	2.4. Experimental Signatures of SUSY at the LHC	16
79	2.4.1. Simplified models	18
80	3. The LHC And The CMS Detector	20
81	3.1. The LHC	20
82	3.2. The CMS Detector	23
83	3.2.1. Detector subsystems	23
84	3.2.2. Tracker	24
85	3.2.3. Electromagnetic calorimeter	25
86	3.2.4. Hadronic calorimeter	26
87	3.2.5. Muon systems	28
88	3.3. Event Reconstruction and Object Definition	28
89	3.3.1. Jets	28
90	3.3.2. B-tagging	30
91	3.4. Triggering System	33
92	3.4.1. The Level-1 trigger	34

93	3.4.2. The L1 trigger jet algorithm	35
94	3.4.3. Measuring L1 jet trigger efficiencies	37
95	3.4.4. Effects of the L1 jet seed	38
96	3.4.5. Robustness of L1 jet performance against pile-up	40
97	3.4.6. Summary	43
98	4. SUSY Searches In Hadronic Final States	45
99	4.1. An Introduction to the α_T Search	46
100	4.1.1. The α_T variable	48
101	4.2. Search Strategy	50
102	4.2.1. Physics objects	53
103	4.2.2. Event selection	57
104	4.2.3. Control sample definition and background estimation	60
105	4.2.4. Estimating the QCD multi-jet background	67
106	4.3. Trigger Strategy	69
107	4.4. Measuring MC Normalisation Factors via H_T Sidebands	70
108	4.5. Determining MC Simulation Yields with Higher Statistical Precision	71
109	4.5.1. The formula method	72
110	4.5.2. Establishing proof of principle	73
111	4.5.3. Correcting measured efficiencies in simulation to data	74
112	4.6. Systematic Uncertainties on Transfer Factors	76
113	4.6.1. Determining systematic uncertainties from closure tests	80
114	4.7. Simplified Models, Efficiencies and Systematic Uncertainties	83
115	4.7.1. Signal efficiency	83
116	4.7.2. Applying b-tag scale factor corrections in signal samples	84
117	4.7.3. Experimental uncertainties	86
118	4.8. Statistical Framework	88
119	4.8.1. Hadronic sample	88
120	4.8.2. H_T evolution model	89
121	4.8.3. Electroweak Sector (EWK) control samples	90
122	4.8.4. Contributions from signal	92
123	4.8.5. Total likelihood	93
124	5. Results and Interpretation	95
125	5.1. Standard Model	95
126	5.2. SUSY	104
127	5.2.1. The CL_s method	104

128	5.2.2. Interpretation in simplified signal models	105
129	6. Searches For Natural SUSY With B-tag Templates.	109
130	6.1. Concept	109
131	6.2. Application to the α_T Search	111
132	6.2.1. Proof of principle in simulation	112
133	6.2.2. Results in a data control sample	115
134	6.2.3. Application to the α_T hadronic search region	117
135	6.3. Summary	119
136	7. Conclusions	120
137	A. Miscellaneous	122
138	A.1. Jet Identification Criteria	122
139	A.2. Primary Vertices	123
140	B. L1 Jets	124
141	B.1. Jet matching efficiencies	124
142	B.2. Leading Jet Energy Resolution	125
143	B.3. Resolution for Energy Sum Quantities	128
144	C. Additional material on background estimation methods	133
145	C.1. Determination of k_{QCD}	133
146	C.2. Effect of varying background cross sections on closure tests	134
147	D. Additional Material For B-tag Template Method	136
148	D.1. Templates Fits in Simulation	136
149	D.2. Pull Distributions for Template Fits	139
150	D.3. Templates Fits in Data Control Sample	140
151	D.4. Templates Fits in Data Signal Region	142
152	Bibliography	145

¹⁵³ List of Figures

¹⁵⁴ 2.1.	One loop quantum corrections to the Higgs squared mass parameter m_h^2 due to a fermion.	14
¹⁵⁶ 2.2.	Two example simplified model decay chains.	19
¹⁵⁷ 3.1.	A top down layout of the LHC, with the position of the four main detectors labelled.	21
¹⁵⁹ 3.2.	The total integrated luminosity delivered to and collected by Compact Muon Solenoid (CMS) during the 2012 8 TeV pp runs	22
¹⁶¹ 3.3.	A pictorial depiction of the CMS detector.	24
¹⁶² 3.4.	Illustration of the CMS Electromagnetic CALorimeter (ECAL).	26
¹⁶³ 3.5.	Schematic of the CMS Hadronic CALorimeter (HCAL).	27
¹⁶⁴ 3.6.	Combined Secondary Vertex (CSV) algorithm discriminator values in enriched ttbar and inclusive multi jet samples	31
¹⁶⁶ 3.7.	Data/MC b-tag scale factors derived using the Combined Secondary Vertex Medium Working Point (CSVM) tagger.	32
¹⁶⁸ 3.8.	Data/MC mis-tag scale factors derived using the CSVM tagger.	33
¹⁶⁹ 3.9.	The CMS Level 1 Trigger (L1) Trigger system.	34
¹⁷⁰ 3.10.	Illustration of the Level-1 jet finding algorithm.	36
¹⁷¹ 3.11.	L1 jet efficiency turn-on curves as a function of the offline CaloJet and PFJet E_T	38
¹⁷³ 3.12.	L1 jet efficiency turn-on curves as a function of the offline CaloJet E_T for the 2012 run period B and C.	39

175	3.13. Trigger cross section for the L1HTT150 trigger path.	40
176	3.14. L1 H_T efficiency turn-on curves as a function of the offline CaloJet H_T	41
177	3.15. L1 jet efficiency turn-on curves as a function of the leading offline E_T Calo	
178	(left) and PF (right) jet, for low, medium and high pile-up conditions.	42
179	3.16. Fit values from an Exponentially Modified Gaussian (EMG) function fitted	
180	to the resolution plots of leading Calo jet E_T measured as a function of	
181	$\frac{(L1\ E_T - \text{Offline}\ E_T)}{\text{Offline}\ E_T}$ for low, medium and high pile-up conditions.	43
182	3.17. Fit values from an EMG function fitted to the resolution plots of leading	
183	PF jet E_T measured as a function of $\frac{(L1\ E_T - \text{Offline}\ E_T)}{\text{Offline}\ E_T}$ for low, medium and	
184	high pile-up conditions.	44
185	4.1. Reconstructed offline H_T distribution in the hadronic signal selection, from	
186	11.7fb^{-1} of data, in which no α_T requirement is made.	48
187	4.2. The event topologies of background QCD dijet events (right) and a generic	
188	SUSY signature with genuine Z_T (left).	48
189	4.3. The α_T distributions for the low 2-3 (left) and high ≥ 4 (right) jet	
190	multiplicities after a full analysis selection and shown for $H_T > 375$	50
191	4.4. Pictorial depiction of the analysis strategy employed by the α_T search to	
192	increase sensitivity to a wide spectra of SUSY models.	53
193	4.5. Data/MC comparisons of key variables for the hadronic signal region.	60
194	4.6. Data/MC comparisons of key variables for the $\mu +$ jets selection.	63
195	4.7. Data/MC comparisons of key variables for the $\mu\mu +$ jets selection.	65
196	4.8. Data/MC comparisons of key variables for the $\gamma +$ jets selection.	66
197	4.9. QCD sideband regions, used for determination of k_{QCD}	68
198	4.10. Tagging efficiencies of (a) b-jets, (b) c-jets, and (c) light-jets determined	
199	from all jets within each individual analysis H_T bin.	75
200	4.11. Sets of closure tests overlaid on top of the systematic uncertainty used for	
201	each of the five H_T regions.	82

202	4.12. Signal efficiencies fo the Simplified Model Spectra (SMS) models (a) T1 203 and (b) T2.	84
204	5.1. Comparison of the observed yields and Standard Model (SM) expectations 205 given by the simultaneous fit in bins of H_T for the (a) hadronic, (b) $\mu +$ 206 jets, (c) $\mu\mu +$ jets and (d) $\gamma +$ jets samples when requiring $n_b^{reco} = 0$ and 207 $n_{jet} \leq 3$	97
208	5.2. Comparison of the observed yields and SM expectations given by the 209 simultaneous fit in bins of H_T for the (a) hadronic, (b) $\mu +$ jets, (c) $\mu\mu +$ 210 jets and (d) $\gamma +$ jets samples when requiring $n_b^{reco} = 1$ and $n_{jet} \leq 3$	98
211	5.3. Comparison of the observed yields and SM expectations given by the 212 simultaneous fit in bins of H_T for the (a) hadronic, (b) $\mu +$ jets, (c) $\mu\mu +$ 213 jets and (d) $\gamma +$ jets samples when requiring $n_b^{reco} = 2$ and $n_{jet} \leq 3$	99
214	5.4. Comparison of the observed yields and SM expectations given by the 215 simultaneous fit in bins of H_T for the (a) hadronic, (b) $\mu +$ jets, (c) $\mu\mu +$ 216 jets and (d) $\gamma +$ jets samples when requiring $n_b^{reco} = 0$ and $n_{jet} \geq 4$	100
217	5.5. Comparison of the observed yields and SM expectations given by the 218 simultaneous fit in bins of H_T for the (a) hadronic, (b) $\mu +$ jets, (c) $\mu\mu +$ 219 jets and (d) $\gamma +$ jets samples when requiring $n_b^{reco} = 1$ and $n_{jet} \geq 4$	101
220	5.6. Comparison of the observed yields and SM expectations given by the 221 simultaneous fit in bins of H_T for the (a) hadronic, (b) $\mu +$ jets, (c) $\mu\mu +$ 222 jets and (d) $\gamma +$ jets samples when requiring $n_b^{reco} = 2$ and $n_{jet} \geq 4$	102
223	5.7. Comparison of the observed yields and SM expectations given by the 224 simultaneous fit in bins of H_T for the (a) hadronic, (b) $\mu +$ jets, (c) $\mu\mu +$ 225 jets and (d) $\gamma +$ jets samples when requiring $n_b^{reco} = 3$ and $n_{jet} \geq 4$	102
226	5.8. Comparison of the observed yields and SM expectations given by the 227 simultaneous fit in bins of H_T for the (a) hadronic, (b) $\mu +$ jets, (c) $\mu\mu +$ 228 jets and (d) $\gamma +$ jets samples when requiring $n_b^{reco} \geq 4$ and $n_{jet} \geq 4$	103
229	5.9. Production and decay modes for the various SMS models interpreted 230 within the analysis.	107
231	5.10. Upper limit of cross section at 95% CL as a function of $m_{\tilde{q}/\tilde{g}}$ and m_{LSP} 232 for various SMS models.	108

233	6.1. The b-tagging (a), c-quark mis-tagging (b), and light-quark mis-tagging rate (c) as measured in simulation after the α_T analysis, $\mu + \text{jets}$ control sample selection in the region $H_T > 375$	111
236	6.2. The results of fitting the $Z = 0$ and $Z = 2$ templates to the $n_b^{reco} = 0, 1, 2$ bins taken directly from simulation in the region $H_T > 375$ GeV, for the $n_{jet} \geq 5$ category.	114
239	6.3. The results of fitting the $Z = 0$ and $Z = 2$ templates to the $n_b^{reco} = 0, 1, 2$ bins taken from data, for the $n_{jet} \geq 5$ category and medium CSV working point.	116
242	6.4. The results of fitting the $Z = 0$ and $Z = 2$ templates to the $n_b^{reco} = 0, 1, 2$ bins taken from data, in the $n_{jet} \geq 5$ and $H_T > 375$ category for all CSV working points.	118
245	B.1. Leading jet matching efficiency as a function of the offline CaloJet E_T	124
246	B.2. Resolution plots of the leading offline Calo E_T measured as a function of $\frac{(L1 E_T - \text{Offline } E_T)}{\text{Offline } E_T}$ for low (a), medium (b) and high (c) pile-up conditions.	126
248	B.3. Resolution plots of the leading off-line PF E_T measured as a function of $\frac{(L1 E_T - \text{Offline } E_T)}{\text{Offline } E_T}$ for low (a), medium (b) and high (c) pile-up conditions.	128
250	B.4. $\sum E_T$ resolution parameters in bins of Calo $\sum E_T$ measured for the defined low, medium and high pile up conditions.	129
252	B.5. $\sum E_T$ resolution parameters in bins of PF $\sum E_T$ measured for the defined low, medium and high pile up conditions.	129
254	B.6. \cancel{E}_T resolution parameters in bins of Calo \cancel{E}_T measured for the defined low, medium and high pile up conditions.	130
256	B.7. \cancel{E}_T resolution parameters in bins of PF \cancel{E}_T measured for the defined low, medium and high pile up conditions.	130
258	B.8. H_T resolution parameters in bins of Calo H_T measured for the defined low, medium and high pile up conditions.	131
260	B.9. H_T resolution parameters in bins of PF H_T measured for the defined low, medium and high pile up conditions.	131

262	B.10. \mathcal{H}_T resolution parameters in bins of \mathcal{H}_T measured for the defined low,	
263	medium and high pile up conditions.	132
264	B.11. \mathcal{H}_T resolution parameters in bins of PF \mathcal{H}_T measured for the defined low,	
265	medium and high pile up conditions.	132
266	C.1. $R_{\alpha_T}(H_T)$ and exponential fits for each of the data sideband regions. Fit is	
267	conducted between the H_T region $275 < H_T < 575$	133
268	C.2. Sets of closure tests overlaid on top of the systematic uncertainty used for	
269	each of the five H_T regions.	134
270	C.3. Sets of closure tests overlaid on top of the systematic uncertainty used for	
271	each of the five H_T regions.	134
272	D.1. The results of fitting the $Z = 0$ and $Z = 2$ templates to the $n_b^{reco} = 0, 1, 2$	
273	bins taken directly from simulation in the region $H_T > 375$ GeV, for the	
274	$n_{jet} = 3$ category.	137
275	D.2. The results of fitting the $Z = 0$ and $Z = 2$ templates to the $n_b^{reco} = 0, 1, 2$	
276	bins taken directly from simulation in the region $H_T > 375$ GeV, for the	
277	$n_{jet} = 4$ category.	138
278	D.3. Pull distributions of $\frac{(\theta - \hat{\theta})}{\sigma}$ for 10^4 pseudo-experiments generated from a	
279	gaussian distribution centred on the n_b^{reco} template values from simulation	
280	with width σ	139
281	D.4. The results of fitting the $Z = 0$ and $Z = 2$ templates to the $n_b^{reco} = 0, 1, 2$	
282	bins taken directly from data, for the $n_{jet} = 3$ category and medium CSV	
283	working point.	140
284	D.5. The results of fitting the $Z = 0$ and $Z = 2$ templates to the $n_b^{reco} = 0, 1, 2$	
285	bins taken directly from data, for the $n_{jet} = 4$ category and medium CSV	
286	working point.	141
287	D.6. The results of fitting the $Z = 0$ and $Z = 2$ templates to the $n_b^{reco} = 0, 1, 2$	
288	bins taken from data, in the $n_{jet} = 3$ and $H_T > 375$ category for all CSV	
289	working points.	142

290	D.7. The results of fitting the $Z = 0$ and $Z = 2$ templates to the $n_b^{reco} = 0, 1, 2$	
291	bins taken from data, in the $n_{jet} = 4$ and $H_T > 375$ category for all CSV	
292	working points.	143

List of Tables

294	2.1. The fundamental particles of the SM, with spin, charge and mass displayed.	6
295	3.1. Results of a cumulative EMG function fit to the turn-on curves for L1	
296	single jet triggers in 2012 Run Period C.	38
297	3.2. Results of a cumulative EMG function fit to the turn-on curves for L1	
298	single jet triggers in the 2012 run period B and C.	40
299	3.3. Results of a cumulative EMG function fit to the turn-on curves for H_T in	
300	2012 run period B and C.	41
301	3.4. Results of a cumulative EMG function fit to the efficiency turn-on curves	
302	for L1 single jet triggers in the 2012 run period C, for low,medium and	
303	high pile-up conditions.	41
304	3.5. Results of a cumulative EMG function fit to the efficiency turn-on curves	
305	for Level-1 single jet triggers in the 2012 run period C, for low,medium	
306	and high pile-up conditions.	42
307	4.1. A summary of the SMS models interpreted in this analysis, involving both	
308	direct (D) and gluino-induced (G) production of squarks and their decays.	46
309	4.2. Muon Identification criteria used within the analysis for selection/veto	
310	purposes in the muon control/signal selections.	54
311	4.3. Photon Identification criteria used within the analysis for selection/veto	
312	purposes in the $\gamma +$ jets control/signal selections.	55
313	4.4. Electron Identification criteria used within the analysis for veto purposes.	56
314	4.5. Noise filters that are applied to remove spurious and non-physical \cancel{E}_T	
315	signatures within the CMS detector.	57

316	4.6. Jet thresholds used in the three H_T regions of the analysis.	58
317	4.7. Best fit values for the parameters k_{QCD} obtained from sideband regions	
318	B,C ₁ ,C ₂ ,C ₃	69
319	4.8. Measured efficiencies of the H_T and α_T legs of the HT and HT_alphaT	
320	triggers in independent analysis bins.	70
321	4.9. k-factors calculated for different EWK processes.	71
322	4.10. Comparing yields in simulation within the $\mu + \text{jets}$ selection determined	
323	from the formula method described in Equation (4.11), and that taken	
324	directly from simulation	74
325	4.11. The absolute change in the Transfer Factor (TF)'s used to predict the	
326	entire signal region SM background, using the $\mu + \text{jets}$ control sample	
327	when the systematic uncertainties of the data to simulation scale factors	
328	are varied by $\pm 1\sigma$	76
329	4.12. A summary of the results obtained from fits of zeroeth order polynomials	
330	(i.e. a constant) to five sets of closure tests performed in the $2 \leq n_{\text{jet}} \leq 3$	
331	bin	79
332	4.13. A summary of the results obtained from fits of zeroeth order polynomials	
333	(i.e. a constant) to five sets of closure tests performed in the $n_{\text{jet}} \geq 4$ bin	
334	79	
335	4.14. A summary of the results obtained from fits of zeroeth order polynomials	
336	(i.e. a constant) to five sets of closure tests performed in the $2 \leq n_{\text{jet}} \leq 3$	
337	bin	79
338	4.15. Calculated systematic uncertainties for the five H_T regions, determined	
339	from the closure tests.	81
340	4.16. Estimates of systematic uncertainties on the signal efficiency (%) for	
341	various SMS models when considering points in the region near to the	
342	diagonal	88
343	4.17. Estimates of systematic uncertainties on the signal efficiency (%) for	
344	various SMS models when considering points in the region near to the	
345	diagonal	88
	4.18. The systematic parameters used in H_T bins.	92

346	4.19. Nuisance parameters used within the different hadronic signal bins of the analysis	94
347		
348	5.1. Summary of control samples used by each fit results, and the Figures in which they are displayed.	96
349		
350	5.2. Comparison of the measured yields in the each H_T , n_{jet} and n_b^{reco} jet multiplicity bins for the hadronic sample with the SM expectations and combined statistical and systematic uncertainties given by the simultaneous fit.	96
351		
352		
353		
354	5.3. A table representing the SMS models interpreted within the analysis.	105
355		
356	6.1. Typical underlying b-quark content of different SM processes which are common to many SUSY searches.	110
357		
358	6.2. Summary of the fit predictions in the n_b^{reco} signal region for $n_{jet} = 3, = 4, \geq 5$. The fit region is $n_b^{reco} = 0, 1, 2$ and simulation yields are normalised to an integrated luminosity of 10 fb^{-1}	113
359		
360	6.3. Summary of the fit predictions in the n_b^{reco} signal region of the $\mu + \text{jets}$ control sample, for $n_{jet} = 3, = 4, \geq 5$. The fit region is $n_b^{reco} = 0, 1, 2$ using 11.5 fb^{-1} of data at $\sqrt{s} = 8\text{TeV}$	115
361		
362		
363	6.4. Summary of the fit predictions in the n_b^{reco} signal region of the $\mu + \text{jets}$ control sample, for $n_{jet} = 3, = 4, \geq 5$. The fit region is $n_b^{reco} = 0, 1, 2$ using 11.5 fb^{-1} of data at $\sqrt{s} = 8\text{TeV}$	117
364		
365		
366	A.1. Criteria for a reconstructed jet to pass the loose calorimeter jet id.	122
367		
368	A.2. Criteria for a reconstructed jet to pass the loose PF jet id.	123
369		
370	A.3. Criteria for a vertex in an event to be classified as a 'good' reconstructed primary vertex.	123
371		
372	B.1. Results of a cumulative EMG function fit to the turn-on curves for the matching efficiency of the leading jet in an event to a Level-1 jet in run 2012C and 2012B data.	125

373	C.1. Translation factors constructed from the $\mu +$ jets control sample and signal selection MC, to predict yields for the $W +$ jets and $t\bar{t}$ back-grounds in the signal region.	135
374		
375		

³⁷⁶

“The Universe is about 1,000,000 years old.”

— Matthew Kenzie, 1987-present : Discoverer of the Higgs Boson.

³⁷⁷

Chapter 1.

³⁷⁸ Introduction

³⁷⁹ During the 20th century, great advances have been made in the human understanding
³⁸⁰ of the universe, it's origins, it's future and its composition. The Standard Model (**SM**)
³⁸¹ first formulated in the 1960's is one of the crowning achievements in science's quest to
³⁸² explain the most fundamental processes and interactions that make up our universe. It
³⁸³ has provided a highly successful explanation of a wide range of phenomena in Particle
³⁸⁴ Physics and has stood up to extensive experimental scrutiny [1].

³⁸⁵ Despite it's successes it is not a complete theory, with significant questions remaining
³⁸⁶ unanswered. It describes only three of the four known forces with gravity not incorporated
³⁸⁷ within the framework of the **SM**. Cosmological experiments infer that just $\sim 4\%$ of the
³⁸⁸ observable universe exists as matter, with elusive "Dark Matter" accounting for a further
³⁸⁹ $\sim 23\%$ [2]. However no particle predicted by the **SM** is able to account for it. At higher
³⁹⁰ energy scales and small distances, the (non-)unification of the fundamental forces point
³⁹¹ to problems with the **SM** at least at higher energies not yet probed experimentally.

³⁹² Many theories exist as extensions to the **SM**, predicting a range of observables that can
³⁹³ be detected at the Large Hadron Collider (**LHC**) of which SUperSYmmetry (**SUSY**) is
³⁹⁴ one such example. It predicts a new symmetry of nature in which all current particles
³⁹⁵ in the **SM** would have a corresponding supersymmetric partner. Common to most
³⁹⁶ Supersymmetric theories is a stable, weakly interacting Lightest Supersymmetric Partner
³⁹⁷ (**LSP**), which has the properties of a possible dark matter candidate. The **SM** and the
³⁹⁸ main principles of Supersymmetric theories are outlined in Chapter 2, with emphasis
³⁹⁹ placed on how experimental signatures of **SUSY** may reveal themselves in proton collisions
⁴⁰⁰ at the **LHC**.

401 The experimental goal of the **LHC** is to further test the framework of the **SM**, exploring the
402 TeV mass scale for the first time, and to seek a connection between the particles produced
403 in proton collisions and dark matter. The first new discovery by this extraordinary
404 machine was announced on the 4th of July 2012. The long-awaited discovery was the
405 culmination of decades of experimental endeavours in the search for the Higgs boson,
406 providing an answer to the mechanism of electroweak symmetry breaking within the **SM**
407 [3][4].

408 This discovery was made possible through data taken by the two multi purpose detectors
409 (**Compact Muon Solenoid (CMS)**) and **A Toroidal LHC ApparatuS (ATLAS)**) located
410 on the **LHC** ring. An experimental description of the **CMS** detector and the **LHC** is
411 described in Chapter 3, including some of the object reconstruction used by **CMS** in
412 searches for **SUSY** signatures.

413 The performance of the **CMS** Level-1 single jet trigger, measured over the course of
414 the year is also included within this chapter. The Level-1 triggers are of paramount
415 importance to the recording of physics events at **CMS**, and to which a change in the jet
416 seed algorithm was introduced approximately half way through the data taking period.
417 The aim of this change, was to facilitate a reduction in the rate at which data from
418 events not of interest to physics analyses were recorded, whilst avoiding impact on those
419 which were.

420 Chapter 4, contains a description of the search for evidence of the production of Su-
421 persymmetric particles at the **LHC**. The main basis of the search centres around the
422 kinematic dimensionless α_T variable, which provides strong rejection of backgrounds with
423 fake missing energy signatures whilst maintaining good sensitivity to a variety of **SUSY**
424 topologies. The author's work (as an integral part of the analysis group) is documented
425 in detail, which has culminated in numerous publications over the past two years, the
426 latest of which was published in the European Physical Journal C (**EPJC**) [5]. The results
427 and interpretations within the framework of a variety of Simplified Model Spectra (**SMS**),
428 which describe an array of possible **SUSY** event topologies is documented in Chapter 5.

429 The author in particular has played a major role in the extension of the α_T analysis into
430 the additional b-tagged and jet multiplicity dimensions increasing the sensitivity of the
431 analysis to a range of **SUSY** topologies. Additionally the author has worked extensively
432 in both increasing the statistical precision of electroweak predictions measured from
433 simulation through analytical techniques, and the derivation of a data driven systematic

- 434 uncertainty through the establishment of closure tests within the control samples of the
435 analysis.
- 436 Finally a method to search for **SUSY** signatures rich in top and bottom flavoured jet final
437 states, is introduced in Chapter 6. These particular **SUSY** topologies are increasingly of
438 interest to physicists in light of the discovery of the Higgs boson, and is discussed within
439 the chapter. A parametrisation of the b-tagging distribution for different Electroweak
440 processes is used to establish template shapes, which are then fitted at low b-tagged jet
441 multiplicity (0-2), to estimate the expected number of 3 and 4 b-tagged jet events from
442 **SM** processes. The α_T event selections are used to test the functionality of this template
443 method in both data and simulation, with background predictions from the signal region
444 selection compared to those presented in Chapter 5.
- 445 Natural units are used throughout this thesis in which $\hbar = c = 1$.

Chapter 2.

⁴⁴⁶ A Theoretical Overview

⁴⁴⁷ Within this chapter, a brief introduction and background to the **SM** is given. Its success
⁴⁴⁸ as a rigorously tested and widely accepted theory is discussed as are its deficiencies,
⁴⁴⁹ leading to the argument that this theory is not a complete description of our universe.
⁴⁵⁰ The motivations for new physics at the TeV scale and in particular Supersymmetric
⁴⁵¹ theories are outlined within Section (2.3), with the chapter concluding with how an
⁴⁵² experimental signature of such theories can be produced and observed at the **LHC**,
⁴⁵³ Section (2.4).

⁴⁵⁴ 2.1. The Standard Model

⁴⁵⁵ The **SM** is the name given to the relativistic Quantum Field Theory (**QFT**), where
⁴⁵⁶ particles are represented as excitations of fields, which describe the interactions and
⁴⁵⁷ properties of all the known elementary particles [6][7][8][9]. It is a renormalisable field
⁴⁵⁸ theory which contains three symmetries: $SU(3)$ for colour charge, $SU(2)$ for weak isospin
⁴⁵⁹ and $U(1)$ relating to weak hyper charge, which require its Lagrangian \mathcal{L}_{SM} to be invariant
⁴⁶⁰ under local gauge transformation.

⁴⁶¹ Within the **SM** theory, matter is composed of spin $\frac{1}{2}$ fermions, which interact with each
⁴⁶² other via the exchange of spin-1 gauge bosons. A summary of the known fundamental
⁴⁶³ fermions and bosons is given in Table 2.1.

⁴⁶⁴ Fermions are separated into quarks and leptons of which only quarks interact with the
⁴⁶⁵ strong nuclear force. Quarks unlike leptons are not seen as free particles in nature, but
⁴⁶⁶ rather exist only within baryons, composed of three quarks with an overall integer charge,
⁴⁶⁷ and quark-anti-quark pairs called mesons. Both leptons and quarks are grouped into

Particle	Symbol	Spin	Charge	Mass (GeV)
First Generation Fermions				
Electron Neutrino	ν_e	$\frac{1}{2}$	0	$< 2.2 \times 10^{-6}$
Electron	e	$\frac{1}{2}$	-1	0.51×10^{-3}
Up Quark	u	$\frac{1}{2}$	$\frac{2}{3}$	$2.3^{+0.7}_{-0.5} \times 10^{-3}$
Down Quark	d	$\frac{1}{2}$	$-\frac{1}{3}$	$4.8^{+0.7}_{-0.3} \times 10^{-3}$
Second Generation Fermions				
Muon Neutrino	ν_μ	$\frac{1}{2}$	0	-
Muon	μ	$\frac{1}{2}$	-1	1.05×10^{-3}
Charm Quark	c	$\frac{1}{2}$	$\frac{2}{3}$	1.275 ± 0.025
Strange Quark	s	$\frac{1}{2}$	$-\frac{1}{3}$	$95 \pm 5 \times 10^{-3}$
Third Generation Fermions				
Tau Neutrino	ν_τ	$\frac{1}{2}$	0	-
Tau	τ	$\frac{1}{2}$	-1	1.77
Top Quark	t	$\frac{1}{2}$	$\frac{2}{3}$	173.5 ± 0.8
Bottom Quark	b	$\frac{1}{2}$	$-\frac{1}{3}$	4.65 ± 0.03
Gauge Bosons				
Photon	γ	1	0	0
W Boson	W^\pm	1	± 1	80.385 ± 0.015
Z Boson	Z	1	0	91.187 ± 0.002
Gluons	g	1	0	0
Higgs Boson	H	0	0	125.3 ± 0.5 [4]

Table 2.1.: The fundamental particles of the SM, with spin, charge and mass displayed. Latest mass measurements taken from [1].

468 three generations which have the same properties, but with ascending mass in each
469 subsequent generation.

470 The gauge bosons mediate the interactions between fermions. The field theories of
471 Quantum Electro-Dynamics (QED) and Quantum Chromo-Dynamics (QCD), yield
472 massless mediator bosons, the photon and eight coloured gluons which are consequences
473 of the gauge invariance of those theories, detailed in Section (2.1.1).

474 The unification of the electromagnetic and weak-nuclear forces into the current Elec-
475 troweak theory yield the weak gauge bosons, W^\pm and Z through the mixing of the
476 associated gauge fields. The force carriers of this theory were experimentally detected by
477 the observation of weak neutral current, discovered in 1973 in the Gargamelle bubble
478 chamber located at European Organization for Nuclear Research (CERN) [10], with the
479 masses of the weak gauge bosons measured by the UA1 and U2 experiments at the Super
480 Proton Synchrotron (SPS) collider in 1983 [11][12].

⁴⁸¹ 2.1.1. Gauge Symmetries of the SM

- ⁴⁸² Symmetries are of fundamental importance in the description of physical phenomena.
⁴⁸³ Noether's theorem states that for a dynamical system, the consequence of any symmetry
⁴⁸⁴ is an associated conserved quantity [13]. Invariance under translations, rotations, and
⁴⁸⁵ Lorentz transformations in physical systems lead to conservation of momentum, energy
⁴⁸⁶ and angular momentum.
- ⁴⁸⁷ In the **SM**, a quantum theory described by Lagrangian formalism, the weak, strong and
⁴⁸⁸ electromagnetic interactions are described in terms of “gauge theories”. A gauge theory
⁴⁸⁹ possesses invariance under a set of “local transformations”, which are transformations
⁴⁹⁰ whose parameters are space-time dependent. The requirement of gauge invariance within
⁴⁹¹ the **SM** necessitates the introduction of force-mediating gauge bosons and interactions
⁴⁹² between fermions and the bosons themselves. Given the nature of the topics covered by
⁴⁹³ this thesis, the formulation of **EWK** within the **SM** Lagrangian is reviewed within this
⁴⁹⁴ section.
- ⁴⁹⁵ The simplest example of the application of the principle of local gauge invariance within
⁴⁹⁶ the **SM** is in Quantum Electro-Dynamics (**QED**), the consequences of which require a
⁴⁹⁷ massless photon field [14][15].
- ⁴⁹⁸ Starting from the free Dirac Lagrangian written as

$$\mathcal{L} = \bar{\psi}(i\gamma^\mu \partial_\mu - m)\psi, \quad (2.1)$$

- ⁴⁹⁹ where ψ represents a free non interacting fermionic field, with the matrices γ^μ , $\mu \in 0, 1, 2, 3$
⁵⁰⁰ defined by the anti commutator relationship $\gamma^\mu \gamma^\nu + \gamma^\nu \gamma^\mu = 2\eta^{\mu\nu} I_4$, with $\eta^{\mu\nu}$ being the
⁵⁰¹ flat space-time metric $(+, -, -, -)$, and I_4 the 4×4 identity matrix.
- ⁵⁰² Under a local U(1) abelian gauge transformation in which ψ transforms as:

$$\psi(x) \rightarrow \psi'(x) = e^{i\theta(x)}\psi(x) \quad \bar{\psi}(x) \rightarrow \bar{\psi}'(x) = e^{i\theta(x)}\bar{\psi}(x) \quad (2.2)$$

- ⁵⁰³ the kinetic term of the Lagrangian will not remain invariant, due to the partial derivative
⁵⁰⁴ interposed between the $\bar{\psi}$ and ψ yielding,

$$\partial_\mu \psi \rightarrow e^{i\theta(x)} \partial_\mu \psi + ie^{i\theta(x)} \psi \partial_\mu \theta. \quad (2.3)$$

To ensure that \mathcal{L} remains invariant, a modified derivative, D_μ , that transforms covariantly under phase transformations is introduced. In doing this a vector field A_μ with transformation properties that cancel out the unwanted term in (2.3) must also be included,

$$D_\mu \equiv \partial_\mu - ieA_\mu, \quad A_\mu \rightarrow A_\mu + \frac{1}{e} \partial_\mu \theta. \quad (2.4)$$

Invariance of the Lagrangian is then achieved by replacing ∂_μ by D_μ :

$$\begin{aligned} \mathcal{L} &= i\bar{\psi}\gamma^\mu D_\mu \psi - m\bar{\psi}\psi \\ &= \bar{\psi}(i\gamma^\mu \partial_\mu - m)\psi + e\bar{\psi}\gamma^\mu \psi A_\mu \end{aligned} \quad (2.5)$$

An additional interaction term is now present in the Lagrangian, coupling the Dirac particle to this vector field, which is interpreted as the photon in QED. To regard this new field as the physical photon field, a term corresponding to its kinetic energy must be added to the Lagrangian from Equation (2.5). Since this term must also be invariant under the conditions of Equation (2.4), it is defined in the form $F_{\mu\nu} = \partial^\mu A^\nu - \partial^\nu A^\mu$.

This then leads to the Lagrangian of QED:

$$\mathcal{L}_{QED} = \underbrace{i\bar{\psi}\gamma^\mu \partial_\mu \psi - \frac{1}{4}F_{\mu\nu}F^{\mu\nu}}_{\text{kinetic term}} + \underbrace{m\bar{\psi}\psi}_{\text{mass term}} + \underbrace{e\bar{\psi}\gamma^\mu \psi A_\mu}_{\text{interaction term}} \quad (2.6)$$

Within the Lagrangian there remains no mass term of the form $m^2 A_\mu A^\mu$, which is prohibited by gauge invariance. This implies that the gauge particle, the photon, must be massless.

519 2.1.2. The Electroweak Sector and Electroweak Symmetry 520 Breaking

- 521 The same application of gauge symmetry and the requirement of local gauge invariance
522 can be used to unify QED and the Weak force in the Electroweak Sector (EWK).
523 The nature of EWK interactions is encompassed within a Lagrangian invariant under
524 transformations of the group $SU(2)_L \times U(1)_Y$.
525 The weak interactions from experimental observation [16], are known to violate parity
526 and are therefore not symmetric under interchange of left and right helicity fermions.
527 Thus within the SM the left and right handed parts of these fermion fields are treated
528 separately. A fermion field is then split into two left and right handed chiral components,
529 $\psi = \psi_L + \psi_R$, where $\psi_{L/R} = (1 \pm \gamma^5)\psi$.
530 The $SU(2)_L$ group is the special unitary group of 2×2 matrices U satisfying $UU^\dagger = I$
531 and $\det(U) = 1$. It may be written in the form $U = e^{-i\omega_i T_i}$, with the generators of the
532 group $T_i = \frac{1}{2}\tau_i$ where τ_i , $i \in 1,2,3$ being the 2×2 Pauli matrices

$$\tau_1 = \begin{pmatrix} 0 & 1 \\ 1 & 0 \end{pmatrix} \quad \tau_2 = \begin{pmatrix} 0 & -i \\ i & 0 \end{pmatrix} \quad \tau_3 = \begin{pmatrix} 1 & 0 \\ 0 & -1 \end{pmatrix}, \quad (2.7)$$

- 533 which form a non Abelian group obeying the commutation relation $[T^a, T^b] \equiv if^{abc}T^c \neq 0$.
534 The gauge fields that accompany this group are represented by $\hat{W}_\mu = (\hat{W}_\mu^1, \hat{W}_\mu^2, \hat{W}_\mu^3)$
535 and act only on the left handed component of the fermion field ψ_L .
536 One additional generator Y which represents the hypercharge of the particle under
537 consideration is introduced through the $U(1)_Y$ group acting on both components of the
538 fermion field, with an associated vector boson field \hat{B}_μ .
539 The $SU(2)_L \times U(1)_Y$ transformations of the left and right handed components of ψ are
540 summarised by,

$$\begin{aligned} \chi_L &\rightarrow \chi'_L = e^{i\theta(x) \cdot T + i\theta(x)Y} \chi_L, \\ \psi_R &\rightarrow \psi'_R = e^{i\theta(x)Y} \psi_R, \end{aligned} \quad (2.8)$$

⁵⁴¹ where the left handed fermions form isospin doubles χ_L and the right handed fermions
⁵⁴² are isosinglets ψ_R . For the first generation of leptons and quarks this represents

$$\chi_L = \begin{pmatrix} \nu_e \\ e \end{pmatrix}_L, \quad \begin{pmatrix} u \\ d \end{pmatrix}_L, \\ \psi_R = e_R, \quad u_R, d_R. \quad (2.9)$$

⁵⁴³ Imposing local gauge invariance within \mathcal{L}_{EWK} is once again achieved by modifying the
⁵⁴⁴ covariant derivative

$$D_\mu = \partial_\mu - \frac{ig}{2}\tau^i W_\mu^i - \frac{ig'}{2}YB_\mu, \quad (2.10)$$

⁵⁴⁵ where g and g' are the coupling constant of the $SU(2)_L$ and $U(1)_Y$ groups respectively.
⁵⁴⁶ Taking the example of the first generation of fermions defined in Equation.(2.9), with input
⁵⁴⁷ hypercharge values of -1 and -2 for χ_L and e_R respectively, would lead to a Lagrangian
⁵⁴⁸ \mathcal{L}_1 of the form,

$$\mathcal{L}_1 = \bar{\chi}_L \gamma^\mu [i\partial_\mu - g \frac{1}{2} \tau \cdot W_\mu - g' (-\frac{1}{2}) B_\mu] \chi_L \\ + \bar{e}_R \gamma^\mu [i\partial_\mu - g' (-1) B_\mu] e_R - \frac{1}{4} W_{\mu\nu} \cdot W^{\mu\nu} - \frac{1}{4} B_{\mu\nu} B^{\mu\nu}. \quad (2.11)$$

⁵⁴⁹ As in QED, these additional gauge fields introduce field strength tensors $B_{\mu\nu}$ and $W_{\mu\nu}$,

$$\hat{B}_{\mu\nu} = \partial_\mu \hat{B}_\nu - \partial_\nu \hat{B}_\mu \quad (2.12)$$

$$\hat{W}_{\mu\nu} = \partial_\mu \hat{W}_\nu - \partial_\nu \hat{W}_\mu - g \hat{W}_\mu \times \hat{W}_\mu \quad (2.13)$$

⁵⁵⁰ corresponding to the kinetic energy and self coupling of the W_μ fields and the kinetic
⁵⁵¹ energy term of the B_μ field.

- 552 None of these gauge bosons are physical particles, and instead linear combinations of
 553 these gauge bosons make up γ and the W and Z bosons, defined as

$$W^\pm = \frac{1}{\sqrt{2}} (W_\mu^1 \mp iW_\mu^2), \quad \begin{pmatrix} Z_\mu \\ A_\mu \end{pmatrix} = \begin{pmatrix} \cos\theta_W & -\sin\theta_W \\ \sin\theta_W & \cos\theta_W \end{pmatrix} \begin{pmatrix} W_\mu^3 \\ B_\mu \end{pmatrix}, \quad (2.14)$$

- 554 where the mixing angle, $\theta_w = \tan^{-1} \frac{g'}{g}$, relates the coupling of the neutral weak and
 555 electromagnetic interactions.

556 As in the case of the formulation of the QED Lagrangian there remains no mass term for
 557 the photon. However this is also the case for the W, Z and fermions in the Lagrangian,
 558 contrary to experimental measurement. Any explicit introduction of mass terms would
 559 break the symmetry of the Lagrangian and instead mass terms can be introduced through
 560 spontaneous breaking of the EWK symmetry via the Higgs mechanism.

- 561 The Higgs mechanism induces spontaneous symmetry breaking through the introduction
 562 of a complex scalar SU(2) doublet field ϕ which attains a non-zero Vacuum Expectation
 563 Value (VEV) [17][18][19][20].

$$\phi = \begin{pmatrix} \phi^+ \\ \phi^0 \end{pmatrix} \quad \text{with} \quad \begin{aligned} \phi^+ &\equiv (\phi_1 + i\phi_2)/\sqrt{2} \\ \phi^0 &\equiv (\phi_3 + i\phi_4)/\sqrt{2} \end{aligned} \quad (2.15)$$

- 564 The Lagrangian defined in Equation (2.11) attains an additional term \mathcal{L}_{Higgs} of the form

$$\mathcal{L}_{Higgs} = \overbrace{(D_\mu\phi)^\dagger(D^\mu\phi)}^{\text{kinetic}} - \overbrace{\mu^2\phi^\dagger\phi - \lambda(\phi^\dagger\phi)^2}^{\text{potential } V(\phi)} \quad (\mu^2, \lambda) > 0 \in \mathbb{R},$$

$$\mathcal{L}_{SM} = \mathcal{L}_{EWK} + \mathcal{L}_{Higgs}, \quad (2.16)$$

- 565 where the covariant derivative D_μ is that defined in Equation (2.10). The last two terms
 566 of \mathcal{L}_{Higgs} correspond to the Higgs potential, in which real positive values of μ^2 and λ are
 567 required to ensure the generation of masses for the bosons and leptons. The minimum of

568 this potential is found at $\phi^\dagger \phi = \frac{1}{2}(\phi_1^2 + \phi_2^2 + \phi_3^2 + \phi_4^2) = \mu^2/\lambda = v^2$, where v represents
 569 the **VEV**.

570 Defining the ground state of the ϕ field to be consistent with the $V(\phi)$ minimum, and
 571 then expanding around a ground state chosen to maintain an unbroken electromagnetic
 572 symmetry thus preserving a zero photon mass [21] leads to

$$\phi_0 = \sqrt{\frac{1}{2}} \begin{pmatrix} 0 \\ v \end{pmatrix}, \quad \phi(x) = e^{i\tau \cdot \theta(x)/v} \sqrt{\frac{1}{2}} \begin{pmatrix} 0 \\ v + h(x) \end{pmatrix}, \quad (2.17)$$

573 where the fluctuations from the vacuum ϕ_0 are parametrized in terms of four real fields,
 574 $\theta_1, \theta_2, \theta_3$ and $h(x)$.

575 Choosing to gauge away the three massless Goldstone boson fields by setting $\theta(x)$ to
 576 zero and substituting $\phi(x)$ back into kinetic term of \mathcal{L}_{Higgs} from Equation (2.16) leads
 577 to mass terms for the W^\pm and Z bosons

$$(D_\mu \phi)^\dagger (D^\mu \phi) = \frac{1}{2} (\partial_\mu h)^2 + \frac{g^2 v^2}{2} W_\mu^+ W^{-\mu} + \frac{v^2 g^2}{8 \cos^2 \theta_w} Z_\mu Z^\mu + 0 A_\mu A^\mu, \quad (2.18)$$

578 where the relations between the physical and electroweak gauge fields from Equation
 579 (2.14) are used. The W^\pm and Z boson masses can then be determined to be

$$M_W = \frac{1}{2} g v \quad M_Z = \frac{1}{2} \frac{g v}{\cos \theta_w}. \quad (2.19)$$

580 This mechanism is also used to generate fermion masses by introducing a Yukawa coupling
 581 between the fermions and the ϕ field [22], with the coupling strength of a particle to
 582 the ϕ field governing its mass. Additionally a scalar boson h with mass $m_h = v \sqrt{\frac{\lambda}{2}}$, is
 583 also predicted as a result of this spontaneous symmetry breaking and became known as
 584 the Higgs boson. Its discovery by the **CMS** and **ATLAS** experiments in 2012 is the first
 585 direct evidence to support this method of mass generation within the **SM**.

586 2.2. Motivation for Physics Beyond the Standard 587 Model

588 As has been described, the **SM** has proven to be a very successful theory, predicting the
589 existence of the W^\pm and Z bosons and the top quark long before they were experimentally
590 observed. However the theory does not accurately describe all observed phenomena and
591 has some fundamental theoretical flaws that hint at the need for additional extensions to
592 the current theory.

593 On a theoretical level, the **SM** is unable to incorporate the gravitational interactions of
594 fundamental particles within the theory. Whilst at the electroweak energy scales the
595 relative strength of gravity is negligible compared to the other three fundamental forces,
596 at much higher energy scales, $M_{\text{planck}} \sim 10^{18} \text{GeV}$, quantum gravitational effects become
597 increasingly dominant. The failure to reconcile gravity within the **SM**, demonstrates that
598 the **SM** must become invalid at some higher energy scale.

599 Other deficiencies with the **SM** include the fact that the predicted rate of Charge-Parity
600 violation does not account for the matter dominated universe which we inhabit, and
601 that the **SM** prediction of a massless neutrino conflicts with the observation of neutrino
602 flavour mixing, attributed to mixing between neutrino mass eigenstates [23][24].

603 Perhaps one of the most glaring gaps in the predictive power of the **SM** is that there
604 exists no candidate to explain the cosmic dark matter observed in galactic structures
605 through indirect techniques including gravitational lensing and measurement of the
606 orbital velocity of stars at galactic edges. Any such candidate must be very weakly
607 interacting but must also be stable, owing to the lack of direct detection of the decay
608 products of such a process. Therefore a stable dark matter candidate, is one of the
609 main obstacles to address for any Beyond Standard Model (**BSM**) physics model.

610 The recent discovery of the Higgs boson whilst a significant victory for the predictive
611 power of the **SM**, brings with it still unresolved questions. This issue is commonly
612 described as the “hierarchy problem”.

613 In the absence of new physics between the TeV and Planck scale, calculating beyond
614 tree-level contributions to the Higgs mass term given by its self interaction, result in
615 divergent terms that push the Higgs mass up to the planck mass M_{planck} .

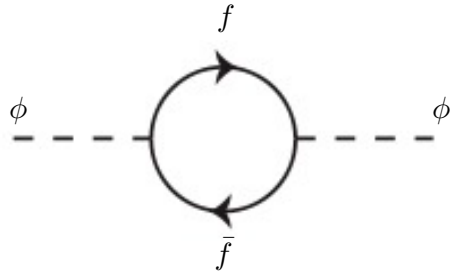


Figure 2.1.: One loop quantum corrections to the Higgs squared mass parameter m_h^2 due to a fermion.

616 This can be demonstrated by considering the one loop quantum correction to the Higgs
 617 mass with a fermion f , shown in Figure 2.1 with mass m_f . The Higgs field couples to f
 618 with a term in the Lagrangian $-\lambda_f h \bar{f} f$, yielding a correction of the form [25],

$$\delta m_h^2 = -\frac{|\lambda_f|^2}{8\pi^2} \Lambda^2 + \dots, \quad (2.20)$$

619 where λ_f represents the coupling strength for each type of fermion $\propto m_f$, and Λ the
 620 cutoff energy scale at which the **SM** ceases to be a valid theory.

621 To recover the mass of the now discovered Higgs boson would require a fine-tuning of
 622 the parameters to cancel out these mass corrections of the Higgs mass to the scale of
 623 30 orders of magnitude. This appears as an unnatural solution to physicists and it is
 624 this hierarchy problem that provides one of the strongest motivations for the theory of
 625 SUperSYmmetry (**SUSY**).

626 2.3. Supersymmetry Overview

627 Supersymmetry provides potential solutions to many of the issues raised in the previous
 628 section. It provides a dark matter candidate, can explain baryogenesis in the early
 629 universe and also provides an elegant solution to the hierarchy problem [26][27][28][29].
 630 At its heart it represents a new space-time symmetry that relates fermions and bosons.
 631 This symmetry converts bosonic states into fermionic states, and vice versa, see Equation
 632 (2.21) ,

$$Q|\text{Boson}\rangle = |\text{Fermion}\rangle \quad Q|\text{Fermion}\rangle = |\text{Boson}\rangle, \quad (2.21)$$

633 where the operator Q is the generator of these transformations. Quantum field theories
 634 which are invariant under such transformations are called supersymmetric.

635 This symmetry operator therefore acts upon a particles spin altering it by a half integer
 636 value. The consequences of the application of this additional space-time symmetry
 637 introduce a new rich phenomenology. For example in supersymmetric theories, both
 638 the left handed $SU(2)$ doublet and right handed singlet of fermions will have a spin-0
 639 superpartner, containing the same electric charge, weak isospin, and colour as its **SM**
 640 partner. In the case of leptons $(\nu_l, l)_L$, they will have two superpartners, a sneutrino $\tilde{\nu}_l{}_L$
 641 and a slepton \tilde{l}_L , whilst the singlet l_R also has a superpartner slepton \tilde{l}_R .

642 Each particle in a supersymmetric theory is paired together with their superpartners as
 643 a result of these supersymmetric transformations in a so called supermultiplet. These
 644 superpartners will then consequently also contribute to the corrections to the Higgs mass.
 645 Bosonic and fermionic loops contributing to the correction appear with opposite signs,
 646 and therefore cancellation of these divergent terms will stabilise the Higgs mass, solving
 647 the hierarchy problem [30][31].

648 One of the simplest forms of **SUSY**, is to simply have a set of **SM** supersymmetric
 649 partners with the same mass and interactions as their counterparts. However the current
 650 lack of any experimental evidence for that predicted sparticle spectrum implies **SUSY**
 651 must be a broken symmetry in which any sparticle masses must be greater than their
 652 **SM** counterparts.

653 There exist many techniques which can induce supersymmetric breaking [32][33][34]. Of
 654 particular interest to experimental physicists are those at which the breaking scale is
 655 of an order that is experimentally accessible to the **LHC** i.e. \sim TeV scale. Whilst
 656 there is no requirement for supersymmetric breaking to occur at this energy scale, for
 657 supersymmetry to provide a solution to the hierarchy problem, it is necessary for this
 658 scale to not differ too drastically from the **EWK** scale [35][36].

659 2.3.1. R-Parity

660 Some supersymmetric theories also present a solution to the dark matter problem. These
 661 theories contain a Lightest Supersymmetric Partner (**LSP**), which matches the criteria
 662 of a Weakly Interacting Massive Particle (**WIMP**) required by cosmological observation
 663 when R-parity is conserved.

664 Baryon (B) and Lepton (L) number conservation is forbidden in the **SM** by renormal-
 665 isability requirements. The violation of Baryon or Lepton number results in a proton
 666 lifetime much shorter than those set by experimental limits [37]. Another symmetry
 667 called R-parity is then often introduced to **SUSY** theories to maintain baryon and lepton
 668 conservation.

669 R-parity is described by the equation

$$R_P = (-1)^{3(B-L)+2s}, \quad (2.22)$$

670 where s represents the spin of the particles. $B = \pm \frac{1}{3}$ for quarks/antiquarks and $B = 0$
 671 for all others, $L = \pm 1$ for leptons/antileptons, $L = 0$ for all others.

672 R-parity ensures the stability of the proton in **SUSY** models, and also has other conse-
 673 quences for the production and decay of supersymmetric particles. In particle colliders
 674 supersymmetric particles can only be pair produced, and similarly the decay of any pro-
 675 duced supersymmetric particle is restricted to a **SM** particle and a lighter supersymmetric
 676 particle as allowed by conservation laws. A further implication of R-parity is that once a
 677 supersymmetric particle has decayed to the **LSP** it remains stable, unable to decay into
 678 a **SM** particle.

679 A **LSP** will not interact in a detector at a particle collider, leaving behind a missing
 680 energy \cancel{E}_T signature. The assumption of R-parity and its consequences are used to
 681 determine the physical motivation and search strategies for **SUSY** models at the **LHC**.

682 2.4. Experimental Signatures of **SUSY** at the **LHC**

683 Should strongly interacting sparticles be within the experimental reach of the **LHC**, then
 684 it is expected that they can be produced in a variety of ways :

- 685 • squark/anti-squark and gluino pairs can be produced via both gluon fusion and
686 quark/anti-quark scattering,
- 687 • a gluino and squark produced together via quark-gluon scattering,
- 688 • squark pairs produced via quark-quark scattering.

689 Whilst most **SUSY** searches invoke the requirement of R-parity to explore parameter
690 phase space, there still exist a whole plethora of possible **SUSY** model topologies which
691 could be waiting to be discovered at the **LHC**.

692 During the 2011 run period at $\sqrt{s} = 7$ TeV, particular models were used to benchmark
693 performance and experimental reach of both **CMS** searches and previous experiments.
694 The Compressed Minimal SuperSymmetric Model (**CMSSM**) was initially chosen for
695 a number of reasons [38], one of the most compelling being the reduction of the up to
696 105 new parameters that can be introduced by **SUSY** (in addition to the existing 19 of
697 the **SM**), to just 5 free extra free parameters. It was this simplicity, combined with the
698 theory not requiring any fine tuning of particle masses to produce experimentally verified
699 **SM** observables that made it an attractive model to interpret physics results.

700 However recent results from the **LHC** now strongly disfavour large swathes of **CMSSM**
701 parameter space [39][40][41]. In the face of such results a more pragmatic model indepen-
702 dent search strategy is now applied across most **SUSY** searches at the **LHC**, see Section
703 (2.4.1).

704 As previously stated, a stable **LSP** that exhibits the properties of a dark matter candidate
705 would be weakly interacting and therefore will not be directly detected in a detector
706 environment. Additionally the cascade decays of supersymmetric particles to this **LSP**
707 state would also result in significant hadronic activity. These signatures will then be
708 characterised through large amounts of hadronic jets (see Section (3.3.1)), leptons and
709 a significant amount of missing energy dependent upon the size of the mass splitting
710 between the **LSP** and the supersymmetric particle it has decayed from.

711 The **SM** contains processes which can exhibit a similar event topology to that described
712 above. The largest contribution coming from the general QCD environment of a hadron
713 collider. A multitude of different analytical techniques are used by experimental physicists
714 to reduce or estimate any reducible or irreducible backgrounds, allowing a possible **SUSY**
715 signature to be extracted. The techniques employed within this thesis are described in
716 great detail within Section (4.1).

⁷¹⁷ 2.4.1. Simplified models

⁷¹⁸ With such a variety of different ways for a **SUSY** signal to manifest itself, it is necessary
⁷¹⁹ to be able to interpret experimental reach through the masses of gluinos and squarks
⁷²⁰ which can be excluded by experimental searches rather than on a model specific basis.

⁷²¹ This is accomplished through **SMS** models, which are defined by a set of hypothetical
⁷²² particles and a sequence of their production and decay modes [42][43]. In the **SMS** models
⁷²³ considered within this thesis, only the production process for the two primary particles
⁷²⁴ are considered. Each primary particle can undergo a direct or a cascade decay through
⁷²⁵ an intermediate new particle. At the end of each decay chain there remains a neutral,
⁷²⁶ undetected **LSP** particle, denoted $\tilde{\chi}_{LSP}$ which can represent a neutralino or gravitino.
⁷²⁷ Essentially it is easier to consider each **SMS** with branching ratios set to 100%. The
⁷²⁸ masses of the primary particle and the **LSP** remain as free parameters, in which the
⁷²⁹ absolute value and relative difference between the primary and **LSP** particle alter the
⁷³⁰ kinematics of the event.

⁷³¹ Different **SMS** models are denoted with a T-prefix, with a summary of the types interpreted
⁷³² within this thesis listed below [44].

- ⁷³³ • **T1,T1xxxx**, models represent a simplified version of gluino pair production with
⁷³⁴ each gluino (superpartner to the gluon) undergoing a three-body decay to a quark-
⁷³⁵ antiquark pair and the **LSP** (i.e. $\tilde{g} \rightarrow q\bar{q}\tilde{\chi}_{LSP}$). The resultant final state from this
⁷³⁶ decay is typically 4 jets + \cancel{E}_T in the absence of initial/final state radiation and
⁷³⁷ detector effects. xxxx denotes models in which the quarks are of a specific flavour,
⁷³⁸ typically t or b quark-antiquarks.

- ⁷³⁹ • **T2,T2xx**, models represent a simplified version of squark anti-squark production
⁷⁴⁰ with each squark undergoing a two-body decay into a light-flavour quark and **LSP**
⁷⁴¹ (i.e. $\tilde{q} \rightarrow q\tilde{\chi}_{LSP}$). This results in final states with less jets than gluino mediated
⁷⁴² production, typically 2 jets + \cancel{E}_T when again ignoring the effect of initial/final state
⁷⁴³ radiation and detector effects. xx models represent decays in which both the quark
⁷⁴⁴ and the squark within the decay is of a specific flavour, which in this thesis are
⁷⁴⁵ again \tilde{t}/t or \tilde{b}/b .

⁷⁴⁶ Models rich in b and t quarks are interpreted within this thesis as they remain of
⁷⁴⁷ particular interest within “Natural **SUSY**” scenarios [45][46]. The largest contribution
⁷⁴⁸ to the quadratic divergence in the Higgs mass parameter comes from a loop of top
⁷⁴⁹ quarks via the Yukawa coupling. Cancellation of these divergences can be achieved in

750 supersymmetric theories by requiring a light right handed top squark, \tilde{t}_R , and left-handed
751 double $SU(2)_L$ doublet containing top and bottom squarks, $(\tilde{t}, \tilde{b})_L$ [47].

752 These theories therefore solve the hierarchy problem by predicting light \sim EWK scale
753 third generation sleptons, to be accessible at the LHC. Search strategies involving the
754 requirement of b-tagging (see Section (3.3.2)) are used to give sensitivity to these type of
755 SUSY scenarios and are discussed in greater detail within Chapter 4.

756 Two example decay chains are shown in Figure 2.2; the pair production of gluinos (T1)
757 and the pair production of squarks (T2) decaying into SM particles and LSP's.

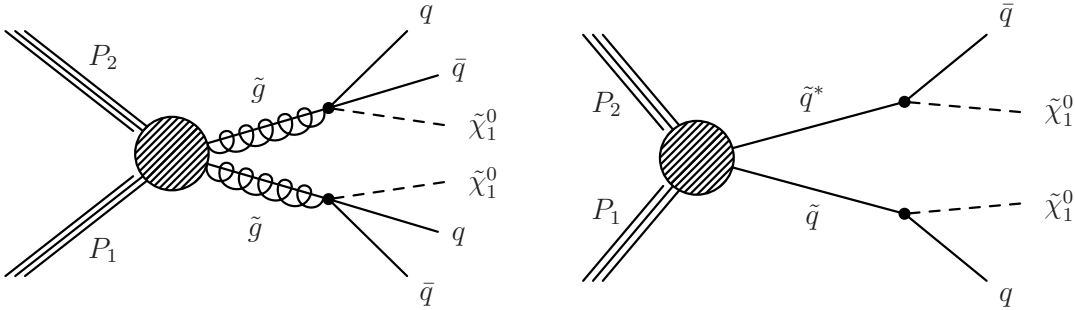


Figure 2.2.: Two example SMS model decays (T1 (left), T2 (right)), which are used in interpretations of physics reach by CMS.

Chapter 3.

⁷⁵⁸ The LHC And The CMS Detector

⁷⁵⁹ Probing the SM for signs of new physics would not be possible without the immensely
⁷⁶⁰ complex electronics and machinery that makes the TeV energy scale accessible to physi-
⁷⁶¹ cists for the first time. This chapter will introduce both the LHC based at European
⁷⁶² Organization for Nuclear Research (CERN) and the Compact Muon Solenoid (CMS)
⁷⁶³ detector (of which the author is a member). Section (3.2) serves to present an overview of
⁷⁶⁴ the different components of the CMS detector, with specific components relevant to the
⁷⁶⁵ search for supersymmetric particles described in greater detail. Section (3.3) will focus on
⁷⁶⁶ event and object reconstruction again with more emphasis on jet level quantities which
⁷⁶⁷ are most relevant to the author’s analysis research. Finally Section (3.4) will describe and
⁷⁶⁸ detail the service work for the CMS Collaboration performed by the author, in measuring
⁷⁶⁹ the performance of L1 single jet triggers in the Global Calorimeter Trigger (GCT) during
⁷⁷⁰ the 2012-2013 run period.

⁷⁷¹ 3.1. The LHC

⁷⁷² The LHC is a storage ring, accelerator, and collider of circulating beams of protons or ions.
⁷⁷³ Housed in the tunnel dug for Large Electron-Positron Collidor (LEP), it is approximately
⁷⁷⁴ 27 km in circumference, 100 m underground, and straddles the border between France
⁷⁷⁵ and Switzerland outside of Geneva. It is currently the only collider in operation that
⁷⁷⁶ is able to study physics at the TeV scale. A double-ring circular synchrotron, it was
⁷⁷⁷ designed to collide both proton-proton (pp) and heavy ion (PbPb) with a centre of mass
⁷⁷⁸ energy $\sqrt{s} = 14$ TeV at a final design luminosity of $10^{34}\text{cm}^{-2}\text{s}^{-1}$.

⁷⁷⁹

These counter-circulating beams of protons or Pb ions are merged in four sections around the ring to enable collisions of the beams, with each interaction point being home to one of the four major experiments; A Large Ion Collider Experiment (**ALICE**) [48] , A Toroidal LHC ApparatuS (**ATLAS**) [49], Compact Muon Solenoid (**CMS**) [50] and Large Hadron Collider Beauty (**LHCb**) [51] which record the resultant collisions. The layout of the **LHC** ring is shown in Figure 3.1. The remaining four sections contain acceleration, collimation and beam dump systems. In the eight arc sections, the beams are steered by magnetic fields of up to 8 T provided by super conduction dipole magnets, which are maintained at temperatures of 2 K using superfluid helium. Additional magnets for focusing and corrections are also present in straight sections within the arcs and near the interaction regions where the detectors are situated.

791

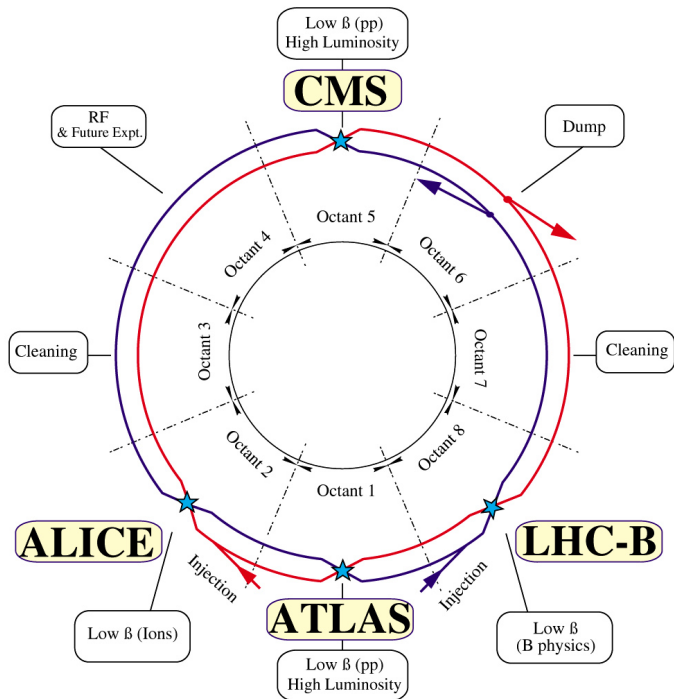


Figure 3.1.: A top down layout of the LHC. [52], with the position of the four main detectors labelled.

Proton beams are formed inside the Proton Synchrotron (**PS**) from bunches of protons 50 ns apart with an energy of 26 GeV. The protons are then accelerated in the Super Proton Synchrotron (**SPS**) to 450 GeV before being injected into the **LHC**. These **LHC** proton beams consists of many “bunches” (i.e. approximately 1.1×10^{11} protons localised into less than 1 ns in the direction of motion). Before collision, the beams are ramped to

797 4 TeV (2012) per beam in a process involving increasing the current passing through the
 798 dipole magnets. Once the desired \sqrt{s} energy is reached then the beams are allowed to
 799 collide at the interaction points. The luminosity falls regularly as the run progresses as
 800 protons are lost in collisions, and eventually the beam is dumped before repeating the
 801 process again.

802

803 Colliding the beams produced an instantaneous luminosity of approximately 5×10^{33}
 804 $\text{cm}^{-2}\text{s}^{-1}$ during the 2012 run. The high number of protons in each bunch increases
 805 the likelihood of multiple interactions with each crossing of the counter-circulating
 806 beams. This leads to isotropic energy depositions within the detectors positioned at these
 807 interaction points, increasing the energy scale of the underlying event. This is known as
 808 pile-up and the counteracting of it's effects are important to the many measurements
 809 performed at the **LHC**.

810 In the early phase of prolonged operation after the initial shutdown the machine operated
 811 in 2010-2011 at 3.5 TeV per beam, $\sqrt{s} = 7$ TeV, delivering 6.13 fb^{-1} of data [53]. During
 812 the 2012-2013 run period, data was collected at an increased $\sqrt{s} = 8$ TeV improving the
 813 sensitivity of searches for new physics. Over the whole run period 23.3 fb^{-1} of data was
 814 delivered, of which 21.8 fb^{-1} was recorded by the **CMS** detector as shown in Figure 3.2
 815 [53]. A total of 12 fb^{-1} of 8 TeV certified data was collected by October 2012, and it is
 816 this data which forms the basis of the results presented within this thesis.

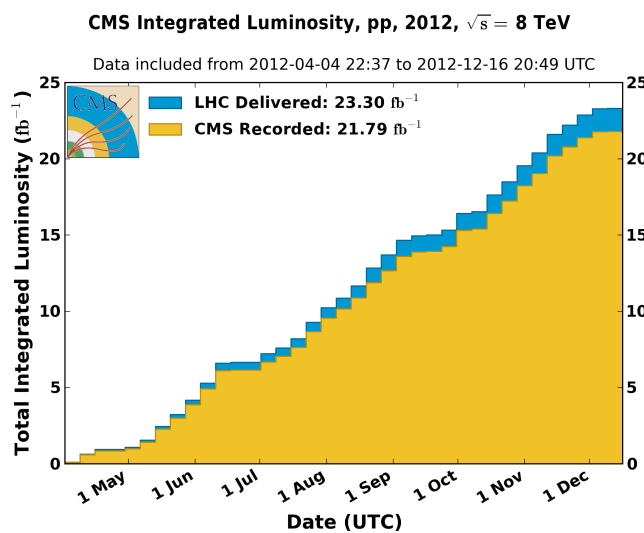


Figure 3.2.: The total integrated luminosity delivered to and collected by **CMS** during the 2012 8 TeV pp runs.

817 3.2. The CMS Detector

818 The Compact Muon Solenoid (**CMS**) detector is one of two general purpose detectors
 819 at the **LHC** designed to search for new physics. The detector is designed to provide
 820 efficient identification and measurement of many physics objects including photons,
 821 electrons, muons, taus, and hadronic showers over wide ranges of transverse momentum
 822 and direction. It's nearly 4π coverage in solid angle allows for accurate measurement of
 823 global transverse momentum imbalance. These design factors give **CMS** the ability to
 824 search for direct production of **SUSY** particles at the TeV scale, making the search for
 825 Supersymmetric particles one of the highest priorities among the wide range of physics
 826 programmes at **CMS**.

827

828 **CMS** uses a right-handed Cartesian coordinate system with the origin at the interaction
 829 point and the z-axis pointing along the beam axis, the x-axis points radially inwards to
 830 the centre of the collider ring, with the y-axis points vertically upward. The azimuthal
 831 angle, ϕ ranging between $[-\pi, \pi]$ is defined in the x-y plane starting from the x-axis. The
 832 polar angle θ is measured from the z axis. The common convention in particle physics is
 833 to express an out going particle in terms of ϕ and its pseudorapidity defined as

$$\eta = -\log \tan \left(\frac{\theta}{2} \right). \quad (3.1)$$

834 The variable $\Delta R = \sqrt{\Delta\phi^2 + \Delta\eta^2}$ is commonly used to define angular distance between
 835 objects within the detector and additionally energy and momentum is typically measured
 836 in the transverse plane perpendicular to the beam line. These values are calculated
 837 from the x and y components of the object and are denoted as $E_T = E \sin \theta$ and
 838 $p_T = \sqrt{p_x^2 + p_y^2}$.

839 3.2.1. Detector subsystems

840 As the range of particles produced from pp collisions interact in different ways with
 841 matter, **CMS** is divided into sub-detector systems, which perform complementary roles
 842 to identify the identity, mass, and momentum of the different physics objects present in
 843 each event. These detector sub-systems contained within **CMS** are wrapped in layers

844 around a central 13 m long 4 T super conducting solenoid as shown in Figure 3.3. With
 845 the endcaps closed, CMS is a cylinder of length 22 m, diameter 15 m, and mass 12.5
 846 kilotons. A more detailed complete description of the detector can be found elsewhere [50].
 847

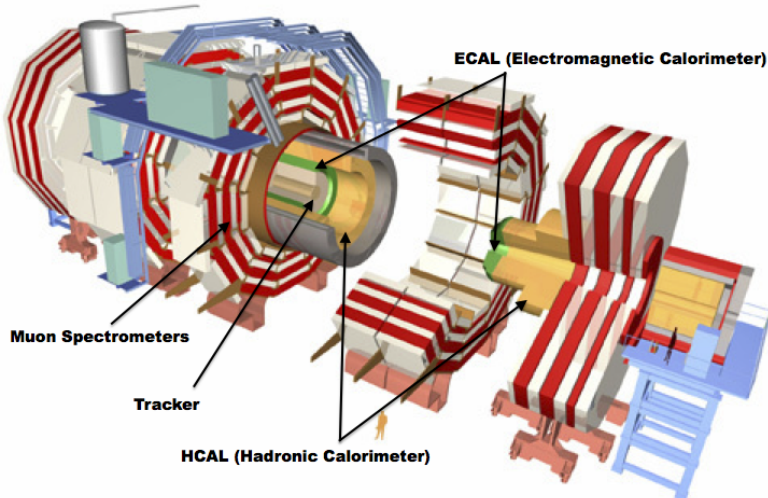


Figure 3.3.: A pictorial depiction of the CMS detector with the main detector subsystems labelled. [54]

848 3.2.2. Tracker

849 The inner-most sub-detector of the barrel is the multi-layer silicon tracker, formed of a
 850 pixel detector component encased by layers of silicon strip detectors. The pixel detector
 851 consists of three layers of silicon pixel sensors providing measurements of the momentum,
 852 position coordinates of the charged particles as they pass, and the location of primary
 853 and secondary vertices between 4 cm and 10 cm transverse to the beam. Outside the
 854 pixel detector, ten cylindrical layers of silicon strip detectors extend the tracking system
 855 out to a radius of 1.20 m from the beam line. The tracking system provides efficient
 856 and precise determination of the charges, momenta, and impact parameters of charged
 857 particles with the geometry of the tracker extending to cover a rapidity range up to $|\eta| <$
 858 2.5.

859

860 The tracking system also plays a crucial part in the identification of jets that originate
 861 from b-quarks through the measurement of displaced secondary vertices. The methods
 862 in which these b-flavoured jets are identified are discussed within Section (3.3.2). The

identification of b-jets is important in many searches for natural SUSY models and forms an important part of the inclusive search strategy described within Section (4.2).

3.2.3. Electromagnetic calorimeter

Immediately outside of the tracker, but still within the magnet core, sits the Electromagnetic CALorimeter (**ECAL**). Covering a pseudorapidity up to $|\eta| < 3$ and comprising of over 75×10^3 PbWO₄ (lead tungstate) crystals that scintillate as particles deposit energy, the **ECAL** provides high resolution measurements of the electromagnetic showers from photons and electrons in the detector.

871

Lead tungstate is used because of its short radiation length ($X_0 \sim 0.9$ cm) and small Molieré radius (~ 2.1 cm) leading to high granularity and resolution. It's fast scintillation time (~ 25 ns) reduces the effects of pile-up, which occurs when energy from previous collisions are still being read out, and its radiation hardness gives it longevity. The crystals are arranged in modules which surround the beam line in a non-projective geometry, angled at 3° with respect to the interaction point to minimise the risk of particles escaping down the cracks between the crystals.

879

The **ECAL** is primarily composed of two sections, the Electromagnetic CALorimeter Barrel (**EB**) which extends in pseudo-rapidity to $|\eta| < 1.479$ with a crystal front cross section of 22×22 mm and a length of 230 mm corresponding to 25.8 radiation lengths, and the Electromagnetic CALorimeter Endcap (**EE**) covering a rapidity range of $1.479 < |\eta| < 3.0$, which consists of two identical detectors on either side of the **EB**. A lead-silicon sampling ‘pre-shower’ detector Electromagnetic CALorimeter pre-Shower (**ES**) is placed before the endcaps to aid in the identification of neutral pions. Their arrangement is shown in Figure 3.4.

888

Scintillation photons from the lead tungstate crystals are instrumented with Avalanche Photo-Diodes (**APD**) and Vacuum Photo-Triodes (**VPT**) located in the **EB** and **EE** respectively, converting the scintillating light into an electric signal which is consequently used to determine the amount of energy deposited within the crystal . These instruments are chosen for their resistance under operation to the strong magnetic field of **CMS**. The scintillation of the **ECAL** crystals as well as the response of the **APDs** varies as a function

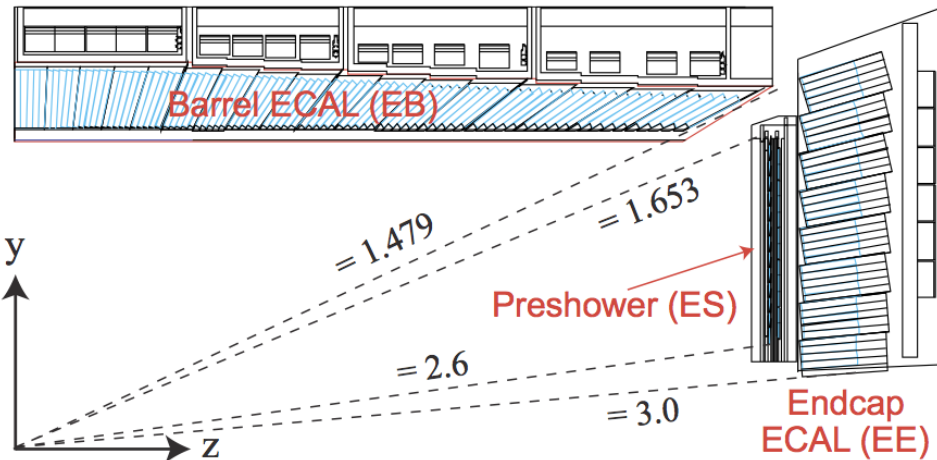


Figure 3.4.: Illustration of the **ECAL** showing the arrangement of the lead tungstate crystals in the **EB** and **EE**. The **ES** is also shown and is located in front of the **EE** [55].

895 of temperature and so cooling systems continually maintain an overall constant **ECAL**
 896 temperature $\pm 0.05^\circ\text{C}$.

897 3.2.4. Hadronic calorimeter

898 Beyond the **ECAL** lies the Hadronic CALorimeter (**HCAL**) which is responsible for
 899 the accurate measurement of hadronic showers, crucial for analyses involving jets or
 900 missing energy signatures. The **HCAL** is a sampling calorimeter which consists of al-
 901 ternating layers of brass absorber and plastic scintillator, except in the hadron forward
 902 ($3.0 < |\eta| < 5.0$) region in which steel absorbers and quartz fibre scintillators are used
 903 because of their increased radiation tolerance. Hadron showers are initiated in the
 904 absorber layers inducing scintillation in the plastic scintillator tiles. These scintillation
 905 photons are converted by wavelength shifting fibres for read-out by hybrid photodiodes.
 906

907 The **HCAL**'s size is constrained to a compact size by the presence of the solenoid, re-
 908 quiring the placement of an additional outer calorimeter on the outside of the solenoid
 909 to increase the sampling depth of the **HCAL**. A schematic of the **HCAL** can be seen in
 910 Figure 3.5.

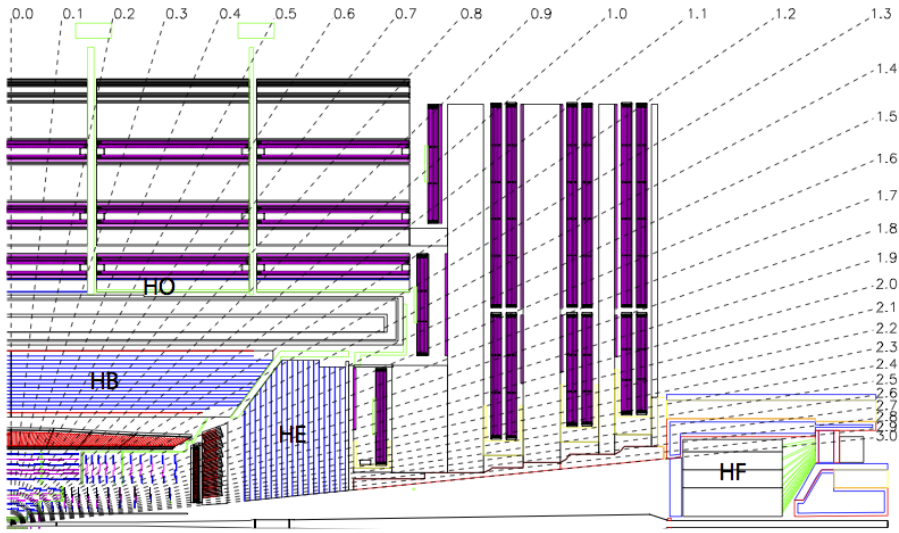


Figure 3.5.: Schematic of the hadron calorimeters in the r - z plane, showing the locations of the **HCAL** components and the **HF**. [50].

912 The **HCAL** covers the range $|\eta| < 5$ and consists of four sub-detectors: the Hadron
 913 Barrel (**HB**) $|\eta| < 1.3$, the Hadron Outer (**HO**), the Hadron Endcaps (**HE**) $1.3 < |\eta| < 3.0$
 914 and the Hadron Forward (**HF**). The **HB**, contained between the outer edge of the **ECAL**
 915 and the inner edge of the solenoid is formed of 36 azimuthal wedges which are split
 916 between two half-barrel segments. Each wedge is segmented into four azimuthal angle
 917 (ϕ) sectors, and each half-barrel is further segmented into 16 η towers. The electronic
 918 readout chain, channels the light from the active scintillator layers from one ϕ -segment
 919 and all η -towers of a half-barrel to a Hybrid Photo Diode (**HPD**).

920 The relatively short number of interaction lengths (λ_l , the distance a hadron will travel
 921 through the absorber material before it has lost $\frac{1}{e}$ of its energy) within the **HB**, the lowest
 922 being $\lambda_l = 5.82$ at $|\eta| = 0$, facilitates the need for the ‘tail catching’ **HO** to increase the
 923 sampling depth in the central barrel rapidity region $|\eta| < 1.3$ to 11 interaction lengths .
 924 Significant fractions of the hadrons energy will be deposited in the **ECAL** as it passed
 925 through the detector. Therefore measurements of hadron energies in the central regions
 926 $|\eta| < 3.0$ use both the **ECAL** and **HCAL** to reconstruct the true energy from showering
 927 hadrons.

928 **3.2.5. Muon systems**

929 Muons being too massive to radiate away energy via Bremsstrahlung, interact little in
930 the calorimeters and mostly pass through the detector until they reach the system of
931 muon detectors which forms the outer most part of the **CMS** detector.

932 Outside of the superconducting solenoid are four muon detection layers interleaved with
933 the iron return yokes which measure the muons energy via ionisation of gas within
934 detector elements. Three types of gaseous chamber are used. The Drift Tube (**DT**),
935 Cathode Stripe Chamber (**CSC**), and Resistive Plate Chamber (**RPC**) systems provide
936 efficient detection of muons with pseudo-rapidity $|\eta| < 2.4$. The best reconstruction
937 performance is obtained when the muon chamber is combined with the inner tracking
938 information to determine muon trajectories and their momenta [56].

939

940 **3.3. Event Reconstruction and Object Definition**

941 The goal of event reconstruction is to take the raw information recorded by the detector
942 and to compute from it higher-level quantities which can be used at an analysis level.
943 These typically correspond to an individual particle’s energy and momenta, or groups of
944 particles which shower in a narrow cone and the overall global energy and momentum
945 balance of the event. The reconstruction of these objects are described in great detail in
946 [57], however covered below are brief descriptions of those which are most relevant to the
947 analysis detailed in Chapter 4.

948 **3.3.1. Jets**

949 Quarks and gluons are produced copiously at the LHC in the hard scattering of partons.
950 As these quarks and gluons fragment, they hadronize and decay into a group of strongly
951 interactive particles and their decay products. These streams of particles travel in the
952 same direction, as they have been “boosted” by the momentum of the primary hadron.
953 These collections of decay products are reconstructed and identified together as a “jet”.

954 At **CMS** jets are reconstructed from energy deposits in the detector using the anti-kt
955 algorithm [58] with size parameter $\Delta R = 0.5$. The anti-kt jet algorithm clusters jets by
956 defining a distance between hard (high p_T) and soft (low p_T) particles such that soft

957 particles are preferentially clustered with hard particles before being clustered between
958 themselves. This produces jets which are robust to soft particle radiation from the pile-up
959 conditions produced by the **LHC**.

960

961 There are two main type of jet reconstruction used at **CMS**, Calorimeter (Calo) and
962 Particle Flow (PF) jets [59]. Calorimeter jets are reconstructed using both the **ECAL**
963 and **HCAL** cells, combined into calorimeter towers . These calorimeter towers consist of
964 geometrically matched **HCAL** cells and **ECAL** crystals. Electronics noise is suppressed by
965 applying a threshold to the calorimeter cells, with pile-up effects reduced by a requirement
966 placed on the tower energy [60]. Calorimeter jets are the jets used within the analysis
967 presented in this thesis.

968 PF jets are formed from combining information from all of the **CMS** sub-detectors systems
969 to determine which final state particles are present in the event. Generally, any particle
970 is expected to produce some combination of a track in the silicon tracker, a deposit in
971 the calorimeters, or a track in the muon system. The PF jet momentum and spatial
972 resolutions are greatly improved with respect to calorimeter jets, as the use of the tracking
973 detectors and of the high granularity of **ECAL** allows resolution and measurement of
974 charged hadrons and photons inside a jet, which together constitute $\sim 85\%$ of the jet
975 energy [61].

976 The jets reconstructed by the clustering algorithm in **CMS** typically have an energy
977 that differs to the ‘true’ energy measured by a perfect detector. This stems from the
978 non-linear and nonuniform response of the calorimeters as well as other residual effects
979 including pile-up and underlying events, and therefore additional corrections are applied
980 to recover a uniform relative response as a function of pseudo-rapidity. These are applied
981 as separate sub corrections [62].

- 982 • A pile-up correction is first applied to the jet. It subtracts the average extra energy
983 deposited in the jet that comes from other vertices present in the event and is
984 therefore not part of the hard jet itself.
- 985 • p_T and η dependant corrections derived from Monte Carlo simulations are used to
986 account for the non-uniform response of the detector.
- 987 • p_T and η residual corrections are applied to data only to correct for difference
988 between data and Monte Carlo. The residual is derived from QCD di-jet samples
989 and the p_T residual from $\gamma+$ jet and $Z+$ jets samples in data.

990 3.3.2. B-tagging

991 The decays of b quarks are suppressed by small CKM matrix elements. As a result, the
 992 lifetimes of b-flavoured hadrons, produced in the fragmentation of b quarks, are relatively
 993 long; \mathcal{O} 1ps. The identification of jets originating from b quarks is very important for
 994 searches for new physics and for measurements of SM processes.

995

996 Many different algorithms developed by CMS select b-quark jets based on variables such
 997 as the impact parameters of the charged-particle tracks, the properties of reconstructed
 998 decay vertices, and the presence or absence of a lepton, or combinations thereof [63]. One
 999 of the most efficient of which is the Combined Secondary Vertex (CSV) which operates
 1000 based on secondary vertex and track-based lifetime information, benchmarked in ‘Loose’,
 1001 ‘Medium’ and ‘Tight’ working points, of which the medium point is the tagger used
 1002 within the α_T search detailed in Section (4.1).

1003 Using the CSV tagger, a likelihood-based discriminator distinguishes between jets from
 1004 b-quarks, and those from charm or light quarks and gluons, which is shown in Figure 3.6.
 1005 The minimum thresholds on the discriminator for each working point correspond to the
 1006 mis-identification probability for light-parton jets of 10%, 1%, and 0.1%, respectively, in
 1007 jets with an average p_T of about 80 GeV.

1008 The b-tagging performance is evaluated to measure the b-jet tagging efficiency ϵ_b , and the
 1009 misidentification probability of charm ϵ_c and light-parton jets ϵ_s . The tagging efficiencies
 1010 for each of these three jet flavours are compared between data and MC simulation, from
 1011 which a series of p_T and $|\eta|$ binned jet corrections are determined,

$$SF_{b,c,s} = \frac{\epsilon_{b,c,s}^{data}}{\epsilon_{b,c,s}^{MC}}. \quad (3.2)$$

1012 These are collectively named ‘Btag Scale Factors’ and allow MC simulation to accu-
 1013 rately reflect the running conditions and performance of the tagging algorithm in data.
 1014 Understanding of the b-tagging efficiency is essential in order to minimise systematic
 1015 uncertainties in physics analyses that employ b-tagging.

1016

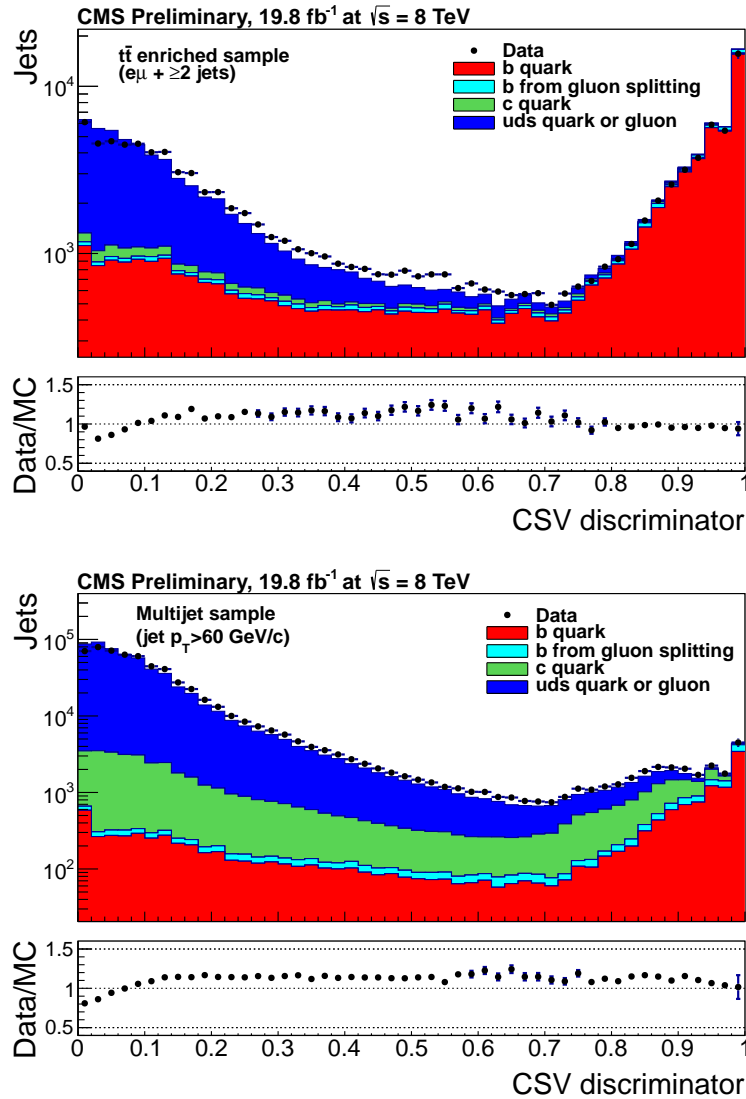


Figure 3.6.: CSV algorithm discriminator values in enriched $t\bar{t}$ (top) and inclusive multi-jet samples (bottom) for b,c and light flavoured jets [64]. The discriminator value used for each working points are determined from the misidentification probability for light-parton jets to be tagged as a b-jet, which are given as 0.244 (10%), 0.679 (1%) and 0.898 (0.1%) for the L, M and T working points respectively.

1017 The b-tagging efficiency is measured in data using several methods applied to multi
 1018 jet events, primarily based on a sample of jets enriched in heavy flavour content. One
 1019 method requires the collection of events with a soft muon within a cone $\Delta R < 0.4$ around
 1020 the jet axis. Because the semi-leptonic branching fraction of b hadrons is significantly
 1021 larger than that for other hadrons, these jets are more likely to arise from b quarks than
 1022 from another flavour, with the resultant momentum component of the muon transverse
 1023 to the jet axis larger for muons from b-hadron decays than from light or charm jets.

1024 Additionally the performance of the tagger can also be benchmarked in $t\bar{t}$ events where
1025 in the SM, the top quark is expected to decay to a W boson and a b quark about 99.8%
1026 of the time [1]. Further selection criteria is applied to these events to further enrich the
1027 b quark content of these events. The methods to identify b-jets in data are discussed
1028 in great detail at [65]. The jet flavours are determined in simulation using truth level
1029 information and are compared to data to determine the correction scale factors (SF_b),
1030 which are displayed for the CSVM tagger in Figure 3.7.

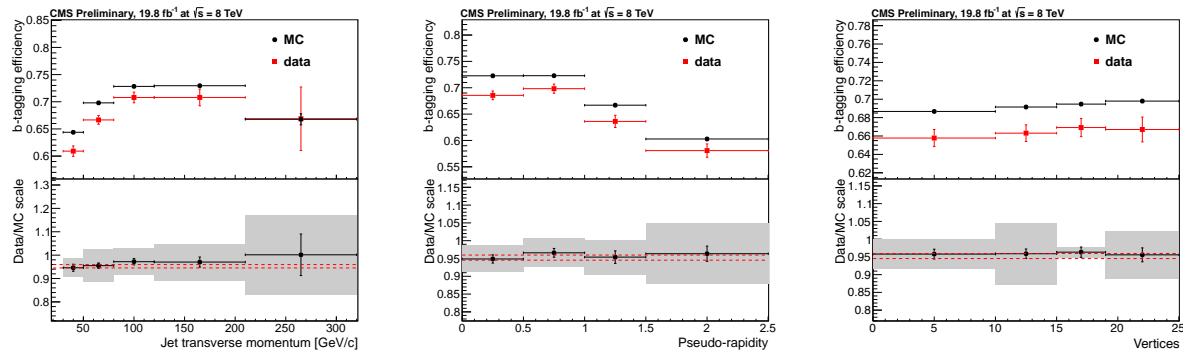


Figure 3.7.: Measured in $t\bar{t} \rightarrow$ di-lepton events using the CSVM tagger: (upper panels) b-tagging efficiencies and (lower panels) data/MC scale factor SF_b as a function of (left) jet p_T , (middle) jet $|\eta|$ and (right) number of primary vertices. In the lower panels, the grey filled areas represent the total statistical and systematic uncertainties, whereas the dotted lines are the average SF_b values within statistical uncertainties.

1031 The measurement of the misidentification probability for light-parton jets relies on the
1032 inversion of tagging algorithms, selecting non-b jets using the same variables and tech-
1033 niques used in benchmarking the b-tagging efficiency. The scale factors (SF_s) to be
1034 applied to MC are shown in Figure 3.8 for the CSVM tagger.

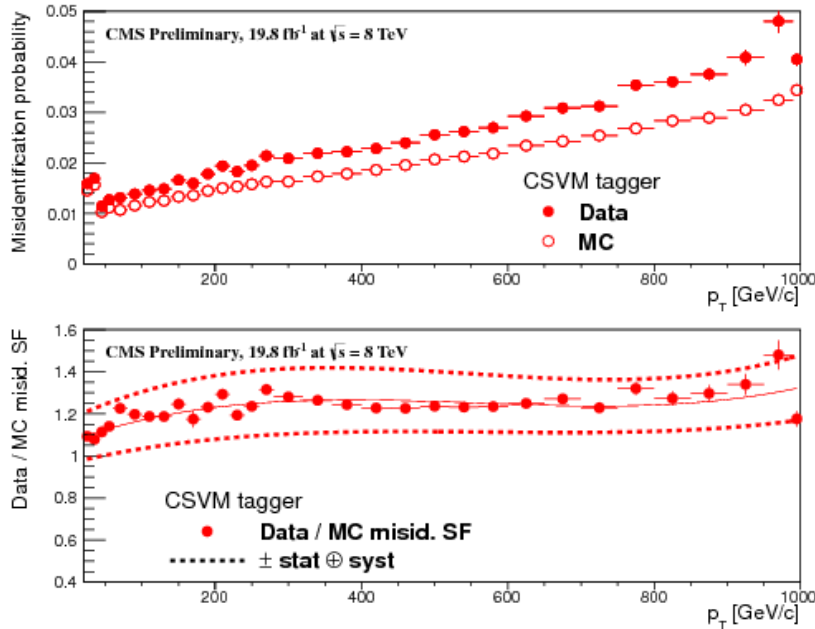


Figure 3.8.: For the **CSVM** tagging criterion: (top) misidentification probability in data (filled circles) and simulation (open circles); (bottom) scale factor for the misidentification probability. The last p_T bin in each plot includes all jets with $p_T > 1000$ GeV. The solid curve is the result of a polynomial fit to the data points. The dashed curves represent the overall statistical and systematic uncertainties on the measurements.

1035 3.4. Triggering System

1036 With bunch crossings separated by just 25 ns, the rate at which data from all collisions
 1037 would have to be written out and processed would be unfeasible. A two-tiered triggering
 1038 system is applied at **CMS** in order to cope with the high collision rate of protons. The
 1039 **CMS** trigger is designed to use limited information from each event to determine whether
 1040 to record the event, reducing the rate of data taking to manageable levels whilst ensuring
 1041 a high efficiency of interesting physics object events are selected.

1042 The **L1** is a pipelined, dead-timeless system based on custom-built electronics [66], and is
 1043 a combination of several sub systems which is shown pictorially in Figure 3.9. The L1
 1044 system is covered in more detail within the following section along with a description
 1045 of the service work undertaken by the author to benchmark the performance of the L1
 1046 calorimeter trigger during the 2012 8 TeV run period.

1047 The Higher Level Trigger (**HLT**) is a large farm of commercial computers [67]. The **HLT**
 1048 processes events with software reconstruction algorithms that are more detailed, giving
 1049 performance more similar to the reconstruction used offline. The **HLT** reduces the event

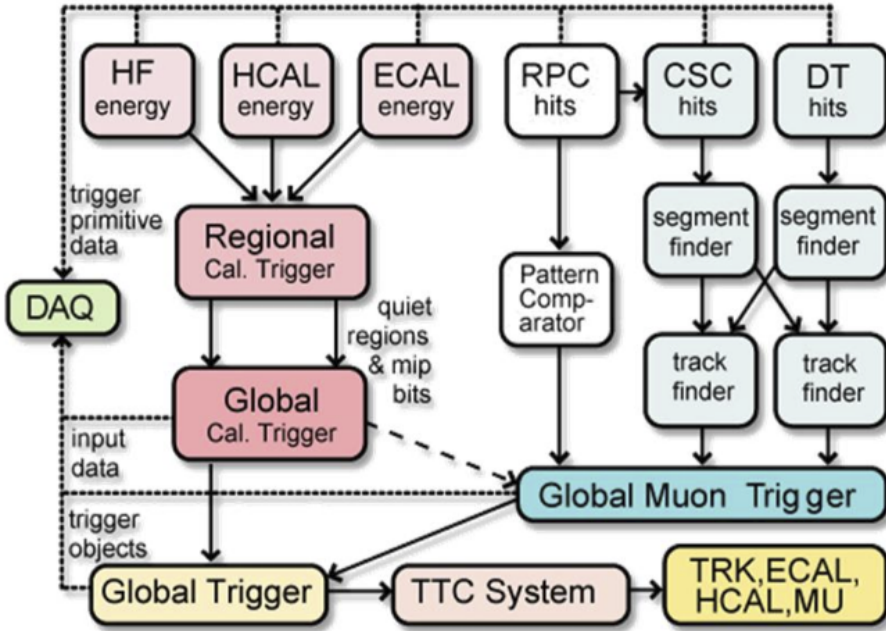


Figure 3.9.: The CMS L1 Trigger system.

rate written to disk by a factor of ~ 500 ($\sim 200\text{Hz}$). The recorded events are transferred from CMS to the CERN computing centre, where event reconstruction is performed, and then distributed to CMS computing sites around the globe for storage and analysis.

3.4.1. The Level-1 trigger

The L1 trigger reduces the rate of events collected from 40 MHz to $\sim 100\text{ kHz}$ using information from the calorimeters and muon chambers, but not the tracker. A tree system of triggers is used to decide whether to pass on an event to the HLT for further reconstruction. Firstly the calorimeter and muon event information is kept separate, with local reconstruction of objects (μ , e , γ , and jets) performed by the Regional Calorimeter Trigger (RCT) and Regional Muon Trigger (RMT) respectively. The RCT generates up to 72 isolated and non-isolated electromagnetic objects. These are sorted by rank, which is equivalent to transverse energy E_T , with the four highest ranked electromagnetic objects being passed via the Global Calorimeter Trigger (GCT) and Global MuonTrigger (GMT) to the Global Trigger (GT).

1064 In the L1 **GCT**, coarse measurements of the energy deposited in the electromagnetic and
1065 hadronic calorimeters are combined, and by using sophisticated algorithms the following
1066 physics objects are formed:

- 1067 • isolated and non-isolated electromagnetic objects (e and γ);
- 1068 • hadronic jets in the central and forward sections of the hadronic calorimeters;
- 1069 • hadronically decaying tau leptons;
- 1070 • total transverse energy (E_T), the scalar sum of the energy measured at L1, and
1071 missing transverse energy (\cancel{E}_T), defined as the vector sum of the energy of L1
1072 objects;
- 1073 • total transverse jet energy (H_T), the scalar sum of the energy of all L1 jet objects,
1074 and missing transverse jet energy (\cancel{H}_T), defined as the vector sum of the energy of
1075 L1 jets, are calculated from uncorrected L1 jets.

1076 In addition quantities suitable for triggering minimum bias events, forward physics and
1077 beam background events are calculated. Additionally relevant muon isolation information
1078 is also passed on to the **GMT** for decisions involving the muon triggers where it is
1079 combined with information from across the three muon sub-systems. The resultant final
1080 accept/reject decision at **L1** is then performed by the **GT** based on the objects received
1081 from the **GCT** and **GMT** (e/γ , μ , jets, E_T , \cancel{E}_T , H_T).

1082 The L1 trigger is therefore of upmost importance to the functioning of the detector.
1083 Without a high-performing trigger and a good understanding of its performance, there
1084 would be no data to analyse. Observations of how the L1 trigger performance is affected
1085 by changing **LHC** running conditions over the 2012 run period and also the introduction
1086 of a jet seed threshold to the L1 jet trigger algorithm is presented in the following Sections
1087 (3.4.2 - 3.4.6).

1088 3.4.2. The L1 trigger jet algorithm

1089 The L1 jet trigger uses the transverse energy sums computed in the calorimeter (both
1090 hadronic and electromagnetic) trigger regions. Each region consists of 4×4 trigger tower
1091 windows, spanning a region of $\Delta\eta \times \Delta\phi = 0.087 \times 0.087$ in pseudorapidity-azimuth. The
1092 jet trigger uses a 3×3 calorimeter region (112 trigger towers) sliding window technique
1093 which spans the full (η, ϕ) coverage of the **CMS** calorimeter as shown in Figure 3.10.

1094 In forming a L1 jet is it required that the central region to be higher than the eight
1095 neighbouring regions E_T central > E_T surround. Additionally a minimum threshold of 5 GeV
1096 on E_T central was introduced during the 2012 run period to suppress noise from pile-up.
1097 A comparison between these two configurations is shown in Section (3.4.4).

1098 The L1 jets are characterised by the E_T , summed over the 3×3 calorimeter regions,
1099 which corresponds to 12×12 trigger towers in barrel and endcap or 3×3 larger **HF**
1100 towers in the **HF**. The ϕ size of the jet window is the same everywhere, whilst the η
1101 binning gets somewhat larger at high η due to calorimeter and trigger tower segmentation.
1102 The jets are labelled by the (η, ϕ) indices of the central calorimeter region.

1103 Jets with $|\eta| > 3.0$ are classified as forward jets, whereas those with $|\eta| < 3.0$ are classified
1104 as central. The four highest energy central, forward and τ jets in the calorimeter are
1105 passed through Look Up Table (**LUT**)’s, which apply a programmable η –dependent jet
1106 energy scale correction. These are then used to make L1 trigger decisions.

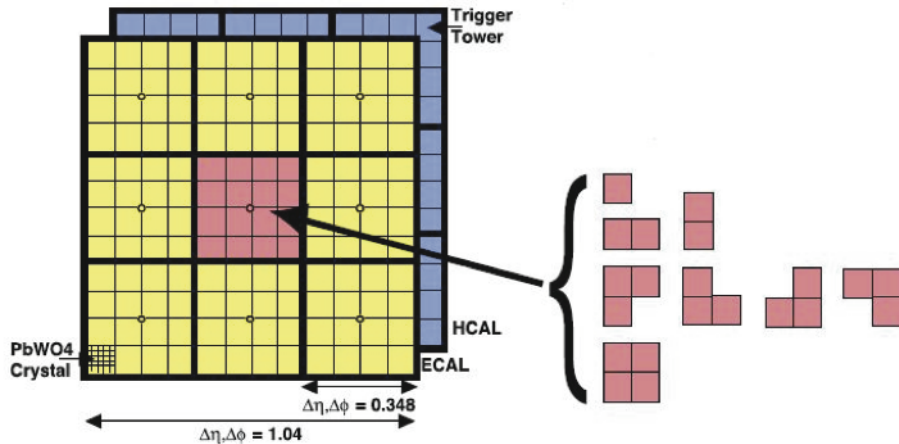


Figure 3.10.: Illustration of the Level-1 jet finding algorithm.

1107 The performance of the L1 jets is evaluated with respect to offline jets, which are taken
1108 from the standard Calo jet and the PF jet reconstruction algorithms of **CMS**. Jets are
1109 corrected for pile-up and detector effects as described in 3.3.1. A moderate level of noise
1110 rejection is applied to the offline jets by selecting jets passing the “loose” identification
1111 criteria for both Calo and PF. These jet criteria are listed in Appendix (A.1).

3.4.3. Measuring L1 jet trigger efficiencies

The L1 jet efficiency is defined as the fraction of leading offline jets which were matched with a L1 tau or central jet above a certain trigger threshold, divided by all the leading offline jets in the event. This quantity is then plotted as a function of the offline jet E_T , η and ϕ .

The efficiency is determined by matching the L1 and reconstructed offline jets spatially in $\eta - \phi$ space. This is done by calculating the minimum separation in ΔR between the highest offline reconstructed jet in E_T ($E_T > 10$ GeV, $|\eta| < 3$) and any L1 jet. A jet will be matched if this value is found to be < 0.5 . Should more than one jet satisfy this, the jet closest in ΔR is taken as the matched jet. The matching efficiency is close to 100%, above 30(45) GeV for run 2012B(C) data (see Appendix B.1).

Each efficiency curve is fitted with a function which is the cumulative distribution function of an Exponentially Modified Gaussian (EMG) distribution:

$$f(x; \mu, \sigma, \lambda) = \frac{\lambda}{2} \cdot e^{\frac{\lambda}{2}(2\mu + \lambda\sigma^2 - 2x)} \cdot \text{erfc}\left(\frac{\mu + \lambda\sigma^2 - x}{\sqrt{2}\sigma}\right) \quad (3.3)$$

where erfc is the complementary error function defined as:

$$\text{erfc}(x) = 1 - \text{erf}(x) = \frac{2}{\sqrt{\pi}} \int_x^\infty e^{-t^2} dt.$$

In this functional form, the parameter μ determines the point of 50% of the plateau efficiency and the σ gives the resolution. This parametrisation is used to benchmark the efficiency at the plateau, the turn-on points and resolution for each L1 Jet trigger. The choice of function is purely empirical. Previous studies used the error function alone, which described the data well at high threshold values but could not describe the efficiencies well at lower thresholds [68].

The efficiency turn-on curves for various L1 jet thresholds are evaluated as a function of the offline reconstructed jet E_T for central jets with $|\eta| < 3$. These are measured using single isolated μ triggers which have high statistics, and are orthogonal and therefore unbiased to the hadronic triggers under study. The efficiency is calculated with respect to offline Calo and PF Jets in Figure 3.11. Table 3.1 shows the values of these parameters, calculated for three example L1 single jet triggers taken from 2012 8 TeV data.

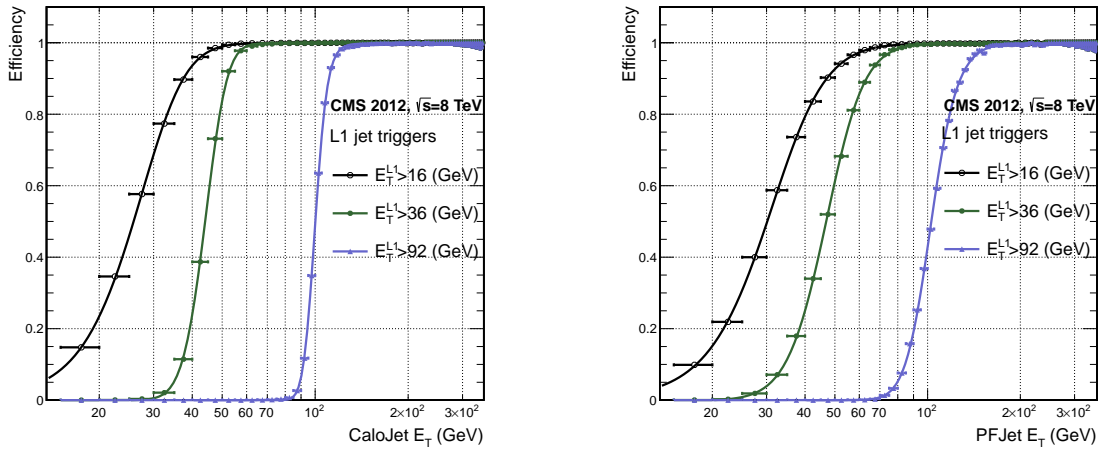


Figure 3.11.: L1 jet efficiency turn-on curves as a function of the offline CaloJet E_T (left) and PFJet E_T (right), measured in 2012 Run Period C data and collected with an isolated single μ data sample.

Trigger	Calo		PF	
	μ	σ	μ	σ
L1_SingleJet16	21.09 ± 0.03	7.01 ± 0.02	22.17 ± 0.04	7.83 ± 0.03
L1_SingleJet36	41.15 ± 0.05	5.11 ± 0.02	39.16 ± 0.06	8.04 ± 0.03
L1_SingleJet92	95.36 ± 0.13	5.62 ± 0.03	90.85 ± 0.19	11.30 ± 0.10

Table 3.1.: Results of a cumulative EMG function fit to the turn-on curves for L1 single jet triggers in run 2012 Run Period C, measured in an isolated μ data sample. The turn-on point, μ , and resolution, σ , of the L1 jet triggers are measured with respect to offline Calo Jets (left) and PF Jets (right).

The results from the L1 single jet triggers shows good performance for both Calo and PF jets. A better resolution for Calo jets with respect to L1 jets quantities is observed. This effect is due to Calo jet reconstruction using the same detector systems as in L1 jets, whereas with PF jet construction using tracker and muon information, a more smeared resolution when compared to L1 is expected.

3.4.4. Effects of the L1 jet seed

Between run period B and C of the 2012 data taking period, a jet seed threshold was introduced into the L1 trigger jet algorithm. There was previously no direct requirement made on the energy deposited in the central region. The introduction of a jet seed threshold required that the central region have $E_T \geq 5\text{GeV}$, and was introduced to

1148 counteract the effects of high pile up running conditions which create a large number of
1149 soft non-collimated jets, that are then added to the jets from the primary interaction or
1150 other soft jets from other secondary interactions [69]. This in turn causes a large increase
1151 in trigger rate due to the increase in the likelihood that the event causes the L1 trigger to
1152 fire. This was implemented to maintain trigger thresholds by cutting the rate of events
1153 recorded without significant reduction in the efficiency of physics events of interest.

1154 The effect of the introduction of this jet seed threshold between these two run periods is
1155 benchmarked through a comparison of the efficiency of the L1 jet triggers with respect
1156 to offline Calo jets shown in Figure 3.12, and the L1 H_T trigger efficiency in Figure 3.14
1157 which is compared to offline H_T constructed from Calo jets with $E_T \geq 40\text{GeV}$.

1158 To negate any effects from different pile-up conditions in the run periods, the efficiencies
1159 are measured in events which contain between 15 and 20 primary vertices as defined in
1160 Appendix (A.2).

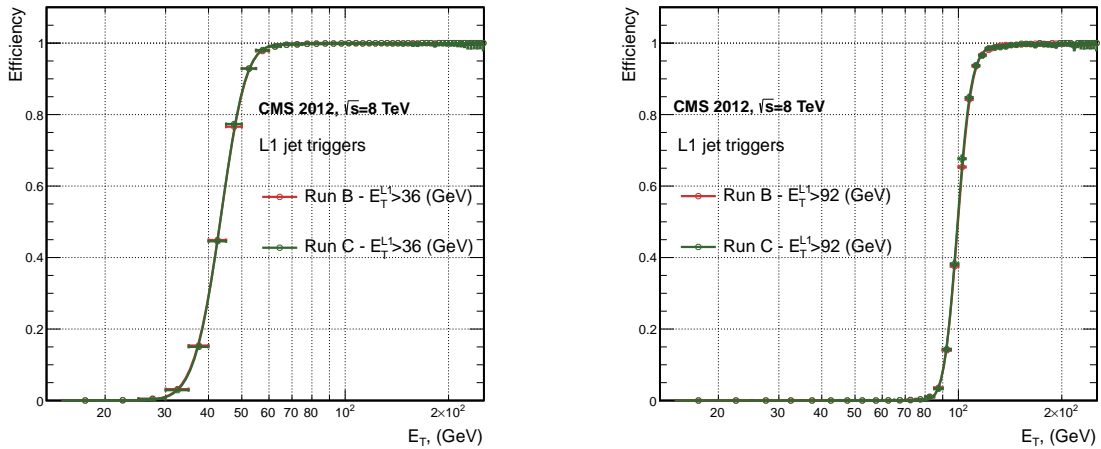


Figure 3.12.: L1 jet efficiency turn-on curves as a function of the offline CaloJet E_T , measured for the L1 SingleJet 36 and 92 trigger in 2012 run period B and C collected with an isolated single μ' sample.

1161 It can be seen that the performance of the $E_T > 36, 92$ single jet are almost identical,
1162 with the jet seed having no measurable effect on these triggers as shown in Table 3.2 .
1163 For the H_T triggers, a large increase in rate during high pile-up conditions is expected.
1164 This is due to the low energy threshold required for a jet to be added to the L1 H_T sum,
1165 which is compiled from all uncorrected L1 jets formed in the RCT. The introduction
1166 of the jet seed threshold removes the creation of many of these soft low E_T jets, thus

Trigger	2012B		2012C	
	μ	σ	μ	σ
L1_SingleJet36	40.29 ± 0.04	5.34 ± 0.02	40.29 ± 0.11	5.21 ± 0.05
L1_SingleJet92	94.99 ± 0.09	5.93 ± 0.06	94.82 ± 0.29	5.74 ± 0.18

Table 3.2.: Results of a cumulative EMG function fit to the turn-on curves for L1 single jet triggers in the 2012 run period B and C, preselected on an isolated muon trigger. The turn-on point μ and resolution σ of the L1 jet triggers are measured with respect to offline Calo Jets in run B (left) and run C (right).

1167 lowering the H_T calculation at L1. The effect on the trigger cross section for L1 H_T 150
1168 trigger can be seen in Figure 3.13.

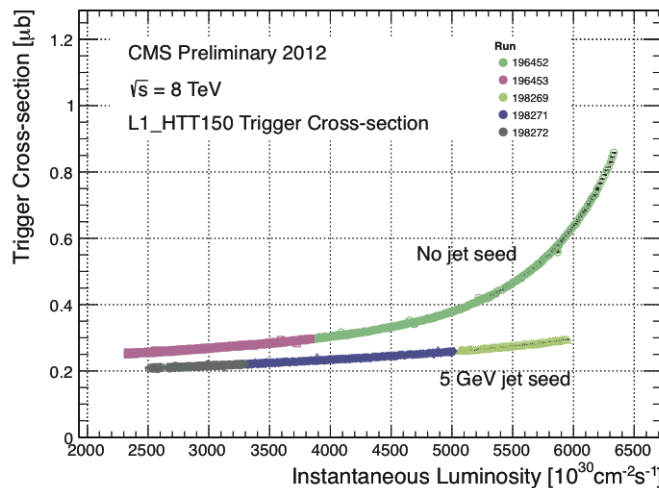


Figure 3.13.: Trigger cross section for the L1HTT150 trigger path. Showing that a 5 GeV jet seed threshold dramatically reduces the dependance of cross section on the instantaneous luminosity for L1 H_T triggers [70].

1169 Different behaviours for the trigger turn ons between these run periods are therefore
1170 expected. The turn on point is observed to shift to higher H_T values after the introduction
1171 of the jet seed threshold, whilst having a sharper resolution due to less pile-up jets being
1172 included the H_T sum. This effect is demonstrated in Table 3.3.

1173 3.4.5. Robustness of L1 jet performance against pile-up

1174 The performance of the L1 single jet triggers is evaluated in different pile-up conditions
1175 to benchmark any dependence on pile-up. Three different pile-up bins of 0-10, 10-20 and
1176 >20 vertices are defined, reflecting the low, medium and high pile-up running conditions

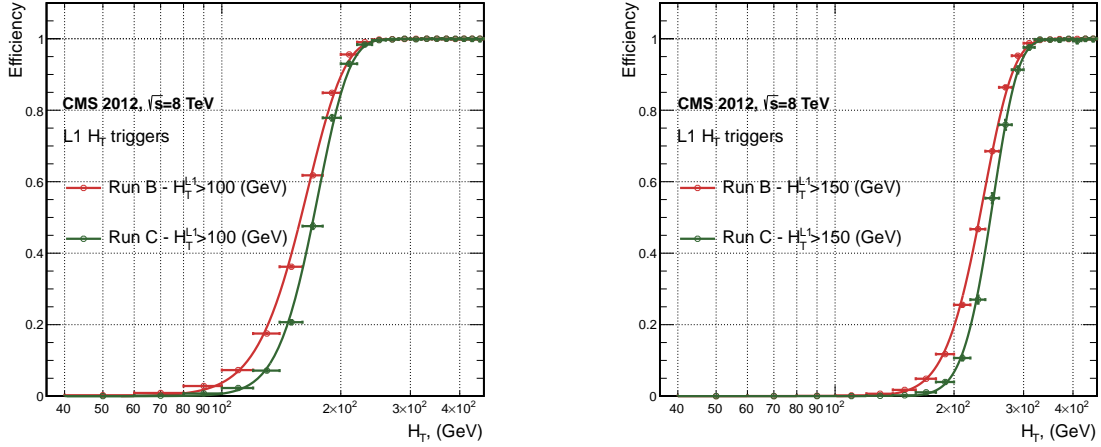


Figure 3.14.: L1 H_T efficiency turn-on curves as a function of the offline CaloJet H_T , measured for the L1 H_T 100 and 150 trigger during the run 2012 B and C collected using an isolated single μ triggered sample.

2012B			2012C		
Trigger	μ	σ	μ	σ	
L1 HT-100	157.5 ± 0.08	32.9 ± 0.08	169.8 ± 0.08	28.7 ± 0.03	
L1 H1-150	230.9 ± 0.02	37.3 ± 0.01	246.4 ± 0.16	31.8 ± 0.05	

Table 3.3.: Results of a cumulative **EMG** function fit to the turn-on curves for H_T in run 2012 B and C, preselected on an isolated single μ trigger. The turn-on point μ , resolution σ of the L1 H_T triggers are measured with respect to offline H_T formed from CaloJets with a $E_T \geq 40$ in run period B (left) and C (right).

at CMS in 2012. This is benchmarked relative to Calo and PF jets for the run 2012 C period where the jet seed threshold is applied, with L1 single jet thresholds of 16, 36 and 92 GeV, shown in Figure 3.15. The results of fits to these efficiency turn-on curves are given in Table 3.4 and Table 3.5 for Calo and PF jets respectively.

Vertices	0-10		11-20		> 20	
	μ	σ	μ	σ	μ	σ
L1_SingleJet16	19.9 ± 0.1	6.1 ± 0.3	20.8 ± 0.1	6.5 ± 0.1	22.3 ± 0.2	7.5 ± 0.1
L1_SingleJet36	41.8 ± 0.1	4.6 ± 0.1	40.9 ± 0.1	5.1 ± 0.1	40.6 ± 0.6	5.9 ± 0.2
L1_SingleJet92	95.9 ± 0.2	5.4 ± 0.1	95.2 ± 0.2	5.6 ± 0.1	94.5 ± 0.6	6.2 ± 0.3

Table 3.4.: Results of a cumulative **EMG** function fit to the efficiency turn-on curves for L1 single jet triggers in the 2012 run period C, measured from isolated μ triggered data. The turn-on point, μ , and resolution, σ , of the L1 jet triggers are measured with respect to offline Calo jets in low (left), medium (middle) and high (right) pile-up conditions.

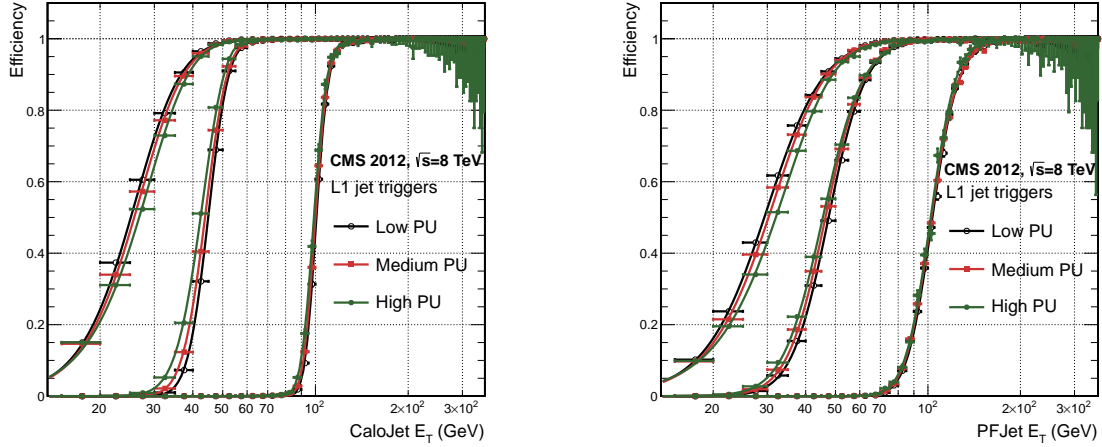


Figure 3.15.: L1 jet efficiency turn-on curves as a function of the leading offline E_T Calo (left) and PF (right) jet, for low, medium and high pile-up conditions.

Vertices	0-10		11-20		> 20	
	μ	σ	μ	σ	μ	σ
L1_SingleJet16	21.1 \pm 0.1	7.16 \pm 0.05	22.34 \pm 0.1	7.9 \pm 0.1	24.6 \pm 0.2	9.5 \pm 0.1
L1_SingleJet36	39.6 \pm 0.1	7.4 \pm 0.1	38.4 \pm 0.1	7.4 \pm 0.1	37.1 \pm 0.2	7.5 \pm 0.1
L1_SingleJet92	91.6 \pm 0.3	11.3 \pm 0.2	90.4 \pm 0.3	11.2 \pm 0.1	92.0 \pm 0.9	12.1 \pm 0.4

Table 3.5.: Results of a cumulative EMG function fit to the efficiency turn-on curves for Level-1 single jet triggers in the 2012 run period C, measured from isolated μ triggered data. The turn-on point, μ , and resolution, σ , of the L1 jet triggers are measured with respect to offline PF jets in low (left), medium (middle) and high (right) pile-up conditions.

1181 No significant drop in efficiency is observed in the presence of a high number of primary
 1182 vertices. The increase in hadronic activity in higher pile-up conditions, combined with
 1183 the absence of pile-up subtraction for L1 jets, results in the expected observation of
 1184 a decrease in the μ value of the efficiency turn-ons as a function of pile-up, while the
 1185 resolution, σ of the turn-ons are found to gradually worsen as expected with increasing
 1186 pile-up.

1187 These features are further emphasised when shown as a function of

$$\frac{(L1 E_T - \text{Offline } E_T)}{\text{Offline } E_T} \quad (3.4)$$

1188 in bins of matched leading offline jet E_T , of which the individual fits can be found in
1189 Appendix (B.2). Each of these distributions are fitted with an EMG function as defined
1190 in Equation (3.3).

1191 The μ , σ and λ values extracted for the low, medium and high pile-up conditions are
1192 shown for Calo and PF jets in Figure 3.16 and Figure 3.17 respectively. The central value
1193 of $\frac{(L1 E_T - \text{Offline } E_T)}{\text{Offline } E_T}$ is observed to increases as a function of jet E_T , whilst the resolution
1194 is also observed to improve at higher offline jet E_T .

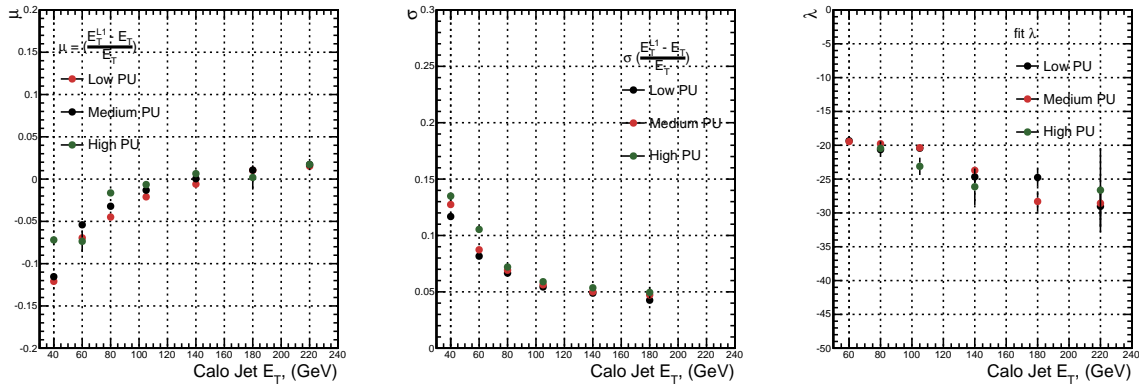


Figure 3.16.: Fit values from an EMG function fitted to the resolution plots of leading Calo jet E_T measured as a function of $\frac{(L1 E_T - \text{Offline } E_T)}{\text{Offline } E_T}$ for low, medium and high pile-up conditions. The plots show the mean μ (left), resolution σ (middle) of the Gaussian as well as the decay term λ (right) of the exponential.

1195 The resolution of other L1 energy sum quantities, H_T , \not{E}_T and $\sum E_T$ parameterised as
1196 in Equation (3.4), can be found in Appendix (B.3). The same behaviour observed for
1197 the single jet triggers is also found for these quantities, where in the presence of higher
1198 pile-up the μ values are shifted to higher values, with a worsening resolution, σ again
1199 due to the increase in soft pile-up jets and the absence of pile-up subtraction at L1.

1200 3.4.6. Summary

1201 The performance of the CMS Level-1 Trigger has been studied and evaluated for jets and
1202 energy sum quantities using data collected during the 2012 LHC 8 TeV run. These studies
1203 include the effect of introduction of a 5 GeV jet seed threshold into the jet algorithm
1204 configuration, the purpose of which is to mitigate the effects of pile-up on the rate of
1205 L1 triggers whilst not adversely affecting the efficiency of these triggers. No significant

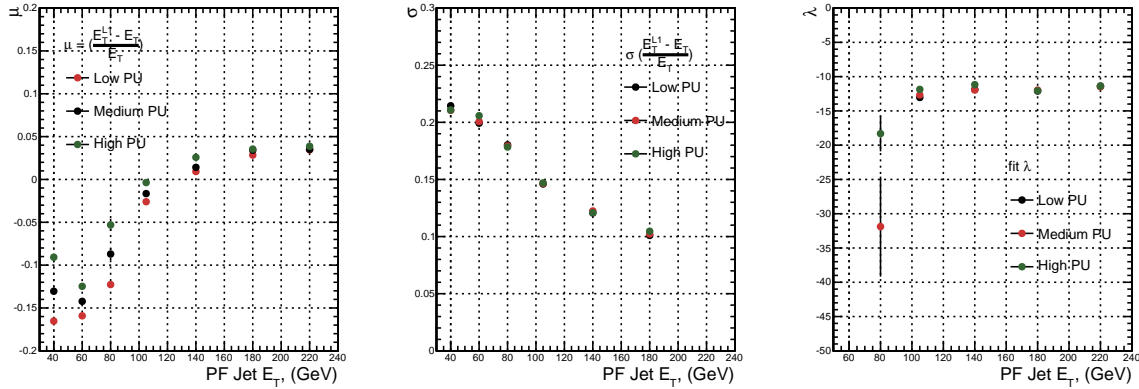


Figure 3.17.: Fit values from an EMG function fitted to the resolution plots of leading PF jet E_T measured as a function of $\frac{(L1\ E_T - \text{Offline}\ E_T)}{\text{Offline}\ E_T}$ for low and medium pile-up conditions. The plots show the mean μ (left), resolution σ (middle) of the Gaussian as well as the decay term λ (right) of the exponential.

1206 change in performance is observed with this change and good performance is observed
 1207 for a range of L1 quantities.

Chapter 4.

1208 SUSY Searches In Hadronic Final 1209 States

1210 In this chapter a model independent search for **SUSY** in hadronic final states with
1211 \cancel{E}_T using the α_T variable at different b-quark and jet multiplicities is introduced and
1212 described in detail. The results presented are based on a data sample of pp collisions
1213 collected in 2012 at $\sqrt{s} = 8$ TeV, corresponding to an integrated luminosity of 11.7 ± 0.5
1214 fb^{-1} [5].

1215 The kinematic variable α_T is motivated as a variable to provide strong rejection of the
1216 overwhelming QCD background, prevalent to jets + \cancel{E}_T final states at the **LHC**. This
1217 is achieved whilst maintaining sensitivity to a possible **SUSY** signal and described in
1218 Section (4.1). The search and trigger strategy in addition to the event reconstruction
1219 and selection are outlined within Sections (4.2 - 4.3).

1220 The method in which the **SM** background is estimated using an analytical technique to
1221 improve statistical precision at higher b-tag multiplicities is detailed within Section (4.5).
1222 Included in this section is a discussion on the impact of b-tagging and mis-tagging scale
1223 factors between data and simulation on any background predictions. Improved precision
1224 in estimating background yields at large number of b-tagged jets, is important in the
1225 context of interpreting natural **SUSY** models, first outlined in Section (2.4.1).

1226 A description of the formulation of appropriate systematic uncertainties applied to the
1227 background predictions to account for theoretical uncertainties and limitations in the
1228 simulation modelling of event kinematics and instrumental effects is covered in Section
1229 (4.6).

Finally the statistical likelihood model to interpret the observations in the signal and control samples is described in Section (4.8). The experimental reach of the analysis discussed within this thesis is interpreted in two classes of **SMS** models, both first introduced in Section (2.4.1). The **SMS** models considered in this analysis are summarised in Table 4.1. For each model, the **LSP** is assumed to be the lightest neutralino.

Within the table are also defined reference points, parameterised in terms of parent gluino/squark and **LSP** sparticle masses, m_{parent} and m_{LSP} , respectively, which are used within the following two chapters to demonstrate potential yields within the signal region of the search.

The masses are chosen to reflect parameter space which is within the expected sensitivity reach of the search, and also in the case of T1tttt and T1bbbb, reflect examples of potential natural **SUSY** topologies.

Model	Production/decay mode	Reference model	
		m_{parent}	m_{LSP}
G1 (T1)	$pp \rightarrow \tilde{g}\tilde{g}^* \rightarrow q\bar{q}\tilde{\chi}_1^0 q\bar{q}\tilde{\chi}_1^0$	700	300
G2 (T1bbbb)	$pp \rightarrow \tilde{g}\tilde{g}^* \rightarrow b\bar{b}\tilde{\chi}_1^0 b\bar{b}\tilde{\chi}_1^0$	900	500
G3 (T1tttt)	$pp \rightarrow \tilde{g}\tilde{g}^* \rightarrow t\bar{t}\tilde{\chi}_1^0 t\bar{t}\tilde{\chi}_1^0$	850	250
D1 (T2)	$pp \rightarrow \tilde{q}\tilde{q}^* \rightarrow q\tilde{\chi}_1^0 q\tilde{\chi}_1^0$	600	250
D2 (T2bb)	$pp \rightarrow \tilde{b}\tilde{b}^* \rightarrow b\tilde{\chi}_1^0 b\tilde{\chi}_1^0$	500	150
D3 (T2tt)	$pp \rightarrow \tilde{t}\tilde{t}^* \rightarrow t\tilde{\chi}_1^0 t\tilde{\chi}_1^0$	400	0

Table 4.1.: A summary of the **SMS** models interpreted in this analysis, involving both direct (D) and gluino-induced (G) production of squarks and their decays. Reference models are also defined in terms of parent and **LSP** sparticle mass

4.1. An Introduction to the α_T Search

A proton-proton collision resulting in the production and decay of supersymmetric particles, would manifest as a final state containing energetic jets and \cancel{E}_T in the hadronic channel. The search focuses on topologies where new heavy supersymmetric, R-parity conserving particles are pair-produced in pp collisions. These particles decaying to a **LSP** escape the detector undetected, leading to significant missing energy and missing hadronic transverse energy,

$$\mathcal{H}_T = \left| \sum_{i=1}^n \vec{p_T}^{jet_i} \right|, \quad (4.1)$$

1249 defined as the vector sum of the transverse energies of jets selected in an event. Energetic
1250 jets produced in the decay of these supersymmetric particles also can produce significant
1251 visible transverse energy,

$$H_T = \sum_{i=1}^n E_T^{jet_i}, \quad (4.2)$$

1252 defined as the scalar sum of the transverse energies of jets selected in an event.

1253 A search within this channel is greatly complicated in a hadron collider environment,
1254 where the overwhelming background comes from inherently balanced multi-jet (“QCD”)
1255 events which are produced with an extremely large cross section as demonstrated within
1256 Figure 4.1. \cancel{E}_T can appear in such events with a substantial mis-measurement or
1257 stochastic fluctuations of jet energy or missed objects due to detector mis-calibration or
1258 noise effects.

1259 Additional SM background from EWK processes with genuine \cancel{E}_T from escaping neutrinos
1260 comprise the irreducible background within this search and come mainly from:

- 1261 • $Z \rightarrow \nu\bar{\nu}$ + jets,
- 1262 • $W \rightarrow l\nu$ + jets in which a lepton falls outside of detector acceptance, is not
1263 reconstructed, is mis-identified, or the lepton decays hadronically $\tau \rightarrow$ had ,
- 1264 • $t\bar{t}$ with at least one leptonically decaying W, which is missed in the detector as
1265 detailed above,
- 1266 • small background contributions from DY, single top and Diboson (WW,ZZ,WZ)
1267 processes.

1268 The search is designed to have a strong separation between events with genuine and
1269 “fake” \cancel{E}_T which is achieved primarily through the dimensionless kinematic variable, α_T
1270 [71][72].

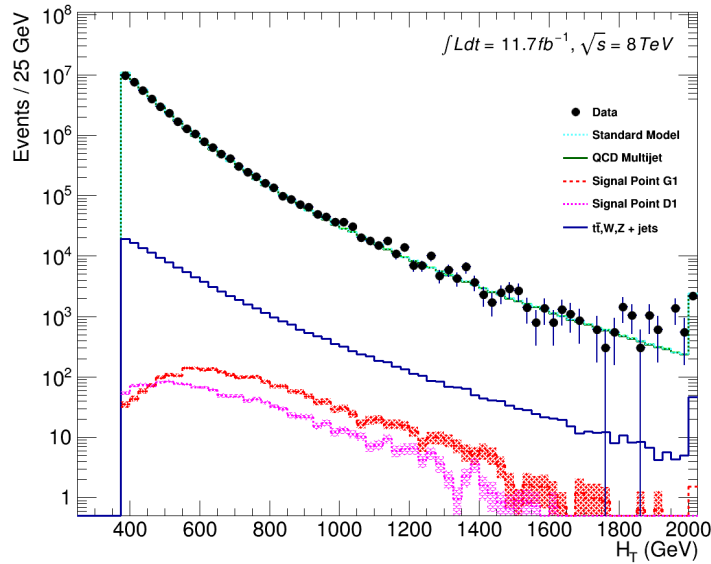


Figure 4.1.: Reconstructed offline H_T distribution in the hadronic signal selection, from 11.7fb^{-1} of data, in which no α_T requirement is made. Sample is collected from prescaled H_T triggers. Overlaid are expectations from MC simulation of EWK processes as well as a reference signal models (labelled G1 and D1 from Table 4.1).

1271 4.1.1. The α_T variable

1272 For a perfectly measured di-jet QCD event, conservation laws dictate that both jets must
 1273 be of equal magnitude and produced in opposite directions. However in the case of di-jet
 1274 events with genuine \cancel{E}_T (as detailed above), no such requirement is made of the two jets,
 as depicted in Figure 4.2.

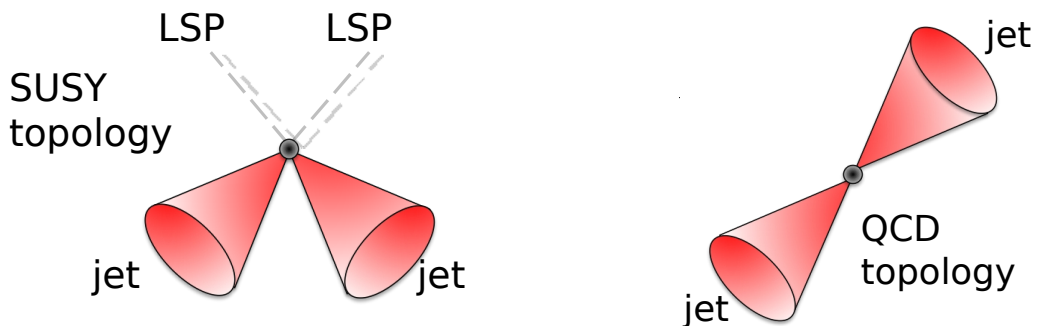


Figure 4.2.: The event topologies of background QCD dijet events (right) and a generic SUSY signature with genuine \cancel{E}_T (left).

1276 Exploiting this feature leads to the formulation of α_T (first inspired by [73]) in di-jet
1277 systems defined as,

$$\alpha_T = \frac{E_T^{j_2}}{M_T}, \quad (4.3)$$

1278 where $E_T^{j_2}$ is the transverse energy of the least energetic of the two jets and M_T defined
1279 as:

$$M_T = \sqrt{\left(\sum_{i=1}^2 E_T^{j_i}\right)^2 - \left(\sum_{i=1}^2 p_x^{j_i}\right)^2 - \left(\sum_{i=1}^2 p_y^{j_i}\right)^2} \equiv \sqrt{H_T^2 - \cancel{H}_T^2}. \quad (4.4)$$

1280 A perfectly balanced di-jet event i.e. $E_T^{j_1} = E_T^{j_2}$ would yield an α_T value of 0.5, where
1281 as events with jets which are not back-to-back, for example in events in which a W or
1282 Z recoils off a system of jets, α_T can achieve values in excess of 0.5. Most importantly
1283 balanced QCD events in which jets are mis-measured, will generally result in an α_T of
1284 less than 0.5, thus giving the α_T variable discriminating power between these processes.

1285 α_T can be extended to apply to any arbitrary number of jets, undertaken by modelling
1286 a system of n jets as a di-jet system, through the formation of two pseudo-jets [74].
1287 The two pseudo-jets are built by merging the jets present in the event such that the
1288 2 pseudo-jets are chosen to be as balanced as possible, i.e the $\Delta H_T \equiv |E_T^{pj_1} - E_T^{pj_2}|$ is
1289 minimised between the two pseudo jets. Using Equation (4.4), α_T can be rewritten as,

$$\alpha_T = \frac{1}{2} \frac{H_T - \Delta H_T}{\sqrt{H_T^2 - \cancel{H}_T^2}} = \frac{1}{2} \frac{1 - \Delta H_T/H_T}{\sqrt{1 - (\cancel{H}_T/H_T)^2}}. \quad (4.5)$$

1290 The distribution of α_T for the two jet categories used within this analysis, $2 \leq n_{jet} \leq 3$
1291 and $n_{jet} \geq 4$ jets, is shown in the Figure 4.3. It can be seen that the distributions peak
1292 at an α_T of 0.5, before falling away sharply and being free of multi-jet background at
1293 larger α_T values. These distributions serve to demonstrate the ability of the α_T variable
1294 to discriminate between multi-jet events and EWK processes with genuine \cancel{E}_T in the
1295 final state.

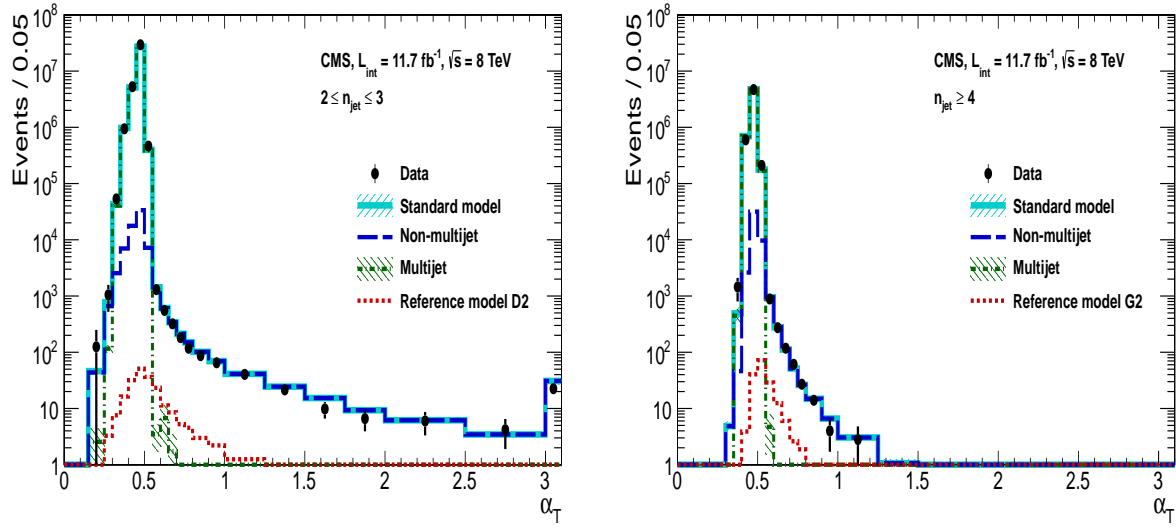


Figure 4.3.: The α_T distributions for the low 2-3 (left) and high ≥ 4 (right) jet multiplicities after a full analysis selection and shown for $H_T > 375$. Data is collected using both prescaled H_T triggers and dedicated α_T triggers for below and above $\alpha_T = 0.55$ respectively. . Expected yields as given by simulation are also shown for multi-jet events (green dash-dotted line), EWK backgrounds with genuine E_T (blue long-dashed line), the sum of all SM processes (cyan solid line) and the reference signal model D2 (left, red dotted line) or G2 (right, red dotted line).

1296 The α_T requirement used within the search is chosen to be $\alpha_T > 0.55$ to ensure that
 1297 the QCD multi-jet background is negligible even in the presence of moderate jet mis-
 1298 measurement. There still remains other effects which can cause multi-jet events to
 1299 artificially have a large α_T value, which are discussed in detail in Section (4.2.2).

1300 4.2. Search Strategy

1301 The aim of the analysis presented in this thesis is to identify an excess of events in data
 1302 over the SM background expectation in multi-jet final states and significant E_T . The
 1303 essential suppression of the dominant QCD background for such a search is addressed by
 1304 the α_T variable described in the previous section. For estimation of the remaining EWK
 1305 backgrounds, three independent data control samples are used to predict the different
 1306 processes that compose the background :

- 1307 • $\mu +$ jets control sample to determine $W +$ jets, $t\bar{t}$ and single top backgrounds,
- 1308 • $\gamma +$ jets control sample to determine the irreducible $Z \rightarrow \nu\bar{\nu} +$ jets background,

- 1309 • $\mu\mu + \text{jets}$ control sample to also determine the irreducible $Z \rightarrow \nu\bar{\nu} + \text{jets}$ background.

1310 These control samples are chosen to both be rich in specific **EWK** processes, be free of
1311 QCD multi-jet events and to also be kinematically similar to the hadronic signal region
1312 that they are estimating the backgrounds of, see Section (4.2.3). The redundancy of
1313 using the $\gamma + \text{jets}$ and $\mu\mu + \text{jets}$ sample to predict the same background within the
1314 signal region, brings an opportunity to reliably cross check and validate the background
1315 estimation method and is utilised in both the determination of background estimation
1316 systematics (Section(4.6)), and in the maximum likelihood fit (Section(4.8)).

1317 To remain inclusive to a large range of possible **SUSY** models, the signal region is split
1318 into the following categories to allow for increased sensitivity in the interpretation of
1319 results for different **SUSY** topologies:

1320 **Sensitivity to a range of SUSY mass splittings**

1321 The hadronic signal region is defined by $H_T > 275$, divided into eight bins in H_T .

- 1322 – Two bins of width 50 GeV in the range $275 < H_T < 375$ GeV,
1323 – five bins of width 100 GeV in the range $375 < H_T < 875$ GeV,
1324 – and a final open bin, $H_T > 875$ GeV.

1325 The choice of the lowest H_T bin in the analysis is driven primarily by trigger
1326 constraints. The mass difference between the **LSP** and the particle that it decays
1327 from is an important factor in the amount of hadronic activity in the event.

1328 A large mass splitting will lead to hard high p_T jets which contribute to the H_T sum.
1329 From Figure 4.1 it can be seen that the **SM** background falls sharply at high H_T
1330 values, therefore binning in H_T will lead to easier of identification of such signals.
1331 Conversely smaller mass splittings lead to softer jet p_T 's which will subsequently
1332 fall into the lower H_T range.

1333 **Sensitivity to production method of SUSY particles**

1334 The production mechanism of any potential **SUSY** signal can lead to different event
1335 topologies. One such way to discriminate between gluino ($g\tilde{g}$ - “high multiplicity”),
1336 and direct squark ($q\tilde{q}$ - “low multiplicity”) induced production of **SUSY** particles is
1337 realised through the number of reconstructed jets in the final state.

1338 The analysis is thus split into two jet categories : 2-3 jets , ≥ 4 jets to give sensitivity
1339 to both of these mechanisms.

1340 **Sensitivity to “Natural SUSY” via tagging jets from b-quarks**

1341 Jets originating from bottom quarks (b-jets) are identified through vertices that
1342 are displaced with respect to the primary interaction. The algorithm used to tag
1343 b-jets is the Combined Secondary Vertex Medium Working Point (**CSVM**) tagger,
1344 described within Section (3.3.2). A cut is placed on the discriminator variable of
1345 > 0.679 , leading to a gluon/light-quark mis-tag rate of approximately 1% and a jet
1346 p_T dependant b-tagging efficiency of 60-70% [64].

1347 Natural **SUSY** models would be characterised through final-state signatures rich
1348 in bottom quarks. A search relying on methods to identify jets originating from
1349 bottom quarks through b-tagging, will significantly improve the sensitivity to this
1350 class of signature. This gain in sensitivity stems from a vast reduction in the vector
1351 boson + jet backgrounds (W,Z) at higher b-tag jet multiplicities, which typically
1352 have no b-flavoured quarks in their decays.

1353 Therefore events are categorised according to the number of b-tagged jets recon-
1354 structed in each event, in the following: 0,1,2,3, ≥ 4 b-tag categories . In the highest
1355 ≥ 4 b-tag category due to a limited number of expected signal and background, just
1356 three H_T bins are employed: 275-325 GeV, 325-375 GeV, ≥ 375 GeV.

1357 This characterisation is identically mirrored in all control samples, with the infor-
1358 mation from all samples and b-tag categories used simultaneously in the likelihood
1359 model, see Section (4.8).

1360 The combination of the H_T , jet multiplicity and b-tag categorisation of the signal region as
1361 described above, resultantly leads to 67 different bins in which the analysis is interpreted
1362 in, and is depicted in Figure 4.4.

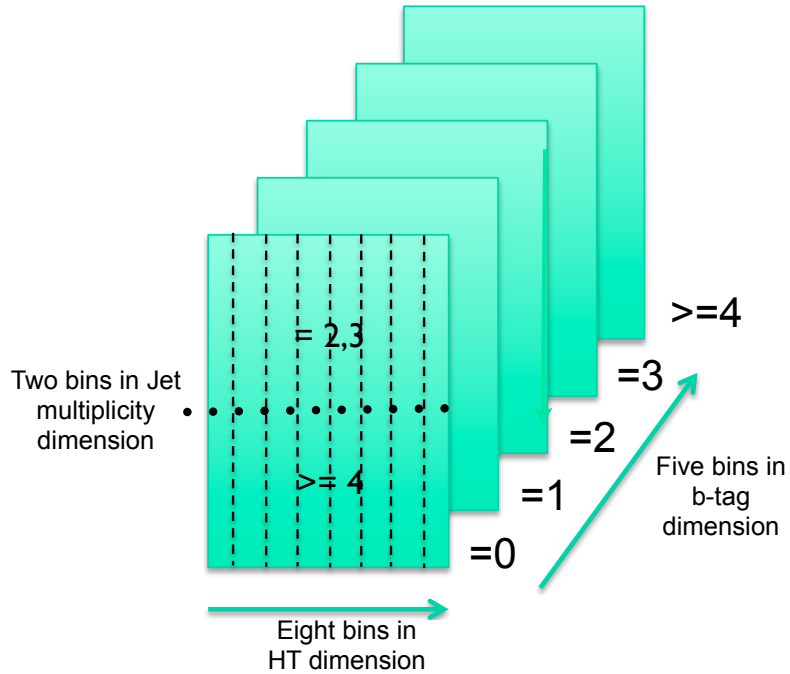


Figure 4.4.: Pictorial depiction of the analysis strategy employed by the α_T search to increase sensitivity to a wide spectra of **SUSY** models.

¹³⁶³ 4.2.1. Physics objects

¹³⁶⁴ The physics objects used in the analysis defined below, follow the recommendation of
¹³⁶⁵ the various **CMS** Physics Object Groups (**POGs**).

¹³⁶⁶ • Jets

¹³⁶⁷ The jets used in this analysis are CaloJets, reconstructed as described in Section
¹³⁶⁸ (3.3.1) using the anti- k_T jet clustering algorithm.

¹³⁶⁹ To ensure the jet object falls within the calorimeter systems a pseudo-rapidity
¹³⁷⁰ requirement of $|\eta| < 3$ is applied. Each jet must pass a “loose” identification criteria
¹³⁷¹ to reject jets resulting from unphysical energy, the criteria of which are detailed in
¹³⁷² Table A.1 [75].

¹³⁷³ • Muons

¹³⁷⁴ Muons are selected in the $\mu + \text{jets}$ and $\mu\mu + \text{jets}$ control samples, and vetoed in
¹³⁷⁵ the signal region. The same cut based identification criteria is applied to muons in
¹³⁷⁶ both search regions and is summarised in Table 4.2 [76].

Variable	Definition
Is Global Muon	Muon contains both a hit in the muon chamber and a matched track in the inner tracking system [77].
$\chi^2 < 10$	χ^2 of global muon track fit. Used to suppress hadronic punch-through and muons from decays in flight.
Muon chamber hits > 0	At least one muon chamber hit included in global muon track fit.
Muon station hits > 1	Muon segment hits in at least two muon stations, which suppresses hadronic punch-through and accidental track-to-segment matches.
$d_{xy} < 0.2\text{mm}$	The tracker track transverse impact parameter w.r.t the primary vertex. Suppresses cosmic muons and muons from decays in flight.
$d_z < 0.5\text{mm}$	The longitudinal distance of the tracker track w.r.t the primary vertex. Loose cut to further suppress cosmic muons, muons from decays in flight and tracks from pileup.
Pixel hits > 0	Suppresses muons from decays in flight by requiring at least one pixel hit in the tracker.
Track layer hits > 5	Number of tracker layers with hits, to guarantee a good p_T measurement. Also suppresses muons from decays in flight.
PF Iso < 0.12	Isolation based upon the sum of the charged and neutral hadrons and photon objects within a ΔR 0.4 cone of the muon object, corrected for pile up effects on the isolation sum.

Table 4.2.: Muon Identification criteria used within the analysis for selection/veto purposes in the muon control/signal selections.

1377 Additionally muons are required to be within the acceptance of the muon tracking
 1378 systems. For the muon control samples, trigger requirements necessitate a $|\eta| <$
 1379 2.1 for the selection of muons. In the signal region where muons are vetoed these
 1380 conditions are relaxed to $|\eta| < 2.5$ and a minimum threshold of $p_T > 10 \text{ GeV}$ is
 1381 required of muon objects.

1382 **• Photons**

1383 Photons are selected within the $\gamma + \text{jets}$ control sample and vetoed in all other
 1384 selections. Photons are identified in both cases according to the cut based criteria
 1385 listed in Table 4.3 [78].

Variable	Definition
H/E < 0.05	The ratio of hadronic energy in the HCAL tower directly behind the ECAL super-cluster and the ECAL super-cluster itself.
$\sigma_{i\eta i\eta} < 0.011$	The log energy weighted width (σ), of the extent of the shower in the η dimension.
R9 < 1.0	The ratio of the energy of the 3×3 crystal core of the super-cluster compared to the total energy stored in the 5×5 super-cluster.
Combined Isolation < 6 GeV	The photons are required to be isolated with no electromagnetic or hadronic activity within a radius $\Delta R = 0.3$ of the photon object. A combination of the pileup subtracted [79], ECAL , HCAL and tracking isolation sums are used to determine the combined total isolation value.

Table 4.3.: Photon Identification criteria used within the analysis for selection/veto purposes in the $\gamma +$ jets control/signal selections.

1386 Photon objects are also required to have a minimum momentum of $p_T > 25$ GeV.

1387 **• Electrons**

1388 Electron identification is defined for veto purposes. They are selected according to
1389 the following cut-based criteria listed in Table 4.4, utilising PF-based isolation.

1390 Electrons are required to be identified at $|\eta| < 2.5$, with a minimum $p_T > 10$ GeV
1391 threshold to ensure that the electron falls within the tracking system of the detector.

Variable	Barrel	EndCap	Definition
$\Delta\eta_{In}$	<0.007	<0.009	$\Delta\eta$ between SuperCluster position and the coordinate of the associated track at the interaction vertex, assuming no radiation.
$\Delta\phi_{In}$	<0.15	<0.10	$\Delta\phi$ between SuperCluster position and track direction at interaction vertex extrapolated to ECAL assuming no radiation.
$\sigma_{in\eta\eta}$	<0.01	<0.03	Cluster shape covariance, measure the η dispersion of the electrons electromagnetic shower over the ECAL supercluster.
H/E	<0.12	<0.10	The ratio of hadronic energy in the HCAL tower directly behind the ECAL super-cluster and the ECAL super-cluster itself.
d0 (vtx)	<0.02	<0.02	The tracker track transverse impact parameter w.r.t the primary vertex.
dZ (vtx)	<0.20	<0.20	The longitudinal distance of the tracker track w.r.t the primary vertex.
$ (\frac{1}{E_{ECAL}} - \frac{1}{p_{track}}) $	<0.05	<0.05	Comparison of energy at supercluster $1/E_{ECAL}$ and that of the track momentum at the vertex $1/p_{track}$. Causes suppression of fake electrons at low p_T .
PF Iso	<0.15	<0.15	Combined PF isolation of charged hadrons, photons, neutral hadrons within a $\Delta R < 0.3$ cone size. Isolation sum is corrected for pileup using effective area corrections for neutral particles.

Table 4.4.: Electron Identification criteria used within the analysis for veto purposes.

• Noise and E_T Filters

A series of Noise filters are applied to veto events which contain spurious non-physical jets that are not picked up by the jet id, and events which give large unphysical E_T values. These filters are listed within Table 4.5.

1392

1393

1394

1395

Noise Filters	Variable	Definition
CSC tight beam halo filter		As proton beams circle the LHC , proton interactions with the residual gas particles or the beam collimators can occur, producing showers of secondary particles which can interact with the CMS detector.
HBHE noise filter with isolated noise rejection		Anomalous noise in the HCAL not due to electronics noise, but rather due to instrumentation issues associated with the HPD 's and Readout Boxes (RBXs).
HCAL laser filter		The HCAL uses laser pulses for monitoring the detector response. Some laser pulses have accidentally been fired in the physics orbit, and ended up polluting events recorded for physics analysis.
ECAL dead cell trigger primitive (TP) filter		EB and EE have single noisy crystals which are masked in reconstruction. Use the Trigger Primitive (TP) information to assess how much energy was lost in masked cells.
Bad EE Supercrystal filter		Two supercrystals in EE are found to occasionally produce high amplitude anomalous pulses in several channels at once, causing a large E_T spike.
ECAL Laser correction filter		A laser calibration multiplicative factor is applied to correct for transparency loss in each crystal during irradiation. A small number of crystals receive unphysically large values of this correction and become very energetic, resulting in E'_T .

Table 4.5.: Noise filters that are applied to remove spurious and non-physical \cancel{E}_T signatures within the **CMS** detector.

¹³⁹⁶ 4.2.2. Event selection

¹³⁹⁷ The selection criteria for events within the analysis are detailed below. A set of common
¹³⁹⁸ cuts are applied to both signal (maximise acceptance to a range of **SUSY** signatures), and
¹³⁹⁹ control samples (retain similar jet kinematics for background predictions), with additional
¹⁴⁰⁰ selection cuts applied to each control sample to enrich the sample in a particular **EWK**
¹⁴⁰¹ processes, see Section (4.2.3).

¹⁴⁰² The jets considered in the analysis are required to have a transverse momentum $p_T > 50$
¹⁴⁰³ GeV, with a minimum of two jets required in the event. The highest E_T jet is required
¹⁴⁰⁴ to lie within the central tracker acceptance $|\eta| < 2.5$, and the two leading p_T jets must
¹⁴⁰⁵ each have $p_T > 100$ GeV. Any event which has a jet with $p_T > 50$ GeV that either fails
¹⁴⁰⁶ the “loose” identification criteria described in Section(4.2.1) or has $|\eta| > 3.0$, is rejected.
¹⁴⁰⁷ Similarly events in which an electron, muon or photon fails object identification but pass
¹⁴⁰⁸ η and p_T restrictions, are identified as an “odd” lepton/photon and the event is vetoed.

¹⁴⁰⁹ At low H_T , the jet threshold requirements applied to be considered as part of the analysis
¹⁴¹⁰ and enter the H_T sum are scaled downwards. These are scaled down in order to extend

- ¹⁴¹¹ phase space at low H_T , preserving similar jet multiplicities and background admixture
¹⁴¹² seen at higher H_T , as listed in Table 4.6.

H_T bin	minimum jet p_T	second leading jet p_T
$275 < H_T < 325$	36.7	73.3
$325 < H_T < 375$	43.3	86.6
$375 < H_T$	50.0	100.0

Table 4.6.: Jet thresholds used in the three H_T regions of the analysis.

- ¹⁴¹³ Within the signal region to suppress **SM** processes with genuine \cancel{E}_T from neutrinos,
¹⁴¹⁴ events containing isolated electrons or muons are vetoed. Furthermore to ensure a pure
¹⁴¹⁵ multi-jet topology, events are vetoed if an isolated photon is found with $p_T > 25$ GeV.
¹⁴¹⁶ An α_T requirement of > 0.55 is required to reduce the QCD multi-jet background
¹⁴¹⁷ to a negligible amount. Finally additional cleaning cuts are applied to protect against
¹⁴¹⁸ pathological deficiencies such as reconstruction failures or severe energy mis-measurements
¹⁴¹⁹ due to detector inefficiencies:

- Significant \cancel{H}_T can arise in events with no real \cancel{E}_T due to multiple jets falling below the p_T threshold for selecting jets. This in turn leads to events which can then incorrectly pass the α_T requirements of the analysis. This effect can be negated by requiring that the missing transverse momentum reconstructed from jets alone does not greatly exceed the missing transverse momentum reconstructed from all of the detector's calorimeter towers,

$$R_{miss} = \cancel{H}_T / \cancel{E}_T < 1.25.$$

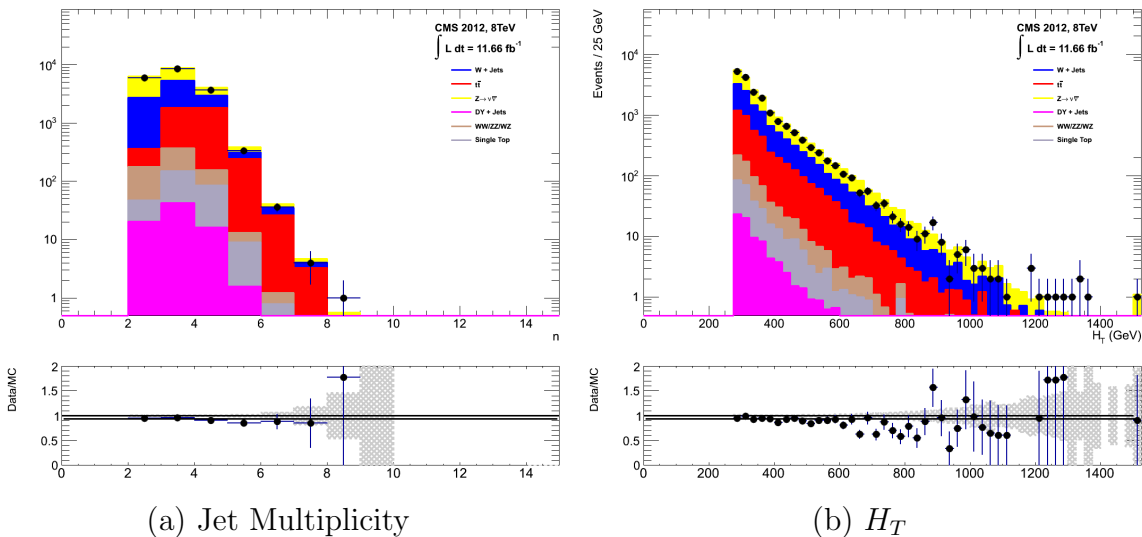
- ¹⁴²⁰ • Fake \cancel{E}_T and \cancel{H}_T can arise due to significant jet mis-measurements caused by a small
¹⁴²¹ number of non-functioning **ECAL** regions. These regions absorb electromagnetic
¹⁴²² showers which are subsequently not added to the jet energy sum. To circumvent
¹⁴²³ this problem the following procedure is employed : For each jet in the event, the
¹⁴²⁴ angular separation

$$\Delta\phi_j^* \equiv \Delta\phi(\vec{p_j} - \sum_{i \neq j} \vec{p_i}), \quad (4.6)$$

is calculated where that jet is itself removed from the event. Here $\Delta\phi^*$ is a measure of how aligned the \mathcal{H}_T of an event is with a jet. A small value (i.e. the \mathcal{H}_T vector lies along the jet axis) is indicative of an inherently balanced event in which a jet has been mis-measured. For every jet in a event with $\Delta\phi^* < 0.5$, if the ΔR distance between the selected jet and the closest dead **ECAL** region is also < 0.3 , then the event is rejected. Similarly events are rejected if the jet points within $\Delta R < 0.3$ of the **ECAL** barrel-endcap gap at $|\eta| = 1.5$.

Some of the key distributions of the data used in this analysis compared to MC simulation are shown in Figure 4.5. The MC samples are normalised to a luminosity of 11.7 fb^{-1} , with no requirement placed upon the number of b-tagged jets or number of jets in the events. In the case of this inclusive selection the dominant backgrounds in the signal regions are, $Z \rightarrow \nu\bar{\nu}$ and $W + \text{jets}$ processes, with a smaller $t\bar{t}$ background accompanied by other residual backgrounds.

The distributions shown are presented for purely illustrative purposes, with the MC simulation itself not used in absolute term to estimate the yields from background processes, see Sections (4.2.3, 4.5). However it is nevertheless important to demonstrate that good agreement exists between simulation and observation in data.



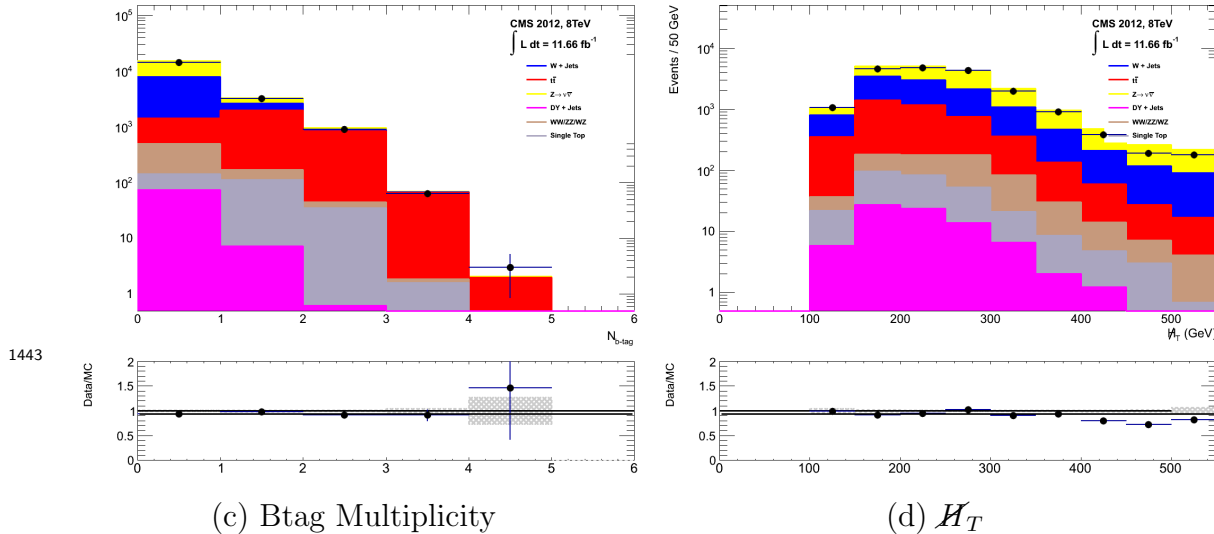


Figure 4.5.: Data/MC comparisons of key variables for the hadronic signal region, following the application of the hadronic selection criteria and the requirements of $H_T > 275$ GeV and $\alpha_T > 0.55$. Bands represent the uncertainties due to the statistical size of the MC samples. No requirement is made upon the number of b-tagged jets or jet multiplicity in these distributions.

1444 4.2.3. Control sample definition and background estimation

1445 The method used to estimate the background contributions in the hadronic signal region
 1446 relies on the use of a Transfer Factor (**TF**). This is determined from MC simulation
 1447 in both the control, N_{MC}^{control} , and signal, N_{MC}^{signal} , region to transform the observed yield
 1448 measured in data for a control sample, $N_{\text{obs}}^{\text{control}}$, into a background prediction, $N_{\text{pred}}^{\text{signal}}$, via
 1449 Equation (4.7),

$$N_{\text{pred}}^{\text{signal}} = \frac{N_{MC}^{\text{signal}}}{N_{MC}^{\text{control}}} \times N_{\text{obs}}^{\text{control}}. \quad (4.7)$$

1450 All MC samples are normalised to the luminosity of the data samples, 11.7 fb^{-1} . Through
 1451 this method, “vanilla” predictions for the **SM** background in the signal region can be
 1452 made by considering separately the sum of the prediction from either the $\mu + \text{jets}$ and γ
 1453 + jets, or $\mu + \text{jets}$ and $\mu\mu + \text{jets}$ samples. However the final background estimation from
 1454 which results are interpreted, is calculated via a fitting procedure defined formally by
 1455 the likelihood model described in Section (4.8).

¹⁴⁵⁶ The sum of the expected yields from all MC processes, in each control sample enter the
¹⁴⁵⁷ denominator, N_{MC}^{control} , of the **TF** defined in Eq (4.7). However for the numerator, N_{MC}^{signal} ,
¹⁴⁵⁸ only the relevant processes that are being estimated, enter into the **TF**.

¹⁴⁵⁹ For the $\mu + \text{jets}$ sample the simulated MC processes which enter the numerator of the
¹⁴⁶⁰ **TF** are,

$$N_{MC}^{\text{signal}}(H_T, n_{\text{jet}}) = N_W + N_{t\bar{t}} + N_{DY} + N_t + N_{di-boson}, \quad (4.8)$$

¹⁴⁶¹ whilst for both the $\mu\mu + \text{jets}$ and $\gamma + \text{jets}$ samples the only MC process used in the
¹⁴⁶² numerator is,

$$N_{MC}^{\text{signal}}(H_T, n_{\text{jet}}) = N_{Z \rightarrow \nu\bar{\nu}}. \quad (4.9)$$

¹⁴⁶³ The control samples and the **EWK** processes they are specifically tuned to select are
¹⁴⁶⁴ defined below, with distributions of key variables for each of the control samples shown
¹⁴⁶⁵ for illustrative purposes in Figures 4.6, 4.7 and 4.8. No requirement is placed upon
¹⁴⁶⁶ the number of b-tagged jets or jet multiplicity in the distributions shown. The MC
¹⁴⁶⁷ distributions highlight the background compositions of each control sample, where in
¹⁴⁶⁸ general, good agreement is observed between data and simulation, giving confidence
¹⁴⁶⁹ that the samples are well understood. The contribution from QCD multi-jet events is
¹⁴⁷⁰ expected to be negligible :

¹⁴⁷¹ The $\mu + \text{jets}$ control sample

¹⁴⁷² Events from $W + \text{jets}$ and $t\bar{t}$ processes enter into the hadronic signal sample due
¹⁴⁷³ to unidentified leptons from acceptance effects or reconstruction inefficiencies and
¹⁴⁷⁴ hadronic tau decays. These leptons originate from the decay of high p_T W bosons.

¹⁴⁷⁵ The control samples specifically identifies $W \rightarrow \mu\bar{\nu}$ decays within a similar phase-
¹⁴⁷⁶ space of the signal region, where the muon is subsequently ignored in the calculation
¹⁴⁷⁷ of event level variables, i.e. H_T , \cancel{H}_T , α_T . All kinematic jet-based cuts are identical
¹⁴⁷⁸ to those applied in the hadronic search region (with the exception of α_T , discussed
¹⁴⁷⁹ below) detailed in Section (4.2.2), with the same H_T , jet multiplicity and b-jet
¹⁴⁸⁰ multiplicity binning described above.

- 1481 – Muons originating from W boson decays are selected by requiring one tightly
1482 isolated muon defined in Table 4.2, with a $p_T > 30$ GeV and $|\eta| < 2.1$. Both of
1483 these threshold arise from trigger restrictions.
- 1484 – The transverse mass of the W candidate must satisfy $M_T(\mu, \cancel{E}_T) > 30$ GeV (to suppress QCD multi-jet events).
- 1485 – Events which contain a jet overlapping with a muon $\Delta R(\mu, \text{jet}) < 0.5$ are vetoed
1486 to remove events from muons produced as part of a jet’s hadronisation process.
- 1487 – Events containing a second muon candidate which has failed id, but passing
1488 p_T and $|\eta|$ requirements, are checked to have an invariant mass that satisfies
1489 $|M_{\mu\mu} - m_Z| > 25$, thus removing $Z \rightarrow \mu\mu$ contamination.
- 1490

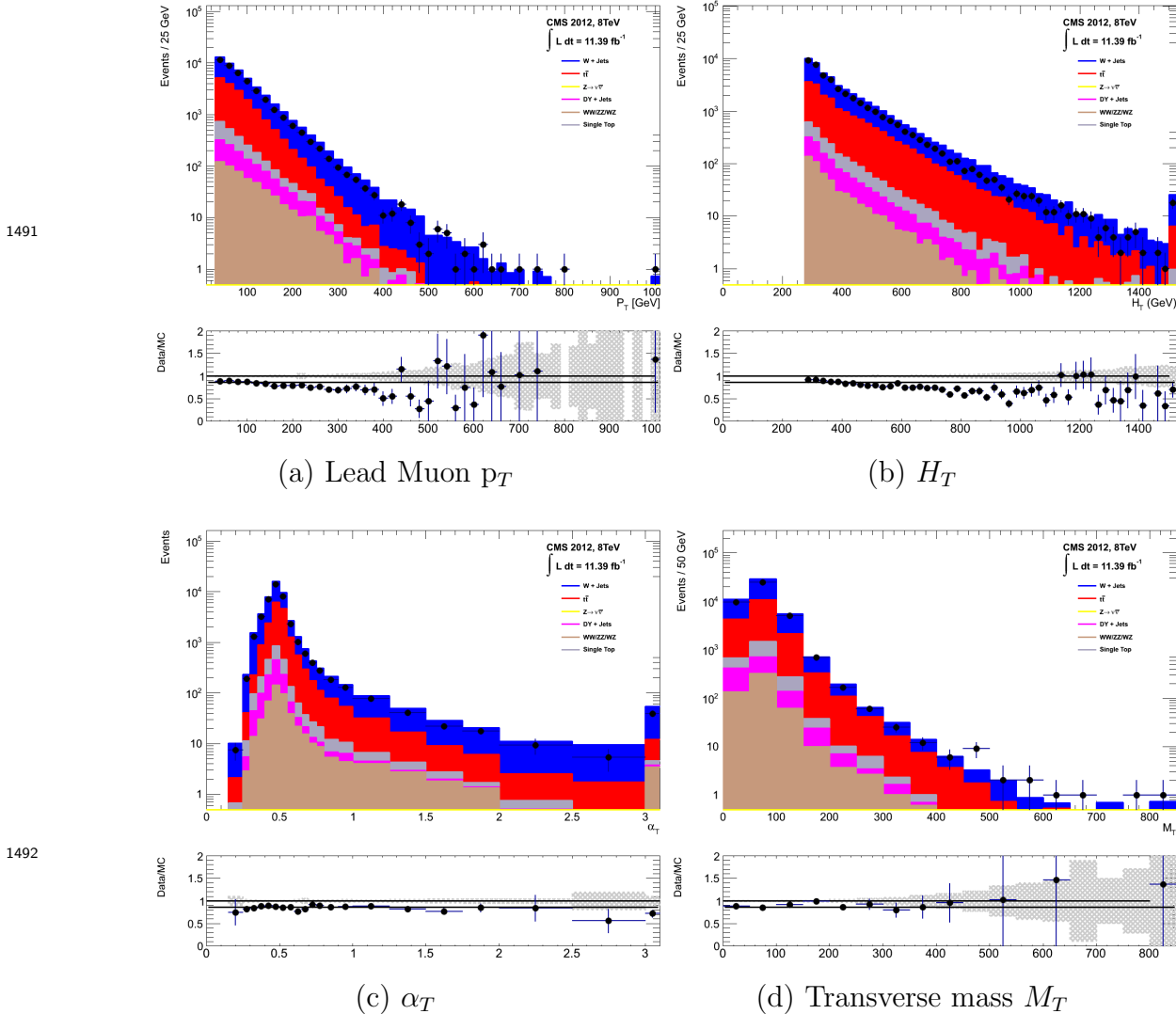


Figure 4.6.: Data/MC comparisons of key variables for the $\mu + \text{jets}$ selection, following the application of selection criteria and the requirements that $H_T > 275$ GeV. Bands represent the uncertainties due to the statistical size of the MC samples. No requirement is made upon the number of b-tagged jets or jet multiplicity in these distributions.

The $\mu\mu + \text{jets}$ control sample

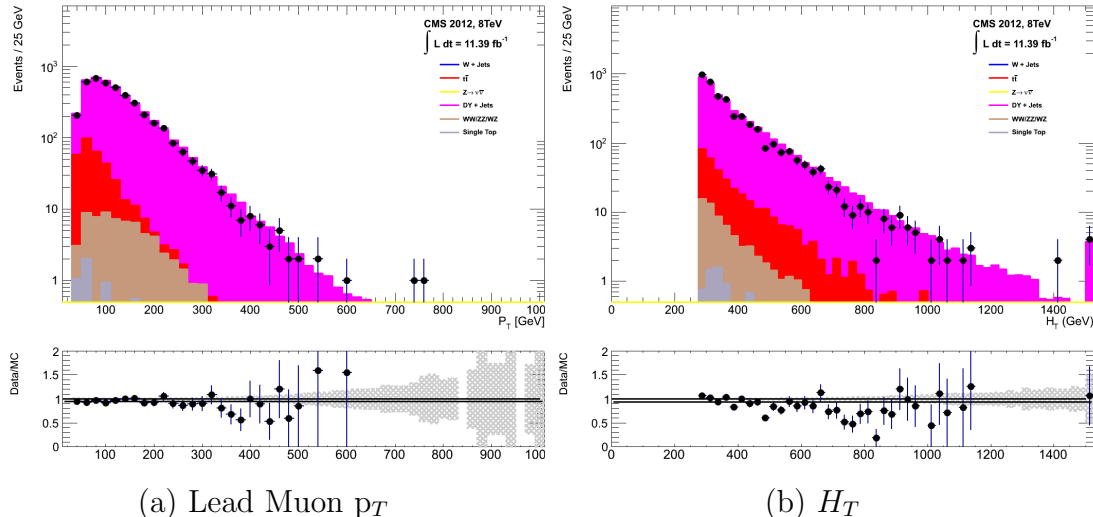
The $Z \rightarrow \nu\bar{\nu} + \text{jets}$ background enters into the signal region from genuine E_T from the escaping neutrinos. This background is estimated using two control samples, the first of which is the $Z \rightarrow \mu\bar{\mu} + \text{jets}$ process, which posses identical kinematic properties, but with different acceptance and branching ratio [1].

The same acceptance requirements as the $\mu + \text{jets}$ selection for muons is applied, as defined in Table 4.2. Muons in the event are ignored for the purpose of the

calculation of event level variables. Kinematic jet-based cuts and phase space binning identical to the hadronic search region are also applied.

- Muons origination from a Z boson decay are selected requiring exactly two tightly isolated muons. Due to trigger requirements the leading muon is required to have $p_T > 30$ GeV and $|\eta| < 2.1$. The requirement of the p_T on the second muon is relaxed to 10 GeV.
- Events are vetoed if containing a jet overlapping with a muon $\Delta R(\mu, \text{jet}) < 0.5$.
- In order to specifically select two muons both originating from a single Z boson decay, the invariant mass of the two muons must satisfy $|M_{\mu\mu} - m_Z| < 25$.

The $\mu\mu + \text{jets}$ sample is used to make predictions in the signal region in the two lowest H_T bins, providing coverage where the $\gamma + \text{jets}$ sample is unable to, due to trigger requirements. In higher H_T bins, the higher statistics of the $\gamma + \text{jets}$ sample is also used in determining the $Z \rightarrow \nu\bar{\nu}$ estimation.



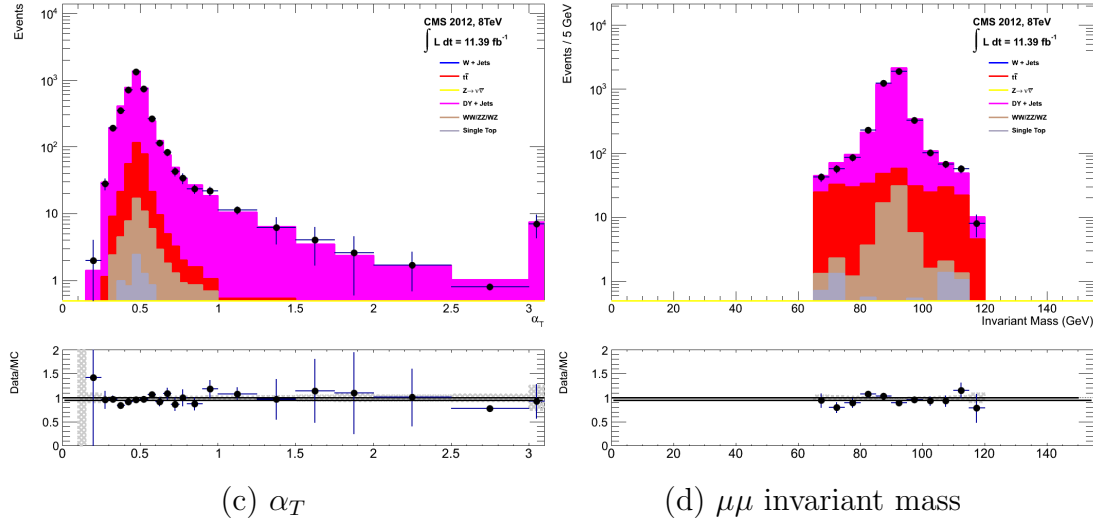


Figure 4.7.: Data/MC comparisons of key variables for the $\mu\mu + \text{jets}$ selection, following the application of selection criteria and the requirements that $H_T > 275$ GeV. Bands represent the uncertainties due to the statistical size of the MC samples. No requirement is made upon the number of b-tagged jets or jet multiplicity in these distributions.

The $\gamma + \text{jets}$ control sample

The $Z \rightarrow \nu\bar{\nu} + \text{jets}$ background is also estimated from a $\gamma + \text{jets}$ control sample. When the E_T of the photon is greater than the mass of the Z , it possesses a larger cross section and kinematic properties similar to those of $Z \rightarrow \mu\bar{\mu}$ events where the photon is ignored [80][81]. The photon is ignored for the purpose of the calculation of event level variables, and identical selection cuts to the hadronic signal region are applied.

- Exactly one photon is selected, satisfying identification criteria as detailed in Table 4.3, with a minimum $p_T > 165$ GeV to satisfy trigger thresholds and $|\eta| < 1.45$ to ensure the photon remains in the barrel of the detector.
- A selection criteria of $\Delta R(\gamma, \text{jet}) < 1.0$, between the photon and all jets is applied to ensure the acceptance of only well isolated $\gamma + \text{jets}$ events.
- Given that the photon is ignored, this control sample can only be applied in the H_T region > 375 GeV, due to the trigger thresholds on the minimum p_T of the photon, and the H_T requirement of an $\alpha_T > 0.55$ cut from Equation (4.5), which is maintained in this control sample due to contamination from QCD in the absence of an α_T cut.

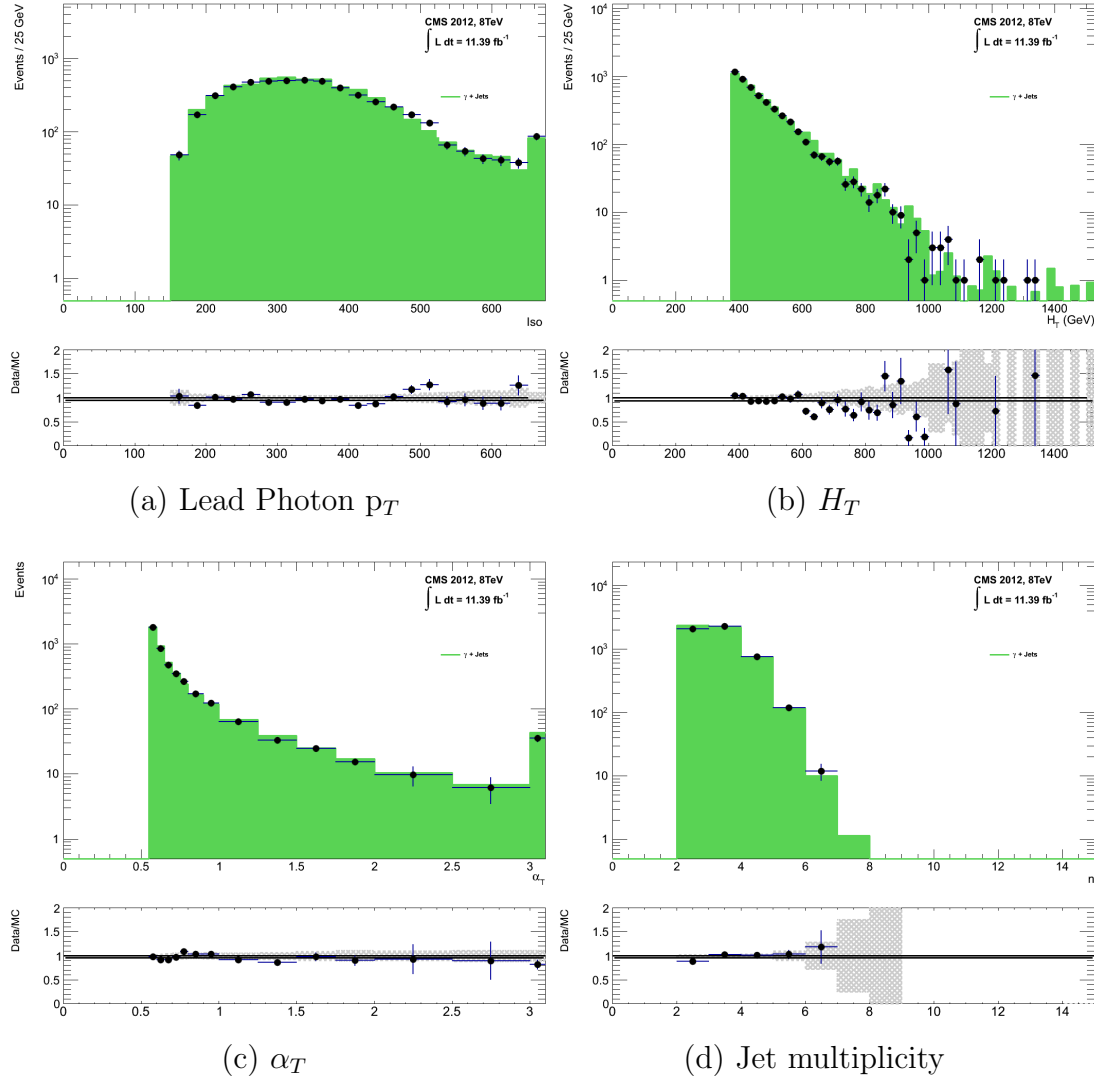


Figure 4.8.: Data/MC comparisons of key variables for the $\gamma + \text{jets}$ selection, following the application of selection criteria and the requirements that $H_T > 375 \text{ GeV}$ and $\alpha_T > 0.55$. Bands represent the uncertainties due to the statistical size of the MC samples. No requirement is made upon the number of b-tagged jets or jet multiplicity in these distributions.

1533 The selection criteria of the three control samples are defined to ensure background
 1534 composition and event kinematics mirror closely the signal region. This is done in order
 1535 to minimise the reliance on MC simulation to model correctly the backgrounds and event
 1536 kinematics in the control and signal samples.

1537 However in the case of the $\mu + \text{jets}$ and $\mu\mu + \text{jets}$ samples, the α_T requirement is relaxed
 1538 in the selection criteria of these samples. This is made possible as contamination from
 1539 QCD multi-jet events is suppressed to a negligible level by the other kinematic selection
 1540 criteria within the two control samples, to select pure EWK processes. Thus in this way,

1541 the acceptance of the two muon control samples can be significantly increased, which
1542 simultaneously improves their predictive power and further reduces the effect of any
1543 potential signal contamination.

1544 The modelling of the α_T variable is probed through a dedicated set of closure tests,
1545 described in Section (4.6), which demonstrate that the different α_T acceptances for the
1546 control and signal samples have no significant systematic bias on the prediction.

1547 4.2.4. Estimating the QCD multi-jet background

1548 A negligible background from QCD multi-jet events within the hadronic signal region
1549 is expected due to the selection requirement, and additional cleaning filters applied.
1550 However a conservative approach is still adopted and the likelihood model, see Section
1551 (4.8.2), is given the freedom to accommodate any potential QCD multi-jet contamination.

1552 Any potential contamination can be identified through the variable R_{α_T} , defined as the
1553 ratio of events above and below the α_T threshold value used in the analysis. This is
1554 modelled by a H_T dependant falling exponential function which takes the form,

$$R_{\alpha_T}(H_T) = A_{\text{QCD}} \exp^{-k_{\text{QCD}} H_T}, \quad (4.10)$$

1555 where the parameters A_{QCD} and k_{QCD} are the normalisation and exponential decay
1556 constants respectively.

1557 For QCD event topologies this exponential behaviour is expected as a function of H_T for
1558 several reasons. The improvement of jet energy resolution at higher H_T due to higher p_T
1559 jets leads to a narrower peaked distribution, causing R_{α_T} to fall. Similarly at higher H_T
1560 values > 375 GeV, the jet multiplicity rises slowly with H_T . As shown in Figure 4.3, at
1561 higher jet multiplicities, the result of the combinatorics used in the determination of α_T ,
1562 then leads to a narrower distribution.

1563 The value of the decay constant k_{QCD} is constrained via measurements within data
1564 sidebands to the signal region. This is also done to validate the falling exponential
1565 assumption for QCD multi-jet topologies. The sidebands are enriched in QCD multi-jet
1566 background and defined as regions where α_T is relaxed or that the R_{miss} cut is inverted.

1567 Figure 4.9 depicts the definition of these data sidebands used to constrain the value of
1568 k_{QCD} .

1569

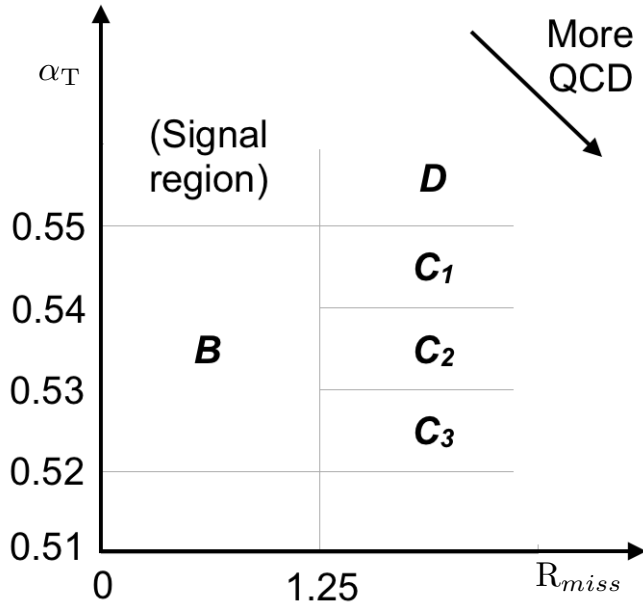


Figure 4.9.: QCD sideband regions, used for determination of k_{QCD} .

1570 The fits to determine the value of k_{QCD} are shown in Appendix (C.1), for which the best
1571 fit value obtained from sideband region B is determined to be $k_{\text{QCD}} = 2.96 \pm 0.64 \times 10^{-2}$
1572 GeV^{-1} .

1573 The best fit values of the remaining three C sideband regions are used to estimate
1574 the systematic uncertainty on the central value obtained from sideband region B. The
1575 variation of these measured values is used to determine the error on the determined
1576 central value, and is calculated to be $1.31 \pm 0.26 \times 10^{-2} \text{ GeV}^{-1}$. This relative error of \sim
1577 20% gives an estimate of the systematic uncertainty of the measurement to be applied to
1578 k_{QCD} .

1579 Finally the same procedure is performed for sideband region D as an independent cross
1580 check, to establish that the value of k_{QCD} extracted from a lower α_T slice, can be applied
1581 to the signal region $\alpha_T > 0.55$. The likelihood fit is performed across all H_T bins within
1582 the QCD enriched region with no constraint applied to k_{QCD} . The resulting best fit
1583 value for k_{QCD} shows good agreement between that and the weighted mean determined
1584 from the three C sidebands regions. This demonstrates that the assumption of using the
1585 central value determined from sideband region B, to provide an unbiased estimator for
1586 k_{QCD} in the signal region ($\alpha_T > 0.55$) is valid.

1587 Table 4.7, summarises the best fit k_{QCD} values determined for each of the sideband
1588 regions to the signal region.

Sideband region	$k_{\text{QCD}} (\times 10^{-2} \text{GeV}^{-1})$	p -value
B	2.96 ± 0.64	0.24
C ₁	1.19 ± 0.45	0.93
C ₂	1.47 ± 0.37	0.42
C ₃	1.17 ± 0.55	0.98
C(weighted mean)	1.31 ± 0.26	-
D(likelihood fit)	1.31 ± 0.09	0.57

Table 4.7.: Best fit values for the parameters k_{QCD} obtained from sideband regions B,C₁,C₂,C₃. The weighted mean is determined from the three measurements made within sideband region C. The maximum likelihood value of k_{QCD} given by the simultaneous fit using sideband region D. Quotes errors are statistical only.

1589 4.3. Trigger Strategy

1590 A cross trigger based on the H_T and α_T values of an event, is used with varying thresholds
1591 across H_T bins to record the events used in the hadronic signal region. The α_T legs of
1592 the HT_alphaT triggers used in the analysis are chosen to suppress QCD multi-jet events
1593 and control trigger rate, whilst maintaining signal acceptance. To further maintain an
1594 acceptable rate for these analysis specific triggers, only calorimeter information is used
1595 in the reconstruction of the H_T sum, leading to the necessity for Calo jets to be used
1596 within the analysis.

1597 A single object prescaled HT trigger is used to collect events for the hadronic control
1598 region described above in Section (4.2.4).

1599 The performance of the α_T and H_T triggers used to collect data for the signal and
1600 hadronic control region is measured with respect to a reference sample collected using the
1601 muon system. This allows measurement of both the Level 1 seed and higher level triggers
1602 simultaneously, as the reference sample is collected independent of any jet requirements.

1603 The selection for the trigger efficiency measurement is identical to that described in
1604 Section (4.2.2), with the requirement of exactly one well identified muon with $p_T > 30$
1605 GeV which is subsequently ignored.

1606 The efficiencies measured for the HT_alphaT triggers in bins individual H_T and α_T legs,
1607 is summarised in Table 4.8.

H_T range (GeV)	ϵ on H_T leg (%)	ϵ on α_T leg (%)
275-325	$87.7^{+1.9}_{-1.9}$	$82.8^{+1.0}_{-1.1}$
325-375	$90.6^{+2.9}_{-2.9}$	$95.9^{+0.7}_{-0.9}$
375-475	$95.7^{+0.1}_{-0.1}$	$98.5^{+0.5}_{-0.9}$
475- ∞	$100.0^{+0.0}_{-0.0}$	$100.0^{+0.0}_{-4.8}$

Table 4.8.: Measured efficiencies of the H_T and α_T legs of the HT and HT_alphaT triggers in independent analysis bins. The product of the two legs gives the total efficiency of the trigger in a given offline H_T bin.

1608 Data for the control samples of the analysis, detailed in Section (4.2.3), are collected
1609 using single object photon trigger for the $\gamma +$ jets sample, and a single object muon
1610 trigger for both the $\mu +$ jets and $\mu\mu +$ jets control samples.

1611 The photon trigger is measured to be full efficient for the threshold $p_T^{\text{photon}} > 150$ GeV,
1612 whilst the single muon efficiency satisfying $p_T^{\text{muon}} > 30$ GeV is measured to have an
1613 efficiency of $(88 \pm 2)\%$ that is independent of H_T . In the case of the $\mu\mu +$ jets control
1614 sample, the efficiency is measured to be $(95 \pm 2)\%$ for the lowest H_T bin, rising (due to
1615 the average p_T of the second muon in the event increasing at larger H_T) to $(98 \pm 2)\%$ for
1616 the highest H_T bin.

1617 4.4. Measuring MC Normalisation Factors via H_T 1618 Sidebands

1619 The theoretical cross sections of different **SM** processes at Next to Next Leading Order
1620 (**NNLO**) and the number of MC simulated events generated for that particular process,
1621 is typically used to determine the appropriate normalisation for a MC sample. However
1622 within the particular high- H_T and high- \cancel{E}_T corners of kinematic phase space probed
1623 within this search, the theoretical cross sections for various processes are far less well
1624 understood.

1625 To mitigate the problem of theoretical uncertainties and arbitrary choices of cross sections,
1626 the normalisation of MC samples used in the analysis are determined through the use
1627 data sidebands. The sidebands are used to calculate sample specific correction factors
1628 (k-factors) that are appropriate for the H_T - \cancel{E}_T phase space covered by this analysis.

1629 They are defined within the $\mu +$ jets and $\mu\mu +$ jets control sample, by the region $200 <$
1630 $H_T < 275$, using the same jet p_T thresholds as the adjacent first analysis bin. Individual

1631 EWK processes are isolated within each of these control samples via requirements on
1632 jet multiplicity and the requirement on b-tags, summarised in Table 4.9. The purity of
1633 the samples are typically $> 90\%$ with any residual contamination corrected for. The
1634 resultant k-factor for each process is determined by then taking ratio of the data yield
1635 over the MC expectation in the sideband. Subsequently these k-factors are then applied
1636 to the processes within the phase space of the analysis.

Process	Selection	Observation	MC expectation	k-factor
W + jets	$\mu + \text{jets}, n_b=0, n_{jet} = 2,3$	26950	29993.2 ± 650.1	0.90 ± 0.02
$Z \rightarrow \mu\mu + \text{jets}$	$\mu\mu + \text{jets}, n_b=0, n_{jet} = 2,3$	3141	3402.0 ± 43.9	0.92 ± 0.02
$t\bar{t}$	$\mu + \text{jets}, n_b=2, n_{jet} = \geq 4$	2190	1967.8 ± 25.1	1.11 ± 0.02

Table 4.9.: k-factors calculated for different EWK processes. All k-factors are derived relative to theoretical cross sections calculated in NNLO. The k-factors measured for the $Z \rightarrow \mu\mu + \text{jets}$ processes, are also applied to the $Z \rightarrow \nu\bar{\nu} + \text{jets}$ and $\gamma + \text{jets}$ MC samples.

1637 It is worth pointing out that these correction factors have a negligible effect when
1638 providing a background estimation for the signal region. The TF's used in the analysis
1639 are found to be unaffected by application of these k-factors due to the similarity in the
1640 background composition of the control and signal regions. However when systematic
1641 uncertainties are determined in Section (4.6), the closure tests performed are sensitive
1642 to these corrections as extrapolations between different n_b^{reco} and n_{jet} categories are
1643 performed.

1644 4.5. Determining MC Simulation Yields with 1645 Higher Statistical Precision

1646 Reconstructing events from EWK processes with many b-tagged jets (≥ 3), n_b^{reco} , is largely
1647 driven by the mis-tagging of light jets within the event. This is clear when considering
1648 the main EWK backgrounds in the analysis, such as $t\bar{t} + \text{jets}$ events, which typically
1649 contain two b-flavoured jets from the decay of the top quarks, whilst W + jets and
1650 Z $\rightarrow \mu\mu + \text{jets}$ events will typically contain no b-flavoured jets.

1651 When the expectation for the number of n_b^{reco} is taken directly from simulation, the
1652 statistical uncertainty at large b-tag multiplicities becomes relatively large. In order to
1653 reduce this uncertainty one approach is to use the information encoded throughout all
1654 events in the simulation sample, to measure each of the four ingredients:

- 1655 1. the b-tagging efficiency in the event selection,
- 1656 2. the charm-tagging efficiency in the event selection
- 1657 3. the mis-tagging rate in the event selection,
- 1658 4. the underlying flavour distribution of the jets in the events,

1659 that determine the n_b^{reco} distribution of the process being measured. This method allows
1660 the determination of higher b-tag multiplicities to a higher degree of accuracy reducing
1661 the stastical uncertainties of the MC which enter into the TF's. For the discussion that
1662 follows, these predictions are determined on average (i.e not on an event-by-event basis),
1663 and is known as the formula method.

1664 **4.5.1. The formula method**

1665 The assigning of jet flavours to reconstruction level jets in simulation is achieved via an
1666 algorithmic method defined as:

- 1667 • Try to find the parton that most likely determines the properties of the jet and
1668 assign that flavour as true flavour,
- 1669 • Here, the “final state” partons (after showering, radiation) are analysed (also within
1670 $\Delta R < 0.3$ of reconstructed jet cone),
- 1671 • Jets from radiation are also matched to a parton flavour,
- 1672 • If there is a b/c flavoured parton within the jet cone: label as b/c flavoured jet,
- 1673 • Otherwise: assign flavour of the hardest parton.

1674 This process is employed within each individual MC process and independently for each
1675 H_T - n_{jet} bin in the analysis, the n_b^{reco} distribution is then constructed in the following
1676 way:

1677 Let $N(n_b^{gen}, n_c^{gen}, n_q^{gen})$ represent the yield in simulation of events with b underlying
1678 b-quarks, c underlying c-quarks and q underlying light quarks which are matched to
1679 reconstructed jets as detailed above. Light quarks defined as those which originate from
1680 a u , d , s , g and τ jets, which having similar mis-tagging rates are grouped together.
1681 Similarly ϵ , β and m represent the measured b-tagging, c-tagging and mis-tagging
1682 efficiency averaged over all the jets within that particular analysis bin.

1683 Using this information the expected n_b^{reco} distribution can be analytically calculated
1684 using the formula :

$$N(n_b) = \sum_{n_b^{gen} + n_c^{gen} + n_q^{gen} = n_{jet}} \sum_{n_b^{tag} + n_c^{tag} + n_q^{tag} = n_b} N(n_b^{gen}, n_c^{gen}, n_q^{gen}) \times P(n_b^{tag}, n_b^{gen}, \epsilon) \times \\ P(n_c^{tag}, n_c^{gen}, \beta) \times P(n_q^{tag}, n_q^{gen}, m), \quad (4.11)$$

1685 with $N(n_b)$ representing the yield where n_b jets have been b-tagged. The variables n_b^{tag} ,
1686 n_c^{tag} and n_q^{tag} represent the number of times that a particular jet flavour results in a
1687 b-tagged jet, and finally $P(n_b^{tag}, n_b^{gen}, \epsilon)$, $P(n_c^{tag}, n_c^{gen}, \beta)$ and $P(n_q^{tag}, n_q^{gen}, m)$ represent
1688 the binomial probabilities for that to happen.

1689 This approach ultimately results in a more precise n_b^{reco} distribution prediction, due to
1690 the utilisation of the entire MC sample in extracting the estimated underlying n_b^{reco}
1691 distribution.

1692 4.5.2. Establishing proof of principle

1693 In order to validate the procedure, the predictions obtained from the formula method
1694 summarised in Equation (4.11), are compared directly to those obtained directly from
1695 simulation. Resultantly no simulation to data correction factors are applied when making
1696 this comparison

1697 This sanity check for the $\mu +$ jets control sample is presented in Table 4.10, for all n_b^{reco}
1698 and H_T bins with no requirement placed upon the jet multiplicity of the events.

1699 It can be seen as expected, that there is good consistency between the results determined
1700 via the formula method and ‘raw’ simulation yields. Similarly the power of this approach
1701 can be seen in the reduction of this statistical error in the prediction across all H_T and
1702 n_b^{reco} bins. In particular the statistical uncertainty is reduced by several factors in the
1703 highest $n_b^{reco} \geq 4$ category.

H_T Bin (GeV)	275–325	325–375	375–475	475–575
Formula $n_b = 0$	12632.66 \pm 195.48	6696.08 \pm 82.59	6368.96 \pm 75.34	2906.27 \pm 39.65
Vanilla $n_b = 0$	12612.95 \pm 198.68	6687.97 \pm 83.78	6359.27 \pm 76.50	2898.27 \pm 36.89
Formula $n_b = 1$	4068.09 \pm 45.71	2272.76 \pm 26.14	2181.32 \pm 25.07	1089.14 \pm 13.82
Vanilla $n_b = 1$	4067.73 \pm 60.30	2268.02 \pm 30.20	2180.69 \pm 28.73	1094.37 \pm 24.14
Formula $n_b = 2$	1963.71 \pm 22.44	1087.55 \pm 13.57	1055.57 \pm 13.25	554.96 \pm 7.95
Vanilla $n_b = 2$	1984.53 \pm 26.19	1094.43 \pm 16.67	1068.96 \pm 16.36	558.14 \pm 10.51
Formula $n_b = 3$	146.94 \pm 2.07	79.97 \pm 1.37	78.05 \pm 1.35	49.84 \pm 1.03
Vanilla $n_b = 3$	149.52 \pm 4.84	85.98 \pm 3.64	74.45 \pm 3.29	49.54 \pm 2.68
Formula $n_b \geq 4$	2.26 \pm 0.12	1.29 \pm 0.10	5.32 \pm 0.20	-
Vanilla $n_b \geq 4$	1.84 \pm 0.50	1.02 \pm 0.39	4.86 \pm 0.83	-
H_T Bin (GeV)	575–675	675–775	775–875	>875
Formula $n_b = 0$	1315.68 \pm 19.49	640.49 \pm 11.90	327.81 \pm 7.91	424.27 \pm 9.27
Vanilla $n_b = 0$	1315.23 \pm 20.20	641.96 \pm 12.48	329.09 \pm 8.36	424.02 \pm 9.73
Formula $n_b = 1$	490.41 \pm 7.45	226.95 \pm 4.42	109.91 \pm 2.84	129.97 \pm 3.07
Vanilla $n_b = 1$	490.52 \pm 9.92	222.22 \pm 6.21	107.46 \pm 4.15	129.64 \pm 4.64
Formula $n_b = 2$	256.75 \pm 4.58	113.45 \pm 2.70	52.10 \pm 1.69	59.29 \pm 1.78
Vanilla $n_b = 2$	253.43 \pm 6.52	117.17 \pm 4.27	52.70 \pm 2.80	59.45 \pm 3.00
Formula $n_b = 3$	25.66 \pm 0.69	12.48 \pm 0.46	5.52 \pm 0.31	6.83 \pm 0.33
Vanilla $n_b = 3$	29.18 \pm 2.06	11.77 \pm 1.26	6.18 \pm 0.95	7.53 \pm 1.05

Table 4.10.: Comparing yields in simulation within the $\mu +$ jets selection determined from the formula method described in Equation (4.11), and that taken directly from simulation . The numbers are normalised to 11.4fb^{-1} . No simulation to data corrections are applied.

4.5.3. Correcting measured efficiencies in simulation to data

As detailed in Section (3.3.2), it is necessary for certain p_T and η dependant corrections, to be applied to both the b-tagging efficiency and mis-tagging rates in order correct the efficiencies from simulation to the distributions seen in data. These corrections factors are considered when determining the simulation yields for each selection, which are used to construct the TF's of the analysis.

Each of the corrections factors for the b, c and light flavoured jets come with an associated systematic uncertainty. The uncertainties across different jet p_T and η bins, are considered as fully correlated. When computing the magnitude of the effect of this systematic uncertainty on the TF's of the analysis, the scale factors are therefore scaled

¹⁷¹⁴ up/down simultaneously within each H_T bin of the analysis for all of the $SF_{b,c,\text{light}}$ scale
¹⁷¹⁵ factors. The magnitude of this correction is shown for each H_T bin within Figure 4.10.

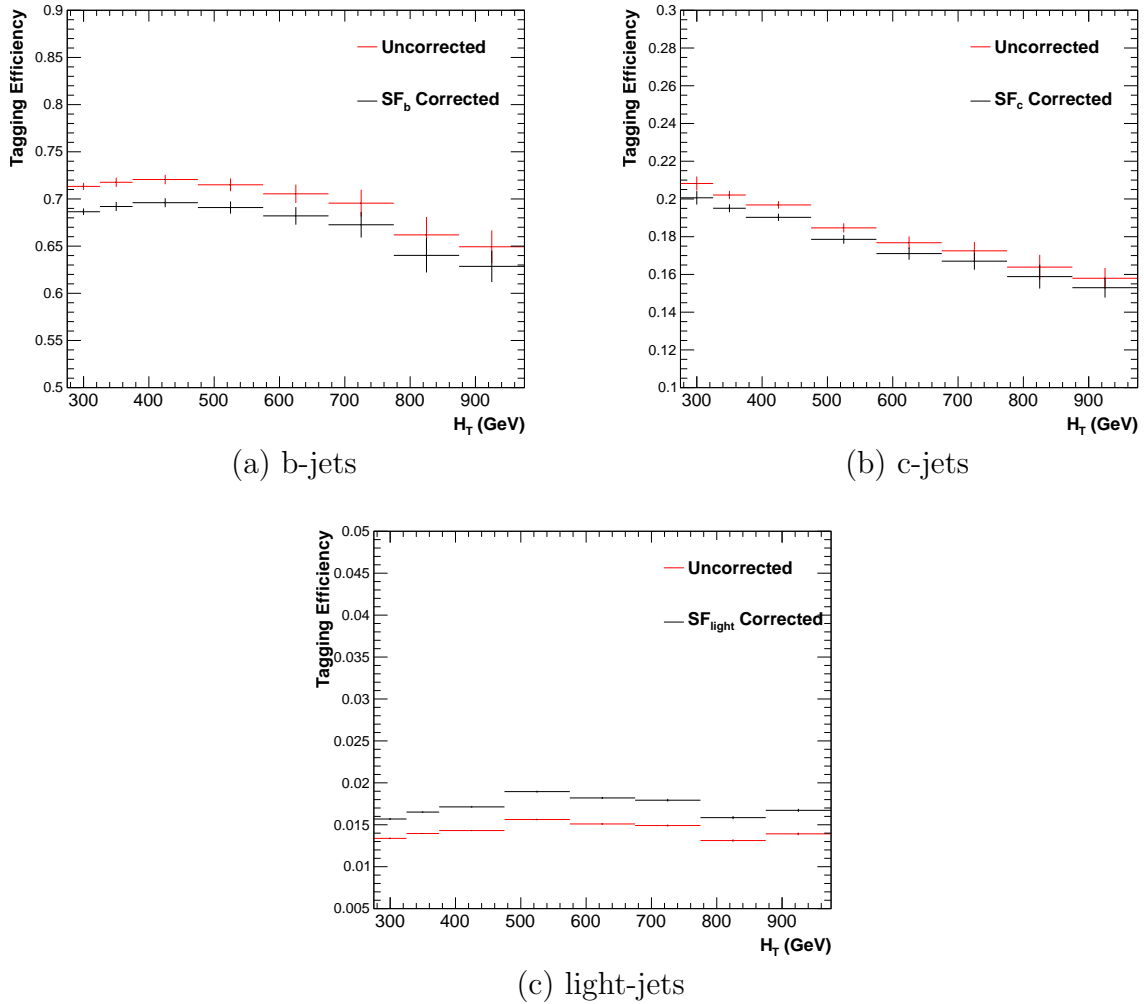


Figure 4.10.: Tagging efficiencies of (a) b-jets, (b) c-jets, and (c) light-jets as a function all jets within each individual analysis H_T bin. Efficiencies measured directly from simulation (black) and with data to simulation $SF_{b,c,\text{light}}$ correction factors (red) are applied.

¹⁷¹⁶ Varying the scale factor corrections by their systematic uncertainty will change the
¹⁷¹⁷ absolute yields within each n_b^{reco} bin of all selections. However, ultimately it is the change
¹⁷¹⁸ in the TF's which influences the final background prediction from each of the control
¹⁷¹⁹ samples. The magnitude of these change is shown in Table 4.11, highlighting the absolute
¹⁷²⁰ change in each TF, constructed from when the $\mu + \text{jets}$ control sample is used to predict
¹⁷²¹ the entire hadronic signal region background.

n_b^{reco}	275–325	325–375	375–475	475–575
= 0	0.557 $^{+0.001}_{-0.001}$ \pm 0.012	0.495 $^{+0.001}_{-0.001}$ \pm 0.009	0.383 $^{+0.001}_{-0.001}$ \pm 0.005	0.307 $^{+0.001}_{-0.002}$ \pm 0.006
= 1	0.374 $^{+0.006}_{-0.006}$ \pm 0.006	0.320 $^{+0.006}_{-0.005}$ \pm 0.005	0.251 $^{+0.005}_{-0.005}$ \pm 0.004	0.185 $^{+0.003}_{-0.003}$ \pm 0.004
= 2	0.226 $^{+0.002}_{-0.002}$ \pm 0.004	0.201 $^{+0.001}_{-0.002}$ \pm 0.004	0.159 $^{+0.001}_{-0.001}$ \pm 0.004	0.134 $^{+0.000}_{-0.001}$ \pm 0.004
= 3	0.221 $^{+0.002}_{-0.002}$ \pm 0.005	0.208 $^{+0.002}_{-0.001}$ \pm 0.007	0.164 $^{+0.001}_{-0.000}$ \pm 0.006	0.144 $^{+0.001}_{-0.001}$ \pm 0.007
≥ 4	0.222 $^{+0.004}_{-0.005}$ \pm 0.015	0.248 $^{+0.003}_{-0.003}$ \pm 0.035	0.123 $^{+0.002}_{-0.003}$ \pm 0.009	-
	575–675	675–775	775–875	≥ 875
= 0	0.263 $^{+0.001}_{-0.002}$ \pm 0.006	0.215 $^{+0.000}_{-0.001}$ \pm 0.007	0.171 $^{+0.000}_{-0.001}$ \pm 0.009	0.111 $^{+0.000}_{-0.001}$ \pm 0.006
= 1	0.154 $^{+0.003}_{-0.003}$ \pm 0.005	0.138 $^{+0.003}_{-0.004}$ \pm 0.006	0.121 $^{+0.005}_{-0.005}$ \pm 0.007	0.091 $^{+0.002}_{-0.002}$ \pm 0.006
= 2	0.104 $^{+0.000}_{-0.001}$ \pm 0.005	0.079 $^{+0.001}_{-0.001}$ \pm 0.006	0.063 $^{+0.001}_{-0.002}$ \pm 0.007	0.071 $^{+0.000}_{-0.000}$ \pm 0.008
= 3	0.116 $^{+0.001}_{-0.001}$ \pm 0.009	0.069 $^{+0.001}_{-0.001}$ \pm 0.007	0.079 $^{+0.001}_{-0.001}$ \pm 0.017	0.095 $^{+0.003}_{-0.002}$ \pm 0.020

Table 4.11.: The absolute change in the **TF**'s used to predict the entire signal region **SM** background, using the $\mu + \text{jets}$ control sample when the systematic uncertainties of the data to simulation scale factors are varied by $\pm 1\sigma$. The impact of the change is shown for each H_T and n_b^{reco} bin with no requirement made on the jet multiplicity of the events. (Also quoted are the statistical uncertainties)

1722 It can be seen that the **TF**'s are found to be relatively insensitive to the systematic
 1723 uncertainty of the b-tag scale factors (showing typically less than $\sim 2\%$ change). This can
 1724 be accounted for by the similar composition of the signal and control sample backgrounds,
 1725 such that any change in the underlying n_b^{reco} distribution will be reflected in both signal
 1726 and control regions and cancel out in the **TF**.

1727 Any overall systematic effect on the overall background prediction of the analysis from
 1728 these b-tag scale factor uncertainties is incorporated within the data driven systematics
 1729 introduced in the following section.

1730 4.6. Systematic Uncertainties on Transfer Factors

1731 Since the **TF**'s used to establish the background prediction are obtained from simulation,
 1732 an appropriate systematic uncertainty is assigned to each factor to account for theoretical
 1733 uncertainties [82] and limitations in the simulation modelling of event kinematics and
 1734 instrumental effects.

1735 The magnitudes of these systematic uncertainties are established through a set of data
 1736 driven method, in which the three independent control samples of the analysis ($\mu + \text{jets}$,
 1737 $\mu\mu + \text{jets}$, $\gamma + \text{jets}$) are used to in a series of closure tests. The yields from one of these
 1738 control samples, along with the corresponding TF obtained from simulation, are used to
 1739 predict the yields in another control sample, using the same method of establishing a
 1740 background prediction for the signal region as described in Section (4.2.3).
 1741 The level of agreement between the predicted and observed yields is expressed as the
 1742 ratio

$$\frac{(N_{obs} - N_{pred})}{N_{pred}}, \quad (4.12)$$

1743 while considering only the statistical uncertainties on N_{pred} , the prediction, and N_{obs} , the
 1744 observation. No systematic uncertainty is assigned to the prediction, and resultantly the
 1745 level of closure is defined by the statistical significance of a deviation from the ratio from
 1746 zero.

1747 This ratio is measured for each H_T bin in the analysis, allowing these closure tests to be
 1748 sensitive to both the presence of any significant biases or any possible H_T dependence on
 1749 the level of closure.

1750 Eight sets of closure tests are defined between the three data control samples, conducted
 1751 independently between the two jet multiplicity ($2 \leq n_{jets} \leq 3$, $n_{jet} \geq 4$) bins. Each of
 1752 these tests are specifically chosen to probe each of the different key ingredients of the
 1753 simulation modelling that can affect the background prediction.

1754 Each of the different modelling components and the relevant closure tests are described
 1755 below :

1756 α_T modelling

1757 The modelling of the α_T distribution in genuine E_T events is probed with the $\mu +$
 1758 jets control sample. This test is important to verify the approach of remove the α_T
 1759 > 0.55 requirement from the $\mu + \text{jets}$ and $\mu\mu + \text{jets}$ samples to increase the precision
 1760 of the background prediction. The test uses the $\mu + \text{jets}$ sample without an α_T cut
 1761 to make a prediction into the $\mu + \text{jets}$ sample defined with the requirement $\alpha_T >$
 1762 0.55.

1763 Background admixture

1764 The sensitivity of the translation factors to the relative admixture of events from
1765 $W + \text{jets}$ and $t\bar{t}$ processes is probed by two closure tests. These tests represent
1766 an extremely conservative approach as the admixture of the background remains
1767 similar between the $\mu + \text{jets}$ sample and the signal region, contrary to the defined
1768 closure tests which make predictions between two very different admixtures of $W +$
1769 jets and $t\bar{t}$ events.

1770 Within the $\mu + \text{jets}$ sample, a W boson enriched sub-sample ($n_b = 0$) is used
1771 to predict yields in a $t\bar{t}$ enriched sub-sample ($n_b = 1$). Similarly the $t\bar{t}$ enriched
1772 sub-sample ($n_b = 1$) is also used to predict yields for a further enriched $t\bar{t}$ sub-sample
1773 ($n_b = 2$), further probing the modelling of the n_b^{reco} distribution.

1774 Similarly a further closure test probes the relative contribution of $Z + \text{jets}$ to $W + \text{jets}$
1775 and $t\bar{t}$ events, through the use of the $\mu + \text{jets}$ sample to predict yields for the $\mu\mu +$
1776 jets control sample. This closure test, also at some level probes the muon trigger
1777 and reconstruction efficiencies, given that exactly one and two muons are required
1778 by the different selections.

1779 Consistency check between $Z \rightarrow \nu\bar{\nu}$ predictions

1780 An important consistency check between the $\mu\mu + \text{jets}$ jets and $\gamma + \text{jets}$, which
1781 are both used in the prediction of the $Z \rightarrow \nu\bar{\nu}$ in the signal region, is measured by
1782 using the $\gamma + \text{jets}$ sample to predict yields for the $\mu\mu + \text{jets}$ control sample. This
1783 test also serves to validate the $\gamma + \text{jets}$ control sample when used to predict $Z + \text{jet}$
1784 processes, which itself is subject to large theory uncertainties [cite].

1785 Modelling of jet multiplicity

1786 The simulation modelling of the jet multiplicity within each control sample is
1787 important due to the exclusive jet multiplicity binning within the analysis. This is
1788 probed via the use of each of the three control samples to independently predict
1789 from the lower jet multiplicity category $2 \leq n_{jet} \leq 3$, to the high jet category ≥ 4 .

1790 For the case of the $\mu + \text{jets}$ and $\mu\mu + \text{jets}$ control samples this test is also a
1791 further probe of the admixture between $W + \text{jets}/Z + \text{jets}$ and $t\bar{t}$.

1792 To test for the assumption that no H_T dependences exist within the background predic-
1793 tions of the analysis, the first five closure tests defined above are taken, with zeroeth and
1794 first order polynomial fits are applied to each. This is summarised in Table 4.12 and

1795 Table 4.13 which show the results for both the $2 \leq n_{jet} \leq 3$ and ≥ 4 jet multiplicity bins
1796 respectively.

Closure test	Symbol	Constant fit		Linear fit	
		Best fit value	p-value	Slope (10^{-4})	p-value
$\alpha_T < 0.55 \rightarrow \alpha_T > 0.55 (\mu + \text{jets})$	Circle	-0.06 ± 0.02	0.93	-1.3 ± 2.2	0.91
$0 \text{ b-jets} \rightarrow 1 \text{ b-jet } (\mu + \text{jets})$	Square	0.07 ± 0.02	0.98	-1.6 ± 1.6	1.00
$1 \text{ b-jets} \rightarrow 2 \text{ b-jet } (\mu + \text{jets})$	Triangle	-0.07 ± 0.03	0.76	-2.7 ± 3.0	0.76
$\mu + \text{jets} \rightarrow \mu\mu + \text{jets}$	Cross	0.10 ± 0.03	0.58	-1.1 ± 2.3	0.49
$\mu\mu + \text{jets} \rightarrow \gamma + \text{jets}$	Star	-0.06 ± 0.04	0.31	4.2 ± 4.3	0.29

Table 4.12.: A summary of the results obtained from fits of zeroeth order polynomials (i.e. a constant) to five sets of closure tests performed in the $2 \leq n_{jet} \leq 3$ bin. The final two columns show the best fit value for the slope obtained when performing a linear fit and the p-value for the linear fit.

Closure test	Symbol	Constant fit		Linear fit	
		Best fit value	p-value	Slope (10^{-4})	p-value
$\alpha_T < 0.55 \rightarrow \alpha_T > 0.55 (\mu + \text{jets})$	Circle	-0.05 ± 0.03	0.21	3.0 ± 2.9	0.21
$0 \text{ b-jets} \rightarrow 1 \text{ b-jet } (\mu + \text{jets})$	Square	-0.03 ± 0.03	0.55	-1.0 ± 1.9	0.47
$1 \text{ b-jets} \rightarrow 2 \text{ b-jet } (\mu + \text{jets})$	Triangle	-0.02 ± 0.03	0.39	1.1 ± 2.2	0.31
$\mu + \text{jets} \rightarrow \mu\mu + \text{jets}$	Cross	0.08 ± 0.07	0.08	4.8 ± 4.3	0.07
$\mu\mu + \text{jets} \rightarrow \gamma + \text{jets}$	Star	-0.03 ± 0.10	0.72	-4.0 ± 7.0	0.64

Table 4.13.: A summary of the results obtained from fits of zeroeth order polynomials (i.e. a constant) to five sets of closure tests performed in the $n_{jet} \geq q$ bin. The final two columns show the best fit value for the slope obtained when performing a linear fit and the p-value for the linear fit.

1797 Table 4.14 shows the same fits applied to the three closure tests that probe the modelling
1798 between the different n_{jet} bins. The best fit value and its uncertainty is listed for each
1799 set of closure tests in all three tables, along with the p-value of the constant and linear
1800 fits applied.

Closure test	Symbol	Constant fit		Linear fit	
		Best fit value	p-value	Slope (10^{-4})	p-value
$\mu + \text{jets}$	Inverted triangle	-0.03 ± 0.02	0.02	0.0 ± 1.0	0.01
$\mu + \text{jets}$ (outlier removed)	Inverted triangle	-0.04 ± 0.01	0.42	-1.4 ± 1.1	0.49
$\gamma + \text{jets}$	Diamond	0.12 ± 0.05	0.79	6.0 ± 4.7	0.94
$\mu\mu + \text{jets}$	Asterisk	-0.04 ± 0.07	0.20	4.9 ± 4.4	0.20

Table 4.14.: A summary of the results obtained from fits of zeroeth order polynomials (i.e. a constant) to five sets of closure tests performed in the $2 \leq n_{jet} \leq 3$ bin. The final two columns show the best fit value for the slope obtained when performing a linear fit and the p-value for the linear fit.

1801 The best fit value for the constant parameter is indicative of the level of closure, averaged
1802 across the full range of H_T bins in the analysis, and the p-value an indicator of any

1803 significant dependence on H_T within the closure tests. The best fit values of all the tests
1804 are either statistically compatible with zero bias (i.e, less than 2σ from zero) or at the
1805 level of 10% or less, with the exception of one closure test discussed below.

1806 Within Table 4.14, there exists one test that does not satisfy the above statement, which
1807 is the $2 \leq n_{jet} \leq 3 \rightarrow n_{jet} \geq 4$ test using the $\mu +$ jets control sample. The low p-value
1808 can be largely attributed to an outlier in the $675 < H_T < 775$ GeV bin, rather than any
1809 significant trend in H_T . Removing this single outlier from the constant fit performed,
1810 gives a best fit value of -0.04 ± 0.01 , $\chi^2/\text{d.o.f} = 6.07/6$. and a p-value of 0.42. These
1811 modified fit results are included within Table 4.14 .

1812 In addition the best fit values for the slope terms of the linear fits in all three tables are
1813 of the order 10^{-4} , which corresponds to a percent level change per 100 GeV. However in
1814 all cases, the best fit values are fully compatible with zero (within 1σ) once again with
1815 the exception detailed above, indicating that the level of closure is H_T independent.

1816 4.6.1. Determining systematic uncertainties from closure tests

1817 Once it has been established that no significant bias or trend has been exist within
1818 the closure tests, systematic uncertainties are determined. The statistical precision
1819 of the closure tests is considered a suitable benchmark for determining the systematic
1820 uncertainties that are assigned to the TF's, which are propagated through to the likelihood
1821 fit.

1822 The systematic uncertainty band is split into five separate regions of H_T . Within each
1823 region the square root of the sample variance, σ^2 , is taken over the eight closure tests to
1824 determine the systematic uncertainties to be applied within that region.

1825 Using this procedure the systematic uncertainties for each region are calculated and are
1826 shown in Table 4.15, with the systematic uncertainty to be used in the likelihood model
1827 conservatively rounded up to the nearest decile, shown in brackets.

1828 Figure 4.11 shows the sets of closure tests overlaid on top of grey bands that represent
1829 the H_T dependent systematic uncertainties. These systematic uncertainties are assumed
1830 to fully uncorrelated between the different n_b multiplicity categories and across the five
1831 H_T regions. This can be considered a more conservative approach given that some
1832 correlations between adjacent H_T bins could be expected due to comparable kinematics.

H_T band (GeV)	$2 \leq n_{jet} \leq 3$	$n_{jet} \geq 4$
$275 < H_T < 325$	6 (10)%	3 (10)%
$325 < H_T < 375$	6 (10)%	6 (10)%
$375 < H_T < 575$	7 (10)%	9 (10)%
$575 < H_T < 775$	13 (20)%	15 (20)%
$H_T > 775$	19 (20)%	21 (30)%

Table 4.15.: Calculated systematic uncertainties for the five H_T regions, determined from the closure tests. Uncertainties shown for both jet multiplicity categories. Values used within the likelihood model are conservatively rounded up to the nearest decile and shown in brackets.

As already referenced. These closure tests represent a conservative estimate of the systematic uncertainty in making a background prediction for the signal region. This is due to significant differences in the background composition and event kinematics between the two sub-samples used in the closure tests. This is contrary to the signal region prediction where the two sub-samples are both have a comparable background admixture and similar kinematics owing to the fact that the predictions are always made using the same (n_{jet}, n_b, H_T) bin.

This point is emphasised when we examine the sensitivity of the TF's to a change in the admixture of $W +$ jets and $t\bar{t}$ with the control and signal samples. This is accomplished by varying the cross sections of the $W +$ jets and $t\bar{t}$ by +20% and -20%, respectively. Figures C.2 and C.3 within Appendix C, show the effect upon the closure tests for both jet multiplicity categories. Given these variations in cross sections, the level of closure is found to be significantly worse, with biases as large as $\sim 30\%$, most apparent in the lowest H_T bins. However the TF's used to extrapolate from control to signal are seen to change only at the percent level by this large change in cross section, shown in Table C.1.

Given the robust behaviour of the translation factors with respect to large (and opposite) variations in the $W +$ jets and $t\bar{t}$ cross sections, one can assume with confidence that any bias in the translation factors is adequately (and conservatively) covered by the systematic uncertainties used in the analysis.

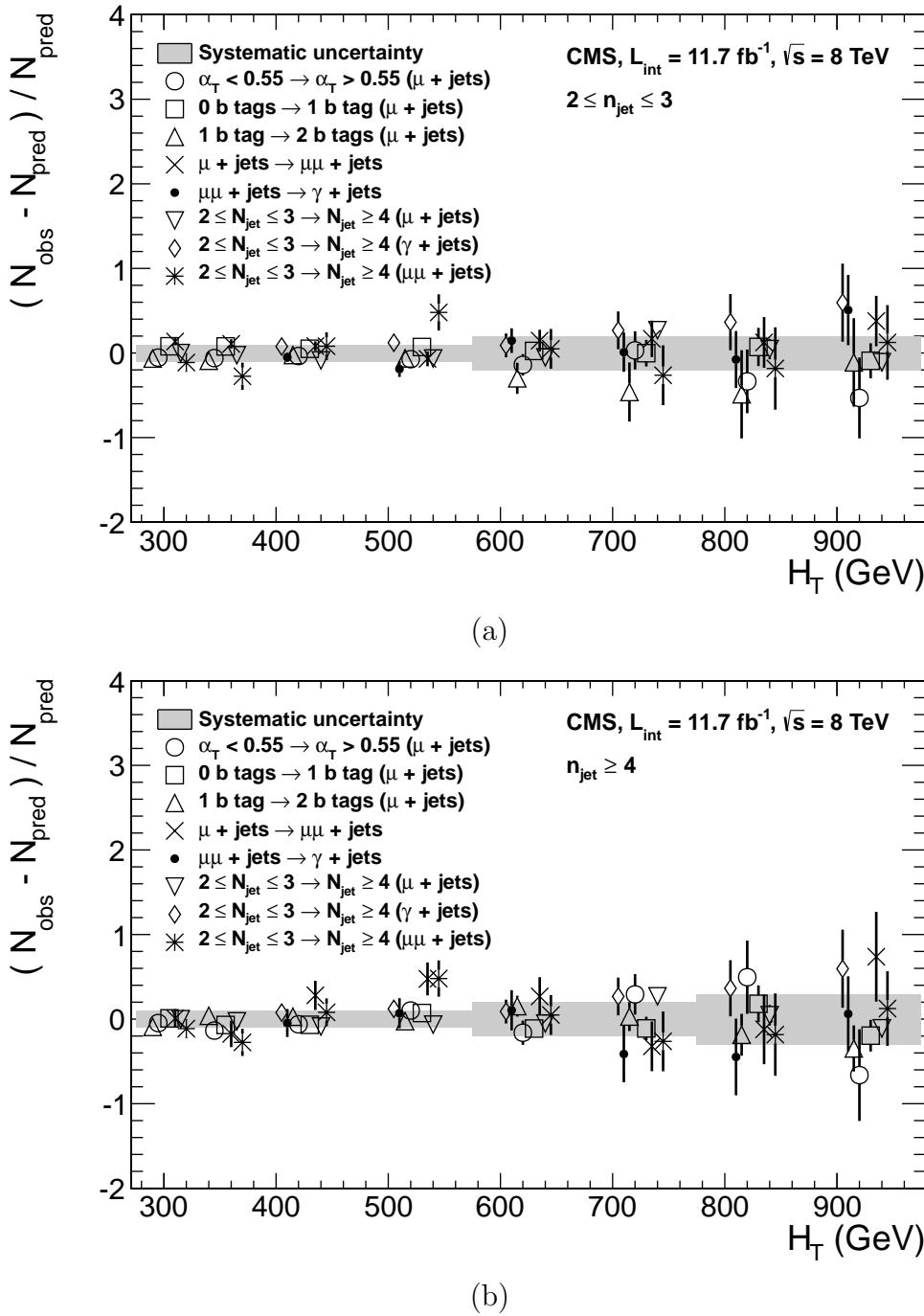


Figure 4.11.: Sets of closure tests (open symbols) overlaid on top of the systematic uncertainty used for each of the five H_T regions (shaded bands) and for the two different jet multiplicity bins: (a) $2 \leq n_{\text{jet}} \leq 3$ and (b) $n_{\text{jet}} \geq 4$.

1852 4.7. Simplified Models, Efficiencies and Systematic 1853 Uncertainties

1854 The results of the analysis are interpreted using various **SMS** signal models as already
1855 introduced in Section (2.4.1). Each model is parameterised in a two dimensional parameter
1856 space, ($m_{\tilde{q}/\tilde{g}}$, m_{LSP}), from which upper limits on the production cross sections of the
1857 various **SMS** models can be set.

1858 Each signal sample is generated at Next to Leading Order (**NLO**) and Next to Leading
1859 Logarithmic Order (**NLL**) [83] using the **Fastsim** framework. This framework represents
1860 a simplified simulation of the **CMS** detector, but allows for faster production of various
1861 signal topologies with different mass parameters. A series of correction factors are applied
1862 to account for the effects on the b-tagging rate between **Fastsim** [84] and **Fullsim** [85]
1863 and are detailed in Section (4.7.2).

1864 4.7.1. Signal efficiency

1865 The analysis selection efficiency, ϵ , is measured for each mass point of the interpreted
1866 model, this serves as a measure of the sensitivity of the signal selection for that particular
1867 sparticle and **LSP** mass . The signal yield is then given by

$$Y(m_{\tilde{q}/\tilde{g}}, m_{LSP}) = \epsilon \times \sigma \times \mathcal{L}, \quad (4.13)$$

1868 where σ represents the model's cross section and \mathcal{L} the luminosity. An upper limit on σ
1869 taken from theory can then allow for the setting of limits in terms of the particle mass.

1870 Figure 4.12 shows the expected signal efficiency of the signal selection for the T1 and
1871 T2 **SMS** models interpreted in this analysis. The efficiency maps are produced with the
1872 requirement $H_T > 275$ GeV (i.e., no binning in H_T) and requirements on n_{jet} and n_b^{reco}
1873 that are appropriate for the model in question.

1874 The same procedure is conducted in the analysis control samples. It is found in the μ
1875 + jets control samples, that the S/B ratios for the expected signal yields in each of the
1876 **SMS** models are many times (~ 40 -100) smaller than in the hadronic signal region. The
1877 relative contamination for the $\mu\mu$ + jets sample is smaller still due to the requirement of

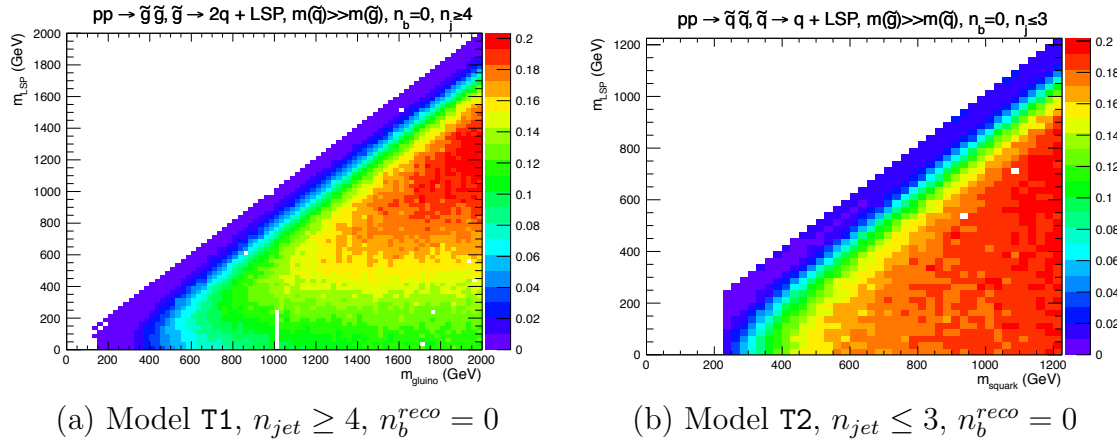


Figure 4.12.: Signal efficiencies for the **SMS** models (a) T1 ($\widetilde{g}\widetilde{g}^* \rightarrow q\widetilde{\chi}_1^0 q\widetilde{\chi}_1^0$) and (b) T2 ($\widetilde{q}\widetilde{q}^* \rightarrow q\widetilde{\chi}_1^0 \bar{q}\widetilde{\chi}_1^0$) when requiring $n_{jet} \geq 4$ and ≤ 3 respectively, and $n_b^{reco} = 0$.

1878 a second muon. The relative contamination for the $\gamma +$ jets sample is expected to be
 1879 zero for the models under consideration. These small, relative levels of contamination
 1880 are accounted for in the fitting procedure, as described in Section (4.8.4).

1881 4.7.2. Applying b-tag scale factor corrections in signal samples

1882 High-statistic **FastSim** signal simulation samples are unavailable for each signal signal
 1883 point, which means that a different procedure to the formula method described in Section
 1884 (4.5) is employed. Furthermore, the use of the **FastSim** framework in the reconstruction
 1885 introduces an extra set of scale-factor corrections, to be applied simultaneously with
 1886 those correcting the full-simulation to the data.

1887 For these signal models, an event-by-event re-weighting procedure is applied. This applied
 1888 weight depends on both the flavour content and the b-tagging status of the reconstruction
 1889 level jets in the event.

1890 The re-weighting procedure can be described by first considering a single jet in an signal
 1891 sample event. The flavour of the jet is determined using the method described in Section
 1892 (4.5.1).

1893 Taking the flavour, p_T and η values of the jet, the expected tagging efficiency, $\epsilon_{MC}(p_T, \eta, f)$,
 1894 in simulation is retrieved from a map of tagging efficiencies determined from the **FullSim**
 1895 **SM** simulation samples, and binned as a function of jet p_T , η and flavour after the
 1896 application of the hadronic signal selection. The binning is chosen to reflect the set of p_T
 1897 and η dependant corrections of simulation to data defined by [86].

1898 The actual tagging efficiency of the **FastSim** jet, $\epsilon_{\text{FastSim}}(p_T, \eta, f)$, differs from that
1899 measured in **FullSim**, $\epsilon_{MC}(p_T, \eta, f)$ and is related via an additional correction factor,

$$\epsilon_{\text{FastSim}}(p_T, \eta, f) = \frac{\epsilon_{MC}(p_T, \eta, f)}{SF_{\text{Fast} \rightarrow \text{Full}}(p_T, \eta, f)}, \quad (4.14)$$

1900 where $SF_{\text{Fast} \rightarrow \text{Full}}(p_T, \eta, f)$ represents a set of p_T and η dependant corrections determined
1901 from the ratio between the efficiency and mis-tagging rates of a $t\bar{t}$ **FullSim** and $t\bar{t}$
1902 **FastSim** sample. The central value for these corrections is the same for all signal samples.
1903 Similarly the tagging efficiencies measured in data [64], $\epsilon_{Data}(p_T, \eta, f)$, are further related
1904 to $\epsilon_{\text{FastSim}}(p_T, \eta, f)$ by the equation,

$$\begin{aligned} \epsilon_{Data}(p_T, \eta, f) &= \epsilon_{MC}(p_T, \eta, f) \times SF_{MC \rightarrow Data}(p_T, \eta, f) \\ &= \epsilon_{\text{FastSim}}(p_T, \eta, f) \times \underbrace{SF_{\text{Fast} \rightarrow \text{Full}}(p_T, \eta, f) \times SF_{MC \rightarrow Data}(p_T, \eta, f)}_{\text{SF}_{\text{Fast} \rightarrow Data}}. \end{aligned} \quad (4.15)$$

1905 For each jet, the weight of the event is re-weighted according to whether the jet fires the
1906 b-tagger. In the instance that the jet *is* b-tagged the event weight is modified by,

$$\text{weight} = SF_{\text{Fast} \rightarrow Data} \times \text{weight}, \quad (4.16)$$

1907 and in the case that the jet *is not* tagged,

$$\text{weight} = \frac{1 - \epsilon_{Data}(p_T, \eta, f)}{1 - \epsilon_{\text{FastSim}}(p_T, \eta, f)} \times \text{weight}. \quad (4.17)$$

1908 Once all events have been reweighted this way, the yields in each n_b^{reco} bin represent the
1909 corrected MC yields.

¹⁹¹⁰ 4.7.3. Experimental uncertainties

¹⁹¹¹ The systematic uncertainty on the expected signal acceptance times analysis efficiency is
¹⁹¹² determined independently for each **SMS** model considered. These systematics stem
¹⁹¹³ from uncertainties on the parton distribution functions, the luminosity measurement,
¹⁹¹⁴ jet energy scale, b-tag scale factor measurements and the efficiencies of various cuts used
¹⁹¹⁵ in the signal selection, including the H_T / E_T , dead **ECAL** cleaning filter and lepton /
¹⁹¹⁶ photon event vetoes.

¹⁹¹⁷ Rather than trying to estimate the level of systematic that is applicable point-by-point in
¹⁹¹⁸ a model space, general behaviours are considered and constant systematics are estimated
¹⁹¹⁹ in two regions of the **SMS** models parameter space. These two regions are defined as
¹⁹²⁰ near to (small mass splittings) and far (large mass splittings) from the diagonal, where
¹⁹²¹ far is realised by the condition

$$m_{\tilde{q}/\tilde{g}} - m_{LSP} > 350 \text{GeV} \quad m_{\tilde{q}/\tilde{g}} > 475 \text{GeV}.$$

¹⁹²² The total systematics in each region are evaluated in the following ways:

¹⁹²³ **Jet energy scale** : The relative change in the signal efficiency is gauged by varying
¹⁹²⁴ the energy of all jets in an event up or down according to a p_T and η dependent jet
¹⁹²⁵ energy scale uncertainty. Within the two systematic regions, the resulting systematic
¹⁹²⁶ uncertainties for each **SMS** model are determined by taking the value of the 68th
¹⁹²⁷ percentile for the distributions of the relative change in the signal efficiency.

¹⁹²⁸ **Luminosity measurement** : The measurement of luminosity taken propagates
¹⁹²⁹ through to an uncertainty on the signal event yield when considering any new
¹⁹³⁰ physics model, which is currently 4.4% [87].

¹⁹³¹ **Parton density function** : The effects of varying the set of parton distribution
¹⁹³² functions used and changing the renormalization/factorisation scale used to compute
¹⁹³³ the cross sections by a factor of two up or down have been found to affect the
¹⁹³⁴ efficiency by up to 10%.

¹⁹³⁵ **H_T/E_T cleaning cut** : The ratio of the efficiencies of the cleaning cut are compared
¹⁹³⁶ in simulation and data after application of the $\mu +$ jets control sample selection.
¹⁹³⁷ No α_T cut or further event cleaning filters are applied. The ratio of the efficiencies

1938 observed in data and simulation for a cut value of $\mathcal{H}_T/\mathcal{E}_T < 1.25$ and the two jet
1939 multiplicity bins, $2 \leq n_{jet} \leq 3$ and $n_{jet} \geq 4$ are 1.028 ± 0.007 and 1.038 ± 0.015
1940 respectively. These deviations are taken to represent the systematic uncertainty on
1941 the simulation modelling of this variable.

1942 **Deal ECAL cleaning filter** : The ratio of the efficiencies observed in data and
1943 simulation for this filter in the two jet multiplicity bins, $2 \leq n_{jet} \leq 3$ and $n_{jet} \geq 4$,
1944 are 0.961 ± 0.008 and 0.961 ± 0.009 , respectively. These deviations from unity
1945 are taken to represent the systematic uncertainties in the modelling in simulation of
1946 this filter.

1947 **Lepton and photon vetoes** : The uncertainty on the efficiency of the lepton and
1948 photon vetoes is established by considering the efficiency of the vetoes after applying
1949 filters with identical logic but based on truth information. If the efficiency is not
1950 100%, then this represents the fraction of signal events that should not be vetoed.
1951 This deviation is taken directly as the systematic uncertainty on the efficiency. The
1952 systematic uncertainty is only non-zero for models which contain third-generation
1953 quarks in the final state.

1954 **B-tag scale factor uncertainties** : The relative change in the signal efficiency is
1955 observed when relevant flavour, p_T and η dependant b-tag correction factors, are
1956 varied up or down by their uncertainty. Within the two systematic regions, the
1957 resulting systematic uncertainties for each **SMS** model are determined by taking
1958 the value of the 68th percentile for the distributions of the relative change in the
1959 signal efficiency, over all mass points.

1960 Tables 4.16 and 4.17 summarise all the aforementioned systematic uncertainties on
1961 the signal efficiencies for each individual **SMS** model interpreted in the analysis. The
1962 systematic uncertainties used for the region near to the diagonal fall in the range 13-15%;
1963 similarly, for the region far from the diagonal, the uncertainties used fall in the range
1964 12-23%. These uncertainties are all included in the limit calculation.

Model	Luminosity	p.d.f	JES	H_T/\bar{E}_T	Dead ECAL	Lepton Veto	b-tagging	Total
T1	4.4	10.0	5.6	3.8	4.1	n/a	3.1	13.9
T2	4.4	10.0	4.1	2.8	4.1	n/a	2.4	12.9
T2tt	4.4	10.0	6.5	3.8	4.1	0.8	0.8	13.9
T2bb	4.4	10.0	4.8	2.8	4.1	0.3	2.2	13.1
T1tttt	n/a	n/a	n/a	n/a	n/a	n/a	n/a	n/a
T1bbbb	4.4	10.0	7.3	3.8	4.1	0.5	2.7	14.5

Table 4.16.: Estimates of systematic uncertainties on the signal efficiency (%) for various **SMS** models when considering points in the region near to the diagonal (i.e. small mass splitting and compressed spectra). The uncertainties are added in quadrature to obtain the total.

Model	Luminosity	p.d.f	JES	H_T/\bar{E}_T	Dead ECAL	Lepton Veto	b-tagging	Total
T1	4.4	10.0	0.8	3.8	4.1	n/a	6.6	14.0
T2	4.4	10.0	1.1	2.8	4.1	n/a	5.8	13.4
T2tt	4.4	10.0	3.5	3.8	4.1	0.6	1.6	12.9
T2bb	4.4	10.0	0.9	2.8	4.1	0.3	2.7	12.3
T1tttt	4.4	10.0	0.5	3.8	4.1	1.4	19.4	23.0
T1bbbb	4.4	10.0	1.5	3.8	4.1	0.4	10.1	16.0

Table 4.17.: Estimates of systematic uncertainties on the signal efficiency (%) for various **SMS** models when considering points in the region far from the diagonal (i.e. large mass splitting). The uncertainties are added in quadrature to obtain the total.

1965 4.8. Statistical Framework

1966 For a given category of events satisfying requirements on both n_{jet} and n_b^{reco} , a likelihood
 1967 model of the observations in multiple data samples is used to gauge agreement between
 1968 the observed yields in the hadronic signal region, and the predicted yields obtained from
 1969 the control samples. In addition to checking whether the predictions are compatible with
 1970 a **SM** only hypothesis, the likelihood model is also used to test for the presence of a
 1971 variety of signal models.

1972 4.8.1. Hadronic sample

1973 Let N be the number of bins on H_T , with n^i the number of events observed satisfying
 1974 all selection requirements in each H_T bin i. The likelihood of the observations can then
 1975 be written :

$$L_{had} = \prod_i \text{Pois}(n^i | b^i + s^i), \quad (4.18)$$

₁₉₇₆ where b^i represents the expected **SM** background

$$b^i = EWK_i + QCD_i, \quad (4.19)$$

₁₉₇₇ and s^i the expected number of signal events from the different **SMS** models interpreted.
₁₉₇₈ Pois refers to the Poisson distribution of these values and is defined as :

$$\text{Pois}(\chi|\lambda) = \frac{\lambda^\chi \exp^{-\lambda}}{k!}. \quad (4.20)$$

₁₉₇₉ 4.8.2. H_T evolution model

₁₉₈₀ The hypothesis, that for a process the α_T ratio falls exponentially see Section (4.2.4)
₁₉₈₁ in H_T is defined by Equation (4.10), where k_{QCD} is constrained by measurements in a
₁₉₈₂ signal sideband region.

₁₉₈₃ The expected QCD background, QCD^i , within a bin i is then modelled as,

$$QCD^i = m^i A_{QCD} e^{-k_{QCD} \langle H_T \rangle}, \quad (4.21)$$

₁₉₈₄ where m_i represent the number of events observed with $\alpha_T \leq 0.55$ in each H_T bin i , and
₁₉₈₅ $\langle H_T \rangle$ represents the mean H_T of each bin. Expressed as functions of just the zeroth bin,
₁₉₈₆ QCD^0 , and k_{QCD} , the QCD expectation is given by

$$QCD^i = QCD^0 \left(\frac{m^i}{m^0} \right) e^{-k_{QCD} (\langle H_T \rangle^i - \langle H_T \rangle^0)}. \quad (4.22)$$

¹⁹⁸⁷ 4.8.3. EWK control samples

¹⁹⁸⁸ The EWK background estimation within each bin, i , is broken into two components, the
¹⁹⁸⁹ expected yield from $Z \rightarrow \nu\bar{\nu}$ and $t\bar{t}$ -W (plus other residual backgrounds) events. This is
¹⁹⁹⁰ written as, Z_{inv}^i and $t\bar{t}W^i$, and it follows that

$$EWK^i = Z_{inv}^i + t\bar{t}W^i. \quad (4.23)$$

¹⁹⁹¹ This can be further expressed as

$$Z_{inv}^i \equiv f_{Zinv}^i \times EWK^i, \quad (4.24)$$

$$t\bar{t}W^i \equiv (1 - f_{Zinv}^i) \times EWK^i, \quad (4.25)$$

¹⁹⁹² where f_{Zinv}^i represents the expected yield from $Z \rightarrow \nu\bar{\nu}$ in bin i divided by the expected
¹⁹⁹³ EWK background EWK^i . This fraction is modelled as a linear component

$$f_{Zinv}^i = f_{Zinv}^0 + \frac{\langle H_T \rangle^i - \langle H_T \rangle^0}{\langle H_T \rangle^{N-1} - \langle H_T \rangle^0} (f_{Zinv}^{N-1} - f_{Zinv}^i), \quad (4.26)$$

¹⁹⁹⁴ where N again represents the number of H_T bins, and f_{Zinv}^i and f_{Zinv}^{N-1} are float parameters
¹⁹⁹⁵ whose final values are limited between zero and one.

¹⁹⁹⁶ Within each H_T bin there are three background measurements for the different control
¹⁹⁹⁷ samples, n_γ^i , n_μ^i and $n_{\mu\mu}^i$, representing the event yields from the $\gamma +$ jets, $\mu +$ jets and
¹⁹⁹⁸ $\mu\mu +$ jets control samples respectively. Each of these have a corresponding yield in
¹⁹⁹⁹ simulation, MC_γ^i , MC_μ^i and $MC_{\mu\mu}^i$. Within the hadronic signal region there are also
²⁰⁰⁰ corresponding simulated yields for $Z \rightarrow \nu\bar{\nu}$ (MC_{Zinv}^i) and $t\bar{t} + W$ ($MC_{t\bar{t}+W}^i$), which are
²⁰⁰¹ used to define

$$r_\gamma^i = \frac{MC_\gamma^i}{MC_{Zinv}^i}; \quad r_{\mu\mu}^i = \frac{MC_{\mu\mu}^i}{MC_{Zinv}^i}; \quad r_\mu^i = \frac{MC_\mu^i}{MC_{t\bar{t}+W}^i}, \quad (4.27)$$

2002 where r_p^i represents the inverse of the **TF**'s used to extrapolate the yield of each background
2003 process.

2004 The likelihoods regarding the three measured yields n_γ^i , $n_{\mu\mu}^i$, n_μ^i can then be fully expressed
2005 as

$$L_\gamma = \prod_i \text{Pois}(n_\gamma^i | \rho_{\gamma Z}^j \cdot r_\gamma^i \cdot Z_{inv}^i), \quad (4.28)$$

$$L_{\mu\mu} = \prod_i \text{Pois}(n_{\mu\mu}^i | \rho_{\mu\mu Z}^j \cdot r_{\mu\mu}^i \cdot Z_{inv}^i), \quad (4.29)$$

$$L_\mu = \prod_i \text{Pois}(n_\mu^i | \rho_{\mu Y}^j \cdot r_\mu^i \cdot Y^i + s_\mu^i), \quad (4.30)$$

$$(4.31)$$

2006 which contain an additional term s_μ^i , which represents the signal contamination in the
2007 $\mu + \text{jets}$ sample. The parameters $\rho_{\gamma Z}^j$, $\rho_{\mu\mu}^j$ and ρ_μ^j represent “correction factors” that
2008 accommodate the systematic uncertainties associated with the control sample based
2009 background constraints.

2010 Each of these equations are used to estimate the maximum likelihood value for relevant
2011 background in the signal region given the observations n_p^i in each of the control samples
2012 (see Section (4.2.3)).

2013 The measurements in each of the control samples and the hadronic signal region, along
2014 with the ratios r_γ^i , $r_{\mu\mu}^i$, and r_μ^i , are all considered simultaneously through the relationships
2015 defined by Equations (4.19),(4.24) and (4.25).

2016 In addition to the Poisson product, an additional log-normal term is introduced to
2017 accommodate the systematic uncertainties given by,

$$L_{EWK \ syst} = \prod_j \text{Logn}(1.0 | \rho_{\mu W}^j, \sigma_{\mu W}^j) \times \text{Logn}(1.0 | \rho_{\mu\mu Z}^j, \sigma_{\mu\mu Z}^j) \times \text{Logn}(1.0 | \rho_{\gamma Z}^j, \sigma_{\gamma Z}^j), \quad (4.32)$$

2018 where $\sigma_{\gamma Z}^j$, $\sigma_{\mu\mu Z}^j$ and $\sigma_{\mu W}^j$ represent the relative systematic uncertainties for the control
2019 sample constraints and Logn is the log-normal distribution [88],

$$\text{Logn}(x \mid \mu, \sigma_{rel}) = \frac{1}{x\sqrt{2\pi}\ln k} \exp\left(\frac{\ln^2(\frac{x}{\mu})}{2\ln^2 k}\right); \quad k = 1 + \sigma_{rel}. \quad (4.33)$$

2020 Five parameters per control sample are used to span the eight H_T bins, with just one
 2021 used for the three H_T bins in the $n_b^{reco} \geq 4$ category. These parameters span the same
 2022 H_T ranges described in Section (4.6) and is shown in Table 4.18.

H_T bin (i)	0	1	2	3	4	5	6	7
syst. parameter (j)	0	1	2	2	3	3	4	4

H_T bin (i)	0	1	2
syst. parameter (j)	0	0	0

Table 4.18.: The systematic parameters used in H_T bins. Left: categories with eight bins; right: category with three bins.

2023 Alternatively, in the higher n_b^{reco} categories ($n_b^{reco} = 3, n_b^{reco} \geq 4$), the single muon sample
 2024 is used to constrain the total EWK background. Therefore the likelihood function is
 2025 greatly simplified and is represented by

$$L'_\mu = \prod_i \text{Pois}(n_\mu^i | \rho_{\mu Y}^j \cdot r_\mu'^i \cdot EWK^i + s_\mu^i), \quad (4.34)$$

2026 where,

$$r_\mu'^i = \frac{MC_\mu^i}{MC_{tot}^i}. \quad (4.35)$$

2027 4.8.4. Contributions from signal

2028 The cross section for each model is represented by x and l represents the total recorded
 2029 luminosity considered by the analysis in the signal region. Let ϵ_{had}^i and ϵ_μ^i represent the
 2030 analysis selection efficiency for that particular signal model in H_T bin i of the hadronic
 2031 and $\mu +$ jets control sample respectively. Letting δ represent the relative uncertainty on
 2032 the signal yield, assumed to be fully correlated across all bins, and ρ_{sig} the “correction
 2033 factor” to the signal yield which accommodates this uncertainty. f represents an unknown
 2034 multiplicative factor on the signal cross section, for which an allowed interval is computed.

2035 The expected signal yield s^i is thus given by

$$s^i \equiv f \rho_{sig} x l \epsilon_{had}^i \quad (4.36)$$

2036 and signal contamination with the $\mu +$ jets control sample by

$$s_\mu^i \equiv f \rho_{sig} x l \epsilon_\mu^i \quad (4.37)$$

2037 The systematic uncertainty on the signal is additionally included by the term

$$L_{sig} = \text{Logn}(1.0 | \rho_{sig}, \delta). \quad (4.38)$$

2038 A discussion of the **SMS** signal models through which the analysis is interpreted can be
2039 found in the following Chapter.

2040 4.8.5. Total likelihood

2041 The total likelihood function for a given signal bin $k(n_b^{reco}, n_{jet})$ is given by the product
2042 of the likelihood functions introduced within the previous sections:

$$L^k = L_{had}^k \times L_\mu^k \times L_\gamma^k \times L_{\mu\mu}^k \times L_{EWKsyst}^k \times L_{QCD}^k. \quad (4.39)$$

2043 In categories containing eight H_T bins and utilising the three control samples ($\mu +$ jets, $\mu\mu$
2044 + jets, $\gamma +$ jets), there are 25 nuisance parameters, whilst when just one control sample is
2045 used to estimate the **EWK** background, there are 15 nuisance parameters. Where three
2046 H_T bins are used (the highest n_b^{reco} category), there are 6 nuisance parameters. This
2047 information is summarised within Table 4.19.

Nuisance parameter	Total
$(EWK^i)_{i:0-7(2)}$	8 (3)
f_{Zinv}^0 *	1
f_{Zinv}^7 *	1
QCD^0	1
k_{QCD}	1
$(\rho_{\gamma Z}^j)_{j:2-4}$ *	3
$(\rho_{\mu\mu Z}^j)_{j:0-4}$ *	5
$(\rho_{\mu W}^j)_{j:0-4(0)}$	5 (1)

Table 4.19.: Nuisance parameters used within the different hadronic signal bins of the analysis. Parameters denoted by a * are not considered in the case of a single control sample being used to predict the EWK background. Numbers within brackets highlight the number of nuisance parameters in the case of three H_T bins being used.

When considering SUSY signal models within the likelihood, an additional parameter is introduced, ρ_{sig} . When multiple categories are fit simultaneously the total likelihood is then represented by

$$L = L_{sig} \times \prod_k L_{had}^k \times L_\mu^k \times L_\gamma^k \times L_{\mu\mu}^k \times L_{EWKsyst}^k \times L_{QCD}^k. \quad (4.40)$$

Chapter 5.

²⁰⁵¹ Results and Interpretation

²⁰⁵² Using the statistical framework outlined in the previous chapter, results are compared to
²⁰⁵³ a **SM**-only hypothesis (Section (5.1)) and interpreted using various **SMS** models (Section
²⁰⁵⁴ (5.2)).

²⁰⁵⁵ 5.1. Standard Model

²⁰⁵⁶ The **SM** background only hypothesis is tested by removing any signal contributions
²⁰⁵⁷ within the signal and control samples, and the likelihood function is maximised over all
²⁰⁵⁸ parameters using Rootfit [89] and MINUIT [90]. The results of the search consist of the
²⁰⁵⁹ observed yields in the hadronic signal sample, and the $\mu + \text{jets}$, $\mu\mu + \text{jets}$ and $\gamma + \text{jets}$
²⁰⁶⁰ control samples.

²⁰⁶¹ These observed yields along with the expectations and uncertainties given by the simulta-
²⁰⁶² neous fit for the hadronic signal region are given in Table 5.2. The results obtained from
²⁰⁶³ the simultaneous fits, including that of the three control samples, are shown in Figure
²⁰⁶⁴ 5.1-5.8, as summarised in Table 5.1.

²⁰⁶⁵ The figures show a comparison between the observed yields and the **SM** expectations
²⁰⁶⁶ across all H_T bins, for events in both n_{jet} and n_b^{reco} multiplicity categories. In all categories
²⁰⁶⁷ the samples are well described by the **SM** only hypothesis. In particular no significant
²⁰⁶⁸ excess is observed above **SM** expectation within the hadronic signal region.

n_{jet}	n_b^{reco}	Control samples fitted	Figure
2-3	0	$\mu + \text{jets}, \mu\mu + \text{jets}, \gamma + \text{jets}$	5.1
2-3	1	$\mu + \text{jets}, \mu\mu + \text{jets}, \gamma + \text{jets}$	5.2
2-3	1	$\mu + \text{jets}$	5.3
≥ 4	0	$\mu + \text{jets}, \mu\mu + \text{jets}, \gamma + \text{jets}$	5.4
≥ 4	1	$\mu + \text{jets}, \mu\mu + \text{jets}, \gamma + \text{jets}$	5.5
≥ 4	2	$\mu + \text{jets}$	5.6
≥ 4	3	$\mu + \text{jets}$	5.7
≥ 4	4	$\mu + \text{jets}$	5.8

Table 5.1.: Summary of control samples used by each fit results, and the Figures in which they are displayed.

Cat	n_b^{reco}	n_{jet}	H_T bin (GeV)							
			275-325	325-375	375-475	474-575	575-675	675-775	775-875	875- ∞
SM Data	0	≤ 3	6235^{+100}_{-67}	2900^{+60}_{-54}	1955^{+34}_{-39}	558^{+14}_{-15}	186^{+11}_{-10}	$51.3^{+3.4}_{-3.8}$	$21.2^{+2.3}_{-2.2}$	$16.1^{+1.7}_{-1.7}$
			6232	2904	1965	552	177	58	16	25
SM Data	0	≥ 4	1010^{+34}_{-24}	447^{+19}_{-16}	390^{+19}_{-15}	250^{+12}_{-11}	111^{+9}_{-7}	$53.3^{+4.3}_{-4.3}$	$18.5^{+2.4}_{-2.4}$	$19.4^{+2.5}_{-2.7}$
			1009	452	375	274	113	56	16	27
SM Data	1	≤ 3	1162^{+37}_{-29}	481^{+18}_{-19}	341^{+15}_{-16}	$86.7^{+4.2}_{-5.6}$	$24.8^{+2.8}_{-2.7}$	$7.2^{+1.1}_{-1.0}$	$3.3^{+0.7}_{-0.7}$	$2.1^{+0.5}_{-0.5}$
			1164	473	329	95	23	8	4	1
SM Data	1	≥ 4	521^{+25}_{-17}	232^{+15}_{-12}	188^{+12}_{-11}	106^{+6}_{-6}	$42.1^{+4.1}_{-4.4}$	$17.9^{+2.2}_{-2.0}$	$9.8^{+1.5}_{-1.4}$	$6.8^{+1.2}_{-1.1}$
			515	236	204	92	51	13	13	6
SM Data	2	≤ 3	224^{+15}_{-14}	$98.2^{+8.4}_{-6.4}$	$59.0^{+5.2}_{-6.0}$	$12.8^{+1.6}_{-1.6}$	$3.0^{+0.9}_{-0.7}$	$0.5^{+0.2}_{-0.2}$	$0.1^{+0.1}_{-0.1}$	$0.1^{+0.1}_{-0.1}$
			222	107	58	12	5	1	0	0
SM Data	2	≥ 4	208^{+17}_{-9}	103^{+9}_{-7}	$85.9^{+7.2}_{-6.9}$	$51.7^{+4.6}_{-4.7}$	$19.9^{+3.4}_{-3.0}$	$6.8^{+1.2}_{-1.3}$	$1.7^{+0.7}_{-0.4}$	$1.3^{+0.4}_{-0.3}$
			204	107	84	59	24	5	1	2
SM Data	3	≥ 4	$25.3^{+5.0}_{-4.2}$	$11.7^{+1.7}_{-1.8}$	$6.7^{+1.4}_{-1.2}$	$3.9^{+0.8}_{-0.8}$	$2.3^{+0.6}_{-0.6}$	$1.2^{+0.3}_{-0.4}$	$0.3^{+0.2}_{-0.1}$	$0.1^{+0.1}_{-0.1}$
			25	13	4	2	2	3	0	0
SM Data	4	≥ 4	$0.9^{+0.4}_{-0.7}$	$0.3^{+0.2}_{-0.2}$				$0.6^{+0.3}_{-0.3}$		
			1	0				2		

Table 5.2.: Comparison of the measured yields in the each H_T , n_{jet} and n_b^{reco} jet multiplicity bins for the hadronic sample with the SM expectations and combined statistical and systematic uncertainties given by the simultaneous fit.

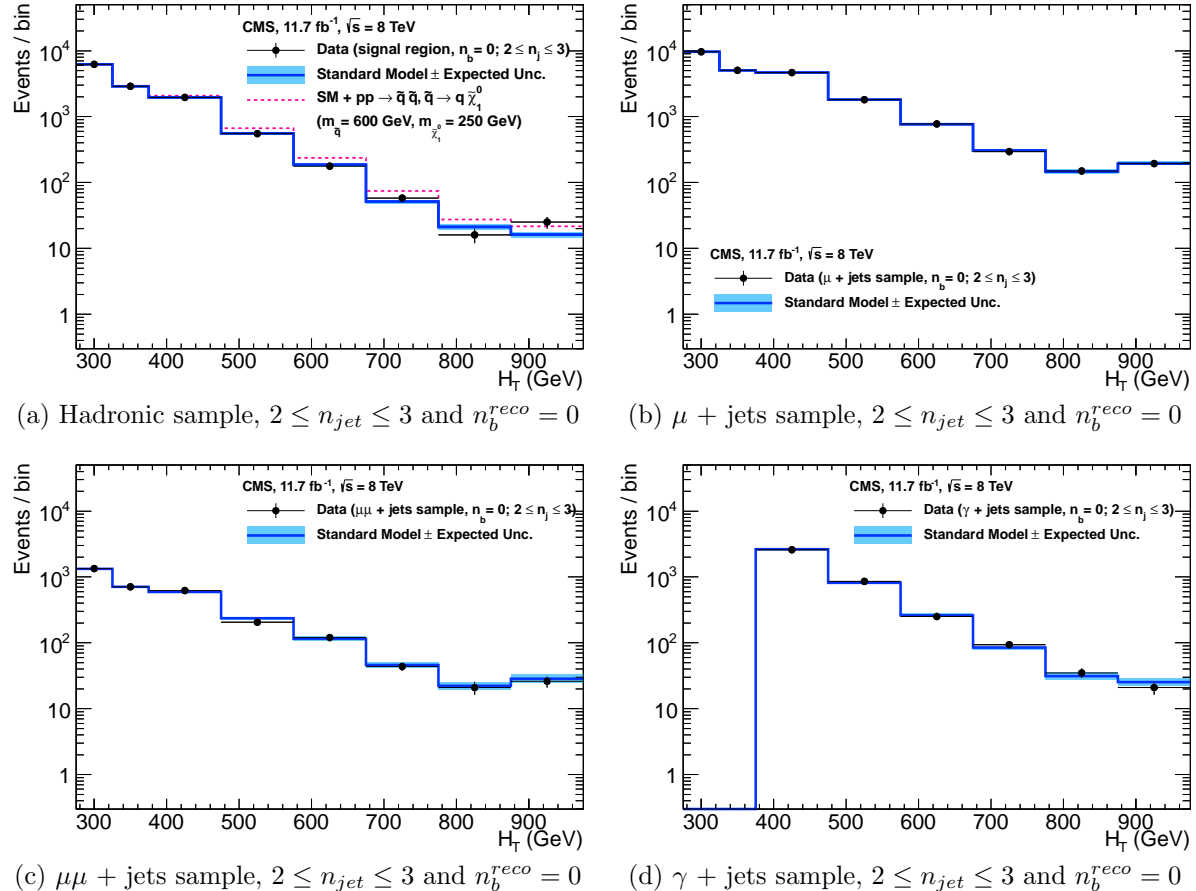


Figure 5.1.: Comparison of the observed yields and SM expectations given by the simultaneous fit in bins of H_T for the (a) hadronic, (b) $\mu +$ jets, (c) $\mu\mu +$ jets and (d) $\gamma +$ jets samples when requiring $n_b^{reco} = 0$ and $n_{jet} \leq 3$. The observed event yields in data (black dots) and the expectations and their uncertainties for all SM processes (blue line with light blue bands) are shown. An example signal expectation (red solid line) for the D1 SMS signal point from Table 4.1 is superimposed on the SM background expectation.

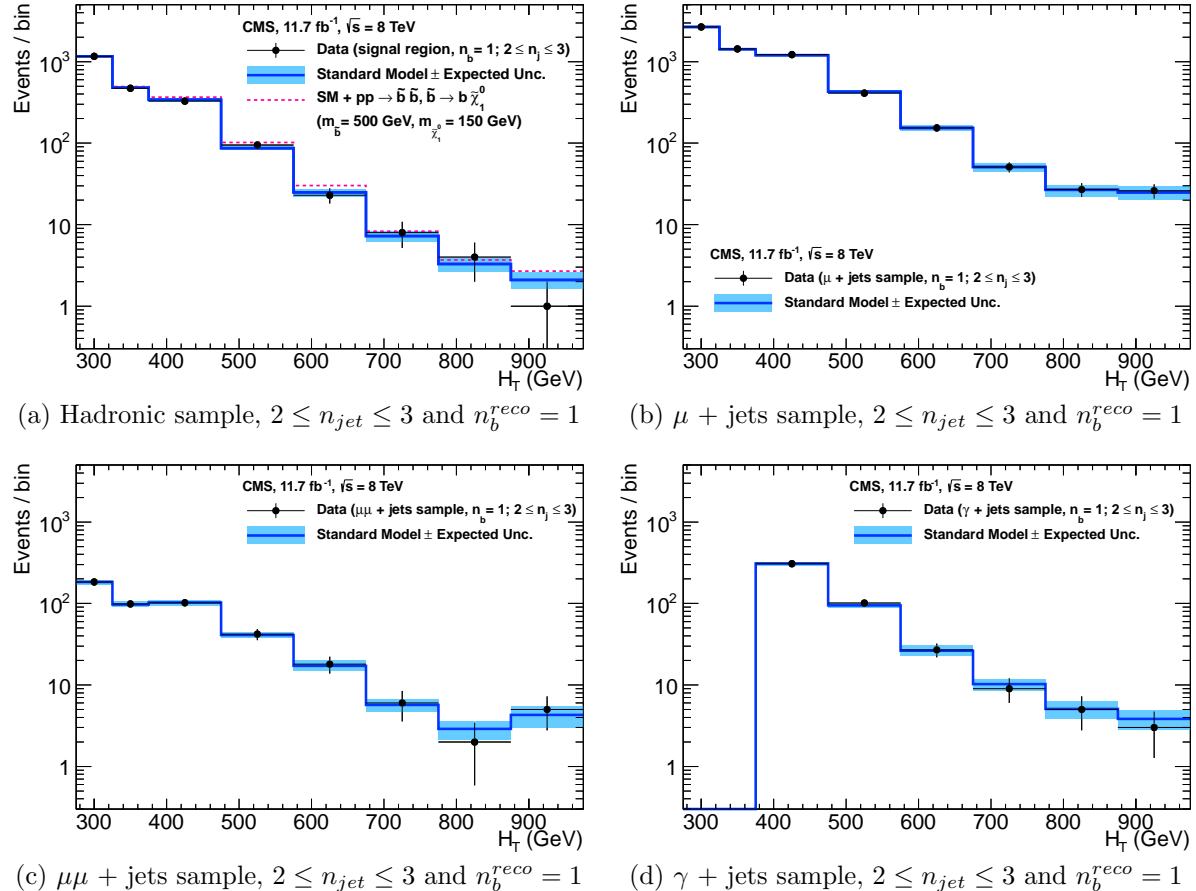


Figure 5.2.: Comparison of the observed yields and SM expectations given by the simultaneous fit in bins of H_T for the (a) hadronic, (b) $\mu +$ jets, (c) $\mu\mu +$ jets and (d) $\gamma +$ jets samples when requiring $n_b^{reco} = 1$ and $n_{jet} \leq 3$. The observed event yields in data (black dots) and the expectations and their uncertainties for all SM processes (blue line with light blue bands) are shown. An example signal expectation (red solid line) for the D2 SMS signal point from Table 4.1 is superimposed on the SM background expectation.

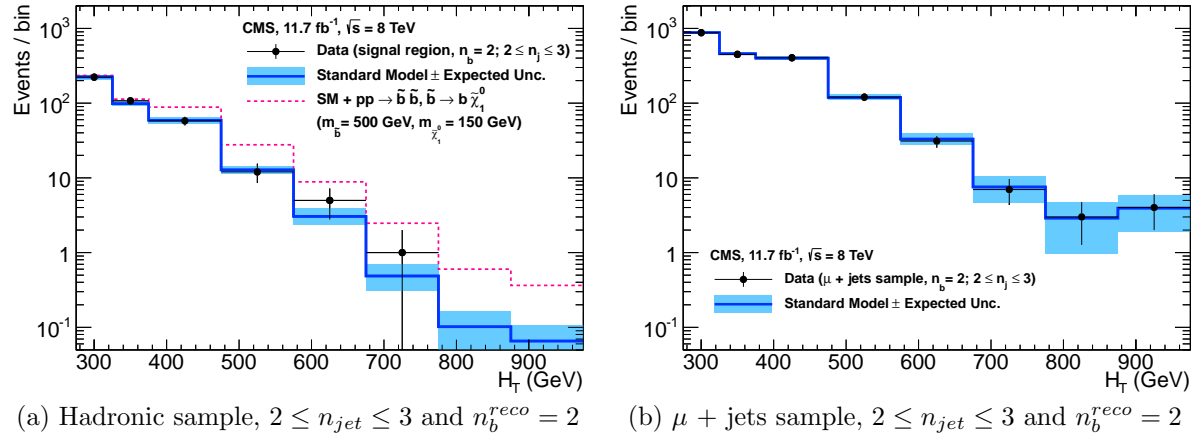


Figure 5.3.: Comparison of the observed yields and SM expectations given by the simultaneous fit in bins of H_T for the (a) hadronic, (b) $\mu +$ jets, (c) $\mu\mu +$ jets and (d) $\gamma +$ jets samples when requiring $n_b^{reco} = 2$ and $n_{jet} \leq 3$. The observed event yields in data (black dots) and the expectations and their uncertainties for all SM processes (blue line with light blue bands) are shown. An example signal expectation (red solid line) for the D2 SMS signal point from Table 4.1 is superimposed on the SM background expectation.

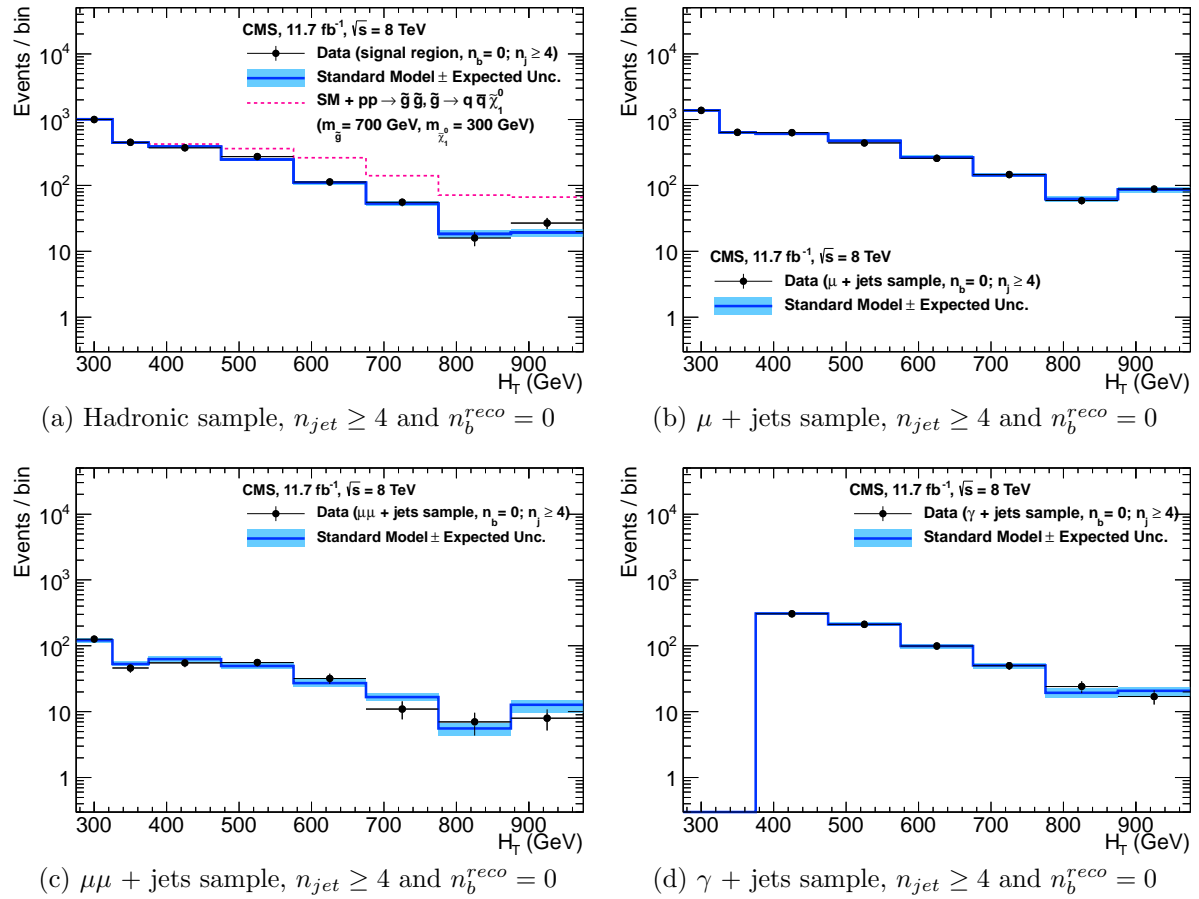


Figure 5.4.: Comparison of the observed yields and SM expectations given by the simultaneous fit in bins of H_T for the (a) hadronic, (b) $\mu +$ jets, (c) $\mu\mu +$ jets and (d) $\gamma +$ jets samples when requiring $n_b^{reco} = 0$ and $n_{jet} \geq 4$. The observed event yields in data (black dots) and the expectations and their uncertainties for all SM processes (blue line with light blue bands) are shown. An example signal expectation (red solid line) for the D2 SMS signal point from Table 4.1 is superimposed on the SM background expectation.

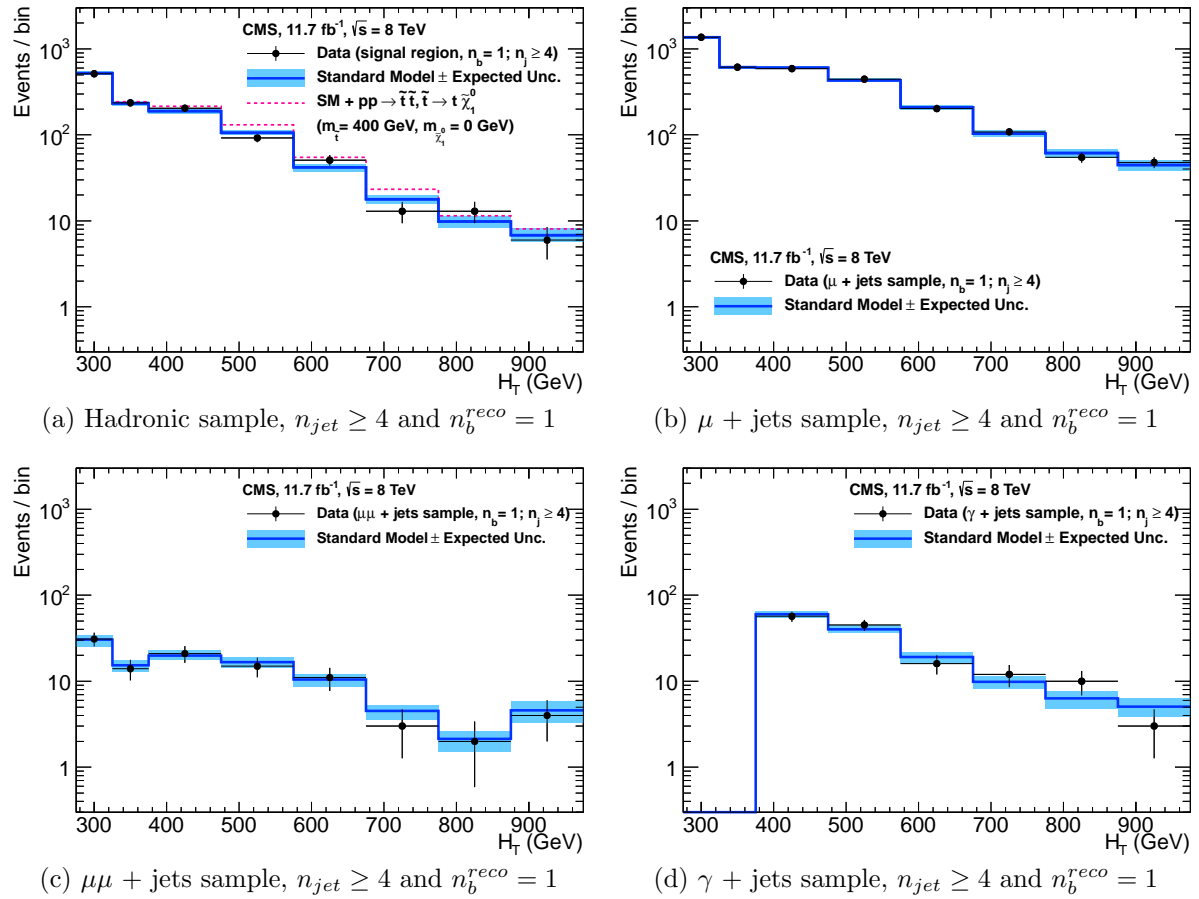


Figure 5.5.: Comparison of the observed yields and SM expectations given by the simultaneous fit in bins of H_T for the (a) hadronic, (b) $\mu +$ jets, (c) $\mu\mu +$ jets and (d) $\gamma +$ jets samples when requiring $n_b^{reco} = 1$ and $n_{jet} \geq 4$. The observed event yields in data (black dots) and the expectations and their uncertainties for all SM processes (blue line with light blue bands) are shown.

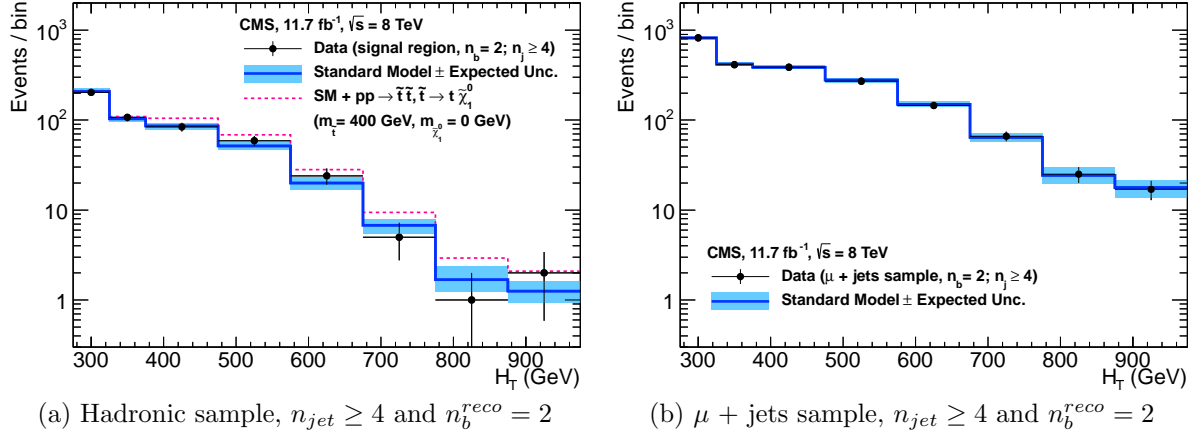


Figure 5.6.: Comparison of the observed yields and SM expectations given by the simultaneous fit in bins of H_T for the (a) hadronic, (b) $\mu +$ jets, (c) $\mu\mu +$ jets and (d) $\gamma +$ jets samples when requiring $n_b^{reco} = 2$ and $n_{jet} \geq 4$. The observed event yields in data (black dots) and the expectations and their uncertainties for all SM processes (blue line with light blue bands) are shown. An example signal expectation (red solid line) for the D3 SMS signal point from Table 4.1 is superimposed on the SM background expectation.

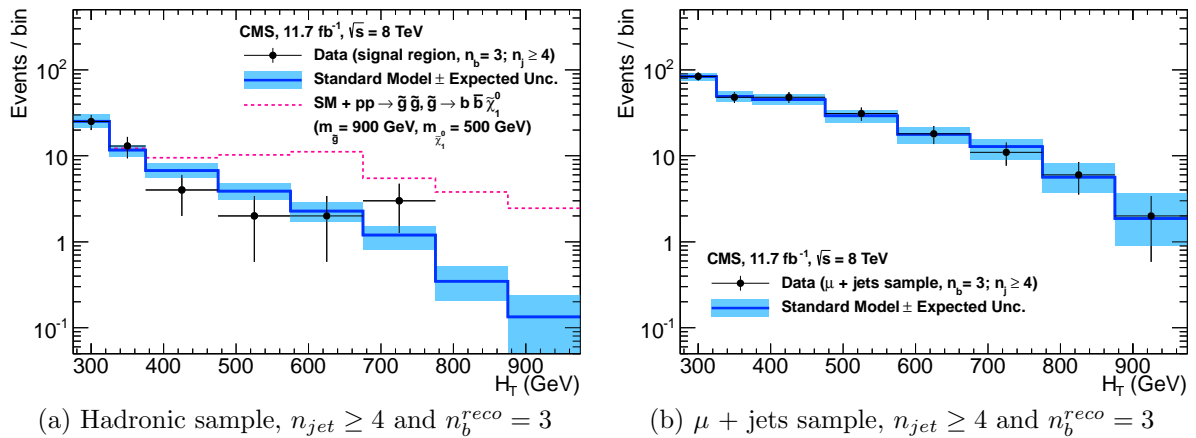


Figure 5.7.: Comparison of the observed yields and SM expectations given by the simultaneous fit in bins of H_T for the (a) hadronic, (b) $\mu +$ jets, (c) $\mu\mu +$ jets and (d) $\gamma +$ jets samples when requiring $n_b^{reco} = 3$ and $n_{jet} \geq 4$. The observed event yields in data (black dots) and the expectations and their uncertainties for all SM processes (blue line with light blue bands) are shown. An example signal expectation (red solid line) for the G2 SMS signal point from Table 4.1 is superimposed on the SM background expectation.

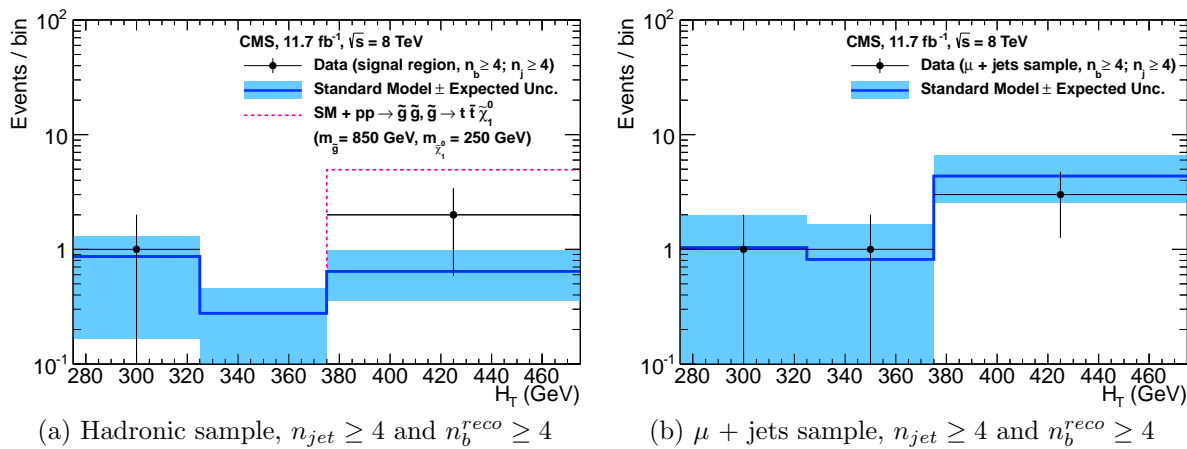


Figure 5.8.: Comparison of the observed yields and SM expectations given by the simultaneous fit in bins of H_T for the (a) hadronic, (b) $\mu +$ jets, (c) $\mu\mu +$ jets and (d) $\gamma +$ jets samples when requiring $n_b^{reco} \geq 4$ and $n_{jet} \geq 4$. The observed event yields in data (black dots) and the expectations and their uncertainties for all SM processes (blue line with light blue bands) are shown. An example signal expectation (red solid line) for the G3 SMS signal point from Table 4.1 is superimposed on the SM background expectation.

2069 **5.2. SUSY**

2070 Limits are set in the parameter space of a set of **SMS** models that characterise both
2071 natural **SUSY** third generation squark production, and compressed spectra where the
2072 mass splitting between the particle and **LSP** is small, leading to soft final state jets.
2073 However as detailed in Section (2.4.1), the individual models are not representative of a
2074 real physical **SUSY** model as only one decay process is considered. Instead these models
2075 represent a way to test for signs of specific signatures indicating new physics.

2076 **5.2.1. The CL_s method**

2077 The CLs method [91][92][93] is used to compute the limits for signal models, with the
2078 one-sided profile likelihood ratio as the test statistic [94].

The test statistic is defined as

$$q(\mu) = \begin{cases} -2\log\lambda(\mu) & \text{when } \mu \geq \hat{\mu}, \\ 0 & \text{otherwise.} \end{cases} \quad (5.1)$$

2079 where

$$\lambda(\mu) = \frac{L(\mu, \theta_\mu)}{L(\hat{\mu}, \hat{\theta})} \quad (5.2)$$

2080 represents the profile likelihood ratio, in which $\mu \equiv f$ from Section (4.8.4), is the
2081 parameter characterising the signal strength. $\hat{\mu}$ is defined at the maximum likelihood
2082 value, $\hat{\theta}$ the set of maximum likelihood values of the nuisance parameters and θ_μ the set
2083 of maximum values of the nuisance parameters for a given value of μ .

2084 When $\mu \equiv f = 1$, the signal model is considered at its nominal production cross section.
2085 The distribution of q_μ is built up via the generation of pseudo experiments in order to
2086 obtain two distributions for the background (B) and signal plus background (S+B) cases.
2087 The compatibility of a signal model with observations in data is determined by the
2088 parameter CL_s ,

$$\text{CL}_S = \frac{\text{CL}_{S+B}}{\text{CL}_B}, \quad (5.3)$$

with CL_B and CL_{S+B} defined as one minus the quantiles of the observed value in the data of the two distributions. A model is considered to be excluded at 95% confidence level when $\text{CL}_s \leq 0.05$ [95].

5.2.2. Interpretation in simplified signal models

Different n_{jet} and n_b^{reco} bins are used in the interpretation of different **SMS** models. The choice of the categories used are made to increase sensitivity to that particular type of final state signature. The production and decay modes of the **SMS** models under consideration are summarised in Table 5.3, with limit plots of the experimental reach in these models shown in Figure 5.10.

The models T1 and T2 are used to characterise the pair production of gluinos and first or second generation squarks, respectively, with parameters for the sparticle mass as well as on the **LSP** mass. The simplified models T2bb, T1tttt, and T1bbbb describe various production and decay mechanisms in the context of third-generation squarks.

Model	Production/decay	n_{jet}	n_b^{reco}	Process	Limit	$m_{\tilde{q}/\tilde{g}}^{\text{best}}$ (GeV)	$m_{\text{LSP}}^{\text{best}}$ (GeV)
T1	$pp \rightarrow \tilde{g}\tilde{g}^* \rightarrow q\bar{q}\tilde{\chi}_1^0 q\bar{q}\tilde{\chi}_1^0$	≥ 4	0	5.9(a)	5.10(a)	~ 950	~ 450
T2	$pp \rightarrow \tilde{q}\tilde{q}^* \rightarrow q\tilde{\chi}_1^0 \bar{q}\tilde{\chi}_1^0$	≤ 3	0	5.9(b)	5.10(b)	~ 775	~ 325
T2bb	$pp \rightarrow \tilde{b}\tilde{b}^* \rightarrow b\tilde{\chi}_1^0 \bar{b}\tilde{\chi}_1^0$	≤ 3	1,2	5.9(c)	5.10(c)	~ 600	~ 200
T1tttt	$pp \rightarrow \tilde{g}\tilde{g}^* \rightarrow t\bar{t}\tilde{\chi}_1^0 t\bar{t}\tilde{\chi}_1^0$	≥ 4	2,3, ≥ 4	5.9(d)	5.10(d)	~ 975	~ 325
T1bbbb	$pp \rightarrow \tilde{b}\tilde{b}^* \rightarrow b\tilde{b}\tilde{\chi}_1^0 b\tilde{b}\tilde{\chi}_1^0$	≥ 4	2,3, ≥ 4	5.9(e)	5.10(e)	~ 1125	~ 650

Table 5.3.: A table representing the **SMS** models interpreted within the analysis. The model name and production and decay chain is specified in the first two columns. Each **SMS** model is interpreted in specific n_{jet} and n_b^{reco} categories which are detailed in the third and fourth columns. The last two columns indicate the search sensitivity for each model, representing the largest $m_{\tilde{q}/\tilde{g}}$ mass beyond which no limit can be set for this particular decay topology. The quotes values are conservatively determined from the observed exclusion based on the theoretical production cross section minus 1σ uncertainty.

Experimental uncertainties on the **SM** background predictions (10 – 30%, Section (4.6.1)), the luminosity measurement (4.4%), and the total acceptance times efficiency of the selection for the considered signal model (12 – 18%, Section (4.7)) are included in the calculation of the limit.

2106 Signal efficiency in the kinematic region defined by $0 < m_{\tilde{g}(\tilde{q})} < 175$ GeV or $m_{\tilde{g}(\tilde{q})} < 300$
2107 GeV is strongly affected by the presence of Initial State Radiation (**ISR**). This region in
2108 which direct (i.e., non-**ISR** induced) production is kinematically forbidden due to the H_T
2109 > 275 GeV requirement, therefore a large percentage of signal acceptance is due to the
2110 effect of **ISR** jets. Given the large associated uncertainties, no interpretation is provided
2111 for this kinematic region.

2112 The estimates on mass limits shown in Table 5.3, are determined conservatively from
2113 the observed exclusion based on the theoretical production cross section, minus 1σ
2114 uncertainty. The most stringent mass limits on pair-produced sparticles are obtained at
2115 low **LSP** masses, while the limits typically weaken for compressed spectra points close to
2116 the diagonal. In particular, for all of the considered **SMS** models, there is an **LSP** mass
2117 beyond which no limit can be set, which can be observed from the figures referenced in the
2118 table.

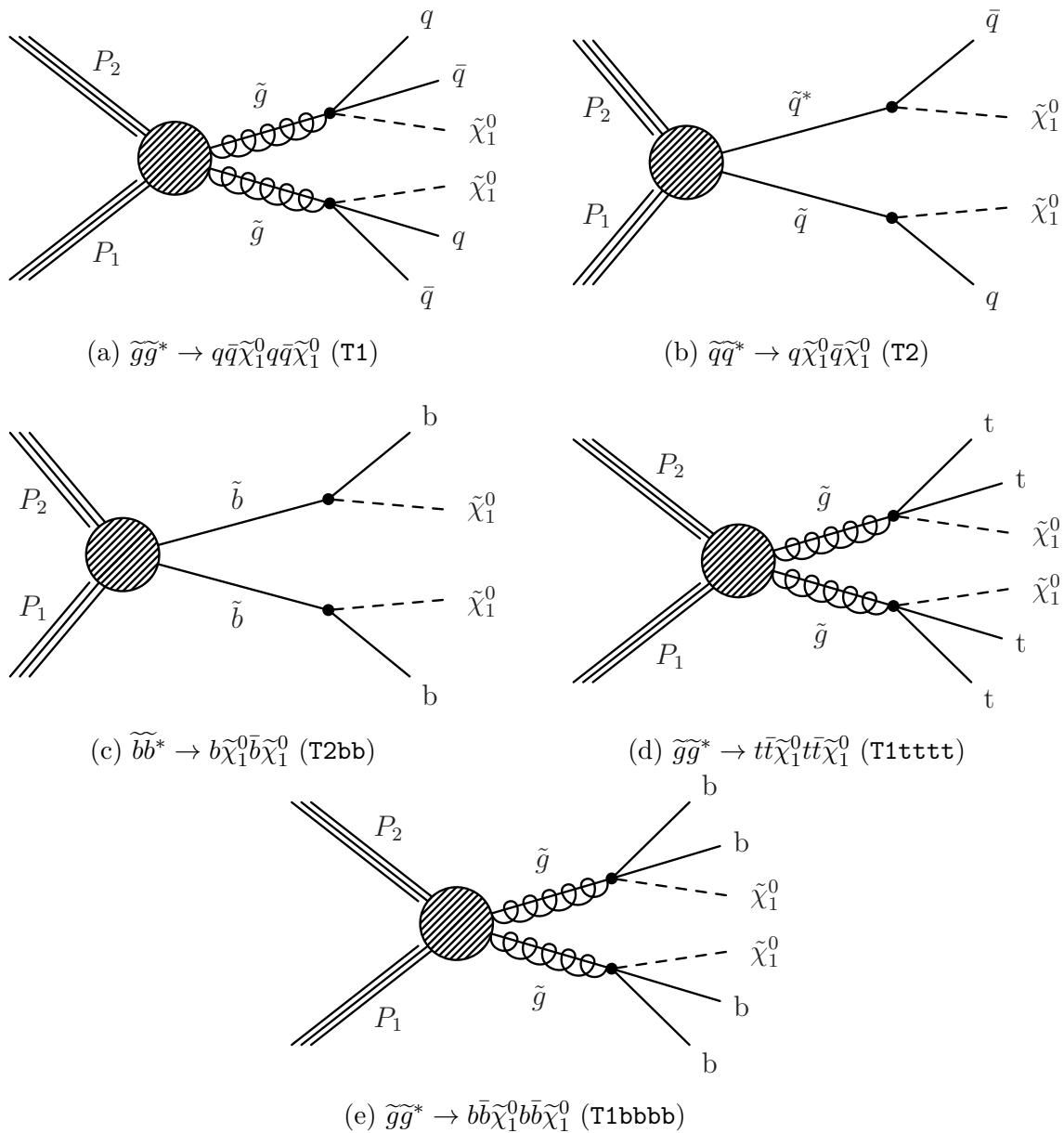


Figure 5.9.: Production and decay modes for the various **SMS** models interpreted within the analysis.

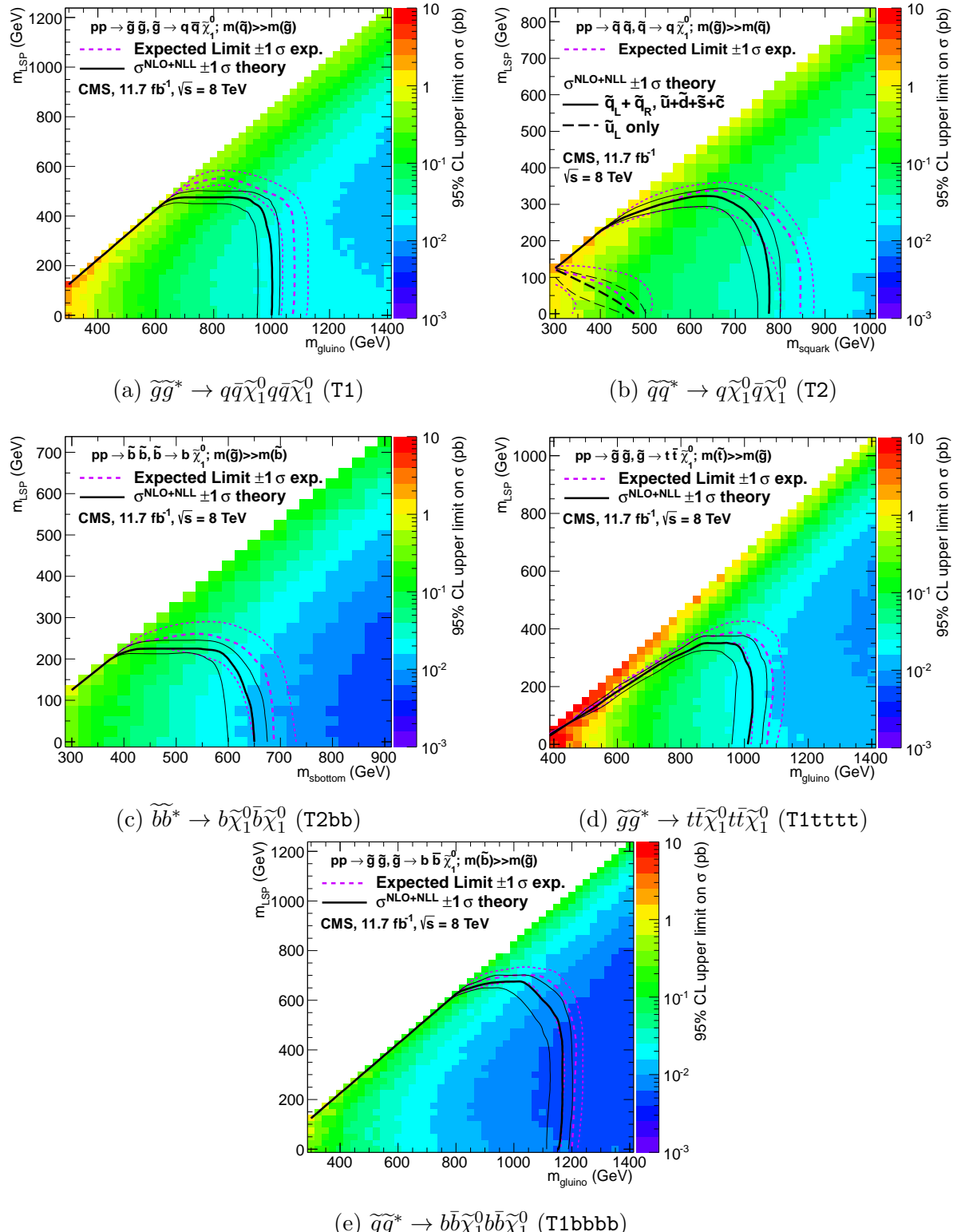


Figure 5.10.: Upper limit of cross section at 95% CL as a function of $m_{\tilde{q}/\tilde{g}}$ and m_{LSP} for various SMS models. The solid thick black line indicates the observed exclusion region assuming NLO and NLL SUSY production cross section. The analysis selection efficiency is measured for each interpreted model, with the signal yield per point given by $\epsilon \times \sigma$. The thin black lines represent the observed excluded region when varying the cross section by its theoretical uncertainty. The dashed purple lines indicate the median (thick line) 1σ (thin lines) expected exclusion regions.

Chapter 6.

²¹¹⁹ Searches For Natural SUSY With ²¹²⁰ B-tag Templates.

²¹²¹ Within this chapter a complimentary technique is discussed as a means to predict the
²¹²² distribution of three and four reconstructed b-quark jets in an event. The recent discovery
²¹²³ of the Higgs boson has made third-generation “Natural SUSY” models attractive, given
²¹²⁴ that light top and bottom squarks are a candidate to stabilise divergent loop corrections
²¹²⁵ to the Higgs boson mass.

²¹²⁶ Using the α_T search as a base, a simple templated fit is employed to estimate the
²¹²⁷ SM background in higher b-tag multiplicities (3-4) from a region of a low number of
²¹²⁸ reconstructed b-jets (0-2). As a proof-of-concept, the procedure after being shown to
²¹²⁹ close in simulation, is applied to the SM enriched $\mu + \text{jets}$ control sample of the α_T
²¹³⁰ all-hadronic search detailed in Chapter 4. To highlight the relative insensitivity of the
²¹³¹ choice of the b-tagging algorithm working points in the effectiveness of the procedure,
²¹³² results are presented using the CSV tagger (introduced in Section (3.3.2)) for the “Loose”,
²¹³³ “Medium” and “Tight” working points.

²¹³⁴ 6.1. Concept

²¹³⁵ The dominant SM backgrounds most SUSY searches are typically $t\bar{t} + \text{jets}$, $W + \text{jets}$ and
²¹³⁶ $Z \rightarrow \nu\bar{\nu} + \text{jets}$. These process are characterised by typically having zero or two underlying
²¹³⁷ b-quarks per event. The first step in this approach is to categorise two templates to be
²¹³⁸ fitted to the low n_b^{reco} multiplicity in terms of these underlying b-quark event topologies.

Typical underlying b-quark content	Process
= 0	$W \rightarrow l\nu + \text{jets}$ $Z \rightarrow \nu\bar{\nu} + \text{jets}$ $Z/\gamma^* \rightarrow \mu\mu + \text{jets}$
= 1	$t + \text{jets}$
= 2	$t\bar{t} + \text{jets}$

Table 6.1.: Typical underlying b-quark content of different SM processes which are common to many SUSY searches.

- 2139 Thus two templates are defined, Z0 and Z2 ($t\bar{t}$ is combined with single top) which
 2140 represent processes which have an underlying b-quark content of zero or two respectively.
- 2141 Both these templates can be generated through the application of the relevant event
 2142 selection and taking the underlying n_b^{reco} distribution directly from simulation. However
 2143 as discussed within Section (4.5), there are large uncertainties for high n_b^{reco} multiplicities
 2144 due to limited MC statistics. This is particularly prominent for the Z0 templates, where
 2145 the number of reconstructed b-tags is driven primarily by the light-quark mis-tagging
 2146 rate. Therefore to improve the statistical precision of the predictions the formula method,
 2147 introduced in Section (4.5.1) is used.
- 2148 The generation of these templates is then dependant upon the jet-flavour content and
 2149 b-tagging rate within the phase space of interest, with the tagging probabilities of a jet
 2150 being a function of the jet p_T , the pseudo-rapidity $|\eta|$, and the jet-flavour. This can be
 2151 observed in Figure 6.1, where the b-tagging / c-quark mis-tagging / light mis-tagging
 2152 efficiency for the three working points of the CSV tagger is shown as a function of jet p_T .
- 2153 Before the templates are generated, the relevant jet p_T and η corrections are applied to
 2154 correct simulation to data, as specified in Section (4.5.3), to then determine the average
 2155 tagging rates per analysis bin.
- 2156 These two templates are then fit to data in the low n_b^{reco} region (0-2). The fit result is
 2157 used, along with the knowledge of the template shapes, to extrapolate an estimate to the
 2158 high n_b^{reco} signal region (3,4), which is then compared to what is observed in data.
- 2159 This method can, in principle, be applied to any analysis where the signal hypothesis
 2160 has a larger underlying b-quark spectra than the SM backgrounds, as it solely relies on
 2161 fitting to the shape of the n_b^{reco} distribution.

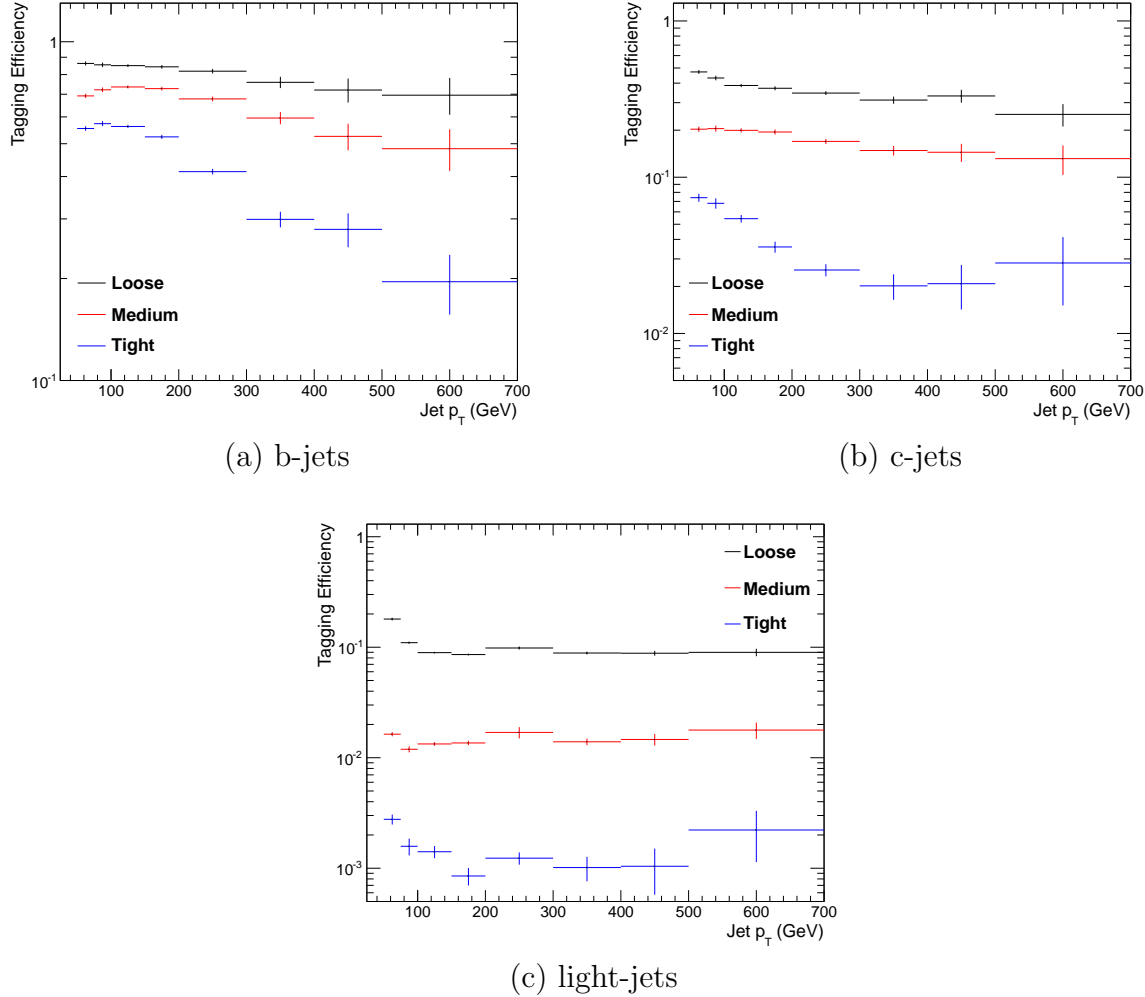


Figure 6.1.: The b-tagging (a), c-quark mis-tagging (b), and light-quark mis-tagging rate (c) as measured in simulation after the α_T analysis, $\mu + \text{jets}$ control sample selection in the region $H_T > 375$.

2162 6.2. Application to the α_T Search

2163 As detailed in the previous chapter, the α_T analysis is a search for **SUSY** particles
 2164 in all-hadronic final states, utilising the kinematic variable α_T to suppress QCD to a
 2165 negligible level. **SM** enriched control samples are used to estimate the background within
 2166 an all-hadronic signal region.

2167 The selection for the $\mu + \text{jets}$ control samples defined in Section (4.2.3) is used to
 2168 demonstrate the template fitting procedure both conceptually in simulation, and also
 2169 when applied in data. This is chosen, as such a selection is dominated by events stemming
 2170 from the **SM** processes with little or no signal contamination from potential new physics..

2171 Neither are contributions from rate SM processes with a higher underlying b-quark
2172 content (e.g. $t\bar{t}b\bar{b}$) expected. For these reasons, there is a degree of confidence that the
2173 procedure should close when applied to this phase space.

2174 The analysis presented here is binning in source jet multiplicity bins, of 3,4 and ≥ 5
2175 reconstructed jets per event (di-jet events are not included as there is no contribution
2176 to the high n_b^{reco} region (3,4)) , in order to reduce the kinematic jet p_T dependence.
2177 Furthermore the analysis is split into three H_T regions,

2178 • 275-325 GeV

2179 • 325-375 GeV

2180 • > 375 GeV

2181 contrary to the eight used within the α_T analysis. Templates for both underlying b-quark
2182 content hypotheses are then generated for the nine defined analysis bins.

2183 6.2.1. Proof of principle in simulation

2184 In order to demonstrate that the template procedure produces accurate predictions
2185 within simulation, the simulation samples in the analysis are firstly split into two to allow
2186 for statistically independent fits to be performed.

2187 By combining the relevant ingredients necessary to employ the formula method, n_b^{reco}
2188 templates for $Z = 0$ and $Z= 2$ are generated individually for each n_{jet} and H_T bin using
2189 one half of each simulation sample. A fit of these two templates is then performed in the
2190 low n_b^{reco} (0-2) region, back to the sum of the other halves of each simulation sample in
2191 order to check that the relevant information can be recovered in the n_b^{reco} signal region
2192 (3-4).

2193 The fits are performed independently within each of the defined analysis bins to reduce the
2194 dependence of the shapes of these distributions on simulation. The half of the simulation
2195 sample for which the templates are fitted too, are taken directly from simulation, extending
2196 this procedure to also be a validation of the formula method to accurately estimate
2197 the n_b^{reco} distribution. Additionally as this test is performed in simulation, the relevant
2198 corrections of the b-tagging rates between data and simulation are *not* applied.

2199 Within Figure 6.2, the results of this fitting procedure is shown for each CSV working
2200 point. Results are presented for the $n_{jet} \geq 5$ category, using the $\mu +$ jets control sample

2201 selection in the inclusive $H_T > 375$ GeV analysis bin. The grey bands represent the
 2202 statistical uncertainty on the template shapes. Additional fits are shown for other n_{jet}
 2203 category within Appendix D.1.

2204 Furthermore the extrapolated fit predictions within the high n_b^{reco} signal region, are
 2205 summarised for all H_T bins and working points in Table 6.2.

H_T	275-325	325-375	>375
Loose working point			
Simulation $n_b = 3$	793.0 ± 14.8	387.9 ± 10.2	794.1 ± 14.34
Template $n_b = 3$	820.4 ± 26.7	376.3 ± 11.9	780.1 ± 15.1
Simulation $n_b = 4$	68.2 ± 3.9	27.6 ± 2.7	91.28 ± 4.9
Template $n_b = 4$	72.5 ± 4.7	28.25 ± 2.34	84.4 ± 3.8
Medium working point			
Simulation $n_b = 3$	133.7 ± 5.7	74.5 ± 4.5	164.2 ± 6.4
Template $n_b = 3$	132.8 ± 4.8	74.5 ± 3.9	159.9 ± 5.7
Simulation $n_b = 4$	1.6 ± 0.6	0.6 ± 0.4	3.4 ± 0.9
Template $n_b = 4$	1.8 ± 0.2	1.1 ± 0.2	4.1 ± 0.4
Tight working point			
Simulation $n_b = 3$	26.9 ± 2.6	13.9 ± 1.9	31.8 ± 2.9
Template $n_b = 3$	24.7 ± 1.5	13.8 ± 1.2	28.1 ± 1.5
Simulation $n_b = 4$	0.5 ± 0.4	-	-
Template $n_b = 4$	0.1 ± 0.1	0.1 ± 0.1	0.2 ± 0.1

Table 6.2.: Summary of the fit predictions in the n_b^{reco} signal region for $n_{jet} = 3, = 4, \geq 5$. The fit region is $n_b^{reco} = 0, 1, 2$ and simulation yields are normalised to an integrated luminosity of 10 fb^{-1} . The uncertainties quoted on the template yields are purely statistical.

2206 The pull distributions for all the fits performed can be found in Appendix D.2, and
 2207 are compatible with a mean of zero and standard deviation of one. The good overall
 2208 agreement summarised in the table validates both the formula method used to generate
 2209 the templates as well as the fitting procedure itself. The application of this method to
 2210 the same selection in a data control sample, is now used to demonstrate necessary control
 2211 over the efficiency and mis-tagging rates when b-tagging scale factors are applied.

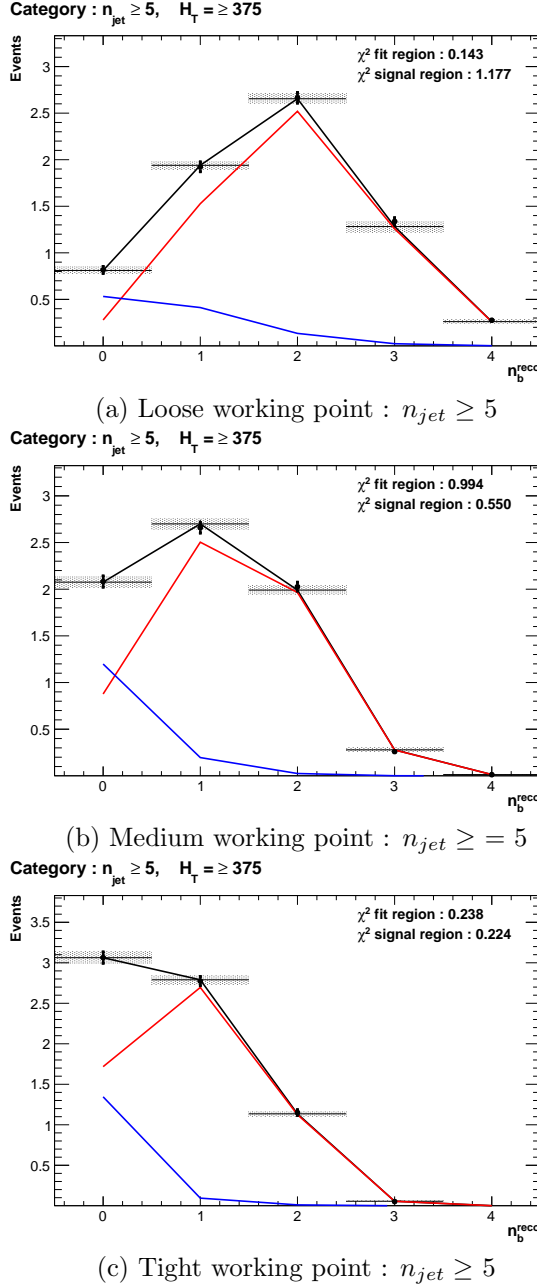


Figure 6.2.: The results of fitting the $Z = 0$ and $Z = 2$ templates to the $n_b^{reco} = 0, 1, 2$ bins taken directly from simulation in the region $H_T > 375$ GeV, for the $n_{jet} \geq 5$ category. The blue template represents $Z = 0$, while the red template represents $Z = 2$. Grey bands represent the statistical uncertainty of the fit. The χ^2 parameter displayed represents the goodness of fit to the low n_b^{reco} (0-2) control region.

6.2.2. Results in a data control sample

The method above is now applied to the 2012 8 TeV dataset in the $\mu +$ jets control sample, to establish the validity of this method in data. The relevant data to simulation scale factors are applied to get corrected values of the efficiency and mis-tagging rates measured in data [64] [86].

Figure 6.3 show the the results of the templates derived from simulation to each of the three defined H_T bins, in the $n_{jet} \geq 5$ category for the medium working point CSV tagger (the same working point used within the α_T analysis). Grey bands represent the statistical uncertainty of the fit combined in quadrature with the systematic uncertainties of varying the data to simulation scale factors up and down by their measured systematic uncertainties. Additional fit results for other jet multiplicities are found in Appendix D.3

The numerical results and extrapolation to the $n_b^{reco} = 3, 4$ bins for all H_T and working points is shown in Table 6.3.

H_T	275-325	325-375	>375
Loose working point			
Data $n_b = 3$	838	394	717
Template $n_b = 3$	861.8 ± 16.7	372.1 ± 10.1	673.2 ± 14.1
Data $n_b = 4$	81	43	81
Template $n_b = 4$	74.5 ± 2.3	27.6 ± 1.2	71.6 ± 2.6
Medium working point			
Data $n_b = 3$	137	79	152
Template $n_b = 3$	131.2 ± 2.3	65.1 ± 1.7	127.8 ± 2.4
Data $n_b = 4$	1	1	3
Template $n_b = 4$	1.8 ± 0.1	0.9 ± 0.1	3.1 ± 0.1
Tight working point			
Data $n_b = 3$	24	15	25
Template $n_b = 3$	23.0 ± 0.4	10.9 ± 0.3	20.3 ± 0.5
Data $n_b = 4$	0	0	1
Template $n_b = 4$	0.1 ± 0.1	0.1 ± 0.1	0.2 ± 0.1

Table 6.3.: Summary of the fit predictions in the n_b^{reco} signal region of the $\mu +$ jets control sample, for $n_{jet} = 3, = 4, \geq 5$. The fit region is $n_b^{reco} = 0, 1, 2$ using 11.4 fb^{-1} of data at $\sqrt{s} = 8\text{TeV}$. The uncertainties quoted on the template yields are purely statistical.

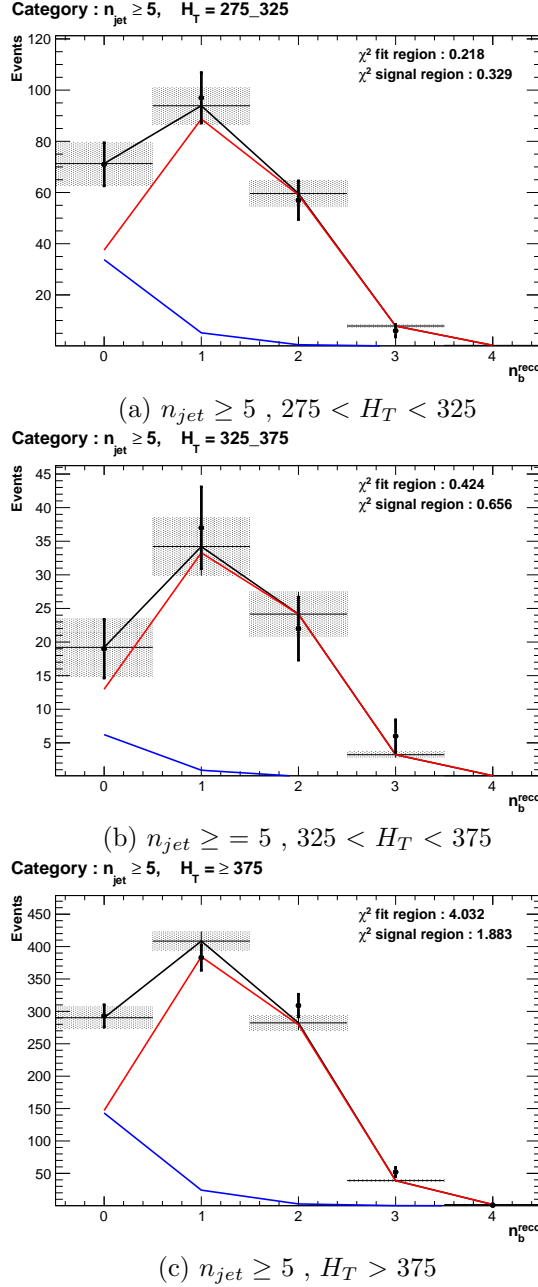


Figure 6.3.: The results of fitting the $Z = 0$ and $Z = 2$ templates to the $n_b^{reco} = 0, 1, 2$ bins taken directly from data, for the $n_{jet} \geq 5$ category and medium CSV working point. The blue template represents $Z = 0$, while the red template represents $Z = 2$. The χ^2 parameter displayed represents the goodness of fit to the low n_b^{reco} (0-2) control region.

2225 The agreement for all working points demonstrates a good control of the b-tagging
 2226 efficiency and mis-tagging rates and gives confidence in the method outlined.

6.2.3. Application to the α_T hadronic search region

As an accompaniment to the background estimation methods outlined by the α_T search.
 The b-tag template method offers a complimentary way of testing the SM only background of the hadronic signal region of the search. In the absence presence of a natural SUSY signature, containing four underlying b or t quarks, the number of reconstructed three/four b-tagged events will be enhanced.
 Figure 6.4 show the the results of the templates derived from simulation to each of the three CSV working points, in the $n_{jet} \geq 5$, $H_T > 375$ GeV category. Grey bands represent the statistical uncertainty of the fit combined in quadrature with the systematic uncertainties of varying the data to simulation scale factors up and down by their measured systematic uncertainties. Additional fit results for other jet multiplicities are found in Appendix D.4
 The numerical results and extrapolation to the $n_b^{reco} = 3, 4$ bins for all H_T and working points is shown in Table 6.4. No excess of data is found and predictions from this method are found to be compatible with the α_T maximum likelihood fit results from Table 5.2.

H_T	275-325	325-375	>375
Loose working point			
Data $n_b = 3$	198	85	126
Template $n_b = 3$	207.1 ± 9.0	103.4 ± 5.9	124.98 ± 7.4
Data $n_b = 4$	15	9	16
Template $n_b = 4$	15.9 ± 1.2	8.05 ± 0.9	13.1 ± 1.3
Medium working point			
Data $n_b = 3$	28	15	12
Template $n_b = 3$	24.4 ± 0.9	12.7 ± 0.8	19.9 ± 2.4
Data $n_b = 4$	1	0	2
Template $n_b = 4$	0.3 ± 0.2	0.3 ± 0.1	0.5 ± 0.1
Tight working point			
Data $n_b = 3$	5	2	0
Template $n_b = 3$	4.03 ± 0.2	2.4 ± 0.2	3.1 ± 0.2
Data $n_b = 4$	1	0	0
Template $n_b = 4$	0.1 ± 0.1	0.1 ± 0.1	0.0 ± 0.1

Table 6.4.: Summary of the fit predictions in the n_b^{reco} signal region of the $\mu +$ jets control sample, for $n_{jet} = 3, 4, \geq 5$. The fit region is $n_b^{reco} = 0, 1, 2$ using 11.7 fb^{-1} of data at $\sqrt{s} = 8\text{TeV}$. The uncertainties quoted on the template yields are purely statistical.

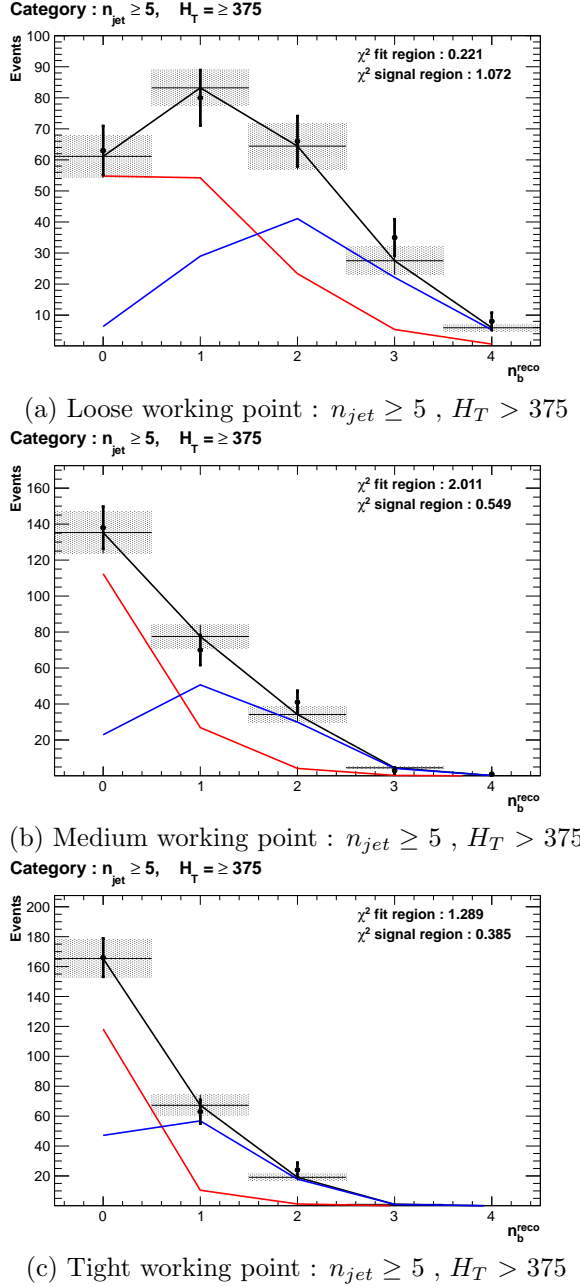


Figure 6.4.: The results of fitting the $Z = 0$ and $Z = 2$ templates to the $n_b^{reco} = 0, 1, 2$ bins taken from data, in the $n_{jet} \geq 5$ and $H_T > 375$ category for all CSV working points. The blue template represents $Z = 0$, while the red template represents $Z = 2$. The χ^2 parameter displayed represents the goodness of fit to the low n_b^{reco} (0-2) control region.

2242 6.3. Summary

2243 A **SUSY** signature such as one from gluino-induced third-generation squark production,
2244 would result in a final state with an underlying b-quark content greater than two. In
2245 order to be able to discriminate such signatures from the **SM** background, templates are
2246 generated based on a parameterisation of the number of the **SM** processes, where the
2247 underlying b-quarks per event is typically zero or two. These templates are then fit to
2248 data in a low n_b^{reco} (0-2) control region in order to extrapolate a prediction in a high
2249 n_b^{reco} (3-4) signal region.

2250 The method was demonstrated both in simulation and also in data, using the **SM** enriched
2251 $\mu + \text{jets}$ selection from the α_T search, to prove conceptually and experimentally that the
2252 method works and there is adequate control over the efficiency and mis-tagging rates in
2253 data for all working points of the **CSV** tagger. Additionally this method was also applied
2254 to the α_T analysis signal region where good agreement is observed between data and the
2255 background estimation method of the α_T analysis.

Chapter 7.

²²⁵⁶ Conclusions

²²⁵⁷ A search for supersymmetry is presented based on a data sample of pp collisions collected
²²⁵⁸ at $\sqrt{s} = 8$ TeV, corresponding to an integrated luminosity of 11.7 ± 0.5 fb⁻¹. Final
²²⁵⁹ states with two or more jets and significant \cancel{E}_T , a typical final state topology of R-parity
²²⁶⁰ conserving SUSY models have been analysed. The sum of standard model backgrounds
²²⁶¹ per bin are estimated from a simultaneous binned likelihood fit to hadronic, $\mu +$ jets,
²²⁶² $\mu\mu +$ jets, and $\gamma +$ jets samples. Systematic errors due to theory, detector effects and
²²⁶³ analysis choices are quantified through the use of data driven closure tests and accounted
²²⁶⁴ for in the final interpretation.

²²⁶⁵ No excess of events is observed over the expected SM background. The analysis is
²²⁶⁶ further interpreted in a set of SMS models, with a special emphasis on third generation
²²⁶⁷ squarks and compressed spectra scenarios. In the considered models with gluino pair
²²⁶⁸ production and for small LSP masses, exclusion limits of the gluino mass are in the range
²²⁶⁹ 950-1125 GeV. For SMS with squark pair production, first or second generation squarks
²²⁷⁰ are excluded up to around 775 GeV and bottom squarks are excluded up to 600 GeV,
²²⁷¹ again for small LSP masses.

²²⁷² A complementary approach using a templated method to estimate the b-tag jet distribu-
²²⁷³ tion of SM processes, is used to search for gluino induced third generation squark SUSY
²²⁷⁴ production. The α_T analysis is used to demonstrate conceptually and experimentally
²²⁷⁵ this technique in the $\mu +$ jets control sample. This method is further applied to the
²²⁷⁶ α_T hadronic search region where good agreement is observed between the data and the
²²⁷⁷ background estimation procedure of the α_T analysis.

²²⁷⁸ The performance of the Level-1 trigger for jets and energy sum quantities is also presented.
²²⁷⁹ These studies quantify any change in level-1 performance after the introduction of a 5

₂₂₈₀ GeV jet seed threshold into the jet algorithm configuration. No significant change in
₂₂₈₁ single jet trigger efficiencies is observed and good performance is observed for a range of
₂₂₈₂ level-1 quantities.

₂₂₈₃

Appendix A.

²²⁸⁴ Miscellaneous

²²⁸⁵ A.1. Jet Identification Criteria

²²⁸⁶ For Calo jets the following criteria were applied:

Loose CaloJet Id	
Variable	Definition
$f_{HPD} < 0.98$	Fraction of jet energy contributed from “hottest” HPD , which rejects HCAL noise.
$f_{EM} > 0.01$	Noise from the HCAL is further suppressed by requiring a minimal electromagnetic component to the jet f_{EM} .
$N_{hits}^{90} \geq 2$	Jets that have $> 90\%$ of its energy from a single channel are rejected, to serve as a safety net that catches jets arising from undiagnosed noisy channels.

Table A.1.: Criteria for a reconstructed jet to pass the loose calorimeter jet id.

²²⁸⁷ For PF jets the following criteria were applied:

Loose PF jet Id	
Variable	Definition
<code>nfhJet < 0.99</code>	Fraction of jet composed of neutral hadrons. HCAL noise tends to populate high values of neutral hadron fraction.
<code>nemfJet < 0.99</code>	Fraction of jet composed of neutral electromagnetic energy. ECAL noise tends to populate high values of neutral EM fraction.
<code>nmultiJet > 1</code>	Number of constituents that jet is composed from.
<code>chfJet > 0</code>	Fraction of jet composed of charged hadrons.
<code>cmultiJet > 0</code>	Number of charged particles that compose jet.
<code>cemfJet < 0.99</code>	Fraction of jet composed of charged electromagnetic energy.

Table A.2.: Criteria for a reconstructed jet to pass the loose PF jet id.

2288 A.2. Primary Vertices

2289 The pileup per event is defined by the number of 'good' reconstructed primary vertices
2290 in the event, with each vertex satisfying the following requirements

Good primary vertex requirement	
Variable	Definition
$N_{dof} > 4$	The number of degree of freedom, from the vertex fit to compute the best estimate of the vertex parameters.
$ \Delta z_{vtx} < 24\text{cm}$	The distance, $ \Delta z_{vtx} $, to the position of the closest HLT primary vertex.
$\rho < 2\text{cm}$	The perpendicular distance of track position to the beam spot.

Table A.3.: Criteria for a vertex in an event to be classified as a 'good' reconstructed primary vertex.

Appendix B.

²²⁹¹ L1 Jets

²²⁹² B.1. Jet matching efficiencies

²²⁹³ The single jet turn-on curves are derived from events independent of whether the leading
²²⁹⁴ jet in an event is matched to a Level 1 jet using ΔR matching detailed in Section (3.4.3)
²²⁹⁵ or not. These turn-ons are produced from events which are not triggered on jet quantities
²²⁹⁶ and therefore it is not guaranteed that the lead jet of an event will be seeded by a Level
²²⁹⁷ 1 jet. Figure B.1 shows the particular matching efficiency of a lead jet to a L1 jet.

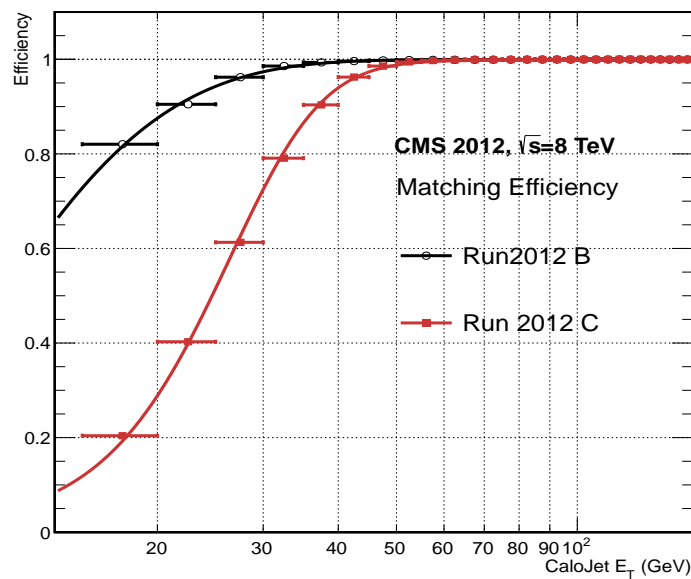


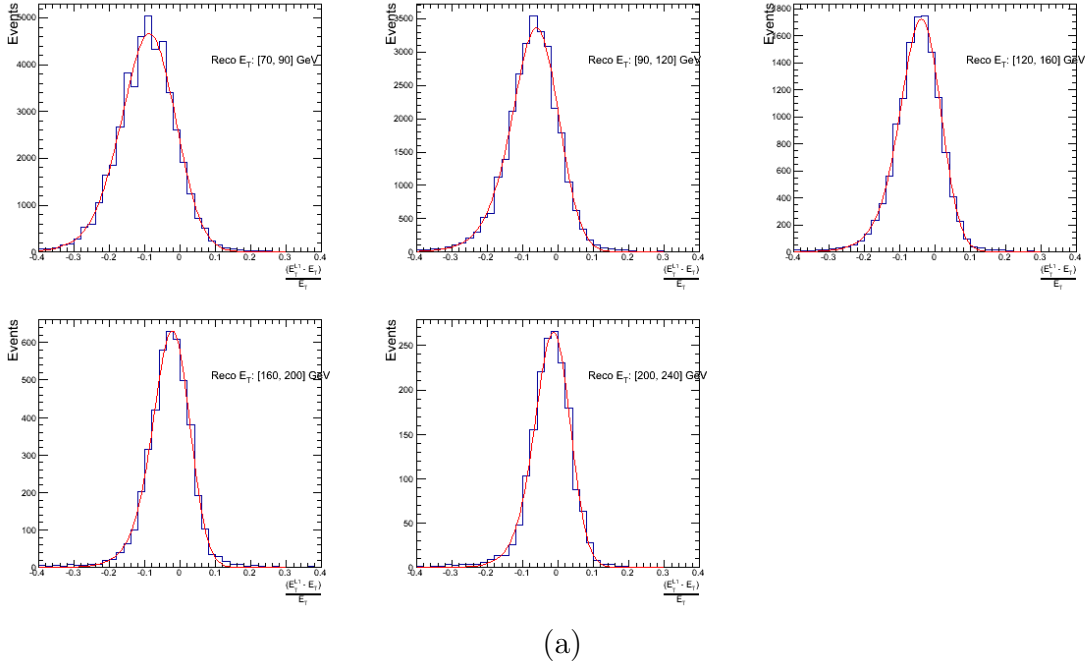
Figure B.1.: Leading jet matching efficiency as a function of the offline CaloJet E_T , measured in an isolated muon triggered dataset in the 2012B and 2012C run periods.

Run Period	μ	σ
2012B	6.62 ± 0.01	0.79 ± 0.03
2012C	19.51 ± 0.03	7.14 ± 0.02

Table B.1.: Results of a cumulative EMG function fit to the turn-on curves for the matching efficiency of the leading jet in an event to a Level-1 jet in run 2012C and 2012B data, measured in an isolated muon triggered sample. The turn-on point, μ , and resolution, σ , are measured with respect to offline Calo Jet E_T .

- 2298 It can be seen that the turn on is sharper during the 2012B run period. The seed
 2299 threshold requirement of a 5 GeV jet seed in run 2012C results in more events in which
 2300 even the lead offline jet does not have an associated L1 jet. For larger jet E_T thresholds,
 2301 typical of thresholds used in physics analyses, 100% efficiency is observed.
 2302 The matching efficiencies have a μ values of 6.62 GeV and 19.51 GeV for Run 2012B
 2303 and 2012C respectively and is shown in Table B.1.

2304 B.2. Leading Jet Energy Resolution



(a)

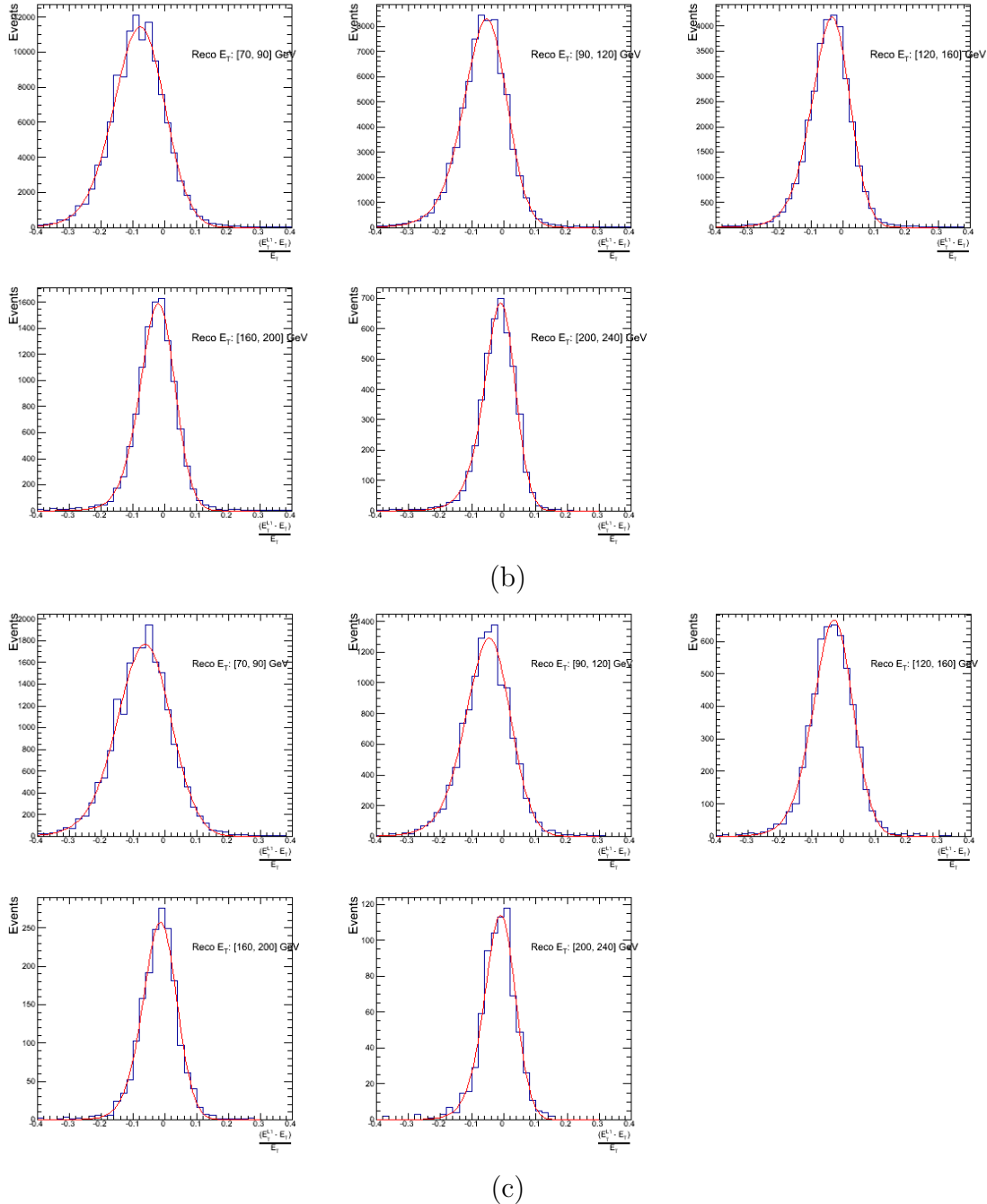
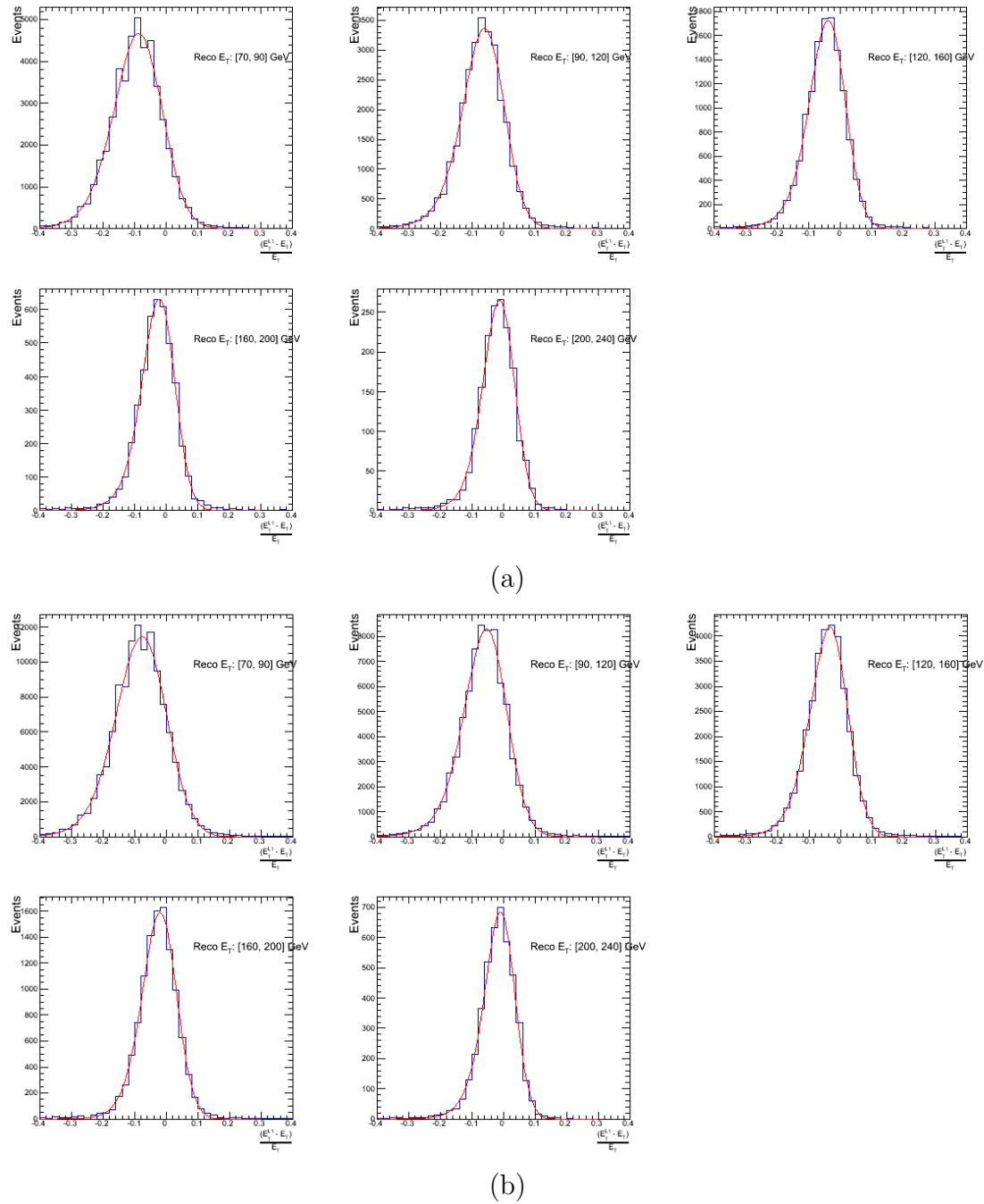
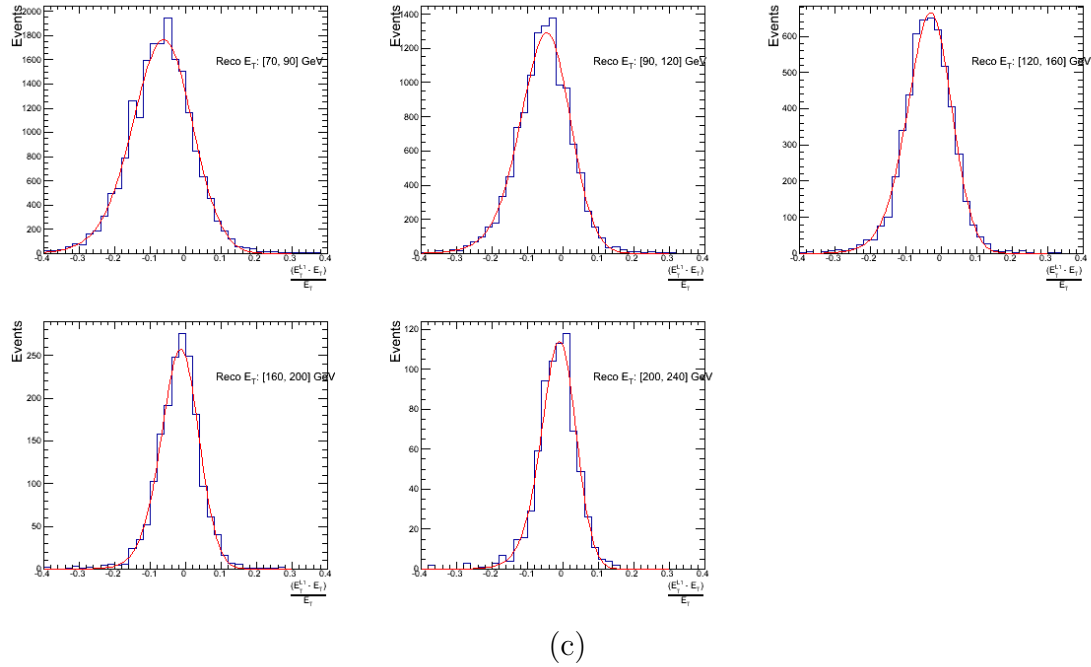


Figure B.2.: Resolution plots of the leading offline jet Calo E_T measured as a function of $\frac{(L1\ E_T - \text{Offline}\ E_T)}{\text{Offline}\ E_T}$ for low (a), medium (b) and high (c) pile-up conditions.





(c)

Figure B.3.: Resolution plots of the leading offline jet PF E_T measured as a function of $\frac{(\text{L1 } E_T - \text{Offline } E_T)}{\text{Offline } E_T}$ for low (a), medium (b) and high (c) pile-up conditions.

2305 B.3. Resolution for Energy Sum Quantities

2306 The following plots show the resolution parameters for the four energy sum quantities as
 2307 a function of the quantity (q) itself. In this case, The mean and RMS of the individual
 2308 $\frac{(\text{L1 } q - \text{Offline } q)}{\text{Offline } q}$ distributions, in bins of the quantity q is displayed.

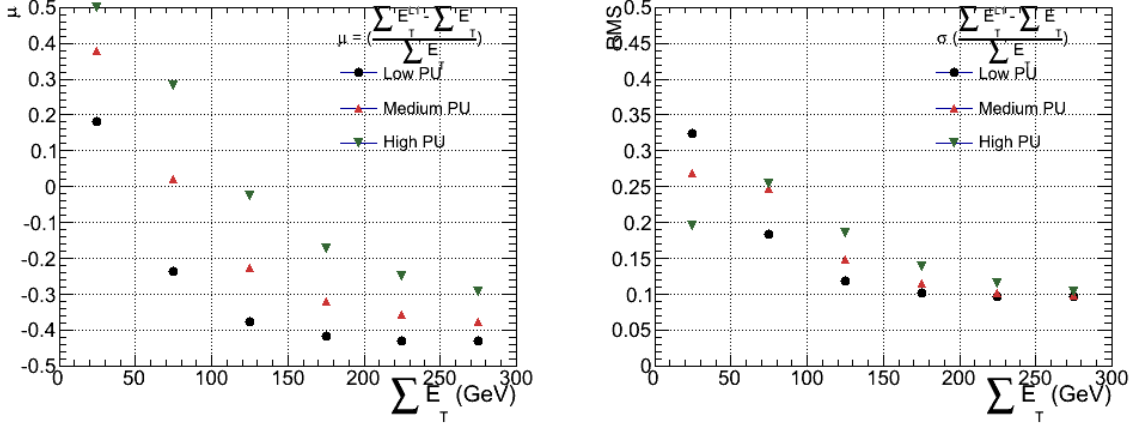


Figure B.4.: $\sum E_T$ resolution parameters in bins of Calo $\sum E_T$ measured for the defined low, medium and high pile up conditions. The plots show the mean μ (left), resolution σ (RMS) of the $\frac{\Delta q}{q}$ distributions.

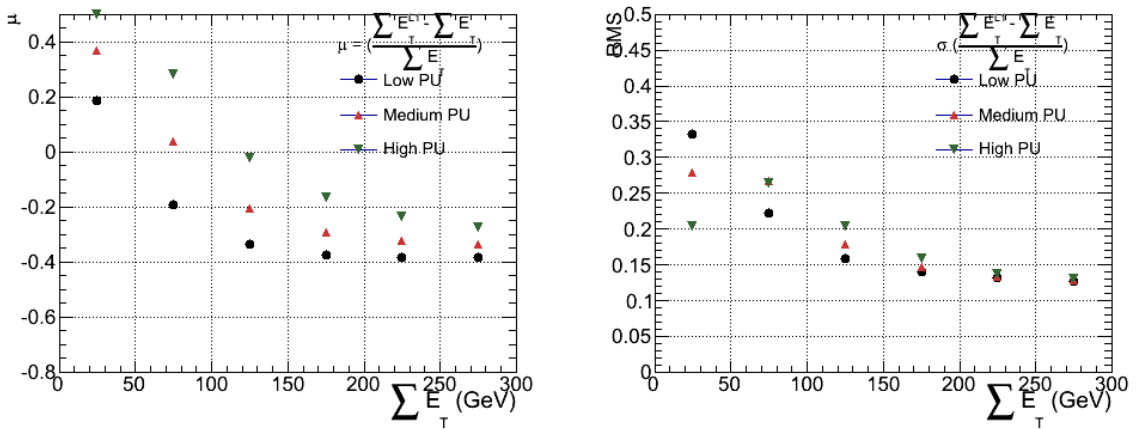


Figure B.5.: $\sum E_T$ resolution parameters in bins of PF $\sum E_T$ measured for the defined low, medium and high pile up conditions. The plots show the mean μ (left), resolution σ (RMS) of the $\frac{\Delta q}{q}$ distributions.

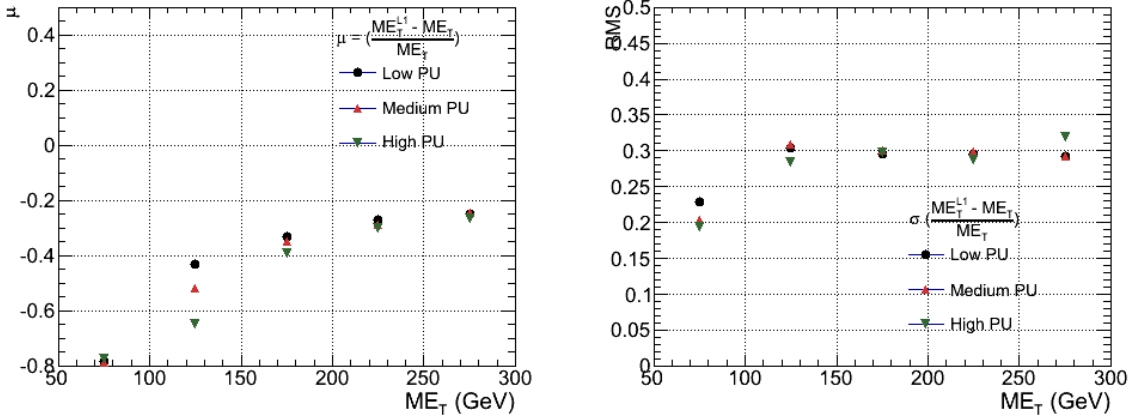


Figure B.6.: \mathcal{E}_T resolution parameters in bins of Calo \mathcal{E}_T measured for the defined low, medium and high pile up conditions. The plots show the mean μ (left), resolution σ (RMS) of the $\frac{\Delta q}{q}$ distributions.

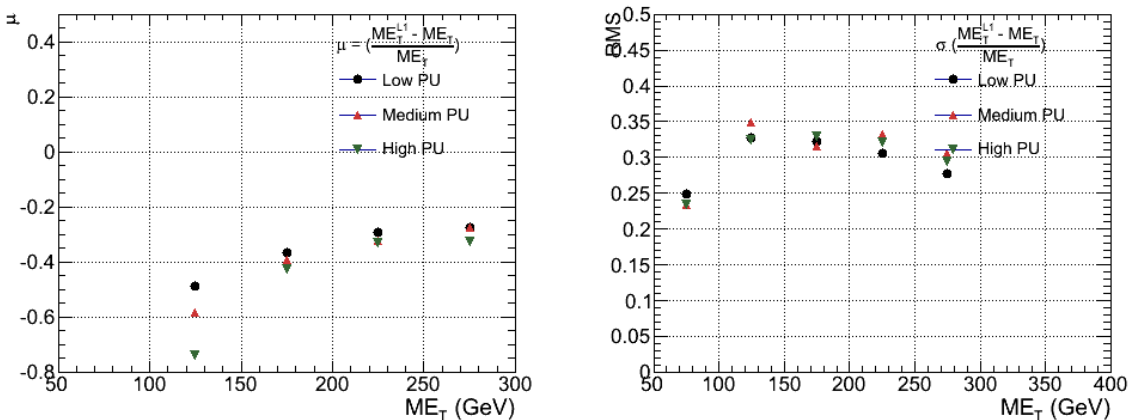


Figure B.7.: \mathcal{E}_T resolution parameters in bins of PF \mathcal{E}_T measured for the defined low, medium and high pile up conditions. The plots show the mean μ (left), resolution σ (RMS) of the $\frac{\Delta q}{q}$ distributions.

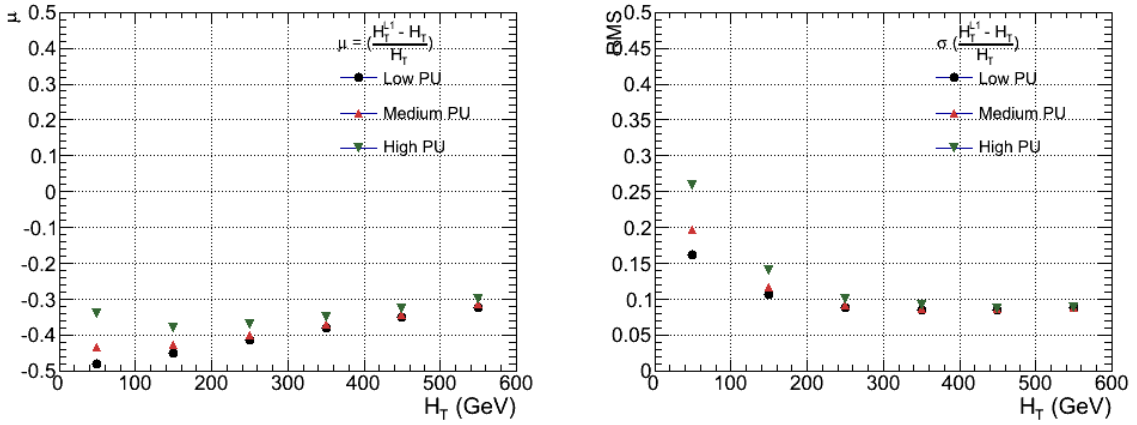


Figure B.8.: H_T resolution parameters in bins of Calo H_T measured for the defined low, medium and high pile up conditions. The plots show the mean μ (left), resolution σ (RMS) of the $\frac{\Delta q}{q}$ distributions.

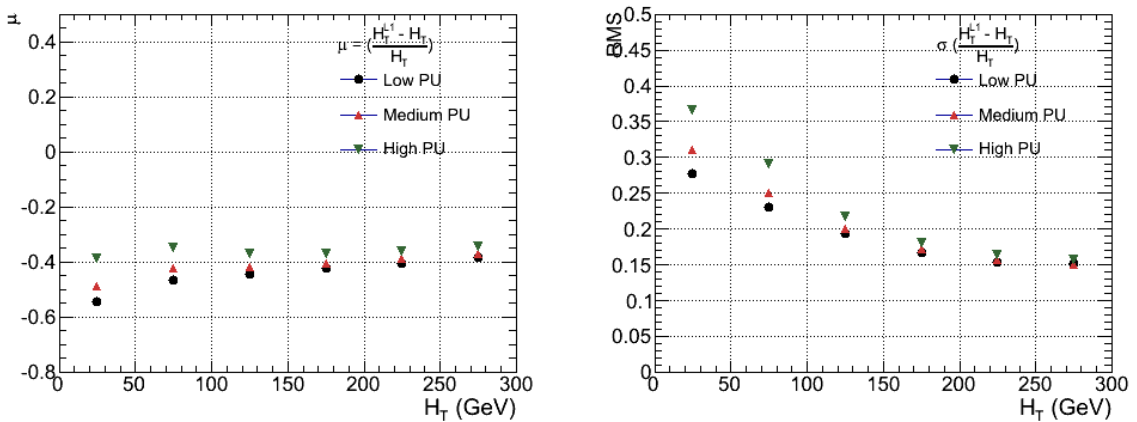


Figure B.9.: H_T resolution parameters in bins of PF H_T measured for the defined low, medium and high pile up conditions. The plots show the mean μ (left), resolution σ (RMS) of the $\frac{\Delta q}{q}$ distributions.

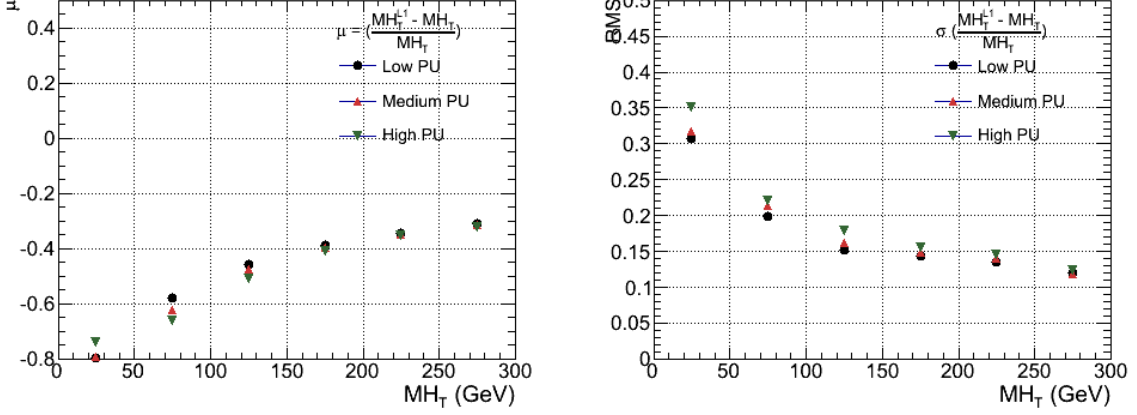


Figure B.10.: H_T resolution parameters in bins of H_T measured for the defined low, medium and high pile up conditions. The plots show the mean μ (left), resolution σ (RMS) of the $\frac{\Delta q}{q}$ distributions.

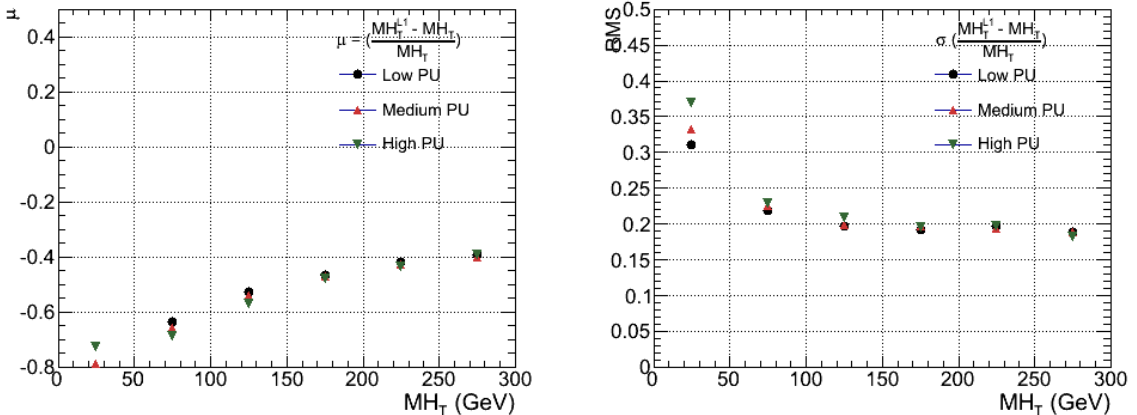


Figure B.11.: H_T resolution parameters in bins of PF H_T measured for the defined low, medium and high pile up conditions. The plots show the mean μ (left), resolution σ (RMS) of the $\frac{\Delta q}{q}$ distributions.

Appendix C.

²³⁰⁹ **Additional material on background
estimation methods**

²³¹⁰

²³¹¹ **C.1. Determination of k_{QCD}**

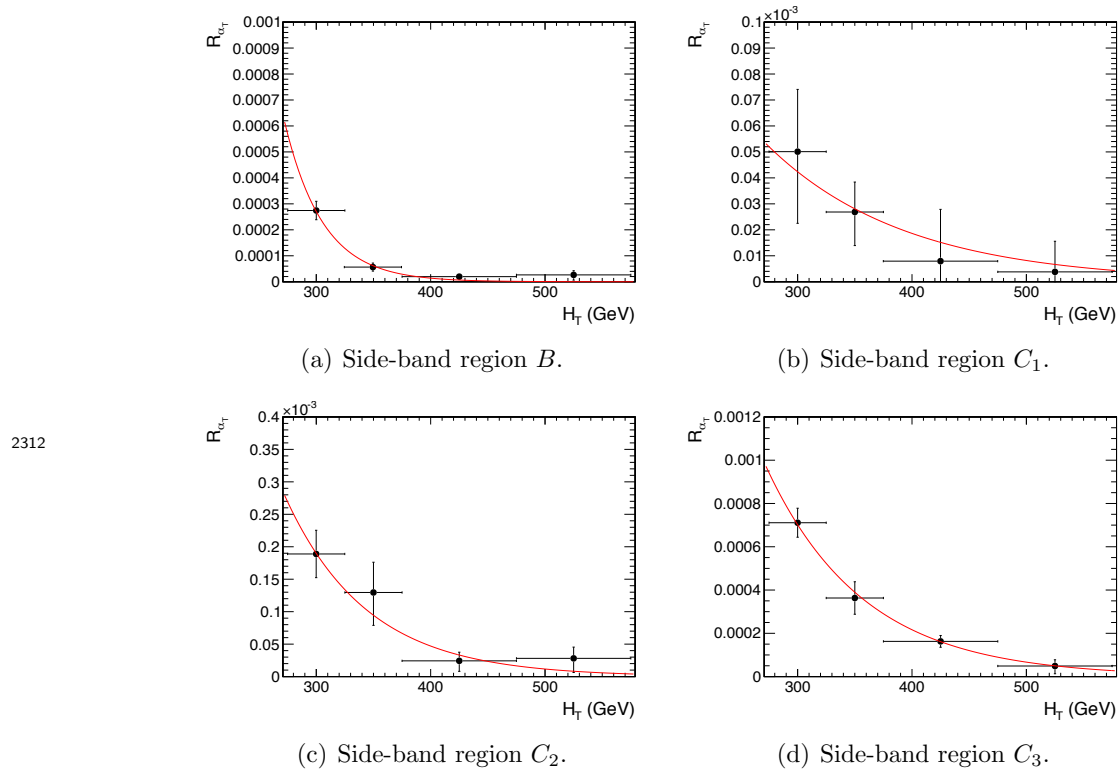


Figure C.1.: $R_{\alpha_T}(H_T)$ and exponential fits for each of the data sideband regions. Fit is conducted between the H_T region $275 < H_T < 575$.

²³¹³ **C.2. Effect of varying background cross sections on**
²³¹⁴ **closure tests**

²³¹⁵ Closure tests with cross section variations of +20% and -20% applied to $W + \text{jets}$ and $t\bar{t}$
²³¹⁶ processes respectively.

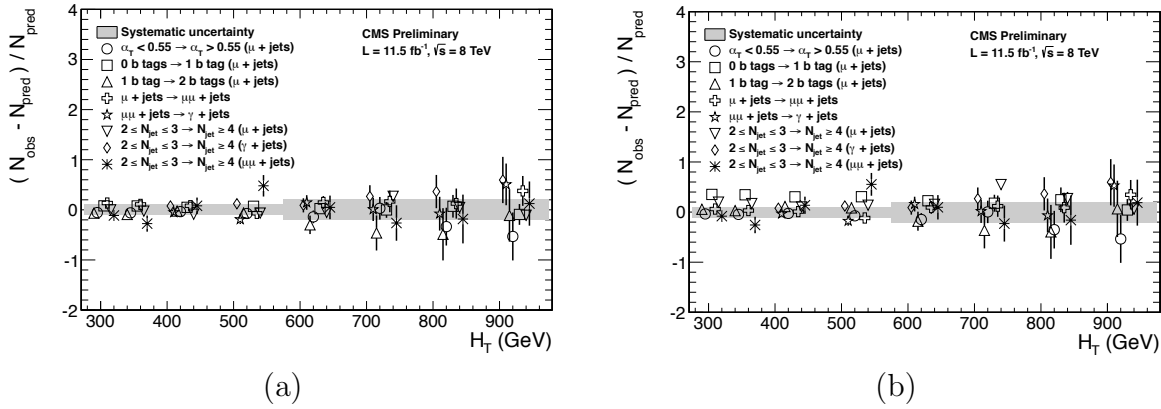


Figure C.2.: Sets of closure tests (open symbols) overlaid on top of the systematic uncertainty used for each of the five H_T regions (shaded bands) and for the two different jet multiplicity bins: (a) $2 \leq n_{jet} \leq 3$ and (b) $n_{jet} \geq 4$.

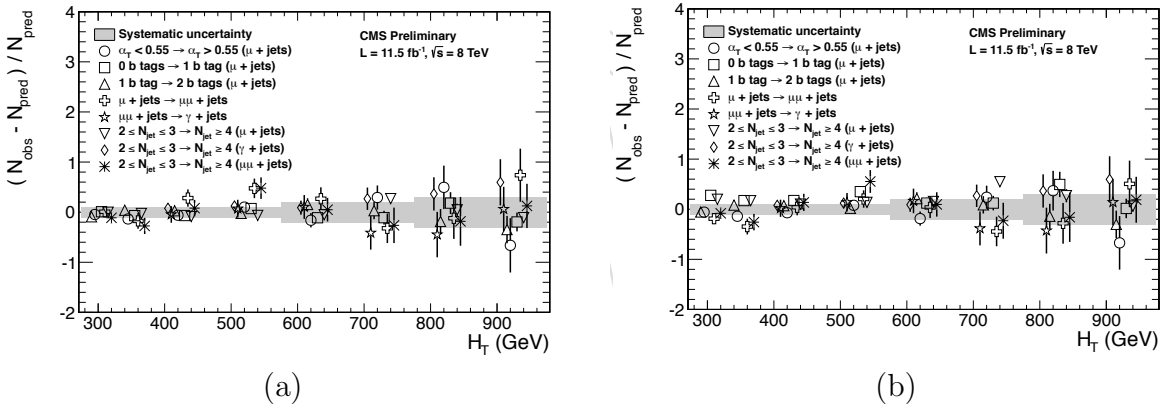


Figure C.3.: Sets of closure tests (open symbols) overlaid on top of the systematic uncertainty used for each of the five H_T regions (shaded bands) and for the two different jet multiplicity bins: (a) $2 \leq n_{jet} \leq 3$ and (b) $n_{jet} \geq 4$.

		H_T (GeV)			
n_b^{reco}	Cross Section	275–325	325–375	375–475	475–575
0	Nominal	0.303 ± 0.010	0.258 ± 0.007	0.192 ± 0.003	0.148 ± 0.004
	Varied	0.300 ± 0.010	0.256 ± 0.007	0.191 ± 0.003	0.147 ± 0.004
1	Nominal	0.294 ± 0.005	0.246 ± 0.004	0.189 ± 0.003	0.139 ± 0.003
	Varied	0.295 ± 0.006	0.248 ± 0.004	0.191 ± 0.003	0.140 ± 0.003
2	Nominal	0.208 ± 0.003	0.183 ± 0.004	0.145 ± 0.003	0.123 ± 0.004
	Varied	0.211 ± 0.004	0.185 ± 0.004	0.147 ± 0.003	0.124 ± 0.004
3	Nominal	0.214 ± 0.005	0.202 ± 0.007	0.159 ± 0.006	0.140 ± 0.007
	Varied	0.215 ± 0.005	0.203 ± 0.007	0.159 ± 0.006	0.140 ± 0.007
≥ 4	Nominal	0.220 ± 0.015	0.245 ± 0.035	0.119 ± 0.009	-
	Varied	0.220 ± 0.015	0.245 ± 0.035	0.119 ± 0.009	-
n_b^{reco}	Cross Section	575–675	675–775	775–875	875– ∞
0	Nominal	0.119 ± 0.004	0.098 ± 0.005	0.077 ± 0.006	0.049 ± 0.005
	Varied	0.120 ± 0.005	0.098 ± 0.006	0.077 ± 0.007	0.049 ± 0.005
1	Nominal	0.115 ± 0.004	0.093 ± 0.005	0.075 ± 0.007	0.063 ± 0.006
	Varied	0.116 ± 0.004	0.098 ± 0.005	0.081 ± 0.007	0.065 ± 0.006
2	Nominal	0.096 ± 0.005	0.070 ± 0.006	0.051 ± 0.007	0.063 ± 0.008
	Varied	0.098 ± 0.005	0.073 ± 0.006	0.053 ± 0.007	0.064 ± 0.008
3	Nominal	0.114 ± 0.009	0.065 ± 0.007	0.070 ± 0.017	0.092 ± 0.020
	Varied	0.114 ± 0.009	0.066 ± 0.007	0.070 ± 0.016	0.093 ± 0.020

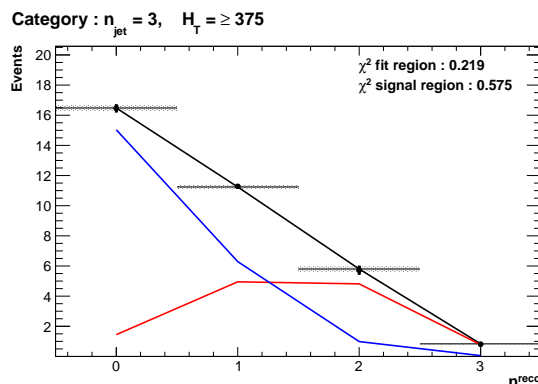
Table C.1.: Translation factors constructed from the $\mu +$ jets control sample and signal selection MC, to predict yields for the $W +$ jets and $t\bar{t}$ back-grounds in the signal region with (a) NNLO cross sections corrected by k-factors determined from a data sideband see Section (4.4), marked as Nominal, and (b) the same cross sections but with those for $W +$ jets and $t\bar{t}$ varied up and down by 20%, respectively, marked as Varied. No requirement is placed on the jet multiplicity of events within this table.

Appendix D.

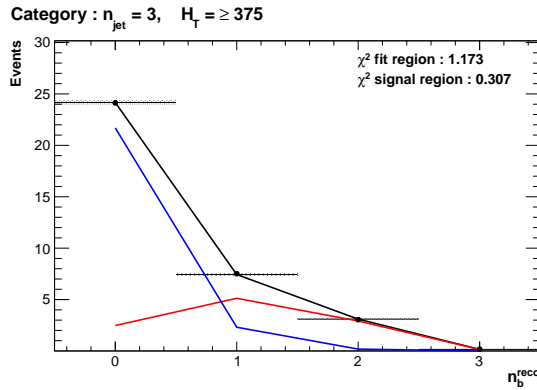
²³¹⁷ Additional Material For B-tag ²³¹⁸ Template Method

²³¹⁹ D.1. Templates Fits in Simulation

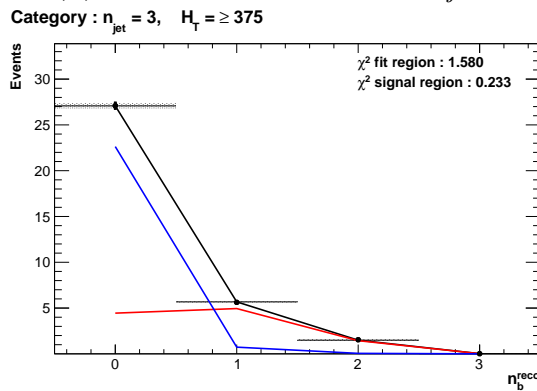
²³²⁰ Template fits for the three **CSV** working points in the $n_{jet} = 3, H_T > 375$ category :



(a) Loose working point $n_{jet} = 3$



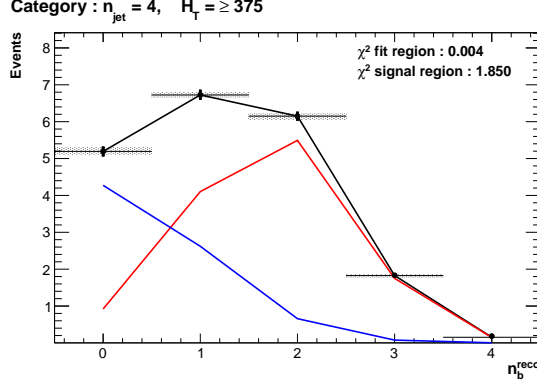
(b) Medium working point $n_{jet} = 3$



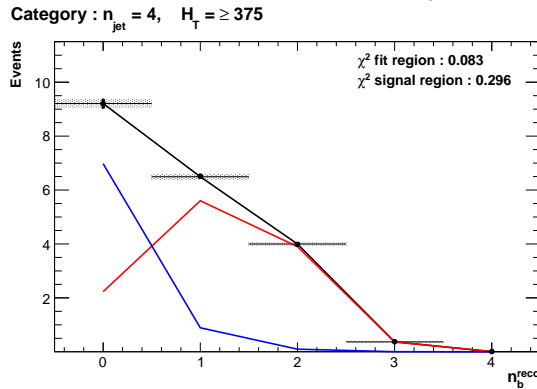
(c) Tight working point $n_{jet} = 3$

Figure D.1.: The results of fitting the $Z = 0$ and $Z = 2$ templates to the $n_b^{reco} = 0, 1, 2$ bins taken directly from simulation in the region $H_T > 375$ GeV, for the $n_{jet} = 3$ category. The blue template represents $Z = 0$, while the red template represents $Z = 2$. Grey bands represent the statistical uncertainty of the fit. The χ^2 parameter displayed represents the goodness of fit to the low n_b^{reco} (0-2) control region.

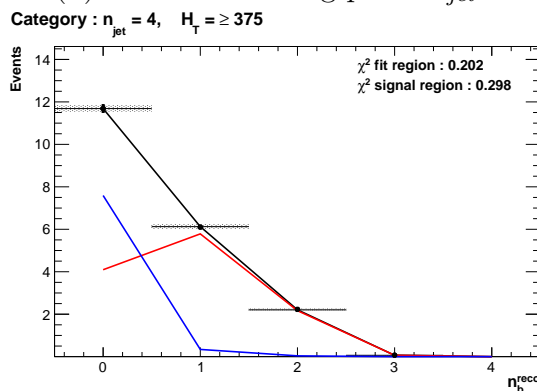
2321 Template fits for the three **CSV** working points in the $n_{jet} = 4$, $H_T > 375$ category :



(a) Loose working point $n_{jet} = 4$



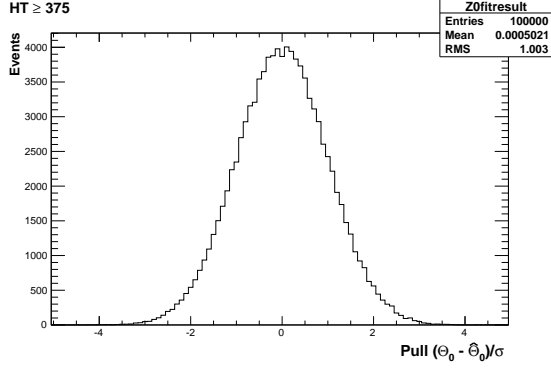
(b) Medium working point $n_{jet} = 4$



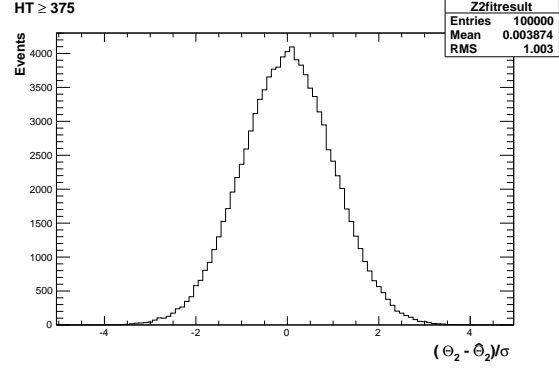
(c) Tight working point $n_{jet} = 4$

Figure D.2.: The results of fitting the $Z = 0$ and $Z = 2$ templates to the $n_b^{reco} = 0, 1, 2$ bins taken directly from simulation in the region $H_T > 375$ GeV, for the $n_{jet} = 4$ category. The blue template represents $Z = 0$, while the red template represents $Z = 2$. Grey bands represent the statistical uncertainty of the fit. The χ^2 parameter displayed represents the goodness of fit to the low n_b^{reco} (0-2) control region.

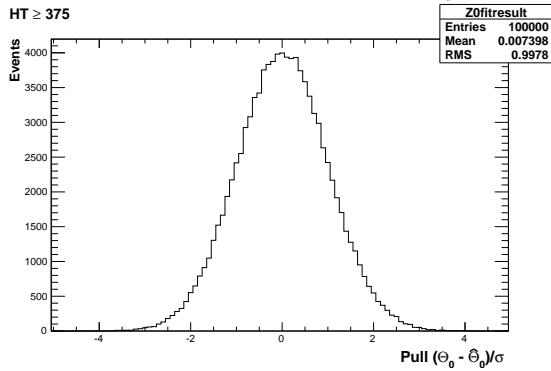
2322 D.2. Pull Distributions for Template Fits



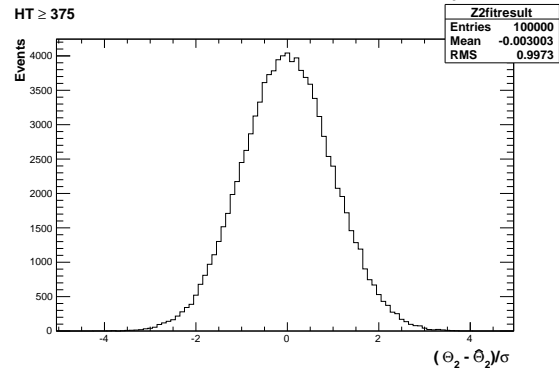
(a) Z0 Template, $H_T > 375$, $n_{jet} = 3$



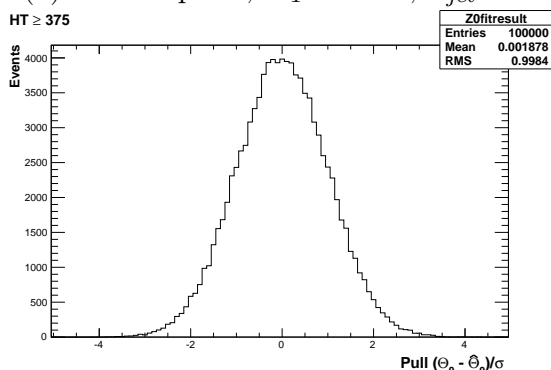
(b) Z2 Template, $H_T > 375$, $n_{jet} = 3$



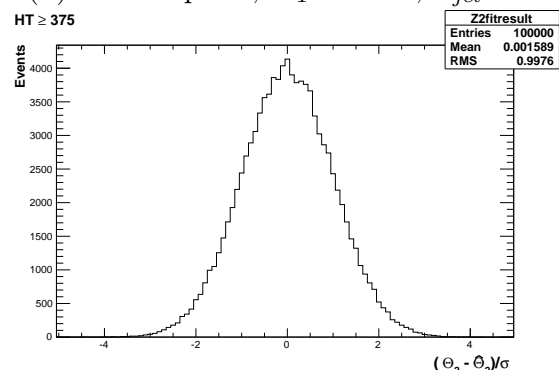
(a) Z0 Template, $H_T > 375$, $n_{jet} = 4$



(b) Z2 Template, $H_T > 375$, $n_{jet} = 4$



(a) Z0 Template, $H_T > 375$, $n_{jet} \geq 5$



(b) Z2 Template, $H_T > 375$, $n_{jet} \geq 5$

Figure D.3.: Pull distributions of $\frac{(\theta - \hat{\theta})}{\sigma}$ for 10^4 pseudo-experiments generated from a gaussian distribution centred on the n_b^{reco} template values from simulation with width σ . Distributions are shown for both Z0 and Z2 templates for the medium CSV working point.

²³²³ **D.3. Templates Fits in Data Control Sample**

²³²⁴ Template fits for the three H_T bins, in the $n_{jet} = 3$, medium **CSV** working point:

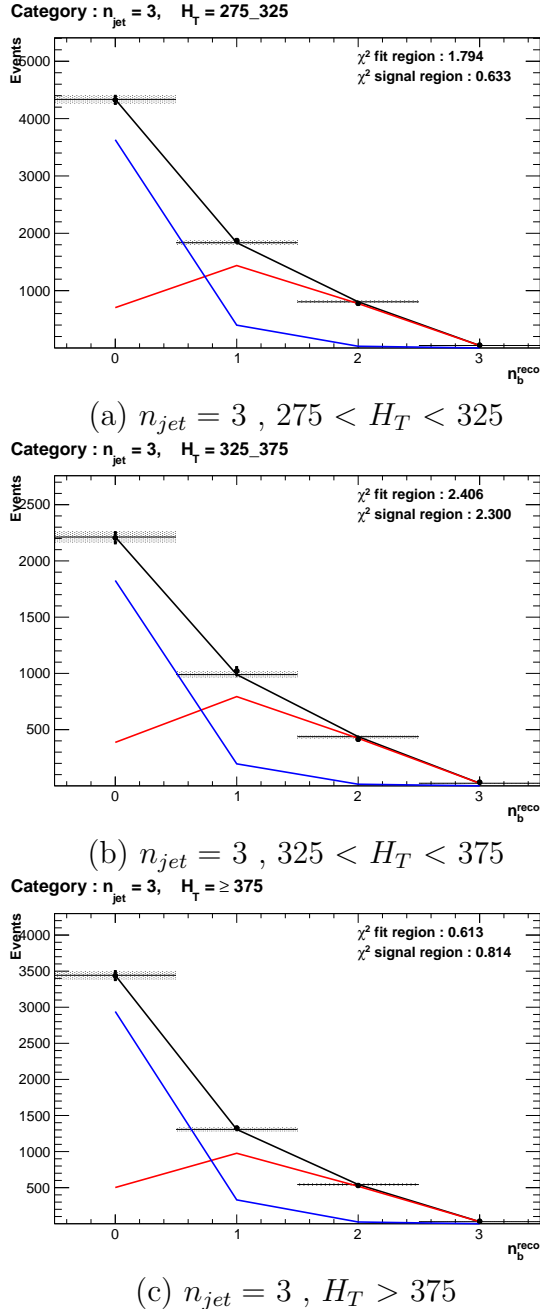


Figure D.4.: The results of fitting the $Z = 0$ and $Z = 2$ templates to the $n_b^{reco} = 0, 1, 2$ bins taken from data, for the $n_{jet} = 3$ category and medium **CSV** working point. The blue template represents $Z = 0$, while the red template represents $Z = 2$. The χ^2 parameter displayed represents the goodness of fit to the low n_b^{reco} (0-2) control region.

2325 Template fits for the three H_T bins, in the $n_{jet} = 4$, medium **CSV** working point:

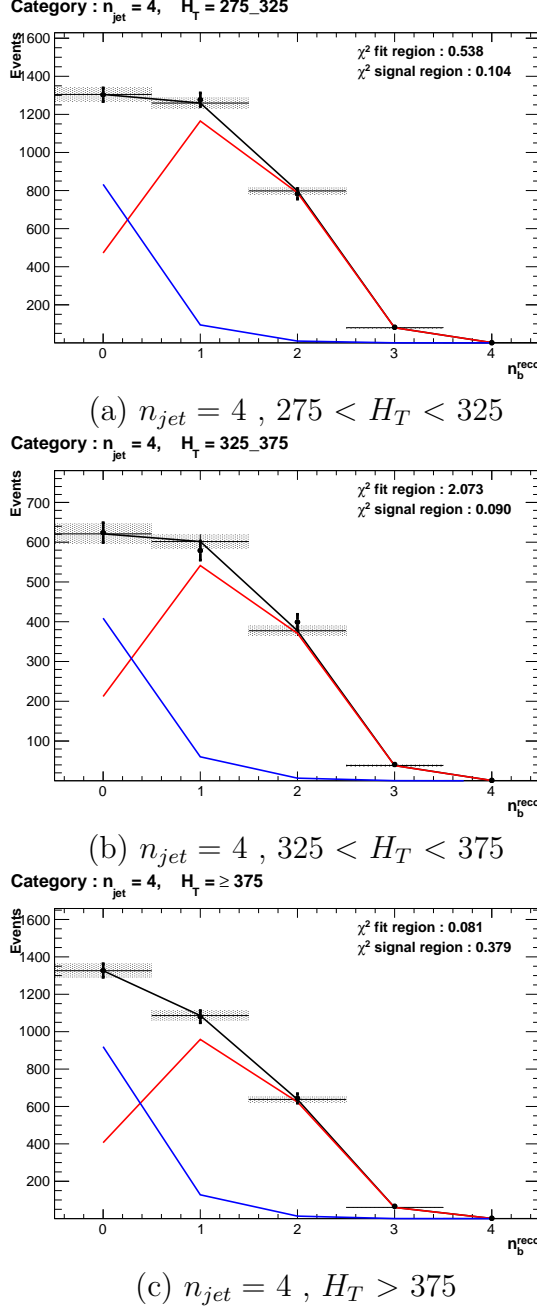
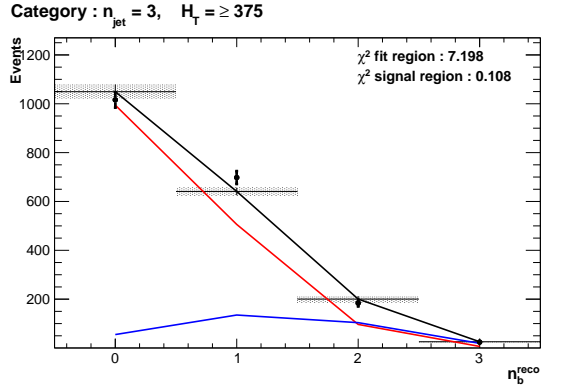


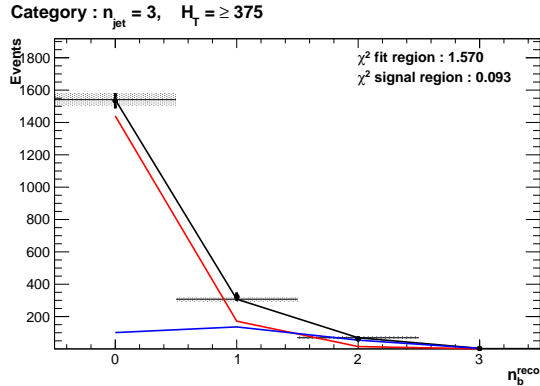
Figure D.5.: The results of fitting the $Z = 0$ and $Z = 2$ templates to the $n_b^{reco} = 0, 1, 2$ bins taken from data, for the $n_{jet} = 4$ category and medium **CSV** working point. The blue template represents $Z = 0$, while the red template represents $Z = 2$. The χ^2 parameter displayed represents the goodness of fit to the low n_b^{reco} (0-2) control region.

2326 **D.4. Templates Fits in Data Signal Region**

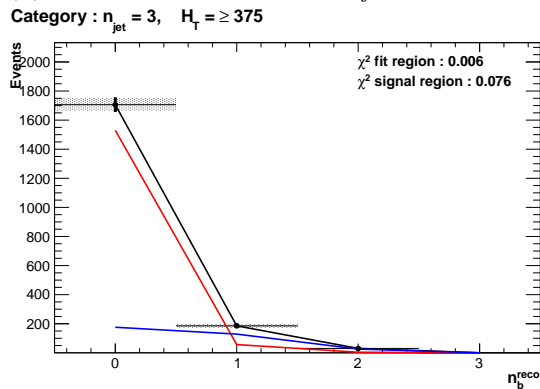
2327 Template fits for the three **CSV** working points, in the $n_{jet} = 3, H_T > 375$ category :



(a) Loose working point : $n_{jet} = 3, H_T > 375$



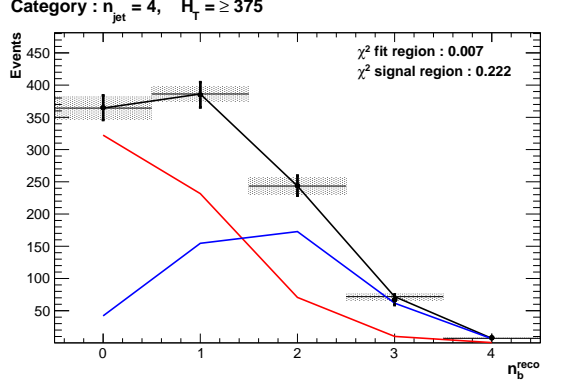
(b) Medium working point : $n_{jet} = 3, H_T > 375$



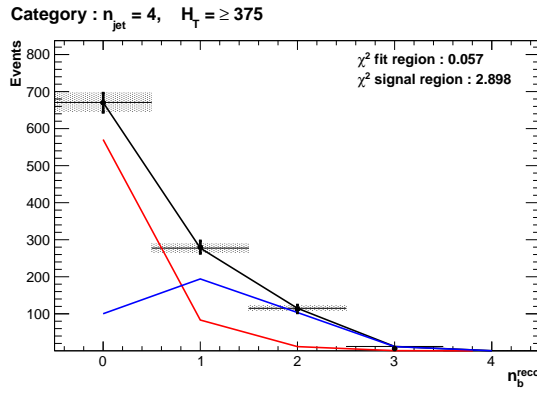
(c) Tight working point : $n_{jet} = 3, H_T > 375$

Figure D.6.: The results of fitting the $Z = 0$ and $Z = 2$ templates to the $n_b^{reco} = 0, 1, 2$ bins taken from data, in the $n_{jet} = 3$ and $H_T > 375$ category for all **CSV** working points. The blue template represents $Z = 0$, while the red template represents $Z = 2$. The χ^2 parameter displayed represents the goodness of fit to the low n_b^{reco} (0-2) control region.

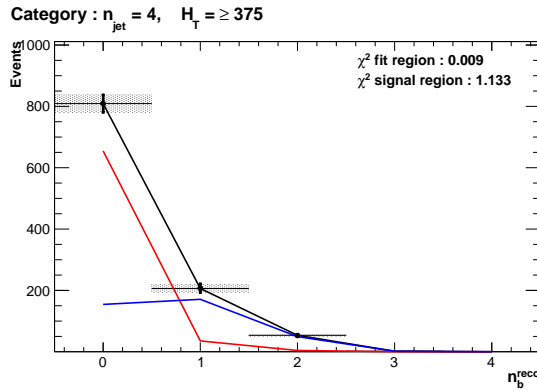
2328 Template fits for the three **CSV** working points, in the $n_{jet} = 4$, $H_T > 375$ category :



(a) Loose working point : $n_{jet} = 4$, $H_T > 375$



(b) Medium working point : $n_{jet} = 4$, $H_T > 375$



(c) Tight working point : $n_{jet} = 4$, $H_T > 375$

Figure D.7.: The results of fitting the $Z = 0$ and $Z = 2$ templates to the $n_b^{reco} = 0, 1, 2$ bins taken from data, in the $n_{jet} = 4$ and $H_T > 375$ category for all **CSV** working points. The blue template represents $Z = 0$, while the red template represents $Z = 2$. The χ^2 parameter displayed represents the goodness of fit to the low n_b^{reco} ($0-2$) control region.

²³³⁰ Bibliography

- ²³³¹ [1] Particle Data Group Collaboration, “Review of Particle Physics (RPP)”, *Phys.Rev.*
²³³² **D86** (2012) 010001, [doi:10.1103/PhysRevD.86.010001](https://doi.org/10.1103/PhysRevD.86.010001).
- ²³³³ [2] G. H. et al., “Nine-year Wilkinson Microwave Anisotropy Probe (WMAP)
²³³⁴ Observations: Cosmological Parameter Results”, *The Astrophysical Journal*
²³³⁵ *Supplement Series* **208** (2013), no. 2, 19.
- ²³³⁶ [3] ATLAS Collaboration Collaboration, “Observation of a new particle in the search
²³³⁷ for the Standard Model Higgs boson with the ATLAS detector at the LHC”,
²³³⁸ *Phys.Lett.* **B716** (2012) 1–29, [doi:10.1016/j.physletb.2012.08.020](https://doi.org/10.1016/j.physletb.2012.08.020),
²³³⁹ [arXiv:1207.7214](https://arxiv.org/abs/1207.7214).
- ²³⁴⁰ [4] CMS Collaboration Collaboration, “Observation of a new boson at a mass of 125
²³⁴¹ GeV with the CMS experiment at the LHC”, *Phys.Lett.* **B716** (2012) 30–61,
²³⁴² [doi:10.1016/j.physletb.2012.08.021](https://doi.org/10.1016/j.physletb.2012.08.021), [arXiv:1207.7235](https://arxiv.org/abs/1207.7235).
- ²³⁴³ [5] CMS Collaboration Collaboration, “Search for supersymmetry in hadronic final
²³⁴⁴ states with missing transverse energy using the variables AlphaT and b-quark
²³⁴⁵ multiplicity in pp collisions at 8 TeV”, *Eur.Phys.J.* **C73** (2013) 2568,
²³⁴⁶ [doi:10.1140/epjc/s10052-013-2568-6](https://doi.org/10.1140/epjc/s10052-013-2568-6), [arXiv:1303.2985](https://arxiv.org/abs/1303.2985).
- ²³⁴⁷ [6] S. Weinberg, “A Model of Leptons”, *Phys. Rev. Lett.* **19** (Nov, 1967) 1264–1266,
²³⁴⁸ [doi:10.1103/PhysRevLett.19.1264](https://doi.org/10.1103/PhysRevLett.19.1264).
- ²³⁴⁹ [7] S. Glashow, “Partial Symmetries of Weak Interactions”, *Nucl.Phys.* **22** (1961)
²³⁵⁰ 579–588, [doi:10.1016/0029-5582\(61\)90469-2](https://doi.org/10.1016/0029-5582(61)90469-2).
- ²³⁵¹ [8] A. Salam, “Weak and Electromagnetic Interactions”, *Conf.Proc.* **C680519** (1968)
²³⁵² 367–377.
- ²³⁵³ [9] G. Hooft, “Renormalizable Lagrangians for massive Yang-Mills fields”, *Nuclear*
²³⁵⁴ *Physics B* **35** (1971), no. 1, 167 – 188,

- 2355 [doi:
http://dx.doi.org/10.1016/0550-3213\(71\)90139-8](http://dx.doi.org/10.1016/0550-3213(71)90139-8).
- 2356 [10] Gargamelle Neutrino Collaboration Collaboration, “Observation of Neutrino Like
2357 Interactions Without Muon Or Electron in the Gargamelle Neutrino Experiment”,
2358 *Phys.Lett.* **B46** (1973) 138–140, [doi:
10.1016/0370-2693\(73\)90499-1](http://dx.doi.org/10.1016/0370-2693(73)90499-1).
- 2359 [11] UA1 Collaboration Collaboration, “Experimental Observation of Lepton Pairs of
2360 Invariant Mass Around 95-GeV/c**2 at the CERN SPS Collider”, *Phys.Lett.*
2361 **B126** (1983) 398–410, [doi:
10.1016/0370-2693\(83\)90188-0](http://dx.doi.org/10.1016/0370-2693(83)90188-0).
- 2362 [12] UA2 Collaboration Collaboration, “Observation of Single Isolated Electrons of High
2363 Transverse Momentum in Events with Missing Transverse Energy at the CERN
2364 anti-p p Collider”, *Phys.Lett.* **B122** (1983) 476–485,
2365 [doi:
10.1016/0370-2693\(83\)91605-2](http://dx.doi.org/10.1016/0370-2693(83)91605-2).
- 2366 [13] E. Noether, “Invariante Variationsprobleme”, *Nachrichten von der Gesellschaft der
2367 Wissenschaften zu Gttingen, Mathematisch-Physikalische Klasse* **1918** (1918)
2368 235–257.
- 2369 [14] F. Halzen and A. D. Martin, “Quarks and Leptons”. Wiley, 1985.
- 2370 [15] “Introduction to Elementary Particles”. Wiley-VCH, 2nd edition, October, 2008.
- 2371 [16] C. S. Wu et al., “Experimental Test of Parity Conservation in Beta Decay”,
2372 *Physical Review* **105** (February, 1957) 1413–1415,
2373 [doi:
10.1103/PhysRev.105.1413](http://dx.doi.org/10.1103/PhysRev.105.1413).
- 2374 [17] P. Higgs, “Broken symmetries, massless particles and gauge fields”, *Physics Letters*
2375 **12** (1964), no. 2, 132 – 133,
2376 [doi:
http://dx.doi.org/10.1016/0031-9163\(64\)91136-9](http://dx.doi.org/10.1016/0031-9163(64)91136-9).
- 2377 [18] F. Englert and R. Brout, “Broken Symmetry and the Mass of Gauge Vector
2378 Mesons”, *Phys. Rev. Lett.* **13** (Aug, 1964) 321–323,
2379 [doi:
10.1103/PhysRevLett.13.321](http://dx.doi.org/10.1103/PhysRevLett.13.321).
- 2380 [19] P. W. Higgs, “Broken Symmetries and the Masses of Gauge Bosons”, *Phys. Rev.
2381 Lett.* **13** (Oct, 1964) 508–509, [doi:
10.1103/PhysRevLett.13.508](http://dx.doi.org/10.1103/PhysRevLett.13.508).
- 2382 [20] G. S. Guralnik, C. R. Hagen, and T. W. B. Kibble, “Global Conservation Laws and
2383 Massless Particles”, *Phys. Rev. Lett.* **13** (Nov, 1964) 585–587,
2384 [doi:
10.1103/PhysRevLett.13.585](http://dx.doi.org/10.1103/PhysRevLett.13.585).

- 2385 [21] S. Weinberg, “A Model of Leptons”, *Phys. Rev. Lett.* **19** (Nov, 1967) 1264–1266,
2386 [doi:10.1103/PhysRevLett.19.1264](https://doi.org/10.1103/PhysRevLett.19.1264).
- 2387 [22] H. Yukawa, “On the Interaction of Elementary Particles. I”, *Progress of
2388 Theoretical Physics Supplement* **1** (1955) 1–10, [doi:10.1143/PTPS.1.1](https://doi.org/10.1143/PTPS.1.1),
2389 [arXiv:<http://ptps.oxfordjournals.org/content/1/1.1.full.pdf+html>](http://ptps.oxfordjournals.org/content/1/1.1.full.pdf+html).
- 2390 [23] (Super-Kamiokande Collaboration) Collaboration, “Evidence for Oscillation of
2391 Atmospheric Neutrinos”, *Phys. Rev. Lett.* **81** (Aug, 1998) 1562–1567,
2392 [doi:10.1103/PhysRevLett.81.1562](https://doi.org/10.1103/PhysRevLett.81.1562).
- 2393 [24] R. Becker-Szendy et al., “A Search for muon-neutrino oscillations with the IMB
2394 detector”, *Phys.Rev.Lett.* **69** (1992) 1010–1013,
2395 [doi:10.1103/PhysRevLett.69.1010](https://doi.org/10.1103/PhysRevLett.69.1010).
- 2396 [25] S. P. Martin, “A Supersymmetry primer”, [arXiv:hep-ph/9709356](https://arxiv.org/abs/hep-ph/9709356).
- 2397 [26] H. Nilles, “Supersymmetry, Supergravity and Particle Physics”. Physics reports.
2398 North-Holland Physics Publ., 1984.
- 2399 [27] H. E. Haber and G. L. Kane, “The Search for Supersymmetry: Probing Physics
2400 Beyond the Standard Model”, *Phys.Rept.* **117** (1985) 75–263,
2401 [doi:10.1016/0370-1573\(85\)90051-1](https://doi.org/10.1016/0370-1573(85)90051-1).
- 2402 [28] E. Witten, “Dynamical Breaking of Supersymmetry”, *Nucl.Phys.* **B188** (1981)
2403 513, [doi:10.1016/0550-3213\(81\)90006-7](https://doi.org/10.1016/0550-3213(81)90006-7).
- 2404 [29] J. Wess and B. Zumino, “Supergauge transformations in four dimensions”, *Nuclear
2405 Physics B* **70** (1974), no. 1, 39 – 50,
2406 [doi:\[http://dx.doi.org/10.1016/0550-3213\\(74\\)90355-1\]\(http://dx.doi.org/10.1016/0550-3213\(74\)90355-1\)](http://dx.doi.org/10.1016/0550-3213(74)90355-1).
- 2407 [30] H. Muller-Kirsten and A. Wiedemann, “Introduction to Supersymmetry”. World
2408 Scientific lecture notes in physics. World Scientific, 2010.
- 2409 [31] I. Aitchison, “Supersymmetry in Particle Physics: An Elementary Introduction”.
2410 Cambridge University Press, 2007.
- 2411 [32] K. A. Intriligator and N. Seiberg, “Lectures on Supersymmetry Breaking”,
2412 *Class.Quant.Grav.* **24** (2007) S741–S772,
2413 [doi:10.1088/0264-9381/24/21/S02](https://doi.org/10.1088/0264-9381/24/21/S02), [10.1016/S0924-8099\(08\)80020-0](https://doi.org/10.1016/S0924-8099(08)80020-0),
2414 [arXiv:hep-ph/0702069](https://arxiv.org/abs/hep-ph/0702069).

- [33] Y. Shadmi, “Supersymmetry breaking”, [arXiv:hep-th/0601076](https://arxiv.org/abs/hep-th/0601076).
- [34] C. Burgess et al., “Warped Supersymmetry Breaking”, *JHEP* **0804** (2008) 053, [doi:10.1088/1126-6708/2008/04/053](https://doi.org/10.1088/1126-6708/2008/04/053), [arXiv:hep-th/0610255](https://arxiv.org/abs/hep-th/0610255).
- [35] H. Murayama, “Supersymmetry breaking made easy, viable, and generic”, [arXiv:0709.3041](https://arxiv.org/abs/0709.3041).
- [36] H. Baer and X. Tata, “Weak Scale Supersymmetry: From Superfields to Scattering Events”. Cambridge University Press, 2006.
- [37] S. P. Martin, “Implications of supersymmetric models with natural R-parity conservation”, [doi:10.1103/PhysRevD.54.2340](https://doi.org/10.1103/PhysRevD.54.2340), [arXiv:hep-ph/9602349](https://arxiv.org/abs/hep-ph/9602349).
- [38] G. L. Kane, C. F. Kolda, L. Roszkowski, and J. D. Wells, “Study of constrained minimal supersymmetry”, *Phys.Rev.* **D49** (1994) 6173–6210, [doi:10.1103/PhysRevD.49.6173](https://doi.org/10.1103/PhysRevD.49.6173), [arXiv:hep-ph/9312272](https://arxiv.org/abs/hep-ph/9312272).
- [39] C. Stuge et al., “Updated global fits of the cMSSM including the latest LHC SUSY and Higgs searches and XENON100 data”, *JCAP* **1203** (2012) 030, [doi:10.1088/1475-7516/2012/03/030](https://doi.org/10.1088/1475-7516/2012/03/030), [arXiv:1112.4192](https://arxiv.org/abs/1112.4192).
- [40] M. Citron et al., “The End of the CMSSM Coannihilation Strip is Nigh”, *Phys.Rev.* **D87** (2013) 036012, [doi:10.1103/PhysRevD.87.036012](https://doi.org/10.1103/PhysRevD.87.036012), [arXiv:1212.2886](https://arxiv.org/abs/1212.2886).
- [41] D. Ghosh, M. Guchait, S. Raychaudhuri, and D. Sengupta, “How Constrained is the cMSSM?”, *Phys.Rev.* **D86** (2012) 055007, [doi:10.1103/PhysRevD.86.055007](https://doi.org/10.1103/PhysRevD.86.055007), [arXiv:1205.2283](https://arxiv.org/abs/1205.2283).
- [42] LHC New Physics Working Group Collaboration, “Simplified Models for LHC New Physics Searches”, *J.Phys.* **G39** (2012) 105005, [doi:10.1088/0954-3899/39/10/105005](https://doi.org/10.1088/0954-3899/39/10/105005), [arXiv:1105.2838](https://arxiv.org/abs/1105.2838).
- [43] J. Alwall, P. Schuster, and N. Toro, “Simplified Models for a First Characterization of New Physics at the LHC”, *Phys.Rev.* **D79** (2009) 075020, [doi:10.1103/PhysRevD.79.075020](https://doi.org/10.1103/PhysRevD.79.075020), [arXiv:0810.3921](https://arxiv.org/abs/0810.3921).
- [44] CMS Collaboration Collaboration, “Interpretation of Searches for Supersymmetry with simplified Models”, *Phys.Rev.* **D88** (2013) 052017, [doi:10.1103/PhysRevD.88.052017](https://doi.org/10.1103/PhysRevD.88.052017), [arXiv:1301.2175](https://arxiv.org/abs/1301.2175).
- [45] J. Hisano, K. Kurosawa, and Y. Nomura, “Natural effective supersymmetry”, [arXiv:0905.4121](https://arxiv.org/abs/0905.4121).

- 2445 *Nucl.Phys.* **B584** (2000) 3–45, [doi:10.1016/S0550-3213\(00\)00343-6](https://doi.org/10.1016/S0550-3213(00)00343-6),
2446 [arXiv:hep-ph/0002286](https://arxiv.org/abs/hep-ph/0002286).
- 2447 [46] M. Papucci, J. T. Ruderman, and A. Weiler, “Natural SUSY Endures”, *JHEP*
2448 **1209** (2012) 035, [doi:10.1007/JHEP09\(2012\)035](https://doi.org/10.1007/JHEP09(2012)035), [arXiv:1110.6926](https://arxiv.org/abs/1110.6926).
- 2449 [47] B. Allanach and B. Gripaios, “Hide and Seek With Natural Supersymmetry at the
2450 LHC”, *JHEP* **1205** (2012) 062, [doi:10.1007/JHEP05\(2012\)062](https://doi.org/10.1007/JHEP05(2012)062),
2451 [arXiv:1202.6616](https://arxiv.org/abs/1202.6616).
- 2452 [48] ALICE Collaboration, “The ALICE experiment at the CERN LHC”, *JINST* **3**
2453 (2008) S08002, [doi:10.1088/1748-0221/3/08/S08002](https://doi.org/10.1088/1748-0221/3/08/S08002).
- 2454 [49] ATLAS Collaboration, “The ATLAS Experiment at the CERN Large Hadron
2455 Collider”, *JINST* **3** (2008) [doi:10.1088/1748-0221/3/08/S08003](https://doi.org/10.1088/1748-0221/3/08/S08003).
- 2456 [50] CMS Collaboration, “The CMS experiment at the CERN LHC”, *JINST* **0803**
2457 (2008) S08004,
2458 [doi:10.1088/1748-0221/3/08/S08004](https://doi.org/10.1088/1748-0221/3/08/S08004), [10.1088/1748-0221/3/08/S08004](https://doi.org/10.1088/1748-0221/3/08/S08004).
- 2459 [51] LHCb Collaboration, “The LHCb Detector at the LHC”, *JINST* **3** (2008) S08005,
2460 [doi:10.1088/1748-0221/3/08/S08005](https://doi.org/10.1088/1748-0221/3/08/S08005).
- 2461 [52] J.-L. Caron, “LHC Layout.. Schema general du LHC.”, (Sep, 1997).
- 2462 [53] C. Collaboration, “CMS Luminosity - Public Results”, (2011).
2463 twiki.cern.ch/twiki/bin/view/CMSPublic/LumiPublicResults.
- 2464 [54] CERN, “CMS Compact Muon Solenoid.”, (Feb, 2010).
2465 <http://public.web.cern.ch/public/Objects/LHC/CMSnc.jpg>.
- 2466 [55] “The CMS electromagnetic calorimeter project: Technical Design Report”.
2467 Technical Design Report CMS. CERN, Geneva, 1997.
- 2468 [56] “The CMS muon project: Technical Design Report”. Technical Design Report
2469 CMS. CERN, Geneva, 1997.
- 2470 [57] CMS Collaboration, “The CMS Physics Technical Design Report, Volume 1”,
2471 *CERN/LHCC* **2006-001** (2006).
- 2472 [58] M. Cacciari, G. P. Salam, and G. Soyez, “The anti- k_t jet clustering algorithm”,
2473 *Journal of High Energy Physics* **2008** (2008), no. 04, 063.

- 2474 [59] “Jet Performance in pp Collisions at 7 TeV”, Technical Report
2475 CMS-PAS-JME-10-003, CERN, Geneva, (2010).
- 2476 [60] X. Janssen, “Underlying event and jet reconstruction in CMS”, Technical Report
2477 CMS-CR-2011-012, CERN, Geneva, (Jan, 2011).
- 2478 [61] T. C. collaboration, “Determination of jet energy calibration and transverse
2479 momentum resolution in CMS”, *Journal of Instrumentation* **6** (2011), no. 11,
2480 P11002.
- 2481 [62] R. Eusebi and on behalf of the CMS collaboration), “Jet energy corrections and
2482 uncertainties in CMS: reducing their impact on physics measurements”, *Journal of
2483 Physics: Conference Series* **404** (2012), no. 1, 012014.
- 2484 [63] CMS Collaboration Collaboration, “Algorithms for b Jet identification in CMS”,
2485 Technical Report CMS-PAS-BTV-09-001, CERN, 2009. Geneva, (Jul, 2009).
- 2486 [64] “Performance of b tagging at $\sqrt{s}=8$ TeV in multijet, ttbar and boosted topology
2487 events”,.
- 2488 [65] T. C. collaboration, “Identification of b-quark jets with the CMS experiment”,
2489 *Journal of Instrumentation* **8** (2013), no. 04, P04013.
- 2490 [66] CMS Collaboration Collaboration, “CMS. The TriDAS project. Technical design
2491 report, vol. 1: The trigger systems”,.
- 2492 [67] CMS Collaboration Collaboration, “CMS: The TriDAS project. Technical design
2493 report, Vol. 2: Data acquisition and high-level trigger”,.
- 2494 [68] J. B. et al., “Calibration and Performance of the Jets and Energy Sums in the
2495 Level-1 Trigger”,.
- 2496 [69] B. et al., “Study of Level-1 Trigger Jet Performance in High Pile-up Running
2497 Conditions”,.
- 2498 [70] J. J. Brooke, “Performance of the CMS Level-1 Trigger”, Technical Report
2499 CMS-CR-2012-322. CERN-CMS-CR-2012-322, CERN, Geneva, (Nov, 2012).
- 2500 [71] CMS Collaboration Collaboration, “Search for supersymmetry in final states with
2501 missing transverse energy and 0, 1, 2, or at least 3 b-quark jets in 7 TeV pp
2502 collisions using the variable alphaT”, *JHEP* **1301** (2013) 077,
2503 [doi:10.1007/JHEP01\(2013\)077](https://doi.org/10.1007/JHEP01(2013)077), [arXiv:1210.8115](https://arxiv.org/abs/1210.8115).

- 2504 [72] CMS Collaboration Collaboration, “SUSY searches with dijet events”,.
- 2505 [73] L. Randall and D. Tucker-Smith, “Dijet Searches for Supersymmetry at the Large
2506 Hadron Collider”, *Phys. Rev. Lett.* **101** (Nov, 2008) 221803,
2507 [doi:10.1103/PhysRevLett.101.221803](https://doi.org/10.1103/PhysRevLett.101.221803).
- 2508 [74] CMS Collaboration Collaboration, “Search strategy for exclusive multi-jet events
2509 from supersymmetry at CMS”, Technical Report CMS-PAS-SUS-09-001, CERN,
2510 2009. Geneva, (Jul, 2009).
- 2511 [75] CMS Collaboration Collaboration, “Calorimeter Jet Quality Criteria for the First
2512 CMS Collision Data”, Technical Report CMS-PAS-JME-09-008, CERN, 2010.
2513 Geneva, (Apr, 2010).
- 2514 [76] T. C. collaboration, “Performance of CMS muon reconstruction in pp collision
2515 events at $\sqrt{s} = 7 \text{ TeV}$ ”, *Journal of Instrumentation* **7** (2012), no. 10, P10002.
- 2516 [77] The CMS Collaboration, “Performance of CMS muon reconstruction in pp collision
2517 events at 7 TeV”, *Journal of Instrumentation* **7** (October, 2012) 2P,
2518 [doi:10.1088/1748-0221/7/10/P10002](https://doi.org/10.1088/1748-0221/7/10/P10002), [arXiv:1206.4071](https://arxiv.org/abs/1206.4071).
- 2519 [78] CMS Collaboration Collaboration, “Search for supersymmetry in events with
2520 photons and missing energy”, Technical Report CMS-PAS-SUS-12-018, CERN,
2521 Geneva, (2012).
- 2522 [79] M. Cacciari and G. P. Salam, “Pileup subtraction using jet areas”, *Phys.Lett.*
2523 **B659** (2008) 119–126, [doi:10.1016/j.physletb.2007.09.077](https://doi.org/10.1016/j.physletb.2007.09.077),
2524 [arXiv:0707.1378](https://arxiv.org/abs/0707.1378).
- 2525 [80] Z. Bern et al., “Driving missing data at next-to-leading order”, *Phys. Rev. D* **84**
2526 (Dec, 2011) 114002, [doi:10.1103/PhysRevD.84.114002](https://doi.org/10.1103/PhysRevD.84.114002).
- 2527 [81] CMS Collaboration Collaboration, “Data-Driven Estimation of the Invisible Z
2528 Background to the SUSY MET Plus Jets Search”, Technical Report
2529 CMS-PAS-SUS-08-002, CERN, 2009. Geneva, (Jan, 2009).
- 2530 [82] Z. Bern et al., “Driving Missing Data at Next-to-Leading Order”, *Phys.Rev.* **D84**
2531 (2011) 114002, [doi:10.1103/PhysRevD.84.114002](https://doi.org/10.1103/PhysRevD.84.114002), [arXiv:1106.1423](https://arxiv.org/abs/1106.1423).
- 2532 [83] W. Beenakker, R. Hopker, M. Spira, and P. Zerwas, “Squark and gluino production
2533 at hadron colliders”, *Nucl.Phys.* **B492** (1997) 51–103,
2534 [doi:10.1016/S0550-3213\(97\)80027-2](https://doi.org/10.1016/S0550-3213(97)80027-2), [arXiv:hep-ph/9610490](https://arxiv.org/abs/hep-ph/9610490).

- 2535 [84] S. Abdullin *et al.*, “The Fast Simulation of the CMS Detector at LHC”, *Journal of*
2536 *Physics: Conference Series* **331** (2011), no. 3, 032049.
- 2537 [85] S. Banerjee, M. D. Hildreth, and the CMS Collaboration, “Validation and Tuning
2538 of the CMS Full Simulation”, *Journal of Physics: Conference Series* **331** (2011),
2539 no. 3, 032015.
- 2540 [86] C. Collaboration, “CMS Btag POG : CMS b-tagging performance database”,
2541 (2013). <https://twiki.cern.ch/twiki/bin/viewauth/CMS/BtagPOG>.
- 2542 [87] CMS Collaboration Collaboration, “CMS Luminosity Based on Pixel Cluster
2543 Counting - Summer 2012 Update”, Technical Report CMS-PAS-LUM-12-001,
2544 CERN, Geneva, (2012).
- 2545 [88] R. Cousins, “Probability Density Functions for Positive Nuisance Parameters”,
2546 (2012). <http://www.physics.ucla.edu/cousins/stats/cousinslognormalprior.pdf>.
- 2547 [89] L. Moneta, K. Cranmer, G. Schott, and W. Verkerke, “The RooStats project”,
2548 2010. [arXiv:1009.1003](https://arxiv.org/abs/1009.1003).
- 2549 [90] F. James and M. Roos, “Minuit: A System for Function Minimization and Analysis
2550 of the Parameter Errors and Correlations”, *Comput.Phys.Commun.* **10** (1975)
2551 343–367, [doi:10.1016/0010-4655\(75\)90039-9](https://doi.org/10.1016/0010-4655(75)90039-9).
- 2552 [91] A. L. Read, “Presentation of search results: the CL_s technique”, *Journal of*
2553 *Physics G: Nuclear and Particle Physics* **28** (2002), no. 10, 2693.
- 2554 [92] T. Junk, “Confidence level computation for combining searches with small
2555 statistics”, *Nuclear Instruments and Methods in Physics Research Section A:*
2556 *Accelerators, Spectrometers, Detectors and Associated Equipment* **434** (1999),
2557 no. 23, 435 – 443, [doi:\[http://dx.doi.org/10.1016/S0168-9002\\(99\\)00498-2\]\(http://dx.doi.org/10.1016/S0168-9002\(99\)00498-2\)](https://doi.org/10.1016/S0168-9002(99)00498-2).
- 2558 [93] A. L. Read, “Modified frequentist analysis of search results (the CL_s method)”,.
- 2559 [94] G. Cowan, K. Cranmer, E. Gross, and O. Vitells, “Asymptotic formulae for
2560 likelihood-based tests of new physics”, *The European Physical Journal C* **71**
2561 (2011), no. 2, 1–19, [doi:10.1140/epjc/s10052-011-1554-0](https://doi.org/10.1140/epjc/s10052-011-1554-0).
- 2562 [95] G. Cowan, K. Cranmer, E. Gross, and O. Vitells, “Asymptotic formulae for
2563 likelihood-based tests of new physics”, *European Physical Journal C* **71** (February,
2564 2011) 1554, [doi:10.1140/epjc/s10052-011-1554-0](https://doi.org/10.1140/epjc/s10052-011-1554-0), [arXiv:1007.1727](https://arxiv.org/abs/1007.1727).

2565 Acronyms

2566	ALICE	A Large Ion Collider Experiment
2567	ATLAS	A Toroidal LHC ApparatuS
2568	APD	Avalanche Photo-Diodes
2569	BSM	Beyond Standard Model
2570	CERN	European Organization for Nuclear Research
2571	CMS	Compact Muon Solenoid
2572	CMSSM	Compressed Minimal SuperSymmetric Model
2573	CSC	Cathode Stripe Chamber
2574	CSV	Combined Secondary Vertex
2575	CSVM	Combined Secondary Vertex Medium Working Point
2576	DT	Drift Tube
2577	ECAL	Electromagnetic CALorimeter
2578	EB	Electromagnetic CALorimeter Barrel
2579	EE	Electromagnetic CALorimeter Endcap
2580	ES	Electromagnetic CALorimeter pre-Shower
2581	EMG	Exponentially Modified Gaussian
2582	EPJC	European Physical Journal C
2583	EWK	Electroweak Sector
2584	GCT	Global Calorimeter Trigger
2585	GMT	Global MuonTrigger
2586	GT	Global Trigger
2587	HB	Hadron Barrel
2588	HCAL	Hadronic CALorimeter

2589	HE	Hadron Endcaps
2590	HF	Hadron Forward
2591	HLT	Higher Level Trigger
2592	HO	Hadron Outer
2593	HPD	Hybrid Photo Diode
2594	ISR	Initial State Radiation
2595	LUT	Look Up Table
2596	L1	Level 1 Trigger
2597	LEP	Large Electron-Positron Collidior
2598	LHC	Large Hadron Collider
2599	LHCb	Large Hadron Collider Beauty
2600	LSP	Lightest Supersymmetric Partner
2601	NLL	Next to Leading Logarithmic Order
2602	NLO	Next to Leading Order
2603	NNLO	Next to Next Leading Order
2604	POGs	Physics Object Groups
2605	PS	Proton Synchrotron
2606	QED	Quantum Electro-Dynamics
2607	QCD	Quantum Chromo-Dynamics
2608	QFT	Quantum Field Theory
2609	RBXs	Readout Boxes
2610	RPC	Resistive Plate Chamber
2611	RCT	Regional Calorimeter Trigger
2612	RMT	Regional Muon Trigger
2613	SUSY	SUperSYmmetry

₂₆₁₄	SM	Standard Model
₂₆₁₅	SMS	Simplified Model Spectra
₂₆₁₆	SPS	Super Proton Synchrotron
₂₆₁₇	TF	Transfer Factor
₂₆₁₈	TP	Trigger Primative
₂₆₁₉	VEV	Vacuum Expectation Value
₂₆₂₀	VPT	Vacuum Photo-Triodes
₂₆₂₁	WIMP	Weakly Interacting Massive Particle